Amperometric Gas Sensor Technologies

Luke James Saunders

A thesis submitted in partial fulfilment of the requirements of

the degree of Doctor of Philosophy

School of Natural and Environmental Sciences

Newcastle University

Newcastle upon Tyne, UK

March 2020

Abstract

This project investigated the electrochemistry of carbon monoxide and various volatile organic compounds (VOCs primary alcohols, ketones and esters) with the aim of understanding the details of the operation of amperometric CO sensors and of developing VOC sensors of similar performance. The electrochemical devices studied were based on commercial CO sensors (supplied by Alphasense Ltd) and specially modified Alphasense sensor devices designed to measure VOCs.

In amperometric response to carbon monoxide, all of the tested sensors (kindly provided by Alphasense) showed an increase in current flowing within the sensor. This increase in current was directly proportional to the concentration of analyte within the zero-air carrier gas. The large capacitance of the devices prevents the use of standard potentiodynamic techniques to interrogate the mechanism. Instead we employed concentration-step experiments at constant potential using a gas flow system under digital mass flow control.

A diffusion-based model for the sensors was derived and solved. Custom modelling software using nonlinear least squares was developed to fit the experimental data and to derive estimates of the apparent membrane/diffusion layer thicknesses and the apparent diffusion coefficient of the analyte.

The standard CO-AF sensors whilst exposed to carbon monoxide were calculated as having (at 20°C) layer thicknesses (L) on the order of 10^{-1} cm, this is commensurate with the physical distance from the top face of the sensor to the electrolyte boundary of approximately 0.3 (±0.1) cm. It also gave CO diffusion coefficients (D) on the order of 10^{-3} - 10^{-2} cm^2 s^{-1} (at 20°C). These values suggest current-limiting diffusion in the gas phase rather than the thin liquid layer (D approximately 10^{-6} cm^2 s^{-1}) covering the working electrode. Increasing the thickness of the semi-permeable membrane in the standard CO-AF sensor gave an increase in L, thus validating the diffusion model.

In response to VOCs, the CO-A1 sensors (kindly provided by Alphasense) only gave a significant amperometric response to alcohol and aldehyde functional groups. This is in line with the current literature and was hypothesised to be due to those functional groups being relatively easily chemisorbed and subsequently electrooxidised at platinum under aqueous acidic conditions. The unresponsive VOCs were thought to be due to a combination of lack of solubility and high oxidation potential. Again, the sensors showed directly proportional current responses to the concentration of VOC analyte within the carrier gas.

At all temperatures the CO-A1 sensors showed layer thicknesses (*L*) on the order of µm or smaller, and VOC diffusion coefficients (*D*) were in the 10^{-8} cm^2s^{-1} range or smaller. Thus, indicating that the rate limiting step for the detection of alcohols and aldehydes was within the 5M sulfuric acid electrolyte solution or perhaps a kinetic barrier, e.g., for dissolution at the air/electrolyte interface.

Finally, some initial studies on alternative electrolytes for amperometric gas sensors were carried out. The motivation for this is that the standard electrolyte (5M H_2SO_4) is corrosive and hygroscopic. The choice of electrolyte for amperometric devices is not simple because it must have a negligible rate of evaporation in air over long periods (1-2 years). Most aqueous electrolytes are unsuitable and only a few organic electrolytes (propylene carbonate) are both non-volatile and non-toxic. An alternative is a polyionic hydrogel; polyacrylate was chosen and the electrochemistry of some simple redox compounds were investigated. However, the hydrogels ultimately proved unsuitable for the long-term requirements of the sensors due to weight loss over time.

Acknowledgements

The author gratefully acknowledges Alphasense Ltd for the opportunity, funding support, and guidance of this project. None of the work would have been possible without their support.

The author would also like to thank Dr Ben Horrocks and Professor Andrew Houlton for their continued guidance and support over the years.

A big thank you is also due to all of the staff and fellow students of Newcastle University Chemistry Department who were vital contributors to this work and the continued sanity of the author. The support staff in the various workshops were also of invaluable help throughout.

Thanks are also given to the author's friends and family. This work is dedicated to my daughter.

Abbreviations

A	area of working electrode	(cm^2)
Ag/AgCl	silver chloride electrode	
C	capacitance	($F = Q\ V^{-1}$)
c	concentration	($mols\ dm^{-3}$)
CE	counter electrode	
CO	carbon monoxide	
CV	cyclic voltammetry	
D	diffusion coefficient	($cm^2\ s^{-1}$)
DMFC	digital mass flow controller	
d_{OHP}	outer Helmholtz plane	
E	cell potential	(V)
E°	formal reduction potential	(V)
EIS	electrochemical impedance spectroscopy	
ε_o	permittivity of free space	($F\ m^{-1}$)
ε_r	permittivity of a medium	($F\ m^{-1}$)
f	Faraday constant	($Q\ mol^{-1}$)
F	Farad	($Q\ V^{-1}$)
f	frequency	(Hz)
H^{cc}	Henry's law solubility constant	dimensionless
H^{cp}	Henry's law pressure constant	dimensionless
Hg/Hg_2SO_4	mercury/mercurous sulphate	
HPLC	high pressure liquid chromatography	
Hz	hertz	(s^{-1})
I	current	(amperes)
IR	infra-red	
j	flux	($I\ cm^{-2}\ s^{-1}$)
K	kelvin	
L	layer thickness	(cm)
LD_{50}	median lethal dose	($g\ kg^{-1}$)
n	number of electrons	
N_2	nitrogen	
P	pressure	(Pa = pascals)
PAA	poly(acrylamide co-acrylic) acid	
ppm	parts per million	
Pt	platinum	
Q	charge	(coulombs = *I* x s)
R	gas constant	($joules\ K^{-1}\ mol^{-1}$)
Ru	ruthenium	
SHE	standard hydrogen electrode	(V)
T	temperature	(K)
T_0	time at start of gas on	
V	volts	
VOC	volatile organic compound	
WE	working electrode	
Z	impedance	(Hz)
ΔI	change in current	(amperes)

Contents

Abstract ……i

Acknowledgements……iii

Abbreviations……iv

Contents……v

List of Figures……x

List of Tables……xix

1.0 Introduction……1

1.1 Environmental Air Quality……3

1.2 Gas Sensor Technologies……4

1.2.1 Polarization Detectors (PIDs)……6

1.2.2 Solid State Semiconductor Sensors……8

1.2.3 Amperometric Gas Sensors……10

1.2.4 Sensor Technology Considerations……12

1.3 Electrochemical Background to Amperometric Gas Sensing……13

1.3.1 Electrode Materials……13

1.3.2 Electrode-Electrolyte Interface……13

1.4 Electrochemical Methods……17

1.4.1 Cyclic Voltammetry……17

1.4.2 Steady-State Voltammetry……23

1.4.3 Impedance Spectroscopy……25

1.4.4 Chronoamperometry……29

1.5 Electron Transfer Theory……30

1.6 Electrode Surface Effects……32

1.7 Stack Configuration……34

1.8 Outline and Motivation of the Project……35

1.8.1 Carbon Monoxide……35

1.8.2 VOCs……36

1.8.3 Hydrogels……38

1.9 Summary……39

1.10 References……40

2.0 Experiment Methods……48

2.1 Electrochemical Measurements in Hydrogel Electrolytes……49

2.1.1 Electrochemical Measurements in Gas Sensors……50

2.2 Electrochemistry Techniques……52

2.2.1 Cyclic Voltammetry……52

2.2.2 Impedance Spectroscopy……52

2.2.3 Chronoamperometry……53

2.2.4 Rate Effects……57

2.3 Gas Testing Rig……59

2.4 Vapour Pressure……..64

2.5 Hydrogel Redox Couple Compounds……66

2.6 Hydrogel Weight Tracking……69

2.7 Hydrogel Rheology……70

2.8 Optical Microscopy and Electron Microscopy……72

2.9 Summary……73

2.10 References……74

3.0 Mathematical Modelling of The Sensor Response……75

3.1 Steady-State Response of Amperometric Gas Sensors……77

3.2 Transient Response of Amperometric Gas Sensor……79

3.3 Multiple Diffusion Barriers……82

3.4 Summary……87

4.0 Carbon Monoxide Detection……88

4.1 CO-AF Response to Carbon Monoxide using Cyclic Voltammetry……93

4.1.1 Impedance Spectroscopy……95

4.1.2 Chronoamperometry……101

4.1.3 Modelling The Chronoamperometric Response……104

4.1.4 Temperature Dependence……107

4.1.5 Voltage Dependence of the CO-AF Sensors……110

4.2 Summary……112

4.3 References……113

5.0 CM-A1 Sensor Response to Carbon Monoxide……114

5.1 Cyclic Voltammetry at CM-A1 Sensors……118

5.2 Impedance Spectroscopy of CM-A1 Sensors……120

5.3 Chronoamperometry at CM-A1 Sensors……122

5.4 Modelling the Chronoamperometric Response……124

5.5 Voltage Dependence of CM-A1 Sensors……128

5.6 Summary……129

5.7 References……130

6.0 CO-A1 Sensor Response to Carbon Monoxide……131

6.1 Cyclic Voltammetry of CO-A1 Sensors……132

6.2 Impedance Spectroscopy of CO-A1 Sensors……133

6.3 Chronoamperometry at CO-A1 Sensors……135

6.4 Modelling the Chronoamperometric Response of CO-A1 Sensors……137

6.5 Voltage Dependence of CO-A1 Sensor……141

6.6 Summary……142

6.7 References……144

7.0 VOC Detection……145

7.1 Electrooxidation of VOCs……147

7.2 Cyclic Voltammetry……150

7.3 Impedance Spectroscopy……152

7.4 Chronoamperometry……155

7.4.1 Selectivity……157

7.4.2 Linearity……159

7.4.3 Sensitivity……162

7.4.4 Reusability……164

7.5 Voltage Bias……165

7.6 Modelling the Chronoamperometric Response to VOCs……167

7.6.1 Temperature Dependence……175

7.7 Summary……179

7.8 References……181

8.0 Hydrogels……183

8.1 Hydrogel Characterisation……187

8.2 Hydrogel Weight Tracking……191

8.3 Cyclic Voltammetry of Hydrogels Containing Redox Couple Compounds……195

8.4 Summary……201

8.5 References……203

9.0 Conclusions……205

9.1 Future Work……208

9.2 References……211

List of Figures

1.1 Schematic of photoionization gas sensor……6

1.2 Diagram of manufactured PID sensor construction……6

1.3 Schematic of tin oxide gas sensor……8

1.4 Diagram of metal oxide sensor circuitry……9

1.5 Schematic of the different layers at the electrode surface and in the liquid electrolyte……14

1.6a Potential against time for a typical cyclic voltammogram……18

1.6b Typical cyclic voltammogram showing peak shape……18

1.6c Species O concentration as a fraction of bulk concentration during cyclic voltammetry……19

1.7 Electron transfer energy levels between the electrode and analyte molecule……22

1.8 Theoretical steady state voltammogram for the oxidation of an analyte……24

1.9 Relationship between real and imaginary parts of the impedance……26

1.10 Combination of a capacitor and a resistor connected in series; the corresponding plot……27

1.11 Graph showing typical chronoamperometric response to the electron transfer reaction at electrode surface……29

1.12 Energy diagram showing energy profile of electron transfer reactions……30

1.13 Schematic of Pt(100) with surface atoms (blue) arranged above sub-surface atoms (silver)……32

1.14a Schematic of Pt(110) with surface atoms (blue) arranged above sub-surface atoms (silver)……33

1.14b Schematic of Pt(111) with surface atoms (blue) arranged above sub-surface atoms (silver)……33

1.15 Stack configuration of CO-AF sensor and top cover……34

1.16 Structures of phenol (left) and para-cresol (right)……..37

1.17 Structure of cross-linked polymer formed as hydrogel……..38

2.1 Schematic of Electrochemical Hydrogel Experiments with three electrode potentiostat as standard……49

2.2 Schematic of Alphasense three electrode sensor……51

2.3 Table and graph of CO-AF sensor showing proportional response……53

2.4 Graph showing linear relationship between analyte concentration and current response……54

2.5 Example graph showing change in analyte concentration when gas valve is turned on……55

2.6 Graph showing chronoamperometric response upon exposure to analyte vapour……56

2.7 Example voltage bias experiment for the CO-AF sensor response to pulsed CO……..58

2.8 Photograph and schematic of gas rig……..59

2.9 Schematic of DMFC device with butterfly valve and air probe to regulate gas flow……60

2.10 Schematic of gas flow setup during sensor experiments to alleviate settling period……61

2.11 Comparison of actual DMFC operation (a) and assumed operation in mathematical model (b)….62

2.12 Graph of pressure against temperature derived from the Antoine parameters for ethanol……65

2.13 Structure of potassium ferrocyanide (counter ions not shown)……..67

2.14 Structure of hexaammineruthenium [III] chloride (counter ions not shown)……..67

2.15 Structure of para-benzoquinone, semi-quinone, hydroquinone (respectively)……68

2.16 Schematic of 100% humidity weight tracking experiment with vials containing known weights of hydrogels in demineralised water sealed by tinfoil……69

2.17 Graph of shear stress against shear rate for typical rheology models……71

2.18 Electron microscopy image of Pt working electrode taken from a CO-AF sensor……..72

2.19 Electron microscopy image of Pt/Ru working electrode taken from a CM-A1 sensor……..72

3.1 Schematic of the different diffusion barriers and phase changes……76

3.2 Plot of concentration against distance from the working electrode……77

3.3 Plot of concentration against distance from the working electrode, with kinetic barriers……78

3.4 Concentration step at a membrane covered electrode……79

3.5 Example calculation of flux as a fraction of the steady-state value against time……81

3.6 Example fit of the regression model to a finite difference simulation……84

3.7 Graph showing typical experimental data for current in a CO sensor against time……..86

4.1a Schematic of layers at the working electrode of a CO-AF sensor……90

4.1b Electron micrograph of the working electrode……...90

4.2 Cyclic voltammogram of Pt response to CO in 5M H_2SO_4 electrolyte……92

4.3 Cyclic voltammogram of a CO-AF sensor in different gases at normal scan rate……..93

4.4 Cyclic voltammogram of CO-AF sensor in different gases at a very slow scan rate……94

4.5 Nyquist plot of Alphasense CO-AF sensor in normal air at different dc voltages……95

4.6 Plot of –Z" against inverse frequency of CO-AF in normal air at 0.0 V applied dc potential……96

4.7 Plot of –Z" against inverse frequency (CO-AF at 0.2 V steady state in normal air at 20° C……96

4.8 Nyquist plot of Alphasense CO-AF sensor in CO at constant gas flow rate at 20° C at different steady state voltages……97

4.9 Plot of –Z" against inverse frequency of CO-AF in CO at 0.0 V steady state……..98

4.10 Plot of –Z" against inverse frequency of CO-AF in CO at 0.3 V steady state……..98

4.11 Graph the initial chronoamperometric response of a CO-AF sensor upon application of different potentials in air……..100

4.12 Graph showing CO-AF sensor selectivity for CO over H_2O at steady flow rate under standard conditions at 0.0 V……101

4.13 Graph showing CO-AF sensor selectivity response to different gases at intervals in standard conditions at 0.0 V steady state……102

4.14 Graph showing proportional response to pulses of increasing CO concentration over time at 0.0 V steady state in standard conditions……103

4.15 Graph showing relationship between amperometric response and CO gas concentration……103

4.16 Graph showing least square regression parameters used within mathematical model……104

4.17 Sensor response at 0.0 V steady state in 20° C pulsed CO (400 ppm) experimental data (blue), line of best fit (red), difference between the two values (green)……105

4.18 Sensor response at 0.0 V steady state in 20° C pulsed CO (200 ppm) experimental data (blue), line of best fit (red), difference between the two values (green)……105

4.19 Sensor response after 200 ppm CO at 0.0 V steady state in 20° C experimental data (blue), line of best fit (red), difference between the two values (green)……..106

4.20 Calculated effective layer thickness values for CO-AF sensor……108

4.21 Calculated effective diffusion coefficient values for CO-AF sensor……108

4.22 Graph showing standard CO-AF sensor response to 1000 ppm CO saturated air at 20° C at different steady state voltages……..110

4.23 Graph showing standard CO-AF sensor response to 1000 ppm CO saturated air at 40° C……..111

5.1a Schematic of CM-A1 sensor……115

5.1b Bright field microscopy image showing edge of Pt working electrode……116

5.1c Bright field microscopy image showing Pt on centre point of PTFE……116

5.1d Bright field image of Pt:Ru mixed metal working electrode on PTFE……117

5.2 Cyclic voltammogram of CM-A1 sensor at 1 mV s^{-1} scan rate……118

5.3 Cyclic voltammogram of CM-A1 sensor at 0.5 mV s^{-1} scan rate……119

5.4 Nyquist plot of CM-A1 sensor in normal air at different steady state voltages……120

5.5 Plot of -Z” against inverse frequency of CM-A1 sensor in normal air at 0.0 V dc potential……120

5.6 Nyquist plot of CM-A1 sensor in CO at constant gas flow rate……121

5.7 Plot of -Z” against inverse frequency of CM-A1 sensor in CO at 0.0 V dc potential……121

5.8 Graph showing CM-A1 sensor proportional response to pulses of increasing CO……..122

5.9 Graph showing relationship between amperometric response and CO gas concentration…..123

5.10 Sensor response at 0.0 V steady state in 300 ppm CO saturated air……124

5.11 Sensor response at 0.0 V steady state in 500 ppm CO saturated air……125

5.12 Sensor response at 0.0 V steady state after 300 ppm CO saturated air……125

5.13 Graph of effective layer thickness (*L*) values for response to CO……127

5.14 Graph of effective diffusion coefficient (*D*) values for response to CO……127

5.15 Graph showing CM-A1 sensor response to 350 ppm CO saturated air……..128

6.1 Cyclic voltammogram of CO-A1 sensor response to CO and zero grade air……132

6.2 Nyquist plot of CO-A1 sensor response to zero grade air at different steady state voltages……133

6.3 Plot of -Z" against inverse frequency of CO-A1 sensor in zero grade air at 0.0 V steady state……..133

6.4 Nyquist plot of CO-A1 sensor response to CO at different steady state voltages……134

6.5 Plot of -Z" against inverse frequency of CO-A1 sensor in zero grade air at 0.0 V steady state……..134

6.6 Graph showing CO-A1 sensor chronoamperometric response to increasing CO concentrations..135

6.7 Calibration plot showing the relationship between CO-A1 current response and CO……..136

6.8 Sensor response of CO-A1 sensor to 100 ppm CO saturated air……137

6.9 CO-A1 sensor response to 300 ppm saturated air……..138

6.10 CO-A1 sensor response after 300 ppm CO saturated air……138

6.11 Graph of *L* values for sensor response to CO with and without permanganate powder……139

6.12 Graph of *D* values for sensor response to CO with and without permanganate powder……139

6.13 Graph showing CO-A1 sensor response to 320 ppm CO at different steady state voltages……141

7.1 Schematic of CO-A1 sensor working electrode……..146

7.2 Reaction steps of alcohol electrooxidation at the Pt electrode……..149

7.3 Cyclic voltammograms of a CO-A1 sensor in air (control) and methanol saturated air……..150

7.4 Cyclic voltammograms of a CO-A1 sensor in air (control) and ethanol saturated air……..151

7.5 Nyquist plot of an Alphasense CO-A1 sensor in heptan-1-ol saturated air at different dc voltages at 20 ^{o}C……..152

7.6 Plot of -Z" against inverse frequency of CO-A1 sensor in heptan-1-ol saturated air at 0.0 V dc at 20 ^{o}C……...152

7.7 Nyquist plot of Alphasense CO-A1 sensor in ethanol saturated air at different dc voltages at 50 ^{o}C……...153

7.8 Plot of -Z" against inverse frequency of CO-A1 sensor in ethanol saturated air at 0.0 V dc at 50 ^{o}C……...153

7.9 Graph showing CO-A1 sensor selectivity response to methanol versus acetone at steady flow rate in 20 ^{o}C at 0.0 V dc……...155

7.10 Graph showing CO-A1 sensor response to pulsed heptan-1-ol versus heptan-4-one saturated air at 20 ^{o}C at 0.0 V dc……...156

7.11 Graph showing CO-A1 sensor selectivity response to pulsed methanol versus pulsed ethyl ethanoate at 20 ^{o}C at 0.0 V dc……...157

7.12 Graph showing CO-A1 sensor response to pulsed acetic acid versus propionic acid versus heptan-1-ol saturated air at 20 ^{o}C at 0.0 V dc……..158

7.13 Graph showing CO-A1 sensor response to pulses of increasingly concentrated propan-2-ol and ethanol saturated air in 20 °C at 0.0 V dc.....160

7.14 Example calibration plots for a CO-A1 sensor to (i) propan-2-ol and (ii) ethanol vapour in separate experiments.....160

7.15a Current response against concentration of hexanal at 20 °C.....161

7.15b Current response against concentration of tert-butanol at 20 °C.....161

7.16 Polarity against molar mass of primary alcohols from methanol to heptanol.....162

7.17 Sensitivity of the CO-A1 sensor to a primary, secondary and a tertiary alcohol.....163

7.18 Graph showing CO-A1 sensor chronoamperometric response to propanal followed by methanol at 20 °C at 0.0 V dc.....164

7.19 Graph showing CO-A1 sensor response to 500 ml min^{-1} methanol saturated air at 20 °C.....165

7.20 Graph showing CO-A1 sensor response to 500 ml min^{-1} propanal saturated air at 20 °C.....166

7.21 Sensor response at 0.0 V dc in isopropanol at 30% of the saturated vapour pressure at 20 °C....167

7.22 Sensor response at 0.0 V dc in hexanal at 50% of the saturated vapour pressure at 20 °C.....168

7.23 Sensor response at 0.0 V dc in tert-butanol at 60% of the saturated vapour pressure at 30 °C....168

7.24 Sensor response at 0.0 V dc after switching to pure air from 50% hexanal saturated air at 20 °C.....170

7.25 Sensor response at 0.0 V dc after 30% propanol saturated air at 30 °C.....171

7.26 Collated effective thickness (*L*) data for the alcohols at all temperatures.....175

7.27 Collated apparent diffusion coefficient data (D) for the alcohols at all temperatures.....176

7.28 Graph of collated *L* data for the aldehydes at all temperatures.....176

7.29 Graph of collated *D* data for the aldehydes at all temperatures.....177

7.30 Example Arrhenius plot for the apparent diffusion coefficient of methanol in a CO-A1 device...178

7.31 Diagram showing the construction of the CO-AF working electrode, porous membrane and permanganate filter layer.....180

7.32 Diagram showing the construction of the CO-A1 working electrode and porous membrane as used in this chapter.....180

8.1 Flooding of the sensor by sulfuric acid electrolyte.....185

8.2 Poly acrylic acid illustrating the interchain hydrogen bonds responsible for gelation.....187

8.3 Shear stress as a function of shear rate. Behaviour typical of non-Newtonian fluids.....188

8.4 Critical strain points of hydrogels at different PAA concentrations.....189

8.5 Graph of different PAA weights with their recorded weights against days spent exposed to air in normal laboratory conditions.....192

8.6 Graph of different PAA weights with their recorded weights against days spent exposed to humid air in a sealed vessel.....193

8.7 Cyclic voltammogram of potassium ferrocyanide gels with different amounts of PAA.....195

8.8 Poly acrylic acid illustrating the interchain hydrogen bonds responsible for gelation.....196

8.9 Cyclic voltammogram of hexaammineruthenium chloride gels with different amounts of PAA.....197

8.10 Hexaammineruthenium chloride diffusion coefficient determined by steady-state microelectrode voltammetry against PAA concentration.....198

8.11 Steady-state microelectrode voltammograms of para-benzoquinone-containing gels with different amounts of PAA.....199

8.12 Para-benzoquinone diffusion coefficient estimated by steady-state microelectrode voltammetry against PAA concentration.....200

9.1 Shear stress of different hydrogel concentrations at constant shear rate.....207

9.2 Cyclic voltammogram of CO-AF sensor response to CO with wide current range.....210

List of Tables

1.1 Commercial Sensor Applications……5

2.1 Components of the different sensors used within the thesis……50

2.2 Chemical composition of zero grade air……59

2.3 Vapour pressures for the VOCs used……64

3.1 Collated Henry's Law constants of carbon monoxide……85

4.1 Calculated values for CO-AF sensor in CO……107

5.1 Compiled values for CM-A1 sensor response to CO……125

6.1 Compiled values for CO-A1 sensor response to CO gas……137

7.1 Compiled linear equations of the calibrations for the different VOCs……159

7.2 Compiled calculated values of *L* and *D* from CO-A1 sensors at 20 ^{o}C……173

7.3 Activation energies for the apparent diffusion coefficients of alcohols and aldehydes……178

Chapter 1

1.0 Introduction

There are many harmful gases that either naturally occur in certain environments or are the result of industrial processes [1]. For this reason, the monitoring of air quality within urban and rural areas is becoming of increasing importance to people [2 - 5]. There are several standard instrumental techniques capable of determining gas concentration, e.g. mass spectrometry, absorption spectroscopy or gas chromatography. However, many instruments are expensive or bulky and are often restricted to centralised laboratories. In this context an analytical instrument is distinguished from a sensor by a combination of cost and portability. That means sensing devices are suited for distributed applications in the environment, e.g., monitoring urban air pollution at multiple sites in a city, even though their analytical performance may not match that of a laboratory instrument. To that end, research into gas sensor technology remains an important aspect of improving health and safety metrics.

Gas sensors can be found in a wide variety of areas, from fire detection and industrial safety to ozone monitoring and ammonia detection [6 - 9]. There are a wide variety of gas sensors available today, each with different detection methods, design, and applications. The main detection methods used range from photoionization detection, infra-red absorption, ultrasound detection, semi-conductor resistance changes (such as tin oxide) and electrochemical methods [10 – 13]. All allow varying degrees of sensitivity and selectivity. This thesis focusses upon the use of electrochemical gas sensors, namely amperometric techniques for the detection of carbon monoxide and a range of VOCs (volatile organic compounds) that are of commercial and scientific interest. The major types of commercially-viable gas sensors are discussed in section 1.2. Amperometric gas sensors are not a new technology [14 - 17], many different approaches to it have been developed over the years [18, 19]. The amperometric method involves current measured at a fixed applied potential as the device is exposed to the sample. An electrochemical reaction at the working electrode produces the current measured.

Gas sensor technology provides quantitative analysis of the analyte gas using Fick's equation for mass transport by diffusion and the gas laws to describe the sensor operation. Electrochemical gas sensors use a similar technology to modern fuel cells (electron transfer reactions in various electrode/electrolyte interfaces generate faradaic currents). Fuel cell research is mainly driven by the need to keep up with global energy demand and to find more efficient means of energy conversion than simply burning fossil fuels [20 - 23]. Fuel cells work as galvanic cells, where a spontaneous chemical reaction produces electrons to drive an electrical circuit. Amperometric gas sensors work in the opposite sense; they are electrolytic cells, where an applied electrical driving force causes a chemical reaction to occur. Despite this difference in the mode of operation, the cell chemistry and composition of fuel cells and amperometric gas sensors may be very similar [24].

Electrochemical gas sensors are widely used within industrial settings and so a greater understanding of their inner workings is important. Whilst there are many analytical techniques available for studying electrochemical systems (such as infra-red spectroscopy, scanning electron microscopy, and atomic force microscopy), these all require physical access to the working electrode (the site of the electrochemical reaction). This may be feasible in a laboratory setting, where a custom electrochemical cell can be built and studied, but investigation of commercial gas sensors requires a different approach. This is because a commercial gas sensor is typically encased inside plastic and not capable of being opened without damaging it, which presents a challenge of investigating the electrochemistry of the sensor. A novel approach is required, a mathematical modelling approach based upon experimental results from different types of Alphasense amperometric gas sensors. The aim of the work was to develop a non-destructive method for analysing the different factors that affect the operation of the Alphasense CO-AF sensor (designed to detect CO gas via chronoamperometry). A mathematical model was developed based upon electrochemical theory and using known quantities of carbon monoxide gas, this model would then enable the derivation of the diffusion rate of analyte through the sensor and the determination of the influence of the different phases present within the sensor. This could then be used to infer the rate limiting step for the electrochemical reaction and give a greater understanding of the complex system employed within the sensor device.

1.1 Environmental Air Quality

The use of gas sensors to monitor air quality levels has recently become of scientific and political significance. The results of real-time tracking of air pollutants such as NO_2 and CO within urban environments can have wide ranging implications, as it is often considered a key element for any future development plans and for informing pollution control policies [25, 26]. The use of multiple monitoring sites (sometimes in remote locations) is considered standard practice and thus the sensors must be easily portable and able to operate for long periods of time without the need to be maintained or regularly collected and replaced. Such sensors are compact and light weight, enabling them to be used on such diverse measurement platforms including UAVs (unmanned aerial vehicles) to measure volcanic ash and other types of gas emissions without risking injury to personnel [27, 28].

Air quality is now considered a global issue that affects ecosystems and climate both globally and locally [29, 30]. It is also now known that changes in the composition of the atmosphere can have knock on effects on other delicate ecosystems such as marine habitats and cause changes in the pH levels of the sea [31, 32]. Air pollution and general air quality affects everyone, but particularly vulnerable groups of people such as the very young and very old and those with respiratory problems or other underlying health issues. There have been several studies in the literature linking human mortality rates to air quality and pollution levels [33 - 36]. Whilst outside air quality is undoubtedly important, the monitoring of indoor air quality is also of growing significance to human health given that more and more people are spending the majority of their time indoors as countries become more industrialised and people lead more sedentary lifestyles. Thus, air quality monitoring devices are often deployed within office complexes and schools. Such devices are often portable, require negligible operating power, and are low cost; enabling use in developing countries and remote locations without adequate infrastructure. Portable gas sensors are also used for personal safety by personnel who work in confined spaces (often amperometric gas sensors). Selectivity and identification techniques for the different analyte gases has also greatly improved in recent years, enabling quantitative analysis even at small concentrations [37, 38].

1.2 Gas Sensor Technologies

Some typical examples of different types of gas detector are now discussed. This is not a comprehensive overview of all proposed gas sensing technologies but is restricted to those which have proven commercially viable in various different applications (Table 1.1). The major commercial gas sensing technologies are photoionization detectors, solid state sensors and amperometric gas sensors. This is mainly due to the fact that they are well established technologies and have been widely researched over the years in numerous different disciplines, from ppm range detection of CO gas, monitoring of the health of stored potatoes, to VOC detection for environmental conservation monitoring and oil prospecting [39 – 42]. Although spectroscopic devices are used in various gas sensing applications, these are generally miniaturized instruments rather than sensors. Other technologies based on ultrasound are for generic leak detection, based on the sound emitted by a gas escaping under pressure and not identification of a particular gas [43].

The major difference between commercially viable gas sensing technologies and ones that work in a small-scale laboratory setting, are costs and scalability. The cost of components is rarely a major consideration when building a prototype gas sensor in a laboratory. However, the cost of building a gas sensor in industry is often the deciding factor in choosing which sensing technology to use. The scalability of a technology in an industrial setting must also be considered. Whilst making one gas sensor by hand using skilled technicians may be feasible in a laboratory, the gas sensor made in industry must be able to be mass produced by automated processes with operators who are not necessarily experts in their field.

It is considered standard amongst manufacturers of amperometric gas sensors to construct sensors with several layers of material in a stack above the working electrode. In the case of the Alphasense sensors studied within this thesis the analyte gas passes through silica supported permanganate powder (in certain build variants), a PTFE semi-permeable membrane, 5 M liquid sulfuric acid electrolyte and then reaches the surface of the metal working electrode. When taken as media that the analyte gas must pass through, each of these can be seen as diffusion barriers with different

diffusion rates. This must be considered when using a mathematical model of the sensors. This is covered in more detail in the mathematical modelling chapter (Chapter 3). A summary of the commercially available technologies and their various pros and cons are listed below (Table 1.1).

Sensor Technology	**Application**	**Advantages**	**Disadvantages**
Photoionization	VOC gas concentration analysis	High accuracy whilst being relatively cheap to run	Low selectivity which can give false readings in complex samples
Solid State (Metal Oxide) Semiconductor	High stability analyte gas analysis	Thermal energy allows reaction analysis of otherwise stable (undetectable) compounds	Only usable where constant large power supply is available
Amperometric	Environmental analysis in remote locations	High selectivity whilst being small and compact, which allows for portable usage	Lower precision than other technologies and smaller limit of detection range

Table 1.1: Commercial Sensor Applications

1.2.1 Photoionization Detectors (PIDs)

A photoionization detector (PID) works by using high energy photons to ionise the analyte gas particles, which are subsequently repelled by the positively charged plate and detected by the negatively charged detector plate [44, 45]. The principle is illustrated below (Fig 1.1). The three common types of commercially available sensors (PID, metal oxide, amperometric) are all usually constructed in a stack configuration (Fig 1.2). This enables a leaner manufacturing process which saves on supplier costs and machine tooling for the PID sensor.

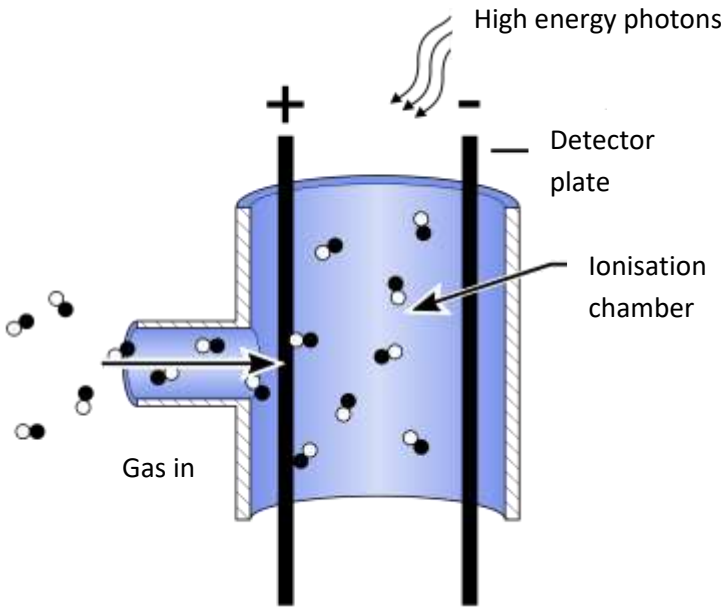

Figure 1.1: Schematic of photoionization gas sensor. The molecules are ionised by the photons and the electrons are detected at the positive plate whilst the ions are collected at the negative plate.

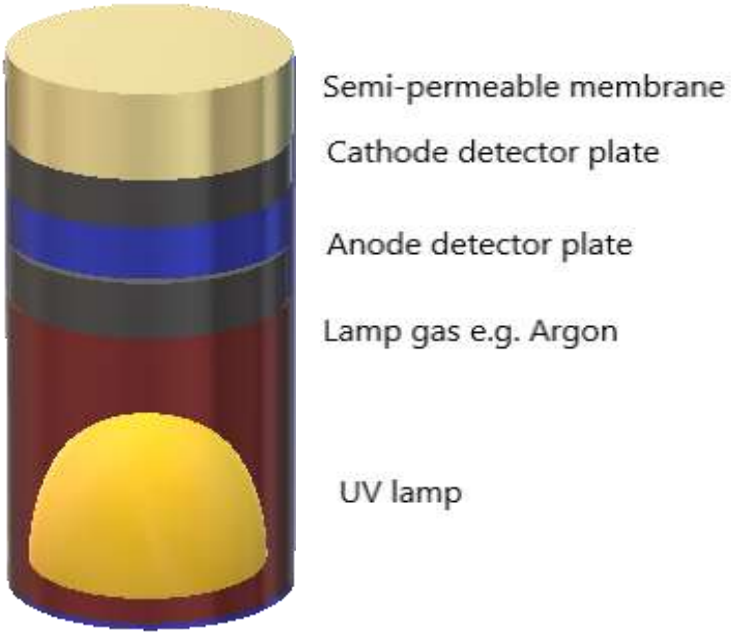

Figure 1.2: Diagram of manufactured PID sensor construction.

Quantitative measurements are achievable with a PID sensor because the current response from the ionised species interacting with the detector plate is proportional to the analyte concentration. Calibration plots can be calculated using known concentrations of analyte gas, which subsequently enables unknown concentrations of an analyte to be found via regression. However, it must be noted that the sensor is non-selective during normal operations because the high energy photons react with many species. This means that a mixture of different VOCs would simply give a large response and so a PID sensor is only usable when the sample contains no VOCs other than the target analyte.

Whilst PID sensors are useful for the detection of analyte gases such as volatile organic compounds (VOCs), they are unable to reliably detect low molecular weight VOCs. This is due to the fact that each VOC has an ionisation potential, which is the energy threshold it must overcome to be ionised by the photons within the PID device. Thus, the photons emitted by the PID photon source must each have an energy greater than the ionisation potential of the target analyte [46, 47]. The photon energy utilised by the PID depends upon the type of gas used as a high energy photon emitter within the lamp section of the device. Noble gases such as argon or xenon are typically used because they emit photon energies greater than the ionisation potentials of most VOCs. Each has a different photon energy (krypton = 10.6 eV, argon = 11.7 eV, xenon = 8.4 eV) and so a different noble gas is used depending upon the requirements of the sensor [48].

For example, a sensor containing a noble gas with a high photon energy will be able to detect a large range of VOCs including smaller ones such as ethane, methanol or propane. However, a sensor using a noble gas with a relatively low photon energy will only be able to detect hexane or larger VOCs. The speed of the photon ionisation interactions with the analyte VOC and the interaction with the detector plate means PID sensors have a response time of only a few seconds, much faster than the response time of amperometric electrochemical sensors (on the order of 20 seconds). The power requirements of the lamp used in the PID sensor are significantly higher than in an amperometric sensor and so are not deployable in remote locations without a large and reliable power source.

1.2.2 Solid State Semiconductor Sensors

A solid-state semiconductor gas detector (Fig 1.3) works by having a layer of semiconductor tin oxide (typically SnO_2) maintained at high temperature by local heating on-chip, that reacts with the analyte gas. Typically, oxidation of the analyte (e.g. CO) releases electrons which are injected into the vacant energy levels of the conduction band. In some devices, where the analyte is a strong oxidant (e.g. ozone) holes may be injected into the valence band. In either case, the injected charge carriers reduce the electrical resistance of the semiconductor, which is detected by a conductance-measuring circuit [49, 50].

The metal oxide sensor is integrated into an electrical circuit (Fig 1.4) and due to the fact that heat energy is being used to activate the reaction with the analyte, these types of sensors are only deployed when there is a reliable source of constant power (such as mains electricity or a portable battery pack). They therefore share the same drawback as PID sensors. It is also worth noting that the high temperatures employed also serve to prevent interfering resistance changes due to condensation of water in humid atmospheres.

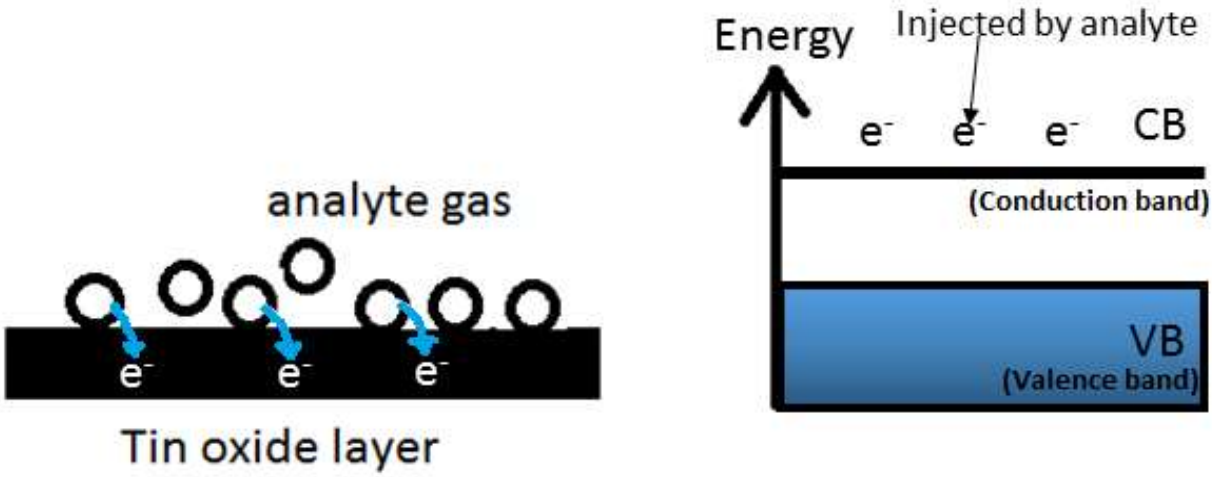

Figure 1.3: Schematic of tin oxide gas sensor. The high temperature causes the analyte molecules to be oxidised at the tin oxide surface and subsequently injects electron into the conduction band of the tin oxide.

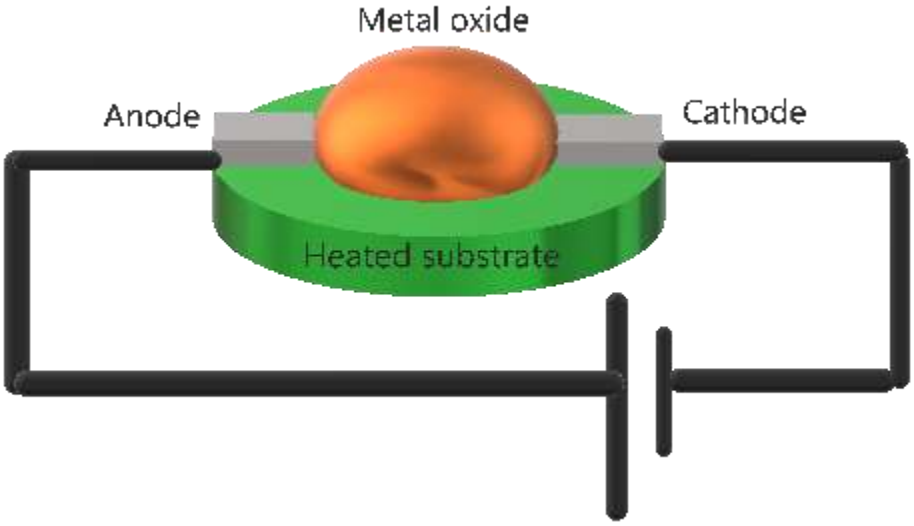

Figure 1.4: Diagram of metal oxide sensor circuitry.

1.2.3 Amperometric Gas Sensors

In amperometric gas sensors, the analyte is detected by oxidation or reduction in a faradaic process at an electrode/electrolyte interface. In contrast to semiconductor gas sensors, the redox reaction directly generates a current to produce the analytical signal [51, 52]. Understanding how amperometric gas sensors operate relies upon a fundamental understanding of electrochemistry. The surface of the electrodes is the reaction site where chemical reactions such as chemisorption, oxidation or reduction occur. In addition to the nature of the electrode, the medium through which the analyte is transported is important because the overall reaction rate, as indicated by the current, may be limited by the transport of the analyte through the device to the surface of the electrode.

A simple electrochemical circuit involves two electrodes and an electrolyte acting as a medium for ion transport between the two electrodes, thus completing the circuit and enabling current to flow. Amperometric sensors work by having one of these electrodes (the working electrode) as the site where the electrochemical reaction of interest takes place. Amperometric gas sensor technology is the subject of this thesis. In a simple model of an amperometric gas sensor the analyte travels into the sensor housing and through various membranes and the electrolyte to the surface of the working electrode. The analyte then reacts at the electrode and electrons are either taken up by the electrode (electrooxidation) or taken up by the analyte (electroreduction) to for the product or an intermediary to the product.

In commercial devices (such as the Alphasense CO-AF sensor) the electrolyte is typically a liquid in order to allow ions and other charge carrying particles to easily access the electrodes and move between them, although solid state electrolytes have been considered [53, 54]. In the amperometric measurement method, the transfer of electrons between the working electrode and the analyte at the electrode surface is recorded as a function of time. The change in circuit current over time indicates the rate of the reaction at the working electrode surface. The amount of current that flows in the circuit is therefore directly related to the concentration of analyte.

When the current is not changing with time (steady state) then the concentration of the analyte at the electrode surface and throughout the device is constant. In principle either the electron transfer rate at the electrode surface or the diffusion rate of analyte through the sensor may determine the current measured. Typically, amperometric devices are operated under conditions where the analyte is being converted into product immediately when it reaches the electrode and the current is therefore limited by the rate of diffusion of analyte molecules to the working electrode surface.

1.2.4 Sensor Technology Considerations

Although amperometric gas sensors use less power than semiconductor sensors or PIDs because no current flows in the absence of analyte, they still require an external power source and electronic interface to enable the user to interpret the results of the electrochemical reactions occurring at the working electrode surface. Hence other detection methods (e.g. colorimetric paper sensors for determining the presence of CO) have been developed where access to electrical supply is impractical or intermittent, such probe systems are often designed to be cheap and easy to use [55, 56]. Although such a system is not as precise as electrochemical gas sensing mechanisms and cannot give details as to the exact concentration levels of CO gas within the surrounding area, it is cheap, easily disposable, can be mass produced, and can be used by someone who is untrained in gas sensor technologies.

At the other end of the scale are catalytic bead gas sensors (sometimes called pellistors) that have been extensively studied in the literature [57 - 60]. These work by having two beads (active and reference) that contain metal wire coils that are maintained at a temperature of several hundred degrees Celsius via electrical heating. Upon exposure to the analyte gas the active bead catalyses the oxidation of the analyte molecule, this exothermic reaction heats the coil even further and subsequently changing its electrical resistance. This causes a potential difference between the active and reference bead, the voltage of which is proportional to the concentration levels of the gaseous analyte. Such sensors are typically used for detection of combustible gases and can provide an early warning system to those working in potentially explosive atmospheres. This technology has limited applications, since the heating of the bead components requires a lot of power and subsequently limits the portability of the sensor. This is a major factor in remote locations such as oil rigs where reliable gas sensing is vitally importance. Whilst there are various commercially available competing technologies for gas sensing systems, each has its own specific strengths and weaknesses which dictates its deployment into certain environments. Gas sensors can generally be considered either portable or used in a fixed position, thus different considerations for each requirement must be made.

1.3 Electrochemical Background to Amperometric Gas Sensing

1.3.1 Electrode Materials

Materials such as carbon, and metals (such as platinum, mercury, gold, etc.) are widely used as electrodes in electrochemistry due to their ability to carry large amounts of current and supply plenty of electrons to drive an electrochemical reaction. With the exception of mercury, they are generally considered resistant to corrosion and electrochemically inert in most common circumstances. Other common metals which are less noble (e.g. iron) will form thick oxide layers on their surfaces which impedes the reaction. Such metals are also easily shaped into electrodes with diameters of just a few micrometres without compromising the structural integrity of the material. This means the electrodes can be bent and shaped without causing surface defects due to stress fractures in the metal. Sometimes these metals are simply a reservoir to allow species in solution to lose or gain electrons accordingly [61]; such reactions are called outer sphere reactions in which there is no chemical interaction of the analyte and the electrode. However, for some reactions the process is more complicated. Those reactions involving strong chemical interaction between the analyte and the electrode are termed inner sphere reactions [62 - 65].

1.3.2 Electrode-Electrolyte Interface

The behaviour of an electrochemical cell can be affected by factors such as charging of the electrode surface, the surface structure of the electrode, the diffusion rate of the analyte and the charge state [66 - 69]. In the specific case of the CO-AF Alphasense sensors, there are several gas-liquid phase barriers the analyte gas must diffuse through. The steady state voltages used during chronoamperometry were chosen experimentally where the current is determined by the rate limiting diffusion barriers in either the gas or liquid phase. The mathematical model described within this thesis calculates the overall diffusion rate for the analyte and gives an indication of the phase layer that has the largest influence on analyte diffusion rate within the gas sensors.

The mathematical model essentially describes the change in analyte concentration gradient at multiple distances from the working electrode surface, as a function of time. The working electrode is the site of the reaction of interest. When a potential is applied to an electrode, the ionic species within the electrolyte solution will respond by migration in the electric field to compensate the charge built up on the electrode surface. In other words, positively charged ions dissolved in the electrolyte will collect at a negatively charged electrode and vice versa. This leads to a double layer of charged electrolyte species at the electrode surface (Fig 1.5).

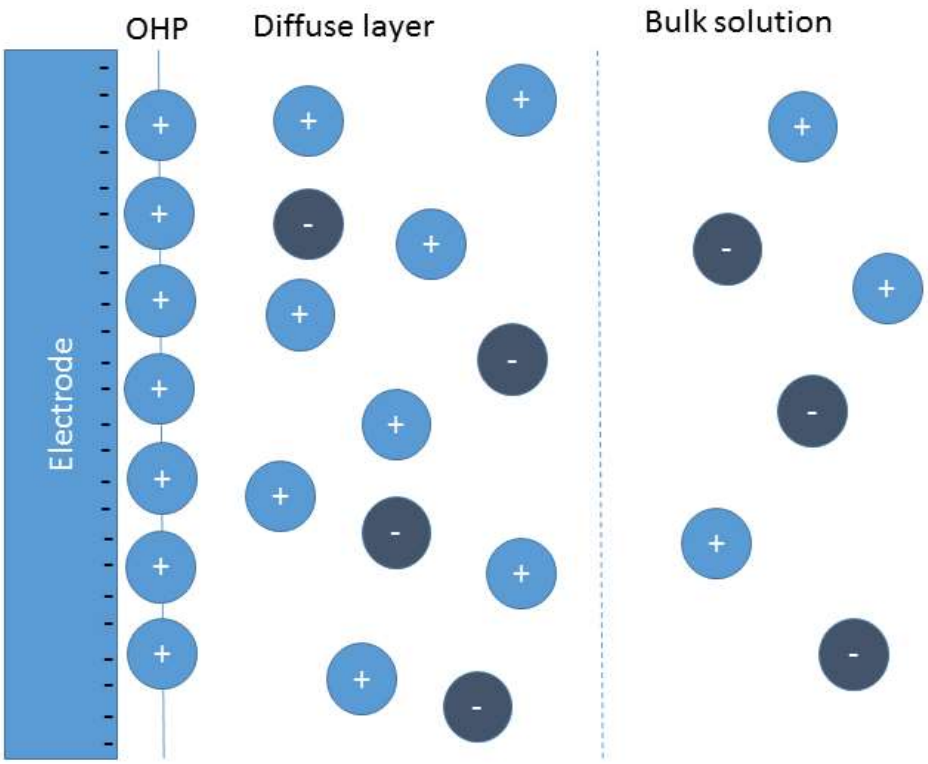

Figure 1.5: Schematic of the different layers at the electrode surface and in the liquid electrolyte. The line marked OHP denotes the position of the outer Helmholtz plane. Adapted from [70]

This difference in the concentrations of the electrolyte species at the electrode surface and within the bulk solution results in a difference in the potential across the electrode/electrolyte interface. In Fig. 1.5 the electrode is drawn as negatively charged; the excess electrons accumulate on the surface of the metal and attract a counter charge (cations in this example) from the electrolyte. some of the counter charge is held rigidly at the electrode surface in the Helmholtz layer at a distance determined by the solvated ionic radius of the species. This distance defines a plane called the outer Helmholtz

plane (OHP). Fig. 1.5 does not show the inner Helmholtz plane, which applies to cases where counterions are strongly chemically interacting with the metal and may be only partially solvated (e.g. I^- on Pt). Beyond the outer Helmholtz plane, there is still an excess of cations, but the counter charges are not rigidly held in place and are subject to thermal motion, this area is the diffuse layer. These two layers are often taken together as the double layer, thus double layer capacitance is simply the change in charge on the electrode per unit potential across the interface from the electrode surface to the electroneutral bulk solution [71].

Shown below (Eqn 1.1) is the Helmholtz capacitance equation, where capacitance (C) is calculated (in Farads, F) using relative permittivity of the Helmholtz layer (ε_r), permittivity of free space (ε_o) (in F/m) and distance from the electrode to the centre of the solvated ions (outer Helmholtz plane, typically 0.25 nm) (d_{OHP}).

$$C = \frac{\varepsilon_r \varepsilon_o}{d_{OHP}} \tag{1.1}$$

It must be noted that the Helmholtz model of the double layer is not the only model used within electrochemistry and has its limitations (as it was developed over 150 years ago) and whilst it is correct in explaining that the double layer stores charge electrostatically, it assumes the double layer is simply a molecular dielectric with a constant differential capacitance (it was later discovered that differential capacitance was not constant and depended upon applied potential and ionic concentration of the solution). It also does not consider several important factors such as adsorption of species on the electrode surface, and diffusion of ions within the solution. The major defect of the Helmholtz model is the lack of consideration of the diffuse layer. The Gouy-Chapman model of the diffuse layer and the Grahame modified Stern model were developed later in the 20th century to account for such factors [72, 73]. The thickness of the diffuse layer is approximately the Debye length r_{DL} (Eqn. 1.2).

$$r_{DL} = \sqrt{\frac{\varepsilon_r \varepsilon_0 RT}{2000F^2 Ic^\theta}} \tag{1.2}$$

Where F is the faraday (96485 C mol^{-1}), c^{θ} is the standard concentration (1 mol kg^{-1}), I is the ionic strength ($^1/_2\Sigma c_i z_i^2/c^{\theta}$), z_i is the charge number of each ion and c_i is the concentration of each ion, i. Nevertheless, at high concentrations of electrolyte, the diffuse layer shrinks, the Helmholtz model becomes a reasonable first approximation and the differential capacitance is constant. For the electrochemical processes within this thesis, the Helmholtz model is considered sufficient because of the high electrolyte concentration employed in the amperometric gas sensor (5M H_2SO_4).

The major impact of double layer capacitance considerations on the amperometric gas sensors studied in this thesis is through the effect of charging current, i.e. the current that flows as the ions move to re-establish the double layer in response to changes in the potential and charge state of the electrode independent of any redox reaction. Such currents may be made negligible by operating at a fixed potential in order that the double layer is unchanged. Determination of capacitance and the charging currents is discussed briefly in the section (1.4) below on electrochemical methods.

1.4 Electrochemical Methods

Electrochemical methods generally consist of the application of a stimulus such as a potential (or current) and the measurement of the response (current or potential) as a function of the applied stimulus and time. By modelling these responses, it is possible to deduce quantitative information concerning the rates and mechanisms of electrode reactions. A large variety of electrochemical methods exist. In this section, the techniques employed in the thesis are reviewed. Whilst the appearance of peaks on cyclic voltammograms is important, there is more information that can be extracted from them and the theory behind such characteristic shapes is briefly outlined.

1.4.1 Cyclic Voltammetry

Cyclic voltammetry (CV) is a 3-electrode technique in which the potential of the working electrode (against a reference) is scanned at a constant rate between pre-set limits. The third electrode is the counter electrode (also called auxiliary), which provides a current path as the reference electrode is connected to the input of an operational amplifier and negligible current passes through this electrode. The absence of current in the reference electrode circuit means that the reference maintains a constant interfacial potential and changes to the applied potential produce changes at the working electrode/electrolyte interface. Cyclic voltammetry is a well-established technique and has been used to study electrochemical systems for decades [74, 75].

Voltammograms at different scan rates give currents of different magnitude during cyclic voltammetry. This difference in current is because the scan rate determines the time taken for the voltammogram, and the average current is the charge passed per unit time. The voltammogram itself is not usually presented with an axis that shows time, so it is encompassed within the shape of the plotted data. The form of the working electrode potential (E) against time (t) is shown (Fig. 1.6a). The scan rate is simply the magnitude of the gradient (dE/dt). The larger (i.e. faster) the scan rate, the larger the current. Qualitatively, this is because it takes longer for an experiment at low scan rate to reach the potential

at which the reaction occurs. Conversely, when a large scan rate is used the peak potential is reached much sooner and so there is a larger current flow.

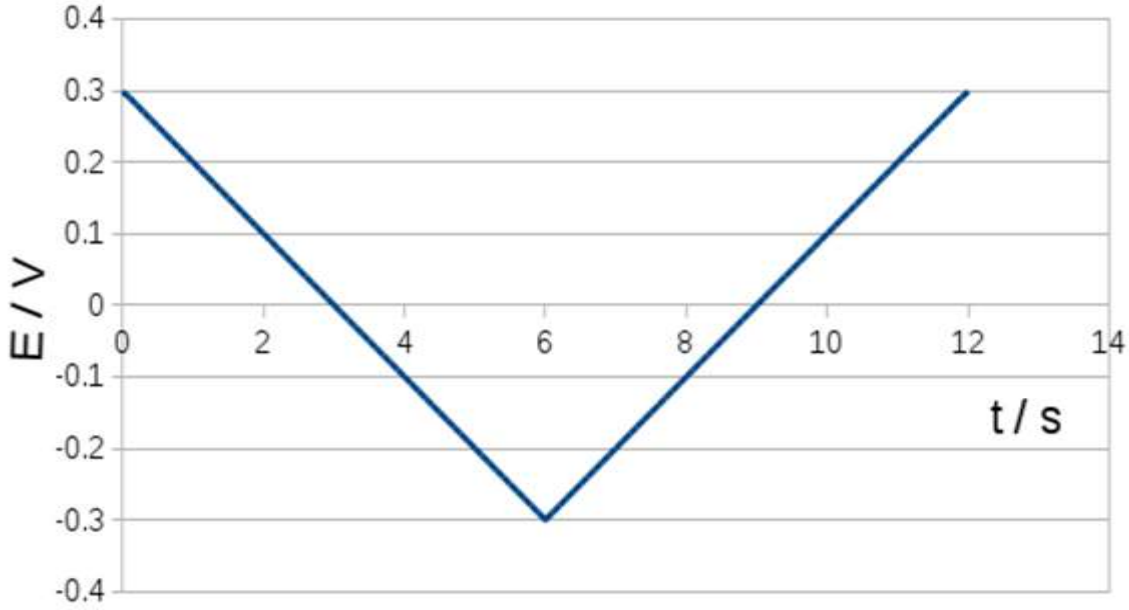

Figure 1.6a: Potential against time for a typical cyclic voltammogram.

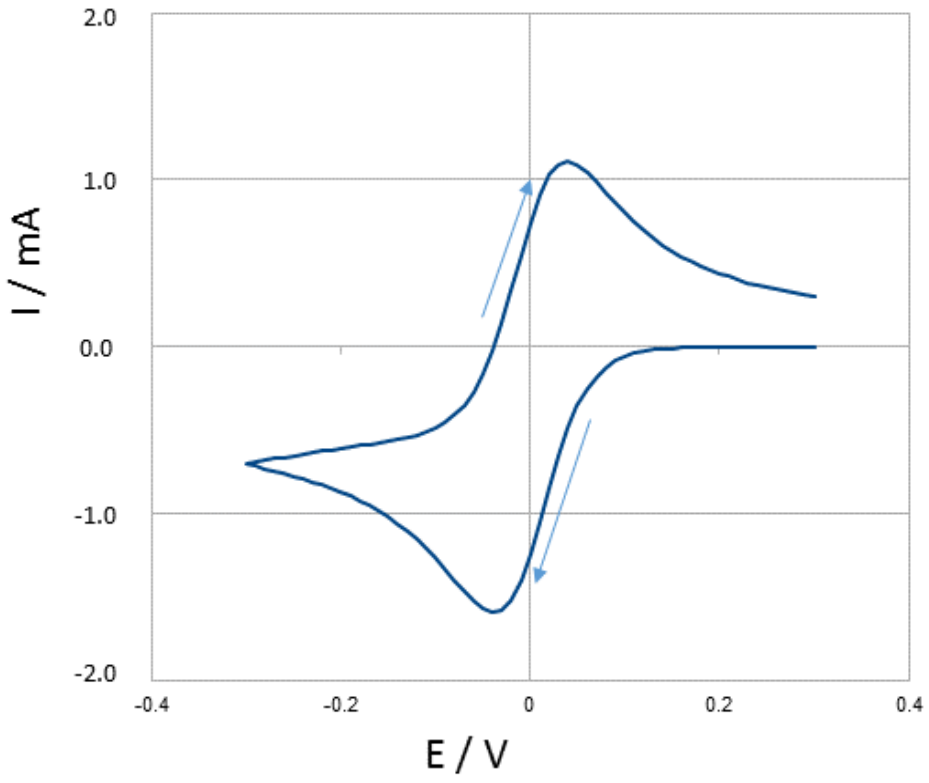

Figure 1.6b: Typical cyclic voltammogram showing the peak shape that is observed when the analyte is present in bulk solution only as the oxidized form and is reduced at negative electrode potentials and then re-oxidized when the sweep returns to positive electrode potentials.

Cyclic voltammetry of a simple, chemically uncomplicated electrode process (Eqn 1.3) usually produces data of the form shown in the cyclic voltammogram (Fig. 1.6b). The reaction shown is a reversible reaction involving the electrooxidation or electroreduction of a species via the transfer of one mole of electrons per mole of reactant to form one mole of product.

$$O + e^- = R \tag{1.3}$$

In Figure 1.6b the species O is present in bulk solution, but not species R. At positive potentials little current flows because the electrons in the electrode are insufficiently energetic to reduce the species O and there is no R to oxidise. As the electrode potential is scanned in the negative direction, the electrode in effect becomes a more powerful reductant and a current corresponding to reduction of O flows. Depletion of molecules of species O near the electrode surface results in a concentration gradient at the electrode surface (Fig. 1.6c). The concentration of species O at the electrode surface tends to zero as the potential of the electrode becomes more negative; the electrode becomes a sufficiently powerful reductant that molecules of the oxidized species are immediately reduced upon reaching its surface.

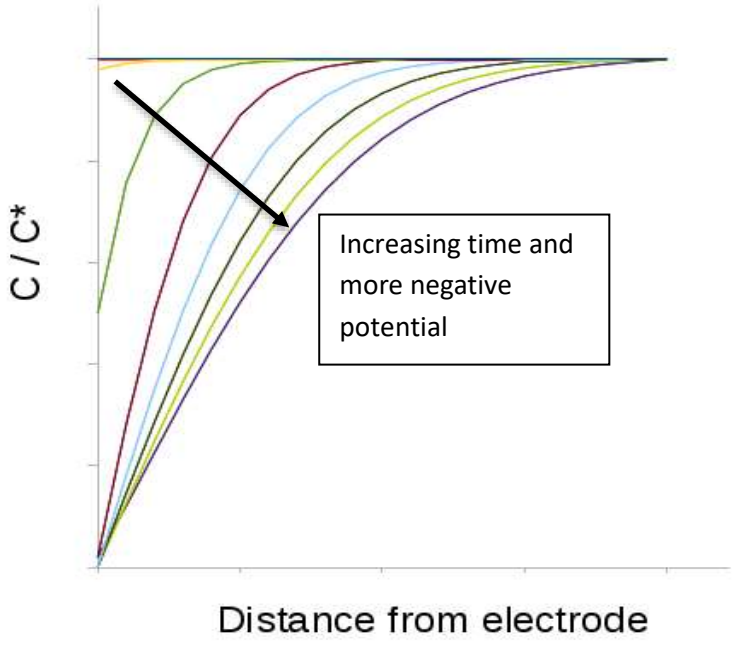

Figure 1.6c: Species O concentration profile (C(x)) as a fraction of bulk concentration (C*) during the negative going scan of Fig. 1.5b. (x) denotes the distance from the electrode surface.

Initially the concentration profile is flat at large positive potential where no current flows. As the potential is scanned in the negative direction, the concentration at the electrode surface drops, but eventually C(x=0) becomes zero. After this point, the current seen during cyclic voltammetry is independent of further potential changes and is limited by diffusion of species O from bulk solution to the electrode surface down the profiles depicted (Fig. 1.6c). This is observed as a peak in the current (Fig. 1.6b), followed by a decrease of the current even as potential becomes more negative. Peaks observed during cyclic voltammetry typically have an asymmetric shape, rising steeply due to the effects of the potential on the reaction and gradually falling away as diffusion limitations become important (Fig. 1.6b). The latter is because the molecules at the electrode surface are exchanging electrons with the metal relatively quickly, but the current is limited by the rate of fresh analyte arriving at the electrode surface which is proportional to the gradient of the concentration profile and which is becoming less and less as the near-electrode region (diffusion layer) becomes depleted of analyte and extends further into the solution.

On the reverse scan, the molecules of species R that were produced in the forward scan are oxidised as the electrode potential approaches and exceeds the formal potential of the electrode reaction. As long as the reaction is reversible (defined below), the formal potential can be estimated from the average of the peak potentials for the cathodic (E_c) and anodic (E_a) processes (Eqn 1.4).

$$E^0 = 0.5(E_c + E_a) \tag{1.4}$$

A reversible process is one for which the concentrations at the electrode surface C(x=0) obeys the Nernst equation of equilibrium thermodynamics (Eqn 1.5) despite the presence of a current flow. It is usually equivalent to the statement that the electron transfer rate is rapid, i.e., that molecules are reduced / oxidised as soon as they reach the electrode surface so that equilibrium is re-established immediately upon any change in potential.

$$E = E^0 - \frac{RT}{nF} ln \frac{[R]}{[O]} \tag{1.5}$$

An exact treatment of the voltammogram of a reversible process is possible, but the major features can be deduced from simple arguments [76]. The average (precisely root mean square distance) travelled by a molecule in a time t and with a diffusion coefficient, *D* is given by Eqn 1.6:

$$x = K\sqrt{Dt} \tag{1.6}$$

Where *K* is a constant that depends on the geometry and dimensions of the system. Eqn 1.6 also implies that the thickness of the diffusion layer of Fig. 1.6c (the region where $C < C^*$) grows in proportion to $\sqrt{t}$. The gradient of those concentration profiles will correspondingly vary inversely with $\sqrt{t}$ and therefore be proportional to $\sqrt{v}$ where v is the scan rate. Since for most redox couples O/R, the diffusion coefficients of the two species are roughly equal, the forward and reverse peak currents will be equal and proportional to $\sqrt{v}$. In addition, the peak potentials, E_c and E_a and the wave-shape will be independent of the scan rate because these are ultimately controlled by the thermodynamics (Eqn 1.5). The difference between the peak potentials will however depend on the number of electrons exchanged per molecule (n) and the temperature (T):

$$|E_c - E_a| = \frac{2.303RT}{nF} = \frac{59}{n}\ mV\ @298\ K \tag{1.7}$$

Voltammograms of species which do not satisfy the criteria for reversibility may be more complex in appearance due to the presence or absence of various peaks. For example, if the product of the forward reaction is unstable on the timescale over which the voltammogram is recorded, no reverse peak may be observed. Or, it may be the case that the same species may be both oxidised and reduced [77]. The general appearance of a voltammogram may be usefully related to molecular orbital theory in a qualitative manner (Fig. 1.7). A molecule may accept electrons in its lowest unoccupied molecular orbital (LUMO) when the energy of electrons in the electrodes exceeds the LUMO energy. It can also donate electrons from its highest occupied molecular orbital (HOMO) when the energy of the electrons in the electrode is lower. On this basis the reduction (oxidation) peak potentials may be correlated to the energies of the LUMO and HOMO or knowledge of the MOs of the molecules may be used to predict the peak potentials in the voltammograms.

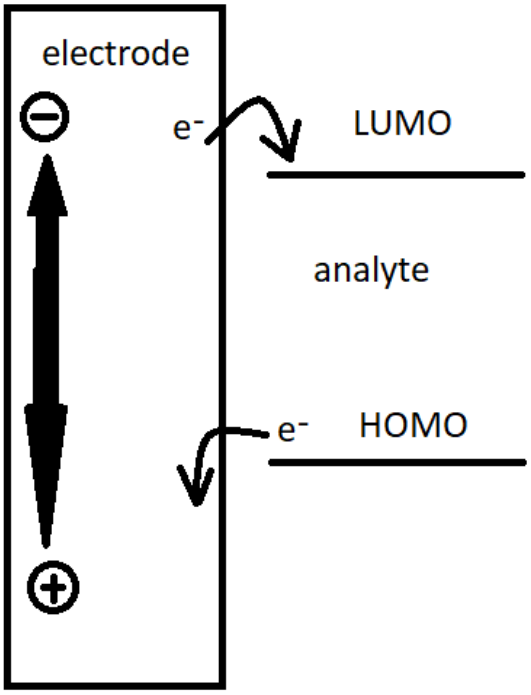

Figure 1.7: Electron transfer energy levels between the electrode and analyte molecule.

1.4.2 Steady-State Voltammetry

The current in a cyclic voltammetry experiment contains a hidden time-dependence described above. However, in certain cases where the depletion layer is prevented from growing indefinitely, a time-independent state can be reached. This happens at very small electrodes, in the presence of convection, or, especially relevant to this thesis, when the electrode is covered by a membrane in which the rate of diffusion is lower than the surrounding medium [78, 79]. In any case, as long as the scan rate is sufficiently slow, the current may be independent of time and, further, does not decay after a peak in the manner represented in Figs 1.5 and 1.6. Such a steady-state voltammogram is illustrated in Fig. 1.8. In this case a potential-independent limiting current is attained where the rate is controlled by mass-transport (convection and / or diffusion). The equation given for this limiting current applies to the oxidation of analyte at an electrode covered by a membrane of thickness *L* and in which the diffusion coefficient is *D* and i_L is the limiting current, *A* the electrode area, *L* the diffusion layer (or membrane) thickness and *c* is the bulk analyte concentration.

$$i_L = nFAD\frac{c}{L} \tag{1.8}$$

Many amperometric gas sensors operate under conditions appropriate to Fig. 1.8. The potentials are chosen such that they are within the electrochemical window of the electrolyte medium and the electron transfer reactions at the electrode occur at the diffusion limited rate, i.e. the current does not change with potential. The advantage of this technique is that any small errors in the reference electrode or drifts in its potential have no effect on the current since the diffusion limited current is independent of electrode kinetics and therefore independent of potential (given that the potential is sufficient to maintain diffusion control). The blue horizontal arrows in Fig. 1.8 indicate where the current is independent of potential (limiting current) and is given by Eqn 1.8.

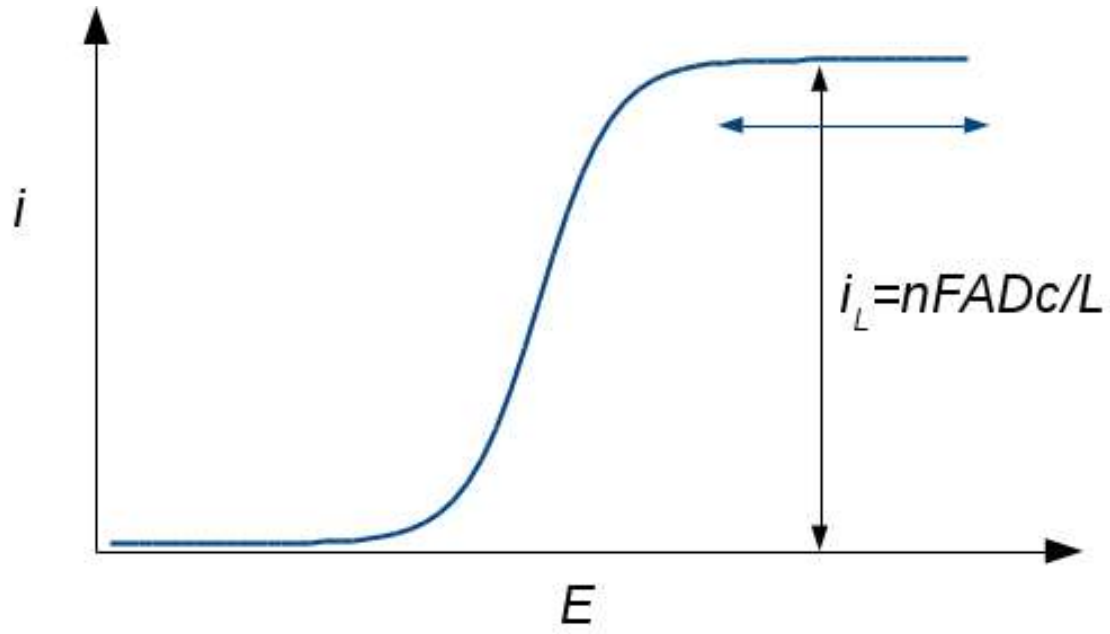

Figure 1.8: Theoretical steady state voltammogram for the oxidation of an analyte (showing the equation that applies when the current is at steady state and independent of potential).

1.4.3 Impedance Spectroscopy

Impedance spectroscopy is used to measure the impedance (resistance) of a circuit. In electrochemical systems, the term impedance is used instead of resistance because impedance takes account of the frequency of the applied potential waveform and the phase difference between the current and voltage through the circuit whilst resistance does not. During impedance spectroscopy a small sinusoidal potential of fixed frequency is applied to the circuit and the phase difference between it and the resulting sinusoidal current is recorded.

$$\Delta E = E_0 \sin \omega t \tag{1.9}$$

$$\Delta i = i_0 \sin(\omega t + \varphi) \tag{1.10}$$

Where $\omega = 2\pi f$ is the angular frequency, *f* the frequency in Hz and φ is the phase angle. E_0 and i_0 are small values representing the amplitudes of the sinusoidal potentials and currents.

For a simple resistor, $\varphi = 0$ and the resistance $R = {}^{\Delta E}/_{\Delta i}$ is just E_0/i_0. This is not true for more complicated circuits, but nevertheless the ratio ${}^{\Delta E}/_{\Delta i}$ remains meaningful and is called the impedance. It depends on both the amplitudes and the phase angle. Instead of representing the ac waveforms with sinusoids, we can use Euler's equation $e^{j\varphi} = \cos\varphi + j\sin\varphi$ where $j = \sqrt{-1}$ and we can write the impedance, *Z*, as:

$$Z = \frac{E_0}{i_0} e^{-j\varphi} \tag{1.11}$$

Or, in terms of real ($Z' = \frac{E_0}{i_0}\cos\varphi$) and imaginary ($Z'' = \frac{E_0}{i_0}\sin\varphi$) parts as:

$$Z = Z' - jZ'' \tag{1.12}$$

An impedance spectrum corresponds to measurements of *Z* over a range of chosen frequencies.

Whilst impedance spectroscopy can be represented in either a Bode plot or a Nyquist plot, Nyquist plots are used exclusively throughout this thesis. Each point plotted on the Nyquist plot represents the impedance at a particular frequency (Fig. 1.9). The frequency range during impedance spectroscopy is usually as broad as possible in order to fully explore as much of the spectrum as possible. The amplitude of the applied potential (or current) is kept deliberately small ($E_0 < \frac{RT}{F}$) to make the system behave in a pseudo-linear manner; this is crucial to ensure the response is proportional to the applied signal and at the same frequency. If this condition is not met, the notion of impedance as a ratio of the potential/current signals is not clearly defined.

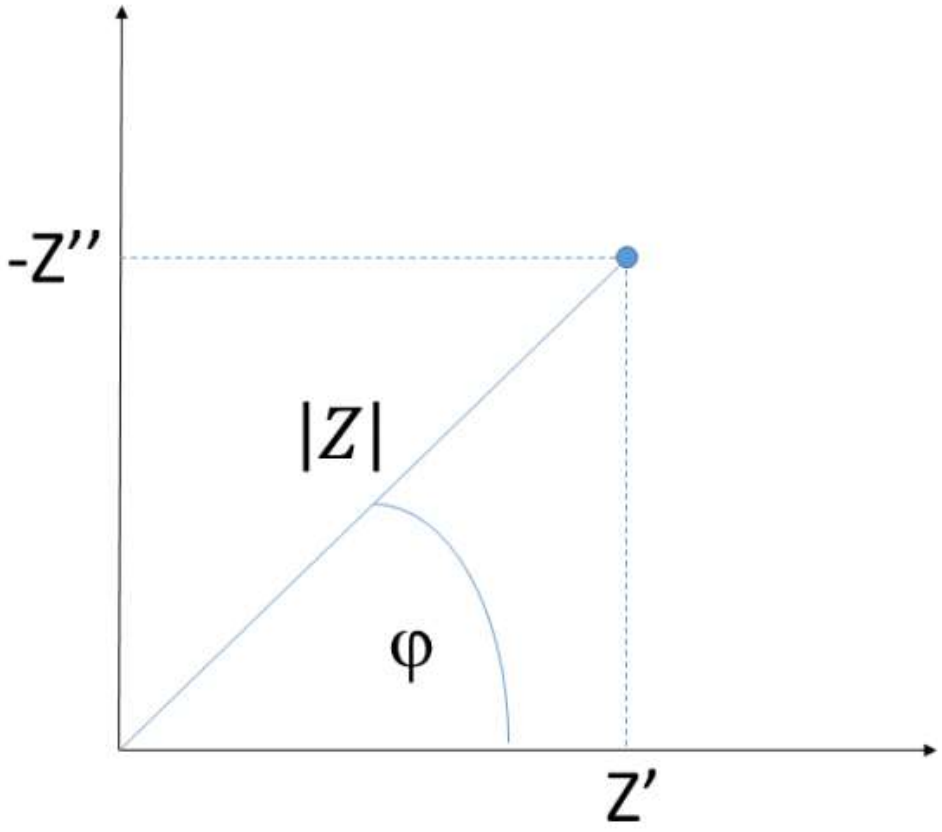

Figure 1.9: Relationship between real Z' and imaginary parts Z'' and the magnitude $|Z|$ and phase φ of the impedance. The blue dot indicates a particular impedance in the Nyquist plot.

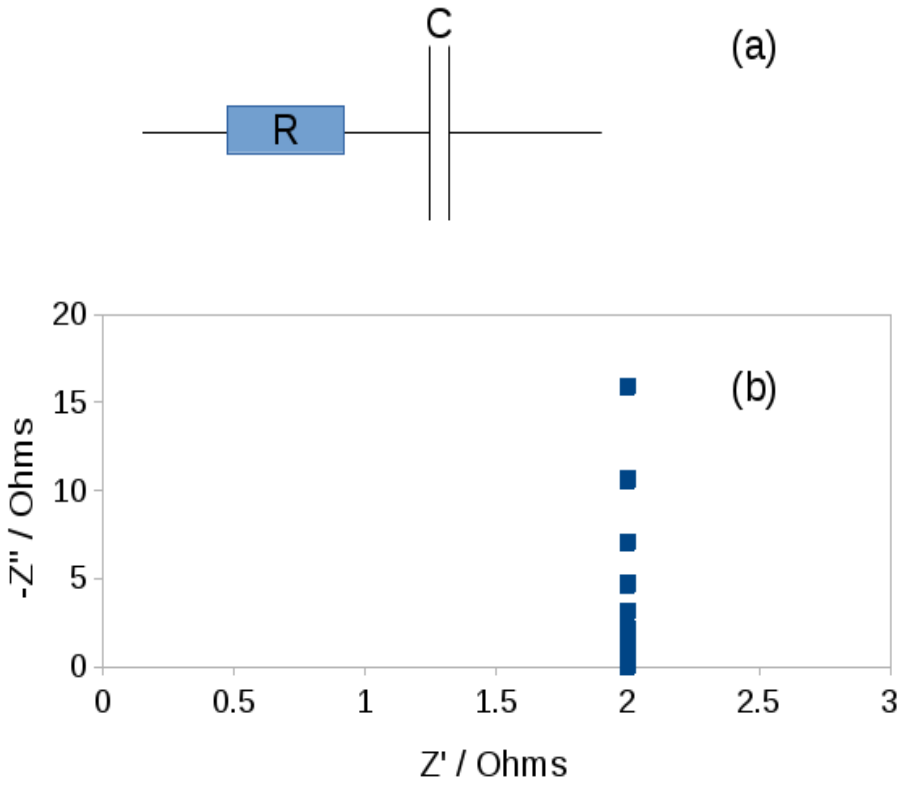

Figure 1.10: (a) A combination of a capacitor and a resistor connected in series; (b) the corresponding Nyquist plot.

Figure 1.10 shows a series RC circuit, which is often a good representation of an electrode/electrolyte interface in the absence of any Faradaic process, and the corresponding Nyquist and Bode plots. The impedance of this, or any other, circuit can be determined from the impedance of the resistor and the capacitor separately using the fact that impedances can be combined in the same manner as simple resistances. The impedance of the resistor, R, is simply:

$$Z = R \tag{1.13}$$

The impedance of an ideal capacitor is purely imaginary:

$$Z = -\frac{j}{\omega C} \tag{1.14}$$

Therefore, the impedance of the series RC circuit in Fig. 1.10 is the sum of Eqn 1.13 and Eqn 1.14:

$$Z = R - \frac{j}{\omega C} \tag{1.15}$$

As can be seen in Fig 1.10, the capacitive element is easily recognised as a vertical line in the Nyquist plot with the imaginary part increasing as the frequency decreases according to $Z'' = \frac{1}{\omega C}$. The resistance is simply the displacement along the real axis. The ease with which these parameters can be obtained from the Nyquist plot facilitates the analysis of the impedance data of the amperometric sensors.

1.4.4 Chronoamperometry

Another electrochemical technique used within this thesis is chronoamperometry; in this technique the potentiostat maintains a constant potential for the duration of the experiment whilst recording current as a function of time (Fig. 1.11). Although chronoamperometry is often used to describe the response of a system after the potential is suddenly changed to a new value, in this work it involves the current response to a sudden change in analyte concentration at constant potential. This enables any change in current to be attributable to reactions at the electrode surface (i.e. Faradaic current), as opposed to a response of the double layer to any changes in potential (i.e. charging current). This turns out to be important for the amperometric gas sensors because the double layer capacitance is very large and the time for the charging current to subside after a change in potential (*RC* in the series circuit of Fig. 1.10) is very long (> 5 mins). Typically, the steady state potential is set at a point at which the mass transfer limited region (Fig. 1.8) has been reached. This means that the diffusion rate of the analyte through the electrolyte medium is the rate limiting step for the reaction at the electrode surface, and the electron transfer reaction is extremely rapid compared to it.

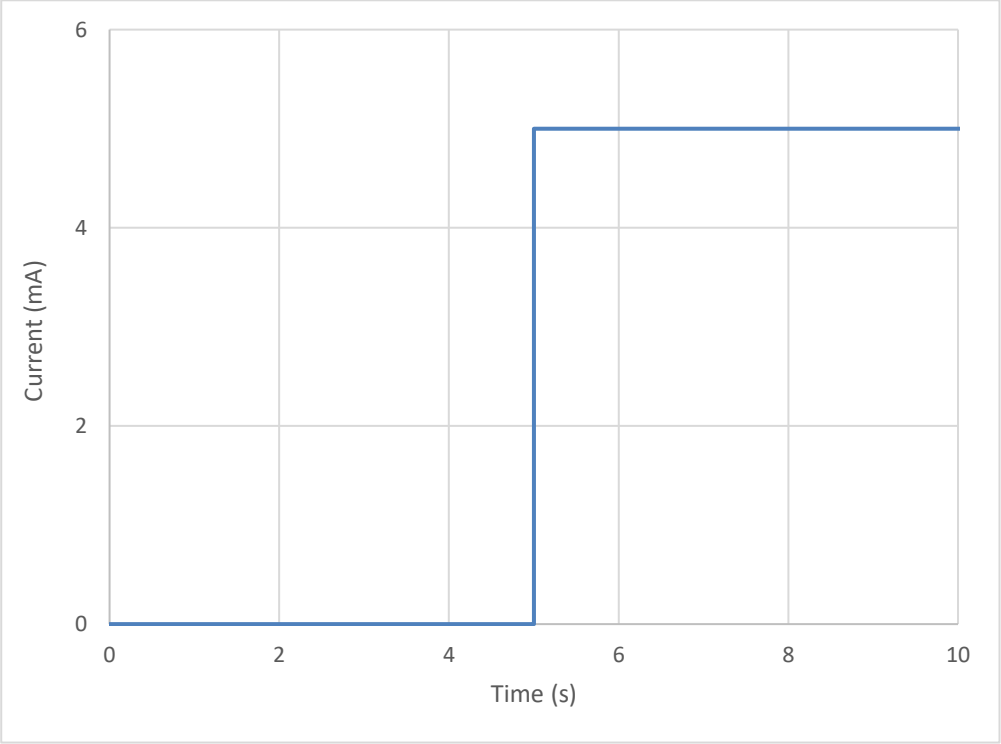

Figure 1.11: Graph showing typical chronoamperometric response to the electron transfer reaction at electrode surface.

1.5 Electron Transfer Theory

The underlying chemical theory behind all of electrochemistry is the theory describing the transfer of electrons between electrode and chemical species at the electrode/electrolyte interface [80]. A brief overview of the relevant aspects is given here, because most of the sensors studied operate in the mass transport limited region of the potential window. An electron transfer necessarily involves a change in the charge state of the molecule or ion; this results in a change of the solvation or the ligands present. However, the motion of electrons is so much faster than the motion of the more massive solvent molecules/ligands that the transfer of the electron and the changes in solvation and complexation cannot occur simultaneously (Fig. 1.12).

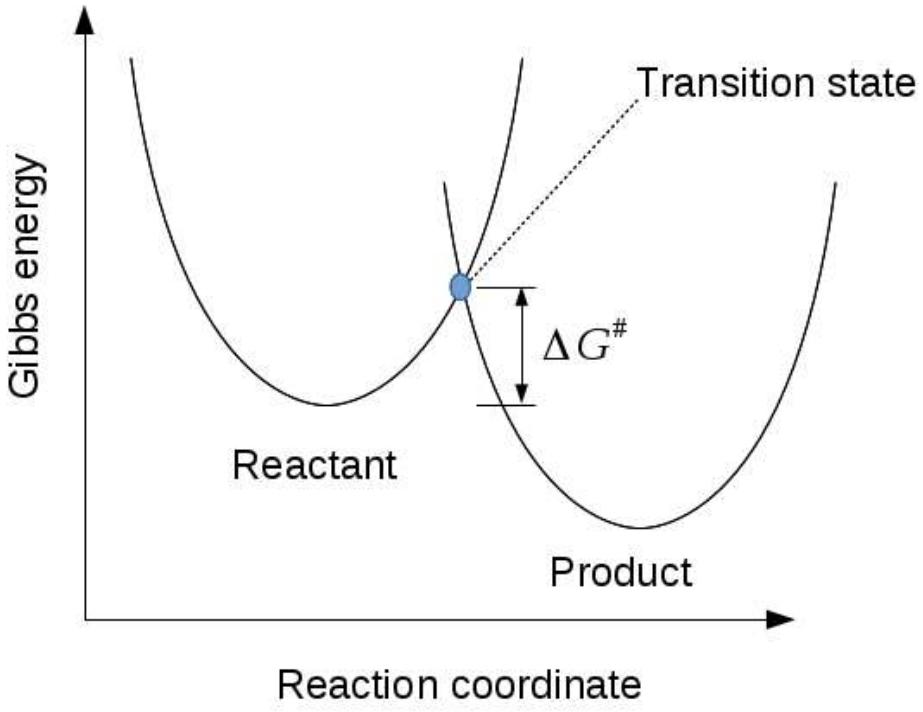

Figure 1.12: Energy diagram showing energy profile of electron transfer reactions

Electron transfer can be considered as a type of quantum transition (tunnelling) [81]. The separation of timescales means that the transfer must occur without a change in electron energy, therefore the rate of electron transfer is limited by the fluctuation of the solvation and coordination spheres to a transition state which allows isoenergetic transfer of the electron. Qualitatively, species where there is a large change in solvation/coordination upon electron transfer will require larger fluctuations to

reach the transition state and will have slower kinetics. This picture of electron transfer reactions applies directly to outer-sphere reactions: those processes in which there is not a strong chemical interaction between the reactant or product and the atoms of the electrode. For such processes, the nature of the electrode material is relatively unimportant.

More complicated reactions, called inner-sphere reactions involve strong interaction of the molecules with the electrode. Upon reaching the electrode surface the molecule (or ion) is chemisorbed onto the surface and forms a chemical bond at the surface site. The transfer of electrons during this surface adsorbed state will follow similar principles to the outer-sphere reactions, but the overall rate may be controlled by electrode-specific factors such as the adsorption and partial de-solvation of the molecule as it does so. Many reactions of interest in gas sensing fall into this category, the best studied is the oxidation of CO at Pt electrodes which is discussed briefly in section 1.6.

1.6 Electrode Surface Effects

A mention must be made of the terminologies typically found within electrochemistry and surface science disciplines. A common reference used is that which describes the crystal face of the metal electrode, in other words, that part of the electrode which is exposed to the electrolyte medium and the analyte of interest. Electrodes can be shaped as disks, linear strips, hemi-spherical, and spherical. This thesis is primarily concerned with macroscopically flat disks of metal as the electrodes. Having specified the macroscopic geometry of the electrode, the microscopic geometry must now be considered. Due to the fact that a solid metal has its atoms arranged in a regular lattice, each atom is essentially co-ordinated to eight other Pt atoms within the lattice. This means that cutting the metal to a specific shape exposes a certain number of atoms depending upon the cutting angle with respect to the crystal planes. The number and configuration of unsatisfied valences of the surface atoms may also be affected, which in turn affects the capacitance and electroactivity. For example, cutting Pt parallel to the *b*,*c* axes at unit distance along the *a* axis of the unit cell exposes a face with an atomic arrangement of four fold symmetry (Fig. 1.13) and is denoted using the Miller index as Pt(100) since it is cut to intersect the *a*-axis but not the *b* or *c* axis. Similarly, a cut that intersects the *a* and *b* axes once each, exposes the Pt(110) face (Fig. 1.14a). Cutting along the intersection of all three axes exposes the Pt(111) face (Fig. 1.14b). Note that in these figures the surface layer atoms are coloured blue and the sub-surface layer atoms are shown in silver.

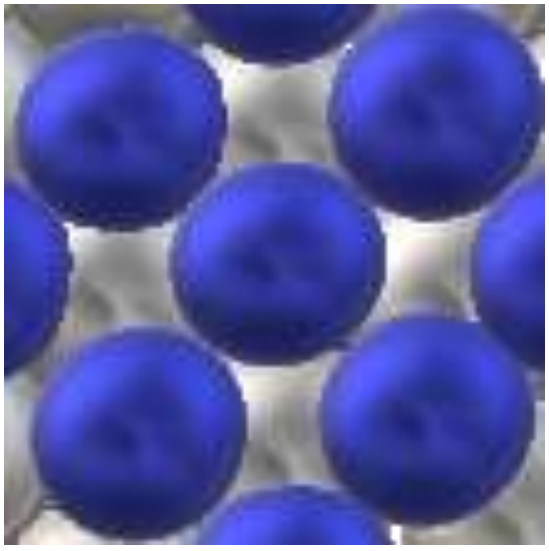

Figure 1.13: Schematic of Pt(100) with surface atoms (blue) arranged above sub-surface atoms (silver).

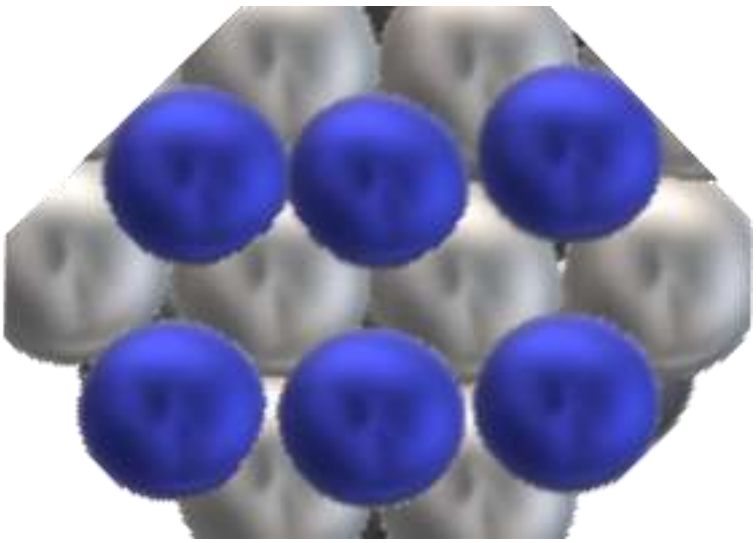

Figure 1.14a: Schematic of Pt(110) with surface atoms (blue) above sub-surface atoms (silver).

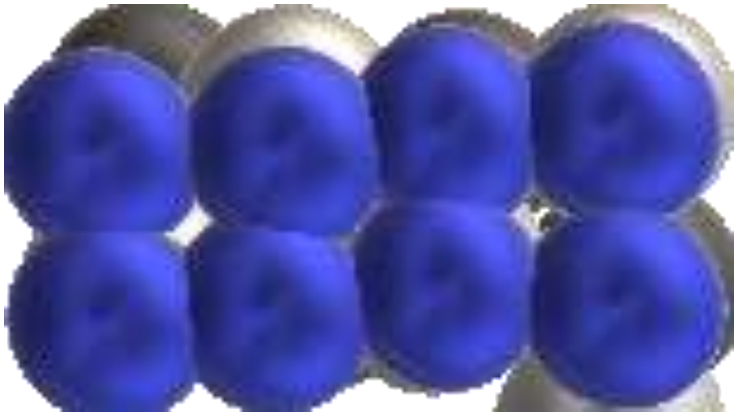

Figure 1.14b: Schematic of Pt(111) with surface atoms (blue) above sub-surface atoms (silver).

The surface geometry of the electrode surface is of importance due to the fact that not only does it change the area available for catalytic activity, but also affects the bonding characteristics of the analyte to the electrode surface. The analyte could be bonded to the surface atoms or bound in a microscopic groove to some of the sub-surface atoms as well. The manufacturing process of the Alphasense sensors uses metal nanoparticles pressed into a disk; such electrodes reveal a variety of crystal faces to the electrolyte, however studies suggest CO electrooxidation proceeds efficiently at the Pt(111) face [82, 83]. Within this thesis, it is assumed there is even distribution of analyte on the electrode surface during electrooxidation.

1.7 Stack Configuration

The accessibility of the working electrode must also be considered, as it can affect the diffusion rate of the analyte and the usable area of the electrode. For example, if the analyte can only travel down a narrow passage and meets the centre of the working electrode before any other part of the electrode, then only that part of the electrode surface which is in direct contact with the analyte can be considered to be taking part in the electrochemical reaction. That is why electrode are typically very thin, because the bulk of the electrode is otherwise merely taking up room within the sensing device. Within the CO-AF sensors the working electrode is considered to be a uniformly accessible Pt disk. This is due to the fact that the stacked configuration of the sensor enables the analyte to travel through the sensor from any part of the top of the device (Fig. 1.15). This stacked configuration also ensures that the area on top of the sensor is the same diameter and circumference as the Pt working electrode.

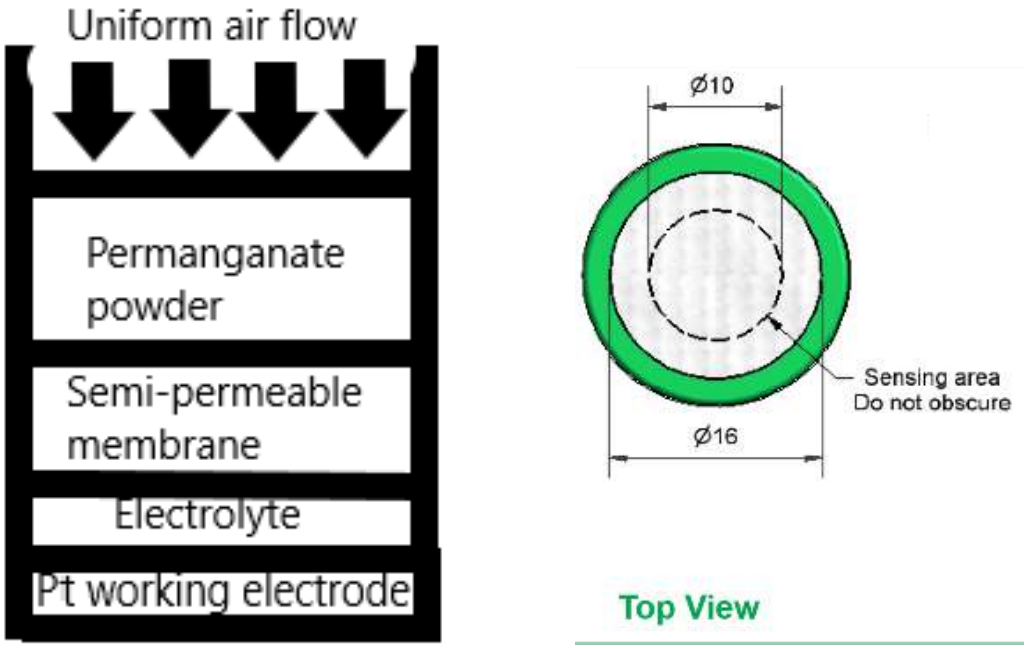

Figure 1.15: Stack configuration of CO-AF sensor and top cover.

1.8 Outline and Motivation of the Project

1.8.1 Carbon Monoxide

Carbon monoxide is a colourless, odourless and tasteless gas under standard conditions. It is well known for being toxic to humans and other animals, which presents a problem as it is undetectable by humans without technological aid. Roughly 200 ppm causes adverse symptoms for humans [84]. Poor ventilation in enclosed spaces often leads to a build-up of toxic carbon monoxide levels over time. Carbon monoxide leak detection is important in both an industrial and household setting, as it is suspected to be the cause of large amounts of inhalation poisoning and subsequent fatalities worldwide [85 - 88].

The Alphasense CO-AF sensor devices use Pt metal nanoparticles immersed in an aqueous acidic electrolyte medium to amperometrically detect the presence of carbon monoxide within the surrounding atmosphere by electrochemical reaction. The proportional response of the sensor to different concentrations of carbon monoxide also allows the back calculation of local atmospheric CO concentration from the current measured. The small size and weight of the device mean that it is easily portable and can be deployed almost anywhere. Artificial detection methods such as this are currently considered the only reliable way to detect CO without risking the health of living things.

The CO-AF sensor is a successful, commercial product [24], however the details of its mechanism of operation are not well understood. The work in chapters 3-4 was aimed at the development of a mathematical model for the sensor response and its use to characterise the behaviour of working devices in non-destructive manner. Chapter 5 concentrates on an alternate design employing Pt/Ru instead of plain Pt electrocatalysts.

1.8.2 VOCs

The rapid and easy detection of VOCs such as alcohols (particularly in aerosol form) has long been a goal for many areas of research; although there are plenty of analysis methods to choose from including HPLC, NMR, LC-MS, GC-MS, and IR spectroscopy. For the past few decades current technology has required these to be large, immobile instruments. Whilst such techniques are undoubtedly useful in a laboratory setting and provide high sensitivity along with precision and accuracy; they cannot be readily taken to the source of the sample, require skilled operators to ensure performance, and the sample must often undergo pre-treatment such as solid phase extraction (SPE). The need for rapid, accurate and portable sensing devices has become more and more prominent as the police use ethanol vapour concentration detectors in portable breath analysers [89 - 92].

It is well established in the literature that platinum electrodes can be used in the electrochemical detection of alcohols [93 - 96], there are also numerous reports in the literature of platinum being used in conjunction with another compound as the working electrode for electrochemical sensors [97 - 100]. Therefore, it was theorised that the CO-AF sensors could be simply and easily modified to detect alcohols such as methanol and ethanol and isomers of alcohols such as secondary alcohols, tertiary alcohols etc. This is even though in certain circumstances such as in low pH solutions, methanol can "poison" platinum electrodes by the carboxylic acid product adhering to the Pt electrode surface and subsequently reducing the reactivity of the Pt to the methanol reactant [101, 102]. Some of the CO-AF sensors were manufactured without the permanganate powder ($KMnO_4$) that normally acts as a chemical filter to remove (by oxidation) unwanted compounds such as sulfides and alcohols that would usually interfere with the chemical selectivity of the platinum electrode attempting to detect CO and no other gases. This batch of modified sensors is thus theoretically able to detect VOCs and is denoted CO-A1. Similar Pt/Ru sensors without the permanganate filter are denoted CM-A1.

The planned experiments involve passing a carrier gas (saturated with the VOC analyte) over the sensors and utilising electrochemical techniques such as cyclic voltammetry, chronoamperometry, and impedance spectroscopy as analytical tools to help determine a mathematical model for the diffusion

of analyte through the sensors. This requires tabulated values such as the vapour pressure of simple aliphatic and aromatic alcohols, which are readily available in the literature [103, 104].

It was hypothesised that alcohols would give an amperometric response during chronoamperometry due to the alcohol functional group being readily available for reaction at the platinum working electrode via surface adsorption and subsequent electron transfer. Whilst there is a greater potential of steric hindrance of a suitable reaction site in a tertiary alcohol than a primary or secondary alcohol it was still theorised that the secondary and tertiary alcohols would give an amperometric response during chronoamperometry, since the steric hindrance in tert-butanol is considered not to be so great as to prevent the electron transfer reaction at the Pt electrode.

The aromatic alcohol para-cresol (also called 4-methylphenol) was also tested. As p-cresol has a low vapour pressure and has a melting point around 30° C, it therefore may not provide enough vapour to give an amperometric response within the temperature range of the experiments. The structures of phenol and para-cresol are shown below (Fig 1.16). A selection of ketones, aldehydes, esters and carboxylic acids were used to determine the limit of electrooxidation for the CO-A1 sensor. At the potentials investigated, the CO-A1 sensor was only able to electrooxidize the alcohol and aldehyde functional groups. This work is described in chapter 7.

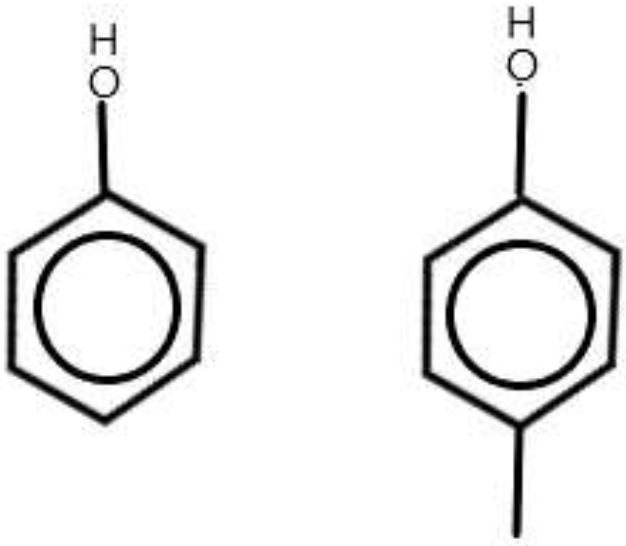

Figure 1.16: Structure of phenol (left) and para-cresol (right).

1.8.3 Hydrogels

The electrolytes commonly used within amperometric gas sensors (such as the CO-AF sensors) is 5M sulfuric acid. This choice represents a compromise between conductivity, volatility and activity of the Pt catalysts. Sulfate can adsorb on Pt and reduce the catalyst activity, but the very low vapour pressure of this electrolyte is the crucial factor – other choices will tend to evaporate and limit the lifetime of the devices. One issue that remains is the hygroscopic behaviour of sulphuric acid, which limits the operating lifetime of the sensors (which is part of the reason why a semi-permeable membrane is fitted across the top and a reservoir is included to allow for volume expansion), thus alternative electrolytes were sought. Existing devices can fail after adsorption of sufficient moisture from the atmosphere overloads the electrolyte reservoir and leaks occur. The corrosive nature of strong sulphuric acid may also be a problem.

Hydrogels were investigated as possible electrolyte because of their low volatility and quasi-solid nature. Hydrogels are cross-linked three-dimensional polymeric structures (Fig 1.17) that are capable of retaining a high amount of water, they swell but do not dissolve when brought into contact with water and their ability to absorb water is due to the presence of hydrophilic groups [105 - 108]. They have been used in a wide array of research areas from bioscience [109 - 112], environmental chemistry and nanochemistry [113 - 116], to materials engineering [117].

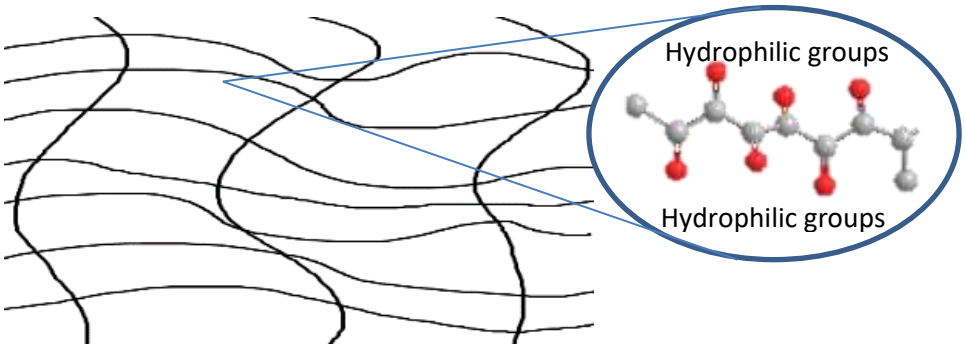

Figure 1.17: Structure of cross-linked polymer formed as a hydrogel (the lattice structure is able to hold a large amount of water due to the presence of hydrophilic groups).

1.9 Summary

There are many different technologies available for sensing gases such as CO and other toxic substances. The electrochemical techniques for analysing and quantifying these substances have been discussed and evaluated for their various strengths and weaknesses. Electrochemical devices, especially amperometric sensors are the technology of choice in industrial safety and urban air quality monitoring where multiple, spatially distributed measurements are desired [37,38]. Nevertheless, the mechanism of operation of these devices remains incompletely understood, in particular, the nature of mass transport of the analyte in the device. This thesis is primarily concerned with developing electrochemical techniques for the evaluation of amperometric gas sensors. The other technologies mentioned are to give an overview of the methodologies used in gas sensing.

Amperometric gas sensors have several advantages: they draw little current in the absence of analyte, have a wide range of linear calibration and, being electronic, are easily interfaced with data logging/storage systems. The limitations of amperometric gas sensors are mainly connected with the long-term stability of the electrolyte. A common choice is 5M sulfuric acid, but this is hygroscopic, and the device must be engineered to accommodate water uptake over time in humid environments. Sulfuric acid is corrosive, and this can also lead to devices failure. Alternative electrolytes are not easy to design, but the possibility of employing aqueous hydrogels was investigated.

The difficulty in producing a rigorous definition for hydrogels stems from the fact that their properties are often so varied (and can sometimes even be ‘tailored’ or ‘tuned’) that new aspects are being discovered all the time (such as measurable responses to changes in pH) [118, 119]. In this thesis, the suitability of polyacrylate hydrogels as an electrolyte was assessed in chapter 8. A variety of simple redox probes (charge and neutral) were employed in order to study the voltammetric properties of the hydrogel electrolyte. The stability of the electrolyte was also assessed gravimetrically.

1.10 References

[1] P. A. Carson, C. J. Mumford
Hazardous Chemicals Handbook, 2002, **2nd Edn.**, Butterworth-Heineman, Woburn

[2] S. Zampolli, I. Elmi, F. Ahmed, M. Passini, G. C. Cardinali, S. Nicoletti, L. Dori
Sensors and Actuators B: Chemical, 2004, **101**, 39-46

[3] P. Höppe, I. Martinac
Int. J. Biometeorol., 1998, **42**, 1-7

[4] A. Chaloulakou, I. Mavroidis
Atmos. Environ., 2002, **36**, 1769-1781

[5] M. van den Bossche, N. T. Rose, S. F. J. De Wekker
Sensors and Actuators B: Chemical, 2017, **238**, 501-509

[6] D. Kohl
J. Phys. D: Appl. Phys., 2001, **34**, 125-149

[7] X. Pang, M. D. Shaw, A. C. Lewis, L. J. Carpenter, T. Batchellier
Sensors and Actuators B: Chemical, 2017, **240**, 829-837

[8] L. Spinelle, M. Gerboles, M. Aleixandre
Procedia Engineering, 2015, **120**, 480-483

[9] B. Timmer, W. Olthuis, A. Van Den Berg
Sensors and Actuators B: Chemical, 2005, **107**, 666-677

[10] P. Werle, F. Slemr, K. Maurer, R. Kormann, R. Mücke, B. Jänker
Optics and lasers in Engineering, 2002, **37**, 101-114

[11] C. Zheng, W. Ye, N. P. Sanchez, C. Li, L. Dong, Y. Wang, R. J. Griffin, F. K. Tittel
Sensors and Actuators B: Chemical, 2017, **244**, 365-372

[12] G. F. Fine, L. M. Cavanagh, A. Afonja, R. Binions
Sensors, 2010, **10**, 5469-5502

[13] K. Suematsu, M. Sasaki, N. Ma, M. Yuasa, K. Shimanoe
ACS Sens., 2016, **1**, 913-920

[14] H. Okamoto, H. Obayashi, T. Kudo
Solid State Ionics, 1980, **1**, 319-326

[15] P. Jacquinot, A. W. E. Hodgson, B. Müller, B. Wehrli, P. C. Hauser
Analyst, 1999, **124**, 871-876

[16] P. Jacquinot, A. W. E. Hodgson, P. C. Hauser
Analytica Chimica Acta, 2001, **443**, 53-61

[17] J. Stetter, J. Li
Chem. Rev., 2008, **108**, 352-366

[18] R. Ghosh, A. K. Nayak, P. K. Guha, S. Santra, D. Pradhan
RSC Adv., 2015, **5**, 50165–50173

[19] H. Yamaura , K. Moriya, N. Miura, N. Yamazoe
Sensors and Actuators B: Chemical, 2000, **65**, 39–41

[20] C. G. Armstrong, K. E. Toghill
Journal of Power Sources, 2017, **349**, 121-129

[21] G. Zhen, X. Lu, G. Kumar, P. Bakonyi, K. Xu, Y. Zhao,
Prog. Energy Combust. Sci., 2017, **63**, 119-145

[22] Q. Xu, T. S. Zhao
Prog. Energy Combust. Sci., 2015, **49**, 40-58

[23] J. Cho, S. Jeong, Y. Kim
Prog. Energy Combust. Sci., 2015, **48**, 84-101

[24] *http://www.alphasense.com/WEB1213/wp-content/uploads/2013/07/AAN_104.pdf*

[25] B. R. Gurjar, T. M. Butler, M. G. Lawrence, J. Lelieveld
Atmos. Environ., 2008, **42**, 1593-1606

[26] A. Bigi, G. Ghermandi, R. M. Harrison
J. Environ. Monit., 2012, **14**, 552-563

[27] T. F. Villa, F. Salimi, K. Morton, L. Morawska, F. Gonzalez
Sensors, 2016, **16**, 2202-2217

[28] H. Yuan, C. Xiao, W. Zhan, Y. Wang, C. Shi, H. Ye, K. Jiang, Z. Ye, C. Zhou, Y. Wen, Q. Li
J. Intell. Robot. Syst., 2018, **91**, 1-12

[29] H. Akimoto
Science, 2003, **302**, 1716-1719

[30] D. Handique, K. G. Bhattacharyya
Asian J. Atmos. Environ., 2017, **11**, 254-269

[31] C. L. Sabine, R. A. Freely, N. Gruber, R. M. Key, K. Lee, J. L. Bullister, R. Wanninkhof, C. S. Wong, D. W. R. Wallace, B. Tilbrook, F. J. Millero, T-H. Peng, A. Kozyr, T. Ono, A. F. Rios
Science, 2004, **305**, 367-371

[32] E. Fritzsche, P. Gruber, S. Schutting, J. P. Fischer, M. Strobl, J. D. Muller, S. M. Borisov, I. Klimant
Anal. Methods, 2017, **9**, 55-65

[33] H. R. Anderson, S. A. Bremner, R. W. Atkinson, R. M. Harrison, S. Walters
Occup. Environ. Med., 2001, **58**, 504-510

[34] B. R. Gurjar, A. Jain, A. Sharma, A. Agarwal, P. Gupta, A. S. Nagpure, J. Lelieveld
Atmos. Environ., 2010, **44**, 4606-4613

[35] B. Brunekreef, S. T. Holgate
The Lancet, 2002, **360**, 1233-1242

[36] M. Guarnieri, J. R. Balmes
The Lancet, 2014, **383**, 1581-1592

[37] M. Hossain, J. Saffell, R. Baron,
ACS Sens., 2016, **1**, 1291-1294

[38] R. Baron, J. Saffell
ACS Sens., 2017, **2**, 1553-1566

[39] A. Kumar, A. Sanger, A. Kumar, R. Chandra
RSC Adv., 2016, **6**, 47178-47184

[40] M. F. Rutolo, J. P. Clarkson, G. Harper, J. Covington
Postharvest Biology and Technology, 2018, **145**, 15-19

[41] S. O. Agbroko, J. Covington
Sensors and Actuators B: Chemical, 2018, **275**, 10-15

[42] A. Favard, K. Aguir, T. Contaret, A. Dumas, M. Bendahan
Materials Today: Proceedings, 2019, **6**, 323-327

[43] P.-S. Murvay, I. Silea
Journal of Loss Prevention in the Process Industries, 2012, **25**, 966-973

[44] J. E. Lovelock
Nature, 1960, **188**, 401

[45] G. C. Rezende, S. Le Calve, J. J. Brandner, D. Newport
Sensors and Actuators B: Chemical, 2019, **287**, 86-94

[46] A. N. Freedman
Journal of Chromatography, 1980, **190**, 263-273

[47] P. J. Hobbs, T. H. Misselbrook, B. F. Pain
Journal of Agricultural Engineering Research, 1995, **60**, 137-144

[48] M. Ahmadi, H. Knoef, B. Van De Beld, T. Liliedahl, K. Engvall
Fuel, 2013, **113**, 113-121

[49] A. Dey
Materials Science and Engineering B, 2018, **229**, 206-217

[50] M. Righettoni, A. Amann, S.E. Pratsinis
Mater. Today, 2015, **18**, 163–171

[51] J. R. Stetter, J. Li
Chem. Rev., 2008, **108**, 352-366

[52] L. Xiong, R. G. Compton
Int. J. Electrochem. Sci., 2014, **9**, 7152-7181

[53] P.-A. Gross, T. Jaramillo, B. Pruitt
Anal. Chem., 2018, **90**, 6102-6108

[54] M. Dosi, I. Lau, Y. Zhuang, D. S. A. Simakov, M. W. Fowler, M. A. Pope
ACS Appl. Mater. Interfaces, 2019, **11**, 6166-6173

[55] W. Feng, D. Liu, Q. Zhai, G. Feng
Sensors and Actuators B: Chemical, 2017, **240**, 625-630

[56] W. Feng, G. Feng
Sensors and Actuators B: Chemical, 2018, **255**, 2314-2320

[57] P. Krebs, A. Grisel
Sensors and Actuators B: Chemical, 1993, **13**, 155-158

[58] M. Gall
Sensors and Actuators B: Chemical, 1993, **16**, 260-264

[59] H. Debeda, D. Rebiere, J. Pistre, F. Menill
Sensors and Actuators B: Chemical, 1995, **27**, 297-300

[60] H. Ma, E. Ding, W. Wang
Sensors and Actuators B: Chemical, 2013, **187**, 221-226

[61] E. Santos, W. Schmickler
Chem. Phys., 2007, **332**, 39-47

[62] M. D. Arce, P. Quaino, E. Santos
Catalysis Today, 2013, **202**, 120-127

[63] Z. Jiang, L. Li, M. Li, R. Li, T. Fang
Applied Surface Science, 2014, **301**, 468-474

[64] L. M. C. Pinto, P. Quaino, M. D. Arce, E. Santos, W. Schmickler
Chem. Phys. Chem., 2014, **15**, 2003-2009

[65] L. M. C. Pinto, G. Maia
J. Phys. Chem. C, 2015, **119**, 8213-8216

[66] J. Huang, A. Malek, J. Zhang, M. H. Eikerling
J. Phys. Chem. C, 2016, **120**, 13587-13595

[67] A. Härtel
J. Phys.: Condens. Matter, 2017, **29**, 423002-423026

[68] C. Zhang, S. Lu, R. Mao, W. Chen, L. Tan, Q. Zhou, J. Yang
J. Appl. Phys., 2017, **121**, 044502-044509

[69] D. A. B. Iozzo, M. Tong, G. Wu, E. P. Furlani
J. Phys. Chem. C, 2015, **119**, 25235-25242

[70] F. L. Leite, C. C. Bueno, A. L. Da Roz, E. C. Ziemath, O. N. Oliveira Jr.
Int. J. Mol. Sci., 2012, **13**, 12773-12856

[71] D. C. Grahame
Chemical Reviews, 1947, **41**, 441-501

[72] B. E. Conway
J. Electrochem. Soc., 1991, **138**, 1539-1548

[73] A. M. Namisnyk
Bsc Thesis, 2003, **University of Technology**, Sydney

[74] D. O. Wipf, E. W. Kristensen, M. R. Deakin, R. M. Wightman
Anal. Chem., 1988, **60**, 306-310

[75] J. F. Rusling, S. L. Suib
Adv. Mats., 1994, **6**, 922-930

[76] Z. Galus, J. Golas, J. Osteryoung
J. Phys. Chem., 1988, **92**, 1103-1107

[77] E. Laviron
J. Electroanal. Chem., 1979, **100**, 263-270

[78] D. A. Scherson, J. Newman
J. Electrochem. Soc., 1980, **127**, 110-113

[79] X.-J. Huang, A. M. O'Mahony, R. G. Compton
Small, 2009, **5**, 776-788

[80] R. A. Marcus
J. Phys. Chem., 1963, **67**, 853-857

[81] S. Fletcher
J. Solid State Electrochem., 2010, **14**, 705-739

[82] P. J. Feibelman, B. Hammer, J. K. Norskov, F. Wagner, M. Scheffler, R. Stumpf, R. Watwe, J. Dumesic
J. Phys. Chem. B, 2001, **105**, 4018-4025

[83] P. Liu, A. Logadottir, J. K. Norskov
Electrochimica Acta, 2003, **48**, 3731-3742

[84] R. Levy
Neurotoxicology and Teratology, 2015, **49**, 31-40

[85] J. A. Raub, M. Mathieu-Nolf, N. B. Hampson, S. R. Thom
Toxicology, 2000, **145**, 1-14

[86] S. R. Thom
N. Engl. J. Med., 2002, **347**, 1105-1106

[87] K. P. Stoller
Neurological Research, 2007, **29**, 146-155

[88] J. D. Roderique, C. S. Josef, M. J. Feldman, B. D. Spiess,
Toxicology, 2015, **334**, 45-58

[89] S. Tsang, C. Bulpitt
Sensors and Actuators B: Chemical, 1998, **52**, 226–235

[90] M. A. Balbino, E. N. Oiye, M. F. M. Ribeiro, J. W. Cruz Júnior, I. C. Eleotério, A. J. Ipólito, M. F. de Oliveira
J. Solid State Electrochem., 2016, **20**, 2435-2443

[91] J. P. Smith, J. P. Metters, D. K. Kampouris, C. Lledo-Fernandez, O. B. Sutcliffe, C. E. Banks
Analyst, 2013, **138**, 6185-6191

[92] L. R. Cumba, J. P. Smith, K. Y. Zuway, O. B. Sutcliffe, D. R. do Carmo, C. E. Banks
Anal. Methods, 2016, **8**, 142-152

[93] J. Gadomska, M. Donten, Z. Stojek, L. Nyholm
Analyst, 1996, **121**, 1869-1871

[94] M. Besson, P. Gallezot
Catalysis Today, 2000, **57**, 127-141

[95] A. V. Tripkovic, S. L-J. Gojkovic, K. DJ. Popovic, J. D. Lovic
J. Serb. Chem. Soc., 2006, **71**, 1333- 1343

[96] S. N. Raicheva, S. V. Kalcheva, M. V. Christov, E. I. Sokolova
Electroanalytical Chemistry and Interfacial Electrochemistry, 1974, **55**, 213-222

[97] P. K. Shen, A. C. C. Tseung
J. Electrochem. Soc., 1994, **141**, 3082-3090

[98] C. X. Yuan, Y. R. Fan, T. Zhang, H. X. Guo, J. X. Zhang, Y. L. Wang, D. L. Shan, X. Q. Lu
Biosensors and Bioelectronics, 2014, **58**, 85-91

[99] Y. Chen, K.Y. Chen, A.C.C. Tseung
J. Electroanal. Chem., 1999, **471**, 151–155

[100] A.V. Tripkovic, K.D. Popovic, B.N. Grgur, B. Blizanac, P.N. Ross, N.M. Markovic
Electrochimica Acta, 2002, **47**, 3707-3714

[101] T.D. Jarvi, S. Sriramulu, E.M. Stuve
Colloids and Surfaces A: Physicochemical and Engineering Aspects, 1998, **134**, 145-153

[102] J. Prabhuram, R. Manoharan
Journal of Power Sources, 1998, **74**, 54-61

[103] D. Ambrose, C. H. S. Sprake, R. Townsend
J. Chem. Thermodynamics, 1975, **7**, 185-190

[104] D. Ambrose, C. H. S. Sprake
J. Chem. Thermodynamics, 1970, **2**, 631-64

[105] N. Yamazoe
Sensors and Actuators B: Chemical, 1991, **5**, 7–19

[106] G. Neri, A. Bonavita, G. Rizzo, S. Galvagno, S. Capone, P. Siciliano
Sensors and Actuators B: Chemical, 2006, **114**, 687–695

[107] T. Jinkawa, G. Sakai, J. Tamaki, N. Miura, N. Yamazoe
Journal of Molecular Catalysis A: Chemical, 2000, **155**, 193–200

[108] N. Barsan, D. Koziej, U. Weimar
Sensors and Actuators B: Chemical, 2007, **121**, 18-35

[109] J. Zhang, B. Wang, B. Xu, G. Cheng, S. Dong
Anal. Chem., 2000, **72**, 3455-3460

[110] J. Park, H. Yee, S. Kim
Biosensors & Bioelectronics, 1995, **10**, 587-594

[111] C. Garzella, E. Comini, E. Bontempi, L. E. Depero, C. Frigeri, G. Sberveglieri
Sensors and Actuators B: Chemical, 2002, **83**, 230-237

[112] E. Comini
Analytica Chimica Acta, 2006, **568**, 28–40

[113] J. Gadomska, M. Donten, Z. Stojek, L. Nyholm
Analyst, 1996, **121**, 1869-1871

[114] M. Besson, P. Gallezot
Catalysis Today, 2000, **57**, 127-141

[115] A. V. Tripkovic, S. L-J. Gojkovic, K. DJ. Popovic, J. D. Lovic
J. Serb. Chem. Soc., 2006, **71**, 1333- 1343

[116] S. N. Raicheva, S. V. Kalcheva, M. V. Christov, E. I. Sokolova
Electroanalytical Chemistry and Interfacial Electrochemistry, 1974, **55**, 213-222

[117] P. K. Shen, A. C. C. Tseung
J. Electrochem. Soc., 1994, **141**, 3082-3090

[118] J. Munk, P.A. Christensen, A. Hamnett, E. Skou
J. Electroanal. Chem., 1996, **401**, 215-222

[119] A.V. Tripkovic, K.D. Popovic, B.N. Grgur, B. Blizanac, P.N. Ross, N.M. Markovic
Electrochimica Acta, 2002, **47**, 3707-3714

Chapter 2

2.0 Experiment Methods

List of Materials and Equipment Used

Materials (all reagent grade, supplied by SigmaAldrich)
polyacrylamide-co-acrylic acid
methanol
ethanol
heptan-1-ol
propan-2-ol
tert-butanol
para-cresol
propanal
hexanal
acetone
heptan-4-one
ethanoic acid
propionic acid
ethyl ethanoate
propyl propionate
deionised water

Equipment
PalmSens 3 potentiostat (model no. PS14D116i)
Digital mass flow controller (DMFC) (Brooks 5850S, 0206 Brooks smart interface)
PStrace electrochemistry software (version 4.0)
CO gas cylinder (2000 ppm in synthetic air) supplied by BOC
Zero grade air cylinder supplied by BOC
HR-2 Discovery Hybrid rheometer (model no. v1.0)

2.1 Electrochemical Measurements in Hydrogel Electrolytes

A potentiostat (PalmSens3 purchased from PalmSens Ltd) with specialised software (PStrace 4.0) on a laptop running Microsoft Windows 7 (Microsoft Corporation) was used to measure the performance of the hydrogels containing different redox couples via cyclic voltammetry, impedance spectroscopy, and fast amperometry. The electrochemical cell was a standard three electrode configuration.

The electrodes used in the electrochemical analysis were as follows: The working electrode (WE) was a 25 µm diameter platinum disk microelectrode in glass, the reference electrode (Ref) was an aqueous silver/silver chloride microelectrode, and the counter electrode (CE) was a 3 mm diameter platinum disc electrode of 99.9 % purity. All were supplied by IJ Cambria Ltd (manufacturer CH Instruments Inc.) and used as originally supplied by the manufacturer in accordance with supplied user guidelines. The placement of the electrodes within the hydrogel and the distances between the electrodes was of negligible consequence owing to the small radius of the counter electrode compared to the working electrode. The setup of the three-electrode cell is shown below (Fig 2.1):

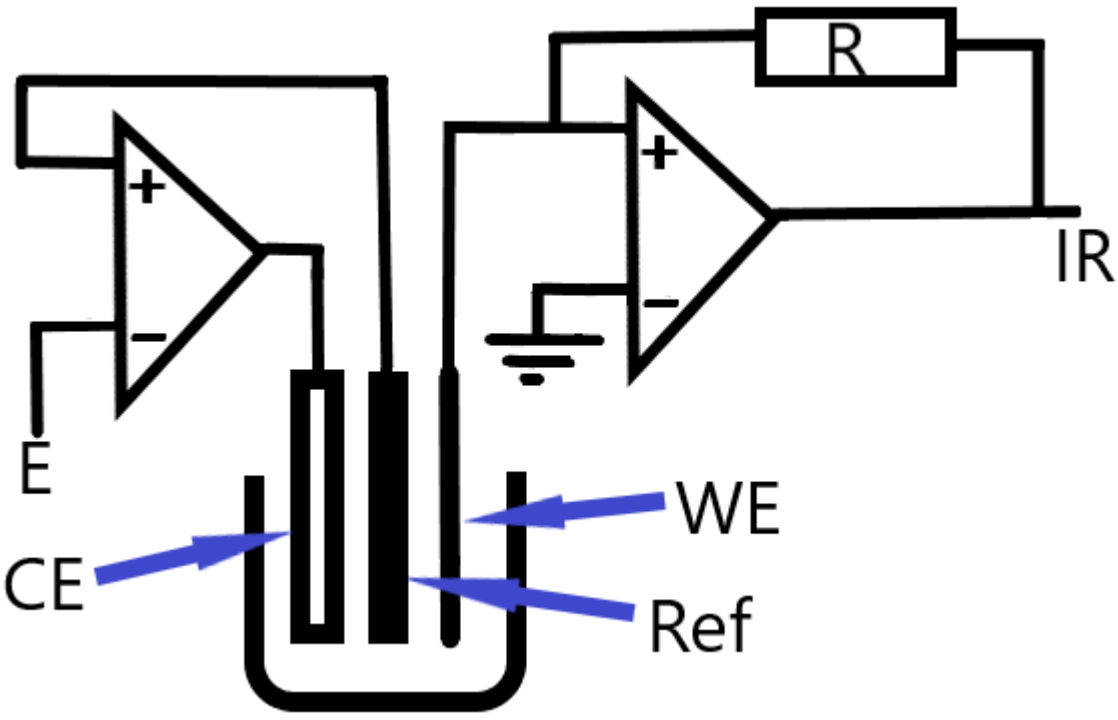

Figure 2.1: Schematic of Electrochemical Hydrogel Experiments with three electrode potentiostat as standard (WE = 25 µm Pt disc, CE = 3 mm Pt disc, Ref = Ag/AgCl aq. 1 M KCl(aq))

2.1.1 Electrochemical Measurements in Gas Sensors

The CO-AF and CO-A1 sensors were used as supplied by Alphasense Ltd (Table 2.1). All of the experiments were conducted within a specially constructed gas rig that allowed the control of the concentration and species of gas for each experiment. The Alphasense sensors use their own internal reference electrode (Pt black) which has a mixed potential determined by redox processes on the Pt particles (O_2 reduction and Pt oxidation). Whilst tables of standard electrode potentials are readily available in the literature [120], mixed potential electrodes are harder to determine. The voltages during all electrochemical experiments were simply the potential applied by the PalmSens potentiostat across the circuit. The compound metal electrode (Pt/Ru) sensor was used without a permanganate filter (CM-A1). The metal ratios were approximately 33% Pt and 67% Ru. All sensors had the same dimensions and three electrode configuration (Fig 2.2).

	Components
CO-AF	Porex semi-permeable PTFE membrane (thickness 0.18 mm)* $KMnO_4$ powder 5M H_2SO_4 electrolyte Pt working electrode
CM-A1	Porex semi-permeable PTFE membrane (thickness 0.18 mm) no $KMnO_4$ powder 5M H_2SO_4 electrolyte Pt/Ru working electrode
CO-A1	Porex semi-permeable PTFE membrane (thickness 0.18 mm) no $KMnO_4$ powder 5M H_2SO_4 electrolyte Pt working electrode

*In some devices a thicker membrane of thickness 0.25 mm was used

Table 2.1: Components of the different sensors used within the thesis

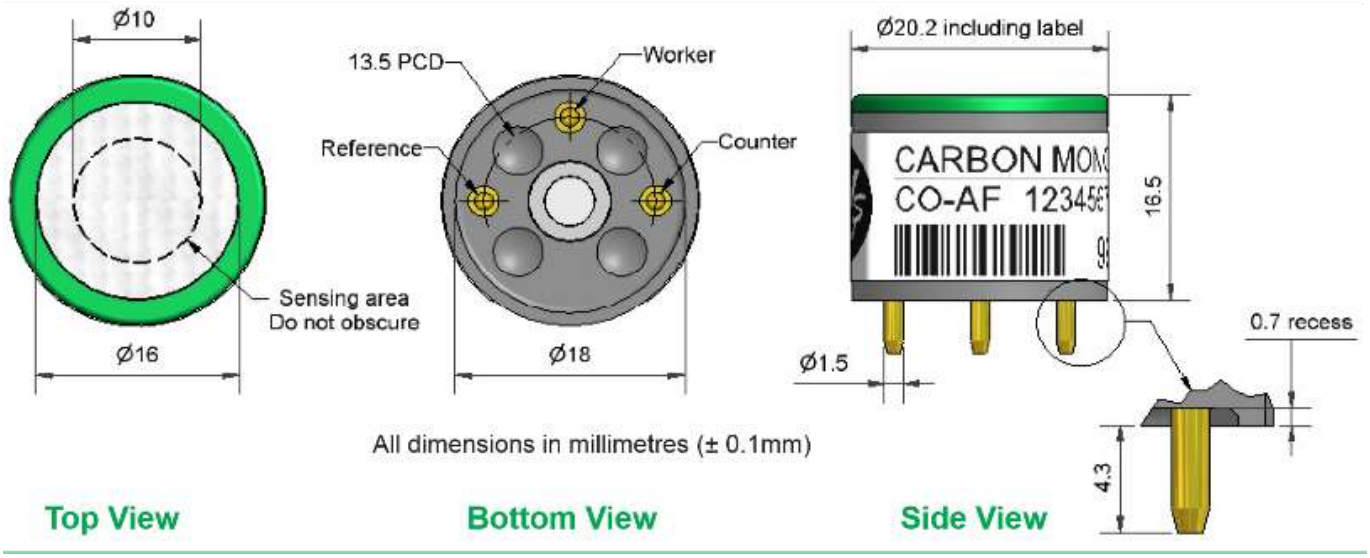

Figure 2.2: Schematic of Alphasense three electrode sensor. Reproduced from [121]

2.2 Electrochemistry Techniques

In this thesis the main techniques employed were chronoamperometry, cyclic voltammetry and impedance spectroscopy. The principles of these methods were introduced in chapter 1, here the practical implementation of such techniques is discussed.

2.2.1 Cyclic Voltammetry

In general, standard cyclic voltammetry is less useful for the analysis of very high surface area devices such as amperometric gas sensors, because of their large capacitance and the large charging currents. Nevertheless, some information on the capacitance and the potential-dependence can be obtained from very slow scan rate data.

CO-AF and other amperometric sensors were connected to a PalmSens 3 potentiostat (Alvatek Ltd, UK) using a PCB board supplied by Alphasense Ltd. Typical scan rates were in the range 0.1 – 1 mV s^{-1} and the internal working, reference and counter electrodes were connected to the corresponding terminals of the potentiostat. The sensors were covered by a plastic hood fitted over the PCB board to allow control of the gas atmosphere during the acquisition of a voltammogram (details in section 2.3 below). The data was collected via a laptop running PSTrace 4.0 ™ under MS Windows 7 ™.

2.2.2 Impedance Spectroscopy

Impedance spectroscopy was used to make quantitative determinations of the differential capacitance and was implemented using the same apparatus as cyclic voltammetry. The amplitude of the applied sinusoidal voltage was 1 mV and the frequency ranges were typically 0.1 – 10 Hz.

2.2.3 Chronoamperometry

Within this thesis, chronoamperometry refers to the measurement of current against time in response to a concentration change (Fig 2.3). This is slightly different to the usual meaning of the term, which indicates the current response to a potential step. The use of chronoamperometry allows changes in current to be tracked whilst keeping the voltage constant, and thus avoiding issues with charging currents obscuring the faradaic process. Owing to the large differential capacitance of amperometric gas sensors, chronoamperometry was the main electroanalytical technique employed. It is also the primary gas detection mode of operation used by Alphasense CO-AF sensors and many other gas sensing electrochemical devices. Finally, the current can be used to back calculate the concentration of gas being detected (using Dalton's law). Fick's first and second laws (when considered with set boundary conditions) are also used as part of the mathematical modelling [122].

Time (secs)	900	1200	1500
Flow rate air (mL /min)	500		
Flow rate CO (mL /min)	214	333	500
Gas concentration (ppm)	600	800	1000

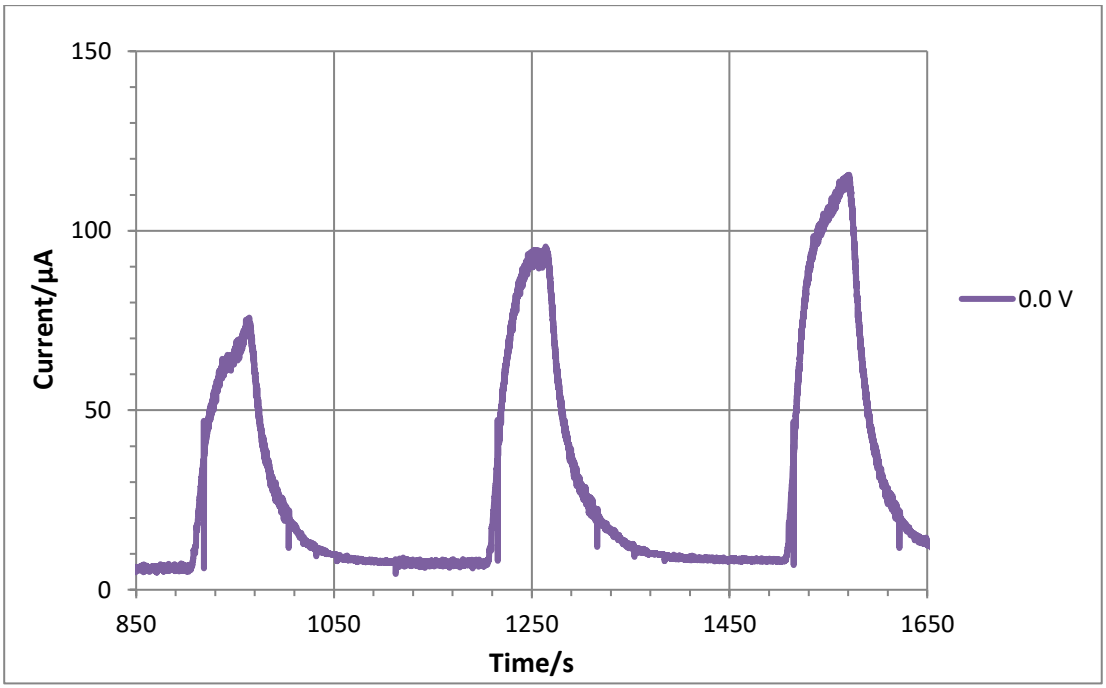

Figure 2.3: Table and graph of CO-AF sensor showing proportional response to pulsed CO at increasing concentrations (200, 400, 600 ppm respectively).

It is known that the sensors exhibit an amperometric response proportional to analyte concentration (Fig 2.4). The analyte concentration at the external surface of the sensor is assumed to rise from zero to a constant value almost instantaneously during the testing of the devices (Fig 2.5). This assumption is justified in section 2.3 below. However, there is a delay in the sensor response before the maximum current at the set concentration is reached (Fig 2.6). The time taken to reach this maximum current and the value of the maximum current, can be used to calculate the diffusion rates across the different parts of the sensor as the analyte must pass through different phases within the sensor before reaching the Pt working electrode. The mathematical model of chapter 3 was fitted to chronoamperometric traces in order to extract effective diffusion coefficients and layer thicknesses, which are then interpreted in terms of the nature of transport inside the sensors.

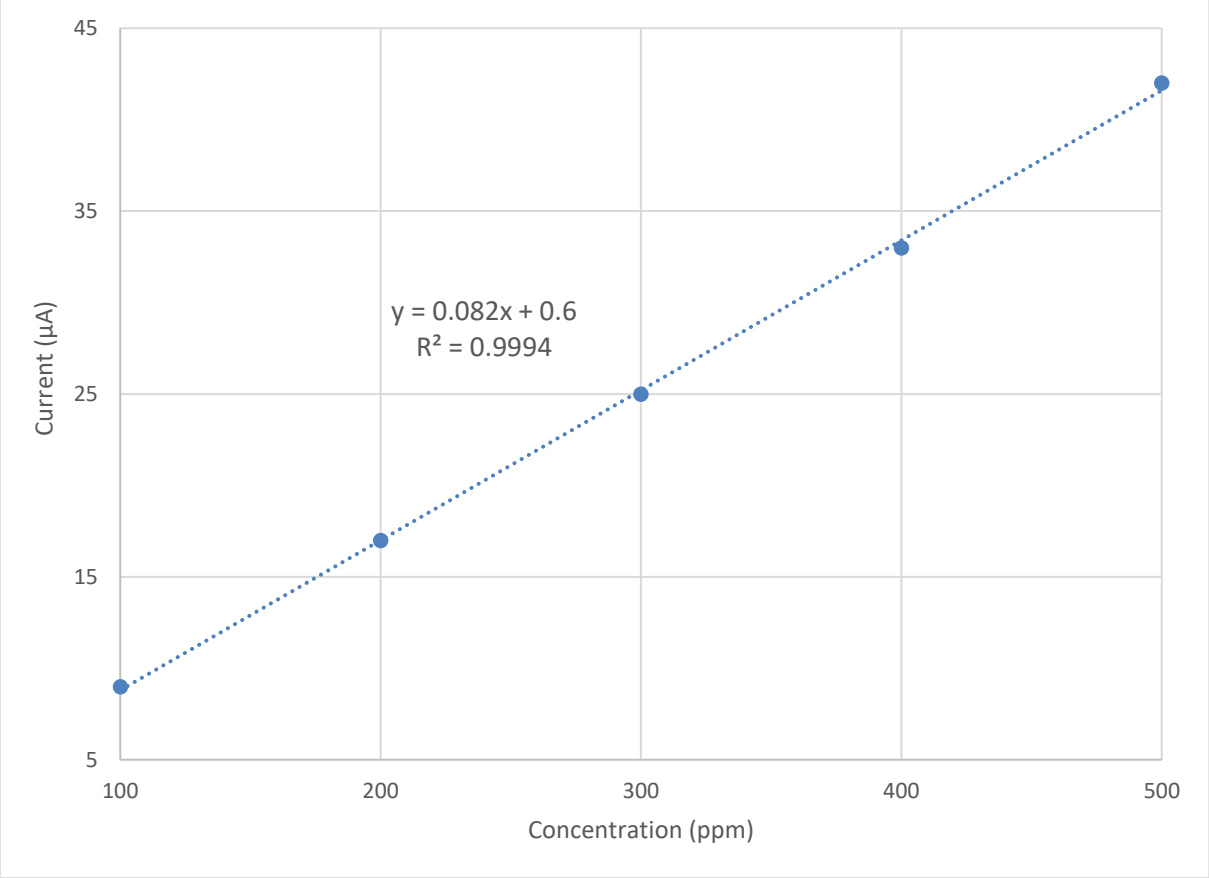

Figure 2.4: Graph showing linear relationship between analyte concentration and current response (CO-AF device in CO at 20 °C)

All experiments were undertaken at 0.0 V (according to the gas sensor) unless otherwise stated. This is the standard operating potential for the majority of Alphasense devices and is chosen due to the fact that at higher potentials the background current becomes very large, and at lower potentials the oxidation of CO is no longer mass transport controlled. It is also possible that unwanted currents due to oxygen reduction occur at lower potentials.

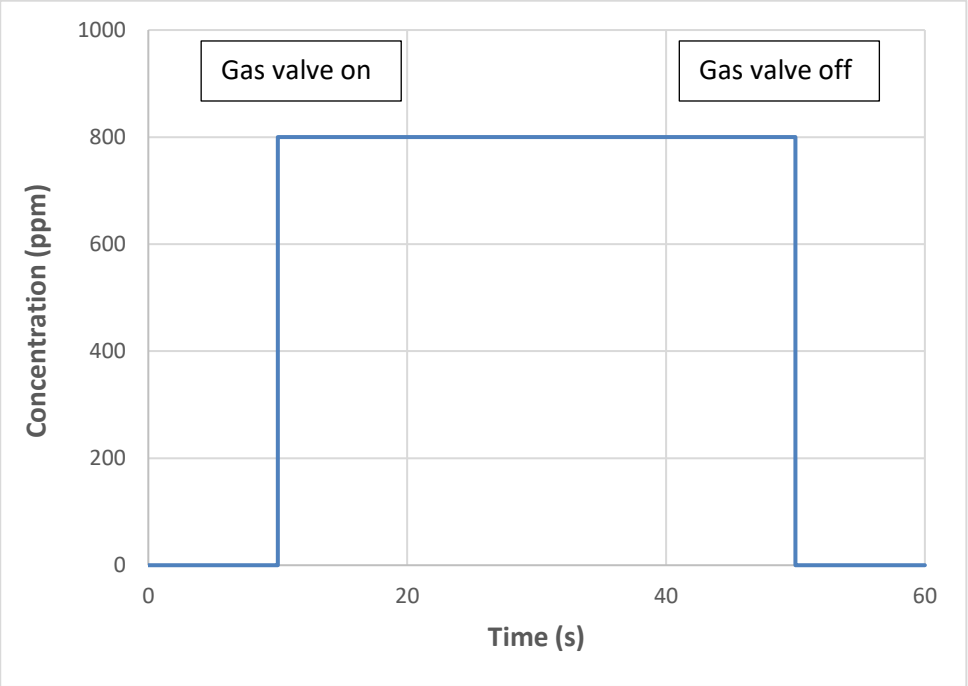

Figure 2.5: Example graph showing change in analyte concentration when gas valve is turned on.

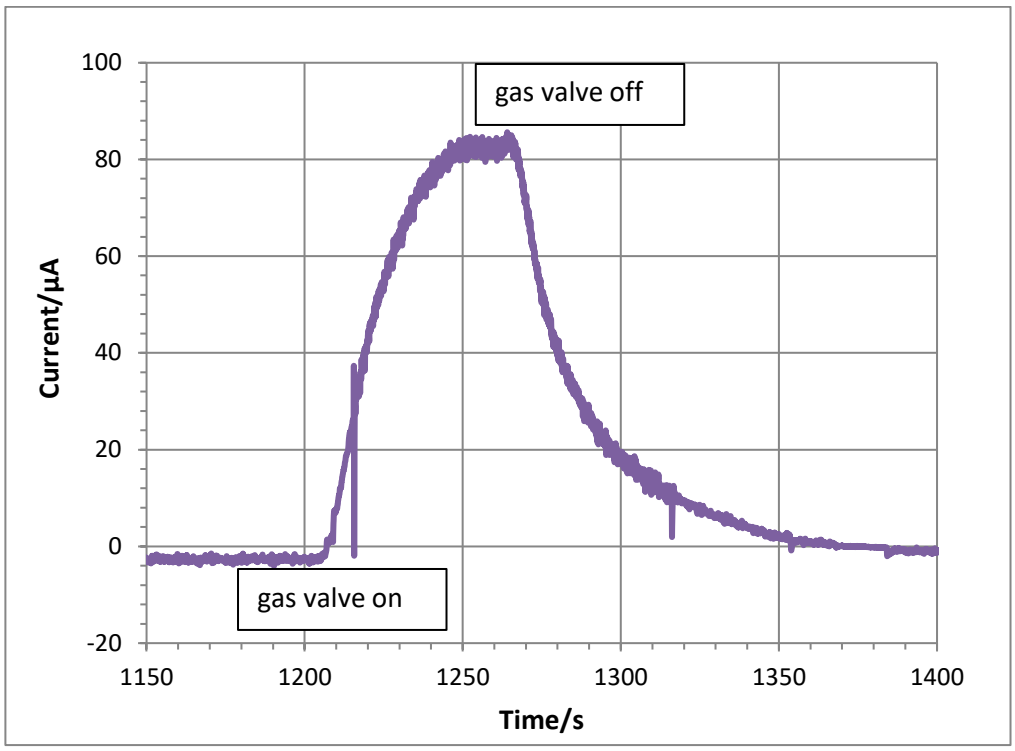

Figure 2.6: Graph showing chronoamperometric response upon exposure to analyte vapour.

2.2.4 Rate Effects

The mathematical model of the Alphasense devices in this thesis (Chapter 3) is based upon rate-limiting mass transport of the analyte. However, in general the observed rate of an electrochemical process depends on both the electrode kinetics and the mass transport rate. The relationship between kinetic effects and mass transport effects (for a uniformly accessible electrode) is shown below (Eqn 2.1):

$$\frac{1}{v} = \frac{1}{v_k} + \frac{1}{v_L} \tag{2.1}$$

Where v is the overall rate, v_k is the rate under conditions of pure kinetic control and v_L is the limiting mass transport-controlled rate.

The mass transport rate is independent of applied potential; however the electrode kinetics are usually strongly potential-dependent, e.g. according to Tafel's Law (Eqn 2.2) and the Butler-Volmer equation (Eqn 2.3).

$$\eta = A \times \log\left(\frac{i}{i_0}\right) \tag{2.2}$$

Where η is the overpotential, A is the Tafel slope (gradient), i is the current density and i_0 is the exchange current density.

$$j = j_0 \cdot \left\{ \exp\left[\frac{\alpha_a z F \eta}{RT}\right] - \exp\left[-\frac{\alpha_c z F \eta}{RT}\right] \right\} \tag{2.3}$$

Where η is the overpotential, j is the current density, j_0 is the exchange current density, z is number of electrons, α is the charge transfer coefficient.

The test for mass transport control is to take chronoamperometry measurements of the same analyte at a known concentration and run each experiment at a different, but constant applied potential. If there is a substantial change in the maximum steady state current at different potentials, then both mass transport and electrode kinetics may be affecting the rate. However, if there is no significant change in maximum steady state current as potential changes then mass transport is the dominant

effect within the electrochemical system (Fig. 2.7). This is indicative of mass transport control being the dominant effect within the sensor.

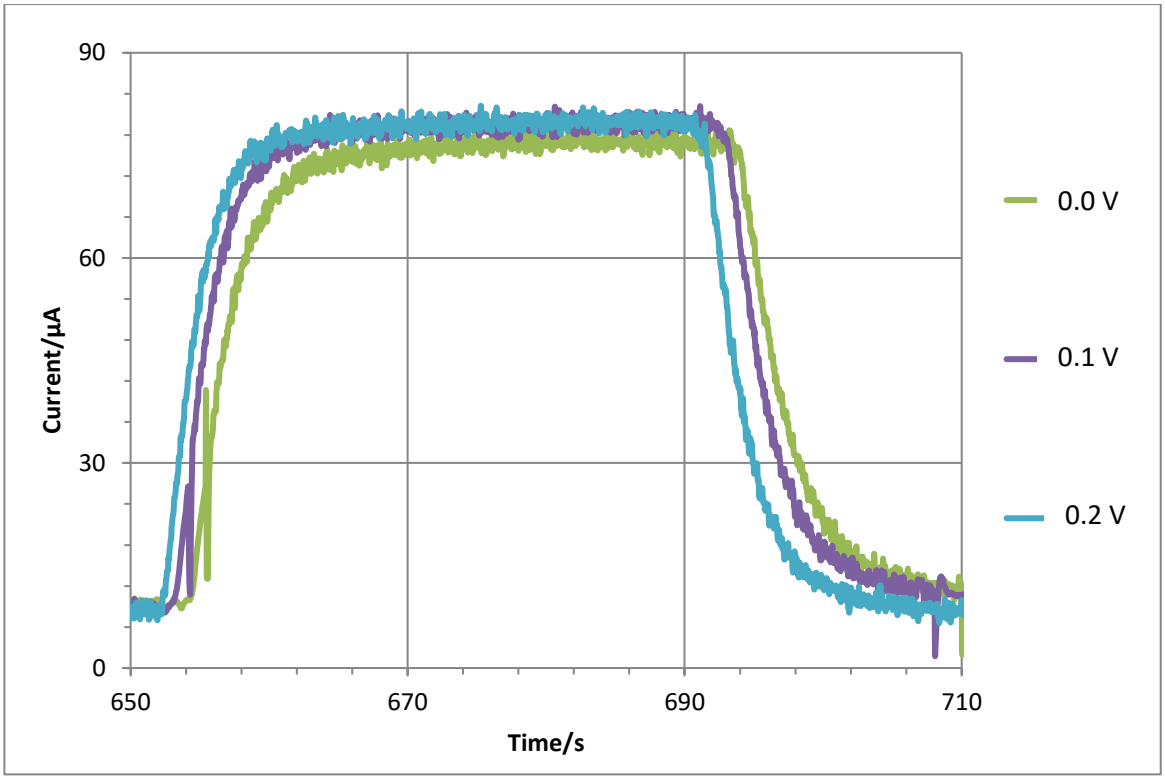

Figure 2.7: Example voltage bias experiment for the CO-AF sensor response to pulsed CO at a known concentration and flow rate (1000 ppm, 500 mL / min gas flow rate) and three different applied potentials.

2.3 Gas Testing Rig

The sensor was housed within a plastic hood (Fig. 2.8) and zero grade air (supplied by BOC Industrial Gases Ltd.) was used as a carrier gas to bubble through the Dreschel bottle containing different liquid compounds. Zero grade air is synthetic air that has been filtered so that it contains only nitrogen and oxygen, and minor trace impurities (BOC product code: 270020-V, CAS number: 132259-10-0).

Component	Concentration (%)
nitrogen	79
oxygen	21
carbon dioxide	< 0.1
hydrocarbons	< 0.3
moisture	< 0.2

Table 2.2: Chemical composition of zero grade air.

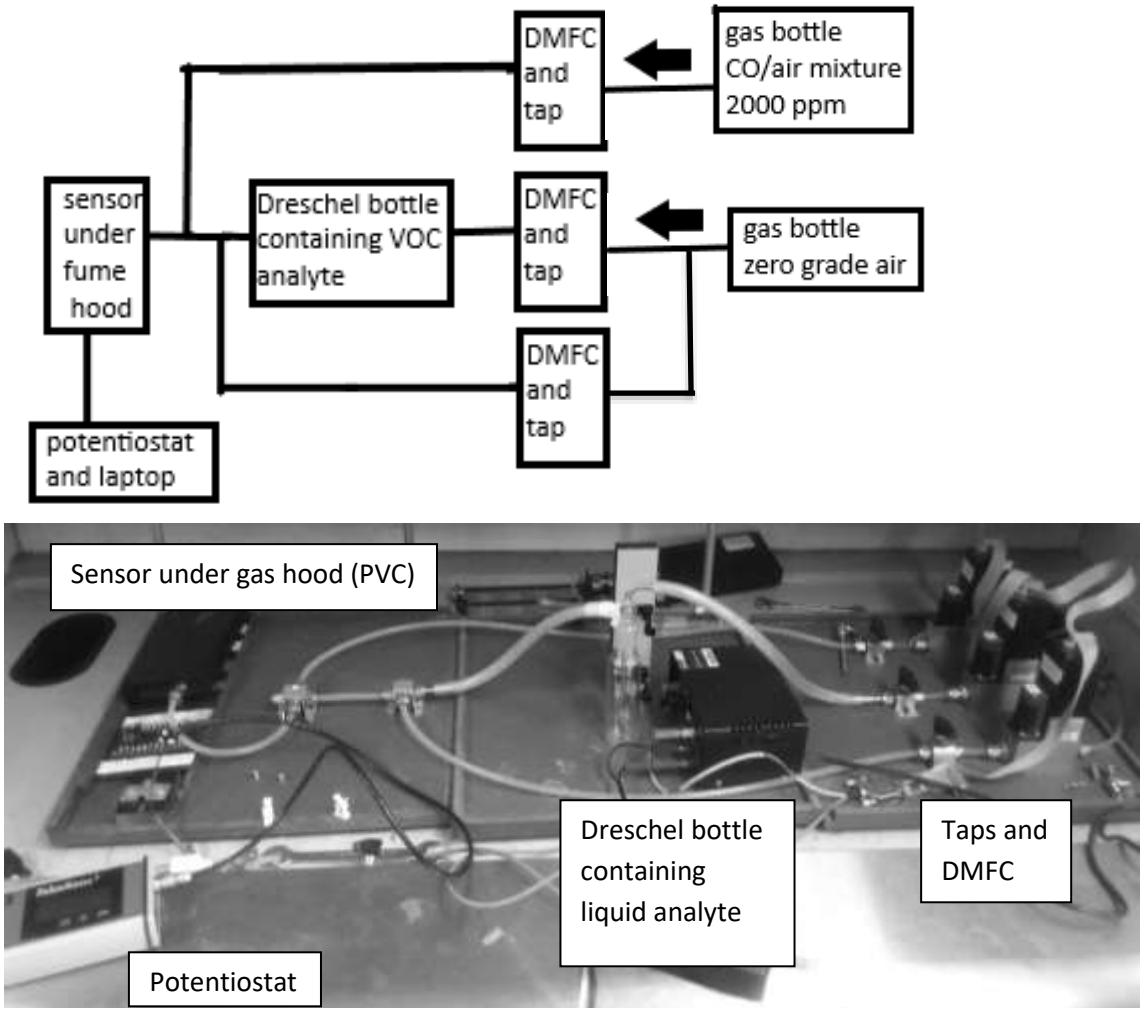

Figure 2.8: Photograph and schematic of gas rig (inside fume hood) showing main components used during experiments.

The apparatus in figure 2.8 is shown setup up for the volatile organic compound measurements (VOCs). It was adapted in a straightforward manner to work with CO detection. In the experiments on CO detection, the Dreschel bottle was omitted and a gas stream of 2000ppm CO in zero air was mixed in controlled ratios with a zero air gas stream. The CO concentration is then determined by equation 2.4 but with P equal to the partial pressure of the CO/air stock bottle. The air saturated with analyte vapour then travelled from the Dreschel bottle to the sensor within the hood. The flow rates (and hence analyte concentrations) could be controlled in software using the DMFC (digital mass flow controller) devices. The DMFC devices (Brooks, 5850S) used on the gas rig work via a constant real-time feedback loop to ensure the correct flow rate. Using the Brooks 0260 Smart Interface software, a butterfly valve is opened or closed depending upon the information from the air flow probe that decides whether it is too hot or cold for the requested flow rate (Fig 2.9).

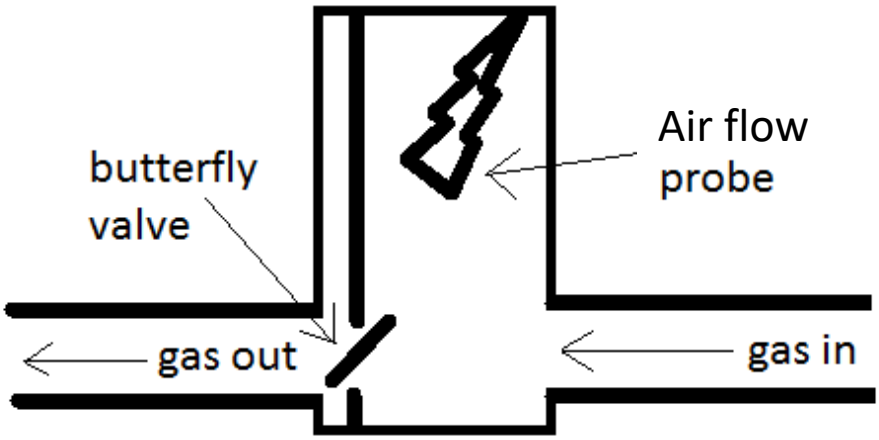

Figure 2.9: Schematic of DMFC device with butterfly valve and air flow probe to regulate gas flow.

By changing the gas flow through the Dreschel bottle at a known concentration and flow rate and combining it with a known constant gas flow rate from the zero-air cylinder, the partial pressure of VOC reaching the sensor can be calculated (Eqn 2.4). Where the partial pressure of the analyte vapour (P_t) is calculated from the standard vapour pressure of the gas at the temperature of the Dreschel bottle measured via thermocouple (P), the volume flow rate of analyte saturated gas (V_g) and the volume flow rate of zero air (V_a). Note in Fig 2.10 below that the connectors on the rig are 6 mm PVC tubing, the sensor and PVC hood are mounted on a PCB board (supplied by Alphasense Ltd).

$$P_t = P\frac{Vg}{Vg+Va} \tag{2.4}$$

The nature of the butterfly valve feedback system within the DMFC can produce pulses of gas that are not exactly taken into account by the mathematical model, as it assumes an immediate increase in analyte concentration when the valve opens. This is alleviated by the setup (Fig 2.10) in which the DMFC flow rates are constant and the analyte gas stream is simply switched into the mixing line – the DMFC valve is therefore always open to the correct flow rate.

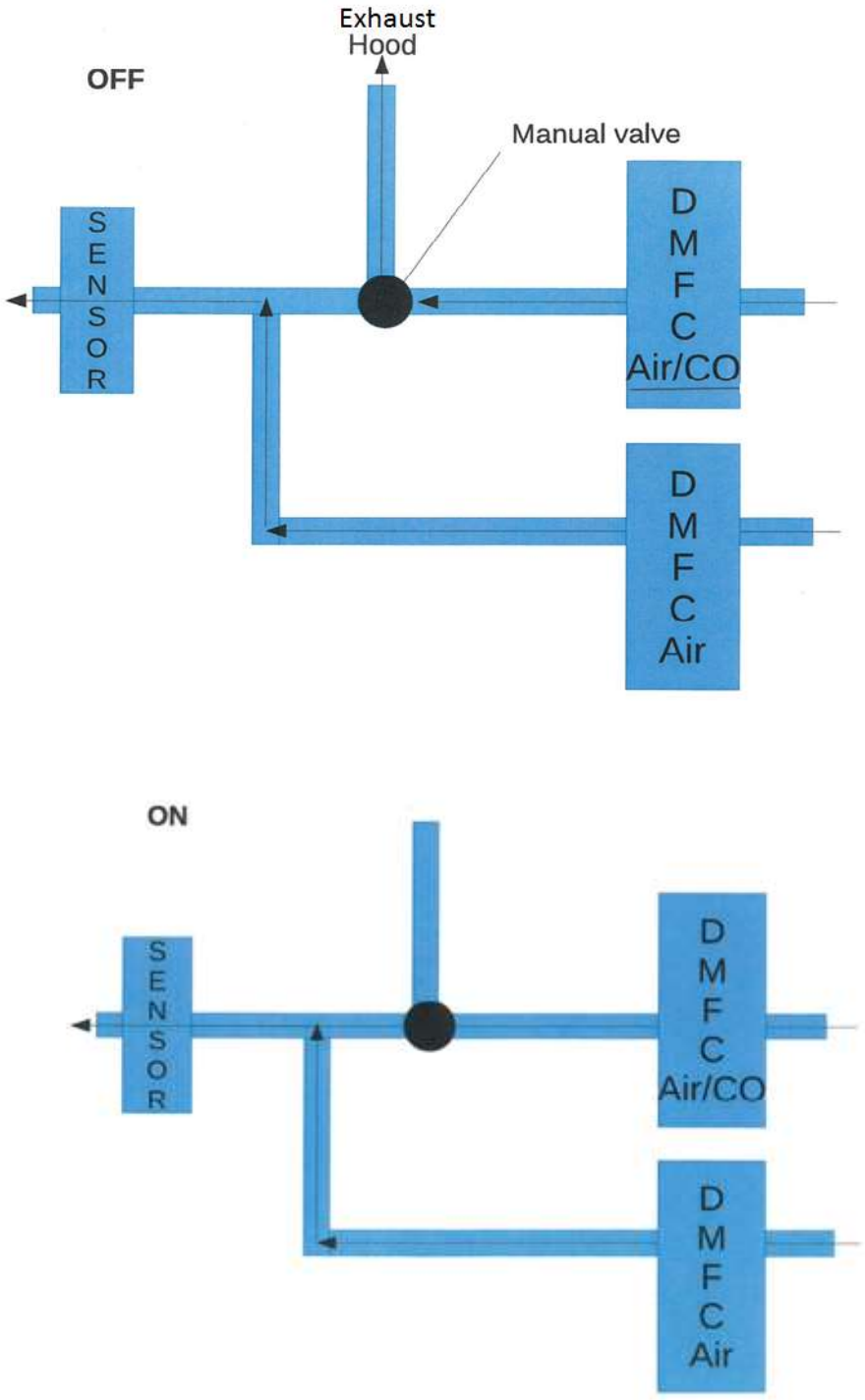

Figure 2.10: Schematic of gas flow setup during sensor experiments to alleviate settling period.

The oscillations, shown schematically, (Figs 2.11a and 2.11b) are a result of the finite time it takes for the feedback system to control the flow rate. The DMFC can open or close the butterfly valve and in combination with the gas pressure supplied, this results in a greater or lesser flow as the valve is opened or closed. However, there is no way to know ahead of time how wide to open the valve to get the flow rate desired. That depends on the gas pressure and on the ease with which the gas can flow through the sensing system. The device operates in an iterative / feedback manner. It opens the valve a bit, measures the flow, if too much, it closes the valve, if too low it opens the valve a bit. This process takes about a second or so to stabilise with the valve opened just enough to get the desired flow rate.

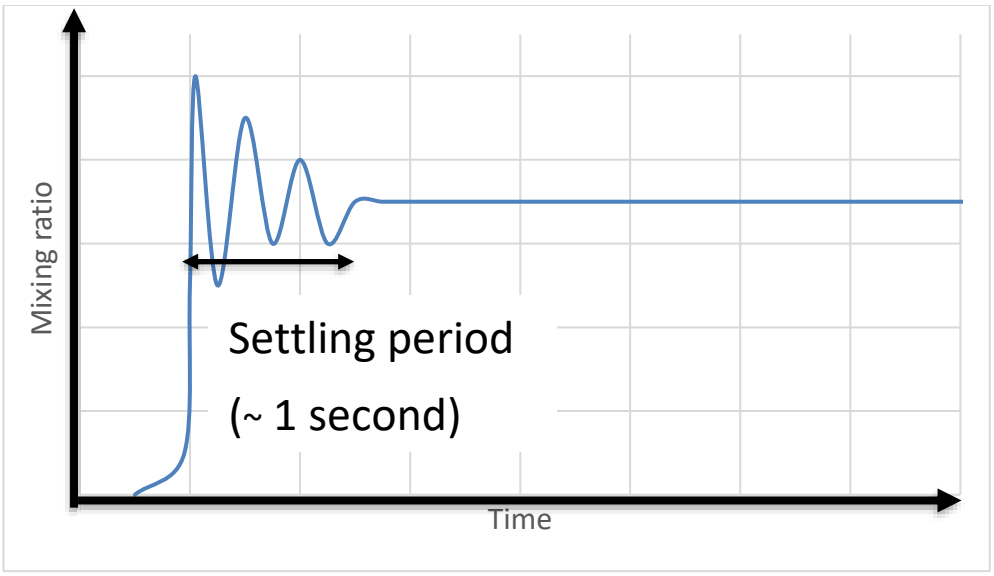

(a)

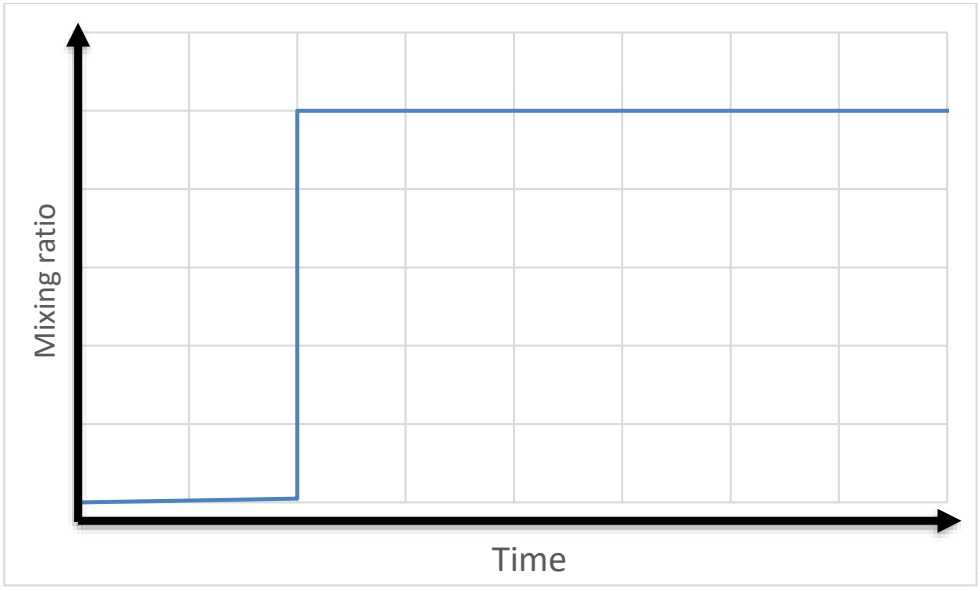

(b)

Figures 2.11a and 2.11b: Comparison of actual DMFC operation (a) and assumed operation in the mathematical model (b).

The settling time of the Brooks DMFCs used in this project is about 1 s – this is the manufacturer rated time and is also visible directly in the 0260 Smart Interface software. It does not pose a significant limitation on the experiments in this thesis, because the rise time of the sensors is much greater. The rise time, quantified as the time to achieve 90% of steady-state current, of the CO-AF devices is discussed in Chapter 4.

Finally, the dead volume of the system must be considered; this is the volume of tubing and the gas hood between the valve and the sensor. There is a finite time taken for the gas pulse to flow between the valve and the sensor. This time-lag is equal to the dead volume divided by the volume flow rate and is sufficiently small at about 1.8 s for the apparatus of figure 2.8 at a flow rate of 500 mL min^{-1} to be neglected in the analysis.

2.4 Vapour Pressure

The concentration of VOCs is determined by equation 2.4 and requires a knowledge of the saturated vapour pressure at the temperature of the Dreschel bottle. The vapour pressures for different temperatures were found from Antoine equation parameters (Eqn 2.5) provided by the NIST webbook website (*https://webbook.nist.gov/chemistry/*), which were subsequently interpolated from experimental data [123, 124]. An example graph using the data is shown for clarity (Fig 2.12). A list of the VOCs used with the CO-A1 sensors is shown below (Table 2.3).

$$logP = A - \frac{B}{C+T} \tag{2.5}$$

P = vapour pressure A, B, C = constants derived from experiment data T = temperature (K)

VOC	**vapour pressure @20° C (kPa)**
methanol	13.3
ethanol	5.95
heptan-1-ol	0.07
propan-2-ol	4.67
tert-butanol	4.10
para-cresol	0.13
propanal	25.0
hexanal	1.30
acetone	26.7
heptan-4-one	0.69
ethanoic acid	1.56
propionic acid	0.32
ethyl ethanoate	9.92
propyl propionate	1.38

Table 2.3: Vapour pressures for the VOCs used.

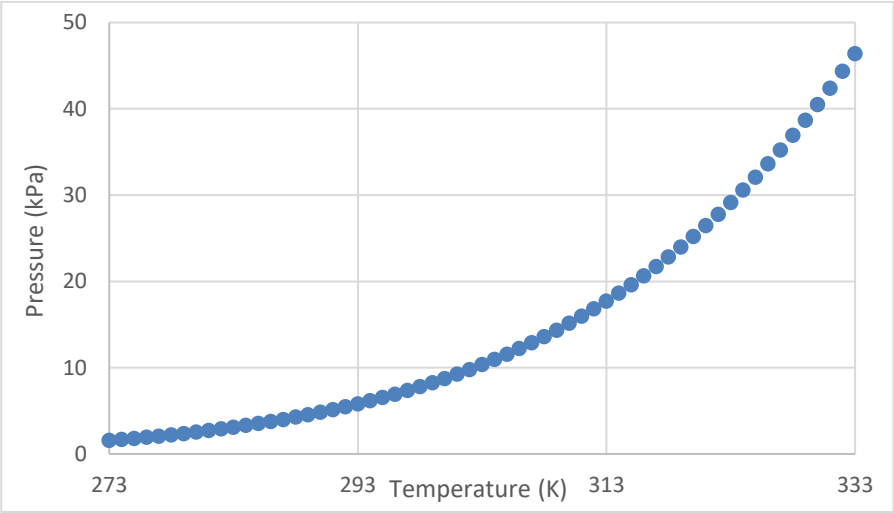

Figure 2.12: Graph of pressure against temperature derived from the Antoine parameters (Eqn 2.5) for ethanol (A = 5.4, B = 1670, C = - 40).

2.5 Hydrogel Redox Couple Compounds

Polyacrylate hydrogels were considered as possible alternative electrolytes to 5M sulfuric acid within the Alphasense gas sensors (chapter 8). Three redox couple compounds were chosen to be investigated as electrochemical probes to study the basic electrochemical properties of the hydrogel with respect to electron transfer and mass transport. The hydrogel used in chapter 8 was prepared in deionised water with the potassium salt of polyacrylamide co-acrylic acid (PAA) added in varying quantities.

All three redox couples are known to be electrochemically or chemically reversible in slow scan cyclic voltammetry and are expected to have few or no side reactions with the other compounds involved in the experiments. It is also commonly assumed that the ligands do not interact strongly with the electrode and the compounds undergo outer sphere electron transfer reactions with the electrode surface. All three were analytical grade reagents purchased from Sigma-Aldrich and used as supplied in their original containers whilst observing the correct PPE (personal protective equipment) and HSE (health and safety executive) directives for handling each compound in the appropriate manner.

They were also chosen with regard to the charge states. One is anionic (potassium ferrocyanide, standard redox potential -0.77 V vs SHE), one is cationic (hexaammineruthenium [III] chloride, standard redox potential 0.10 V vs SHE), and one is neutral (para-benzoquinone, standard redox potential 0.70 V vs SHE) [125]. Thus, very different interactions are expected with the anionic PAA polymer chains of the hydrogel. $K_4Fe^{II}(CN)_6$ (potassium ferrocyanide) (Fig 2.13) is oxidised from Fe(II) to Fe(III) when a sufficiently positive potential is applied to the electrode. Approximately 0.004g (0.001M) was used per experiment.

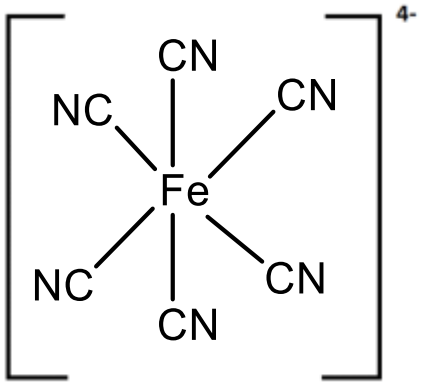

Figure 2.13: Structure of potassium ferrocyanide (counter ions not shown).

$Ru(NH_3)_6Cl_3$ (hexaammineruthenium [III] chloride) (Fig 2.14) is reduced from Ru(III) to Ru(II) when a sufficiently negative potential is applied to the electrode. It should be noted that the ruthenium hexamine chloride hydrogels were kept away from direct sunlight in order to prevent the decomposition of the ruthenium complex. Approximately 0.003g (0.001M) was used per experiment.

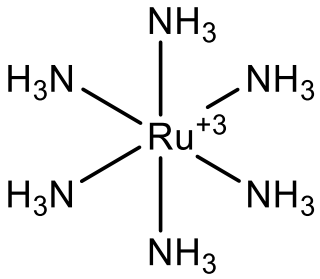

Figure 2.14: Structure of hexaammineruthenium [III] chloride (counter ions not shown).

Para-benzoquinone (sometimes called 1,4-benzoquinone) ($C_6H_4O_2$) was also used and is reduced to BH_2Q in a multi-step process shown below. Approximately 0.001g (0.001M) was used per experiment. Note that BHQ refers to the semiquinone and BH_2Q is the fully reduced form, known as hydroquinone, benzene-1,4-diol or quinol (Fig 2.15).

$$BQ + e^- \rightleftharpoons BQ^{\cdot -}$$

$$BQ^{\cdot -} + H^+ \rightleftharpoons BHQ$$

$$BHQ + e^- \rightleftharpoons BHQ^{\cdot -}$$

$$BHQ^{\cdot -} + H^+ \rightleftharpoons BH_2Q$$

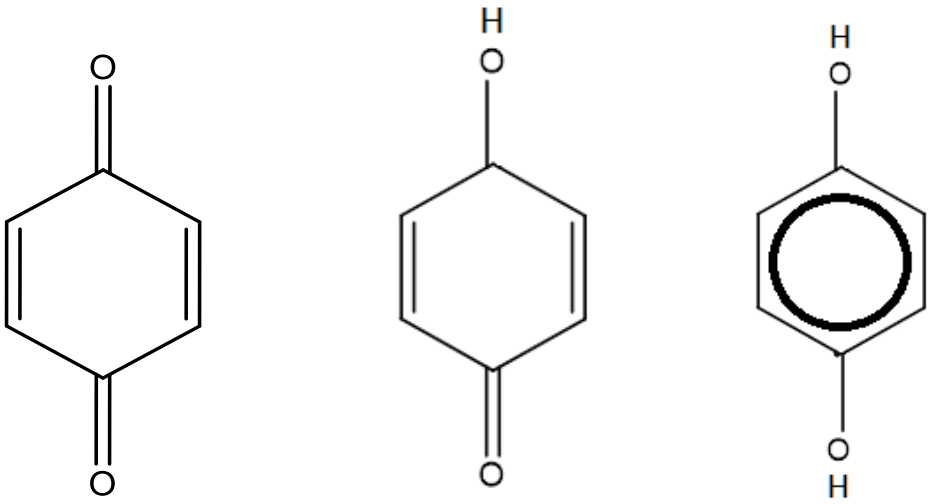

Figure 2.15: Structures of para-benzoquinone, semi-quinone, hydroquinone (respectively)

2.6 Hydrogel Weight Tracking

Due to the varied nature of locations where the electrochemical sensors might be operated (such as remote/ hard to access areas and in adverse conditions), it is important to know whether the various components will last for long enough to be practically useful. The semi-porous nature of the membranes and the strong sulphuric acid (5M) used in the Alphasense sensors means that humidity effects are considered one of the key limiting factors in sensor operating lifetime. To that end, evaporation rates of the water contained within the hydrogel were studied gravimetrically. Different concentrations of PAA hydrogels (no redox couples added) were made up in separate vials and left exposed to the air without lids on. They were kept on the laboratory benchtop and therefore subject to uncontrolled fluctuations in temperature and pressure, however the average temperature was about 20 °C and the fluctuations no more than a few degrees. A similar experiment where the vials were left in a sealed container in high humidity conditions was conducted concurrently to assess the evaporation rates in different conditions. The vials were taken out and weighed at the start of the experiment and then at intervals to ascertain the amount of hydrogel weight lost over time. The 100% humidity experiment was set up as shown below (Fig 2.16):

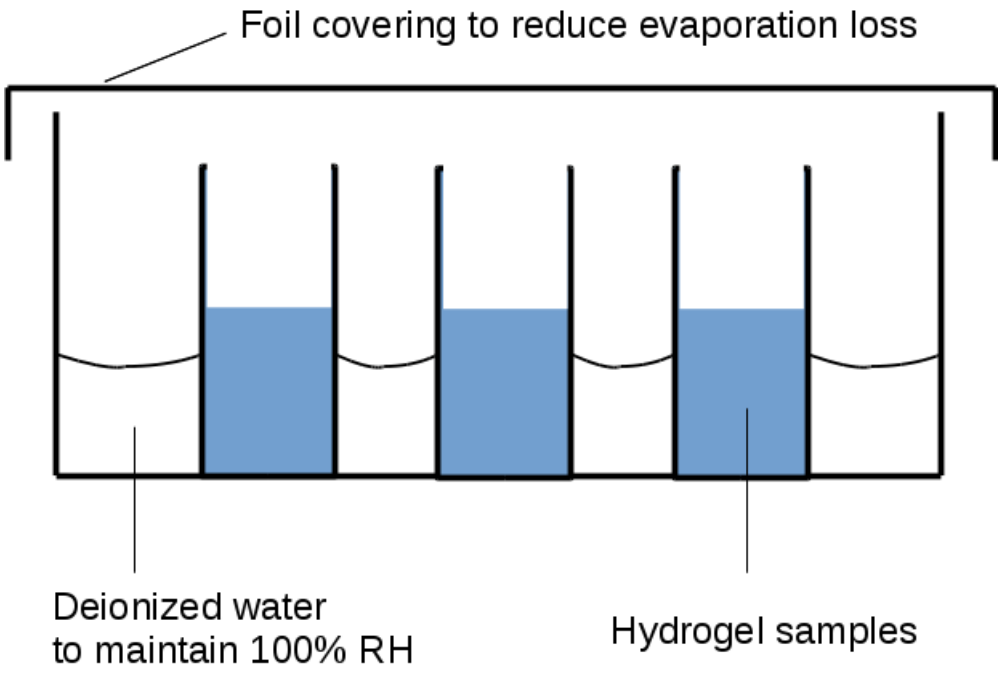

Figure 2.16: Schematic of 100% humidity weight tracking experiment with vials containing known weights of hydrogels in demineralised water sealed by tin foil.

2.7 Hydrogel Rheology

Rheology is the study of the flow characteristics of matter. Historically this has been primarily focussed upon liquids, although it also extends to gels and polymer suspensions. The different classes of fluid are generally considered either Newtonian or non-Newtonian. Newtonian fluids are those which has a viscosity that (at a given temperature) does not change with the strain rate applied to the fluid. Water and glycerol are typical examples of Newtonian fluids. Non-Newtonian fluids are those whose viscosity changes with the amount of strain applied to the system (again, at a given temperature). Many fluids that are studied (including hydrogels) fall into the category of non-Newtonian fluids. Blood, peanut butter, and corn starch dissolved in water are all examples of non-Newtonian fluids.

In order to measure the rheological properties of a fluid, rheometers are used. Specifically, in this thesis oscillatory shear rheology is used to measure the shear stress of the hydrogel at different shear rates. Rheological measurements were performed with a HR-2 Discovery Hybrid Rheometer (TA Instruments) with a standard steel parallel-plate geometry of 20 mm diameter with a gap of 1 mm and testing conducted at room temperature. The hydrogel samples were prepared by adding PAA into deionised water. Each sample had a final weight of 10 g which was a combination of the weight of the water and the weight of the PAA. Different concentrations of PAA were achieved by adding different amounts of PAA to deionised water.

The results are then plotted against oscillation frequency and the shape of this graph can give indications into the rheological behaviour of the fluid being studied (Fig 2.17). The shear stress of a material is the measure of deformation of the material from its original dimensions. The shear rate is the angular frequency of the plate that is moving against the material to apply force on the material. A linear relationship between shear stress and shear rate suggests the material behaves as a standard liquid, where applying greater force to the material causes greater deformation on the material. A non-linear relationship suggests behaviour that is somewhere between a liquid and a solid. Results following the power law relationship between shear rate and shear stress suggests the material behaves as a liquid at low shear rate but as a solid at high shear rate.

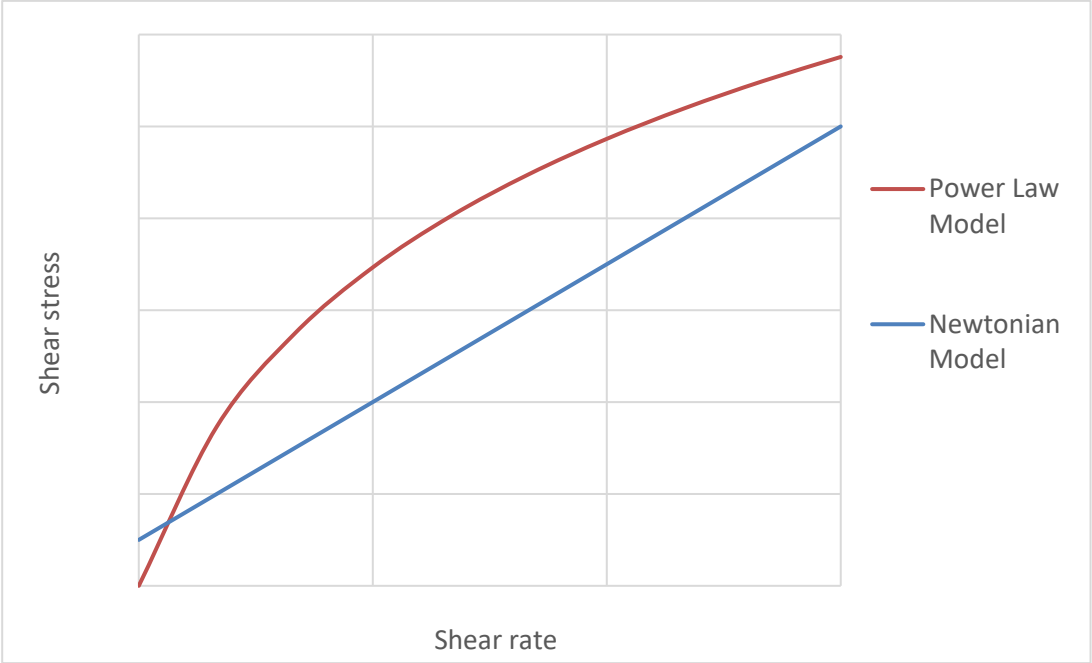

Figure 2.17: Graph of shear stress against shear rate for typical rheology models.

2.8 Optical Microscopy and Electron Microscopy

Optical microscopy allows for the study of the surface morphology of a substance using visible light through a magnification lens. Electron microscopy uses electrons instead of photons, which enables imaging to a much smaller scale. This is because electrons have a smaller wavelength than photons and so are deflected by smaller imperfections on the surface of the substance being analysed. Figures 2.18 and 2.19 below show the tightly packed nature and regular spacing arrangement of the metal nanoparticles on the working electrode surface of the sensor devices.

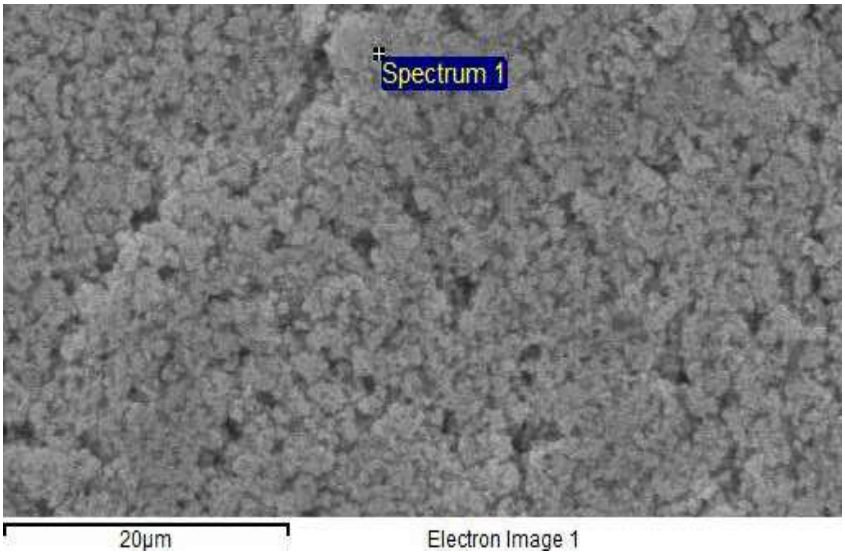

Figure 2.18: Electron microscopy image of Pt working electrode taken from a CO-AF sensor.

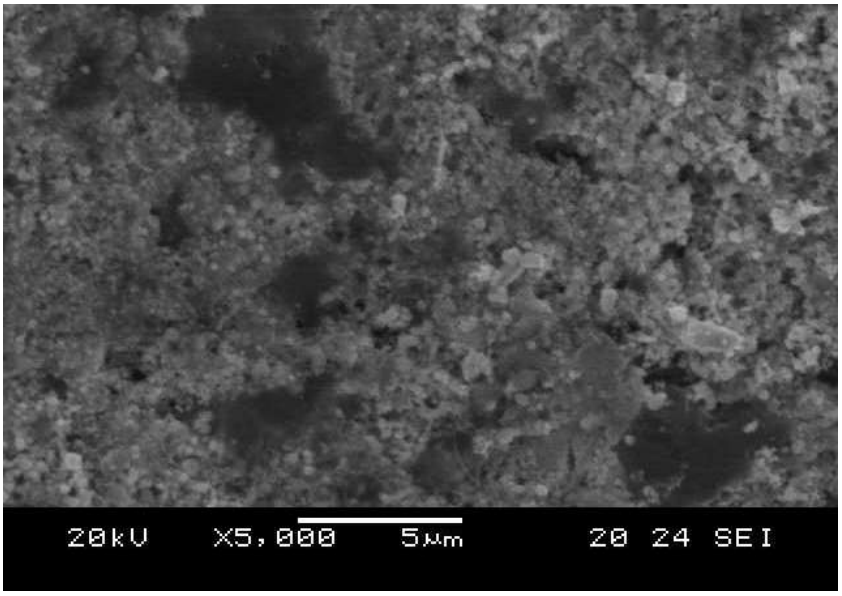

Figure 2.19: Electron microscopy image of Pt/Ru working electrode taken from a CM-A1 sensor.

2.9 Summary

The setup of the instruments and their interpretations have been discussed in this chapter. The techniques complement each other and will help to establish supporting evidence for any conclusions drawn from the experimental data. The gas testing rig is setup to allow the control of the concentration of analyte. This is important as it enables the use of the amperometric response data to produce calibration plots and determine the sensitivity and detection limits of the sensors. The various different physical effects on the analyte such as the vapour pressure and rate effects have been considered.

The use of redox couples within the PAA hydrogel has been discussed, using species that are positively charged, negatively charged, and charge neutral. This ensures a wide range of PAA hydrogel diffusion properties can be investigated. The rheology and hygroscopic nature of the PAA hydrogel is also discussed as a part of the experiments undertaken.

As can be seen from the nearly identical traces for a CO-AF device at potentials in the range 0.0 V – 0.2 V in figure 2.12, both the steady-state current and the response and recovery time are unaffected by the potential. This supports the theory that mass transport is the dominant rate limiting step within that potential range. In comparison, a purely kinetically controlled process governed by the Tafel law would typically show a one order of magnitude increase for a potential increment of 118 mV at 298 K (assuming a transfer coefficient of 0.5).

2.10 References

[120] A. J. Bard, L. R. Faulkner
Electrochemical Methods: Fundamentals and Applications, 2001, **2nd Edn**., Wiley, London

[121] *http://www.Alphasense.com/WEB1213/wp-content/uploads/2013/07/COAF.pdf*

[122] J. Huang, Z. Li, B. Y. Liaw, J. Zhang
J. Power Sources, 2016, **309**, 82-98

[123] J. Crank
Mathematics of Diffusion, 1975, **2nd Edn**., Clarendon Press, Oxford

[124] R. Sander
Atmos. Chem. Phys., 2015, **15**, 4399–4981

[125] H. R. Kemme, S. I. Kreps
J. Chem. Eng. Data, 1969, **14**, 98-102

Chapter 3

3.0 Mathematical Modelling of the Sensor Response

A nonlinear regression programme to model the response of the sensor to the presence of carbon monoxide or VOC saturated air (during chronoamperometry) was kindly developed and provided by Dr. Benjamin Horrocks. The background theory used in the modelling software is based on the assumptions that the response of the sensor is assumed to be governed by one of three steps: diffusion of analyte through $KMnO_4$ powder on a silica support scaffold (i), diffusion of analyte through the semi-permeable membrane (ii), diffusion of the analyte through the electrolyte to the working electrode surface (iii). Fig.3.1 shows the areas within which the three steps are applicable.

The analyte is assumed to be in the gas phase during stages (i) and (ii), whilst the analyte is taken to be in the liquid phase during stage (iii). Based on the lack of any observed potential-dependence, it is assumed that any reaction at the electrode surface is not affected by electrode kinetics at the potential used within this thesis (0.0 V vs internal sensor reference). The potential remains fixed throughout the chronoamperometry experiments. In the model it is also assumed that the concentration of analyte immediately outside the sensor instantly rises to a known concentration (C^*) determined by the mixing ratio (Eqn 2.2) when the valve is open (Fig. 2.12). Apart from the precision of the t = 0 estimate, the other limitation on short time data is the dead volume of the system. The flow rates used were > 500 mL/min and the estimated 'dead' volume (tubing + hood) was about 15 mL, which gives a dead time of less than 1.8 seconds. In order to study sensors with a much shorter response time than the CO-AF devices, the dead volume should be minimized by reducing the length of tubing between the gas mixing point and the sensor. Partition equilibria between the different phases are ignored for the sake of simplicity, however they will be briefly discussed as an aspect of consideration within the sensor.

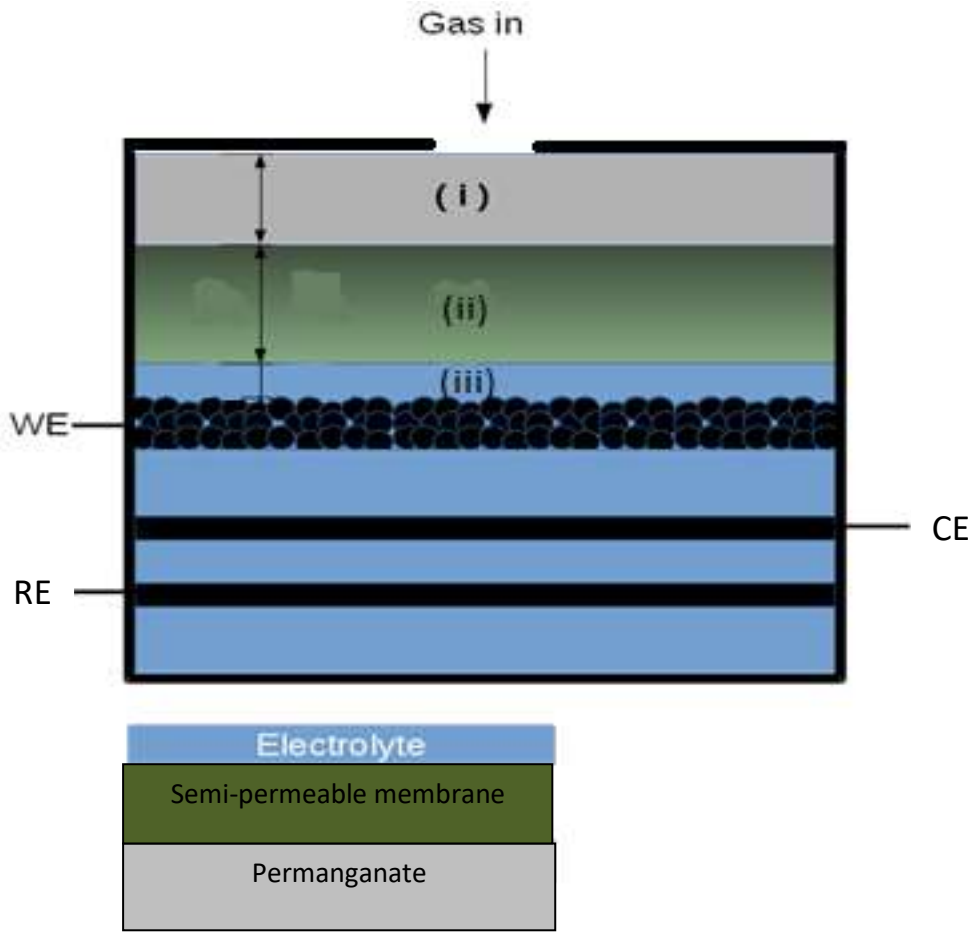

Figure 3.1: Schematic of the different diffusion barriers and phase changes present within the amperometric CO-AF sensors. Note that the diagram is not to scale and the thickness of the electrolyte layer (iii) is exaggerated compared to the other layers for reasons of diagrammatic clarity only.

3.1 Steady-State Response of Amperometric Gas Sensors

Firstly, the steady-state response of the sensor is considered. When the model is assumed to be simple and to have no kinetic barriers for the analyte (or at least so small relative to the other diffusion coefficients so as to be negligible) during the changes of phase within the sensor, a graph of concentration (C) can be plotted against distance (x) from the working electrode and takes the form of a series of straight lines (Fig. 3.2). Where the maximum concentration (C^*) is outside of the sensor and diffusion coefficient (D_n) and layer thickness (L_n) are numbered sequentially according to the distance from the working electrode.

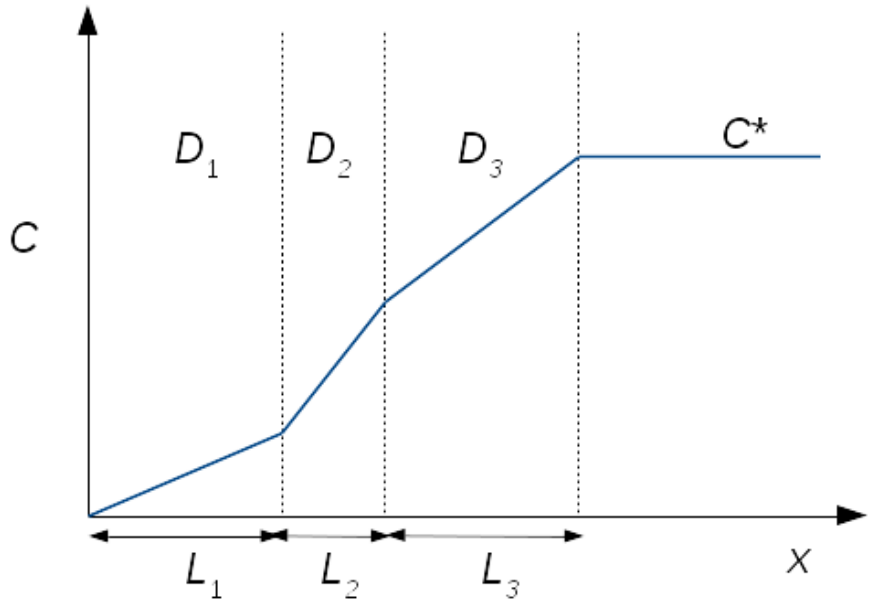

Figure 3.2: Plot of concentration (C) against distance (x) from the working electrode (under steady state current conditions) for a uniformly accessible amperometric sensor.

However, if there are in fact significant kinetic barriers to the analyte between the different phases (gas, membrane, liquid) within the sensor, then a slightly different concentration profile forms. Whilst the fact that it is assumed that current and potential are independent of each other means that an electron transfer kinetic barrier at the electrode surface can be ruled out, interfacial kinetic barriers (k) at other interfaces that do not respond to the potential remain a theoretical possibility.

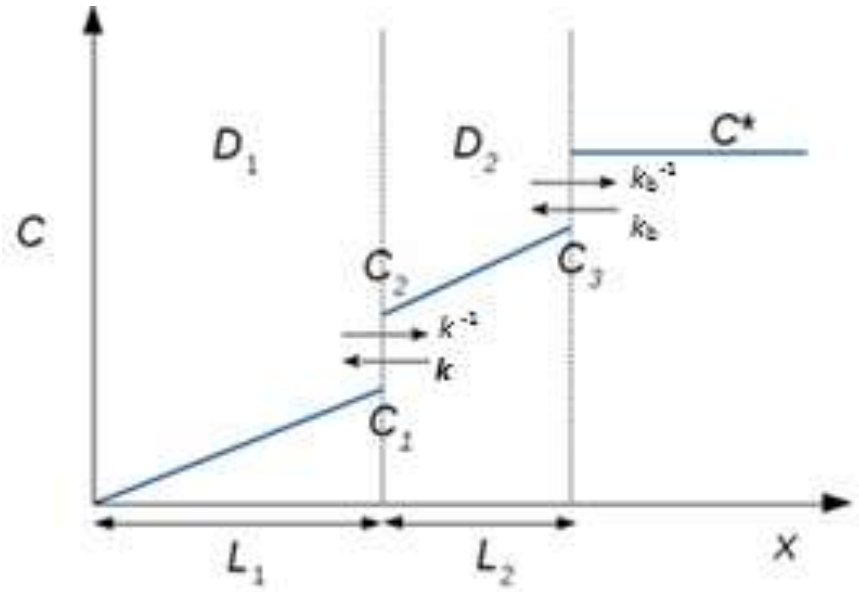

Figure 3.3: Plot of concentration (*C*) against distance (*x*) from the working electrode (under steady state current conditions) for a uniformly accessible amperometric sensor, with possible kinetic barriers at the phase interfaces (*K*, K^1).

In the mathematical analysis of the model, the slopes shown in figures 3.2 and 3.3 can be calculated using the gradient of a straight line (m = Δ*c*/ Δ*x*). The flux (*j*) entering one region must be the same as the flux leaving the previous one if the local concentration is at steady-state (time independent). Indeed, the flux (*j*) is constant from the external surface of the sensor where the bulk concentration (*C**) applies, to the electrode surface (*C* = 0) under steady state conditions. Further, under conditions of mass transport control the flux is given below (Eqn 3.1).

$$j^{-1} = j_1^{-1} + j_2^{-1} + j_3^{-1} \tag{3.1}$$

Thus, the limiting fluxes j_n for each layer are simply added in reciprocal and the result for any number of barriers (n) can be calculated using Equation 3.2 below. This is logically understood as the overall flux being limited by the slowest step in the sequence.

$$j^{-1} = \sum_{n=1}^{N} j_n^{-1} \tag{3.2}$$

Next, we consider the evolution of the concentration profiles inside the sensor towards the steady-state profiles of figures 3.2 and 3.3. Rather than considering the realistic case of a multilayer device, we first consider a sensor with a single diffusion barrier (the blue area of figure 3.4) and then justify the use of this as a regression model with an *effective* diffusion coefficient and thickness to model more general cases.

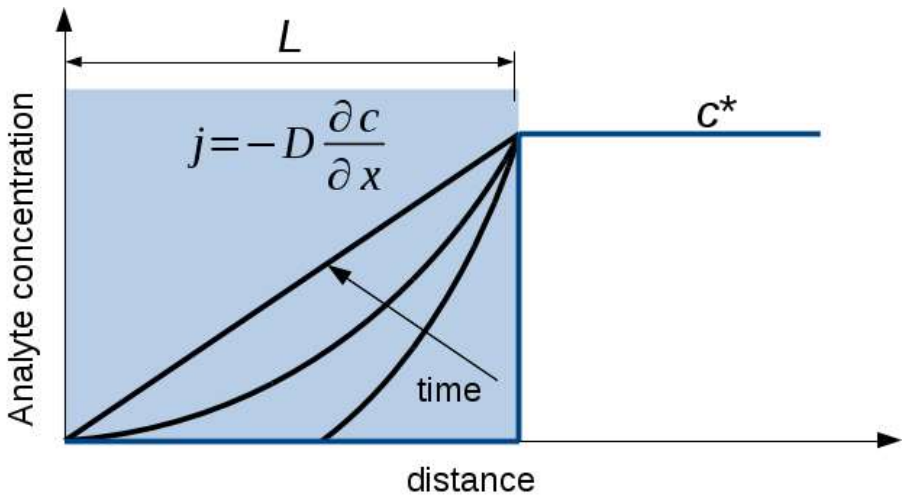

Figure 3.4: Concentration step at a membrane covered electrode. Analyte concentration instantaneously jumps to C* outside of the membrane.

Inside the membrane (blue area) at long times, the concentration profile ($C(x,t)$) tends towards a straight line from the electrode surface ($x = 0$) to the outside of the sensor membrane ($x = L$) (Fig. 3.2). This indicates that a steady state is being reached when the concentration profile (black curves) becomes a straight line. The steady state current is given by the effective mass transport coefficient $\frac{D}{L}$ as the current has reached a time-independent value $\frac{i}{nFA} = \frac{D}{L}C^*$ where number of electrons (n), Faraday constant (F) and geometric area of the working electrode (A) are all known quantities. The time evolution of the concentration profile can be described by a diffusion equation with boundary conditions appropriate to mass transport control at the electrode surface ($C(0,t) = 0$), with constant external concentration ($C(L,t) = C^*$ for $t > 0$) and an initial condition ($C(x,0) = 0$ for $x < L$).

As can be seen from the diagram above, flux ($j = i/nFA$) can be calculated from the gradient of the concentration profile. Whilst several assumptions have been made to allow for the parametrization of the model, it should be understood that the calculated values D and L represent averages over the different phases within the sensor in a manner to be described below. Fick's Second Law (Eqn 3.3), the diffusion equation, which is solved subject to boundary conditions and the initial condition described above [123].

$$D\frac{\partial^2 c}{\partial z^2} = \frac{\partial c}{\partial t} \tag{3.3}$$

Given Fick's second law above and the previously mentioned concentration profiles, it is possible to apply the Laplace transformation and calculate the flux in the electrochemical system subject to the boundary conditions and either the initial condition that $t > 0$ when the gas is turned on (Eqn 3.4) or when it is turned off (Eqn 3.5). The equations shown below describe the variation of the current i or flux j with time and also the variation of the concentration inside the membrane after the gas flow is switched on (Eqn 3.6) and when the gas is turned off (Eqn 3.7).

The time when the gas is switched on and heads towards the sensor is taken as t = 0 assuming immediate detection by the sensor. Equations 3.4 and 3.5 constitute the regression model used throughout the thesis for the transient response upon exposing the sensors to a sudden change analyte concentration. Equation 3.4 is appropriate to the "gas valve on" situation of figure 2.11 and equation 3.5 corresponds to the recovery of the sensor when the gas valve is switched "off" in figure 2.11. The response time of the sensor (τ) depends on the effective diffusion coefficient (D) and the diffusion barrier thickness (L) via the parameter D/L^2. Equations 3.6 and 3.7 are the corresponding profiles which have the form of the black curves in figure 3.4.

n = no. of electrons in reaction F = faradays constant = 96,485 C mol^{-1} A = area of electrode (cm^2)

D = diffusion coefficient of the analyte L = thickness of the diffusion barrier

$$j = \frac{i}{nFA} = \frac{Dc^*}{L}\left[1 - 2\Sigma_{n=1}^{\infty}(-1)^{n-1}e^{-n^2\pi^2\frac{Dt}{L^2}}\right] \quad (3.4)$$

$$j = \frac{i}{nFA} = 2\frac{Dc^*}{L}\left[\Sigma_{n=1}^{\infty}(-1)^{n-1}e^{-n^2\pi^2\frac{Dt}{L^2}}\right] \quad (3.5)$$

$$\frac{c(x,t)}{c^*} = \frac{x}{L} - 2\Sigma_{n=1}^{\infty}\frac{(-1)^{n-1}}{n\pi}e^{-n^2\pi^2\frac{Dt}{L^2}}\sin\left(\frac{n\pi x}{L}\right) \quad (3.6)$$

$$\frac{c(x,t)}{c^*} = 2\Sigma_{n=1}^{\infty}\frac{(-1)^{n-1}}{n\pi}e^{-n^2\pi^2\frac{Dt}{L^2}}\sin\left(\frac{n\pi x}{L}\right) \quad (3.7)$$

The equations described above (Eqn 3.3 – 3.7) also describe the variation of the current (*i*) or flux (*j*) with time after the gas flow is switched off. Whilst this is not used to calculate the values of apparent layer thickness (*L*) or diffusion coefficient (*D*), it is useful in providing a way to validate the model since the values of L^2/D and ΔI for the increasing current response and the corresponding recovery transient upon gas-off should be the same. An example chronoamperometric response to gas on and gas off is shown below (Fig. 3.5).

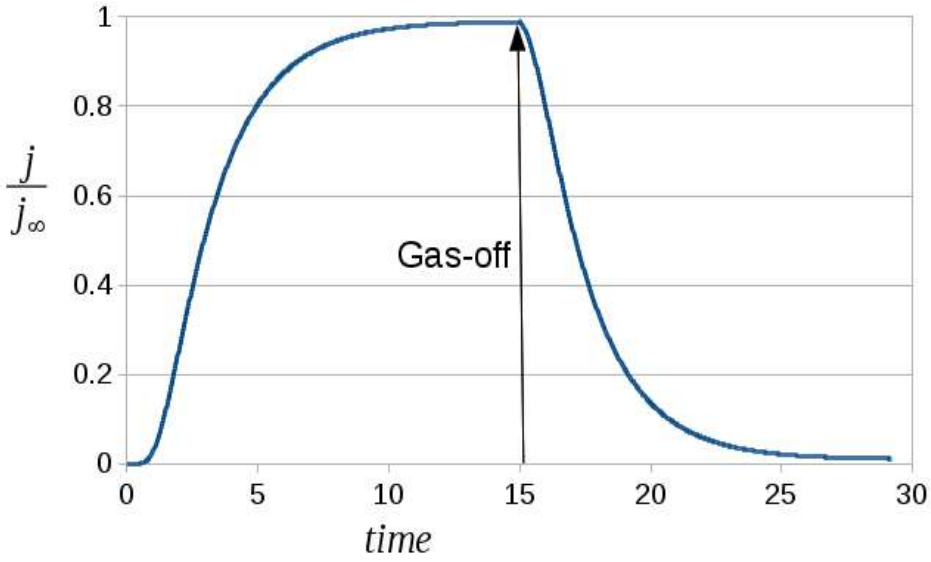

Figure 3.5: Example calculation of flux (*j*) as a fraction of the steady-state value j_{∞} against time in response to a sudden increase in the analyte concentration and then a sudden decrease.

3.3 Multiple Diffusion Barriers

Typical commercial amperometric gas sensors employ a structure (Fig. 3.1) which is more complex than the single diffusion barrier illustrated (Fig. 3.2). Nevertheless, the theory developed in the previous section can still be applied as the regression model for the analysis of practical sensor devices. To understand this, it is simplest to consider first a two-barrier model (Fig. 3.2 without any kinetic limitations). In such a model there are two layers of thickness L_1 and L_2 with diffusion coefficients of D_1 and D_2 respectively. It is straightforward using the procedure outlined (Eqn 3.4 to 3.7) to compute the steady-state current and the *effective* value of *D* and *L* (for the whole device) which reproduces this:

$$\frac{L}{D} = \frac{L_1}{D_1} + \frac{L_2}{D_2} \tag{3.8}$$

However, Eqn 3.8 does not on its own allow a separate determination of *D* and *L*, only their ratio. In order to determine separate values, it is necessary to analyse the time-dependent behaviour either upon switching on the analyte gas stream or after switching it off (Eqns 3.6 or 3.7). To do this one can consider the characteristic times associated with the two barriers:

$$\tau_1 = \frac{L_1^2}{D_1} \text{ and } \tau_2 = \frac{L_2^2}{D_2} \tag{3.9}$$

The overall characteristic time (τ) is not simply the sum of these two quantities (Eqn 3.9) because that does not give the correct limit when the two diffusion coefficients become equal.

$$\tau = \frac{(L_1+L_2)^2}{D} \tag{3.10}$$

However, it is clear from Eqn 3.10 that if the diffusion coefficients were equal, one could evaluate τ simply by adding the two barrier thicknesses. This observation suggests the correct way to combine the two characteristic times is to first adjust the thickness of the second barrier and its diffusion coefficient so that τ_2 is unchanged, but $D_2 = D_1$. This new thickness is $L' = \sqrt{\frac{D_1}{D_2}} L_2$.

Using *L'* in place of L_2 and $D = D_1$, we can combine the characteristic times using Eqn 3.10 to get:

$$\tau = \frac{L_1^2}{D_1} + \frac{2L_1L_2}{\sqrt{D_1D_2}} + \frac{L_2^2}{D_2}. \tag{3.11}$$

Eqn 3.11 gives the correct limit as the diffusion coefficients become equal (Eqn 3.10) and also the correct limit as either of the diffusion coefficients dominates. It is not an exact solution, but the numerical solution of the two-barrier problem (Fig. 3.2) and fitting to Eqns 3.6 and 3.7 as regression models indicates that Eqn 3.11 provides a sufficiently good approximation that it can be used to analyse experimental data without significant loss of accuracy. Using Eqn 3.11 It is possible to derive effective values of *L* and *D* for the whole device.

$$L = \frac{\frac{L_1^2}{D_1} + \frac{2L_1L_2}{\sqrt{D_1D_2}} + \frac{L_2^2}{D_2}}{\frac{L_1}{D_1} + \frac{L_2}{D_2}} \tag{3.12}$$

$$D = \frac{\frac{L_1^2}{D_1} + \frac{2L_1L_2}{\sqrt{D_1D_2}} + \frac{L_2^2}{D_2}}{\left(\frac{L_1}{D_1} + \frac{L_2}{D_2}\right)^2} \tag{3.13}$$

Eqns 3.12 and 3.13 have a useful, simple interpretation: the response of a two-barrier device is the same as that of a single barrier device (Eqns 3.3 – 3.7) but the values of *L* and *D* obtained by fitting those equations to experimental data are effective values for the whole device. By comparing them to typical values of diffusion coefficients in the gas and in condensed phases and some of the known barrier thicknesses in the device, it is possible to infer the rate limiting mass transport process in a real device. Real devices may contain multiple barriers, but the same conclusion holds for any number of barriers because the argument leading to Eqns 3.12 and 3.13 can be iterated; once effective values of *L* and *D* have been found for 2 barriers, they can be combined in the same manner with the values for a third, then a fourth barrier and so on. In summary, Eqns 3.3 – 3.7 constitute a satisfactory regression model for the analysis of the transient response of any amperometric gas sensor subject only to the following limitations: (i) the current density is uniform and (ii) there are no kinetic limitations in the device.

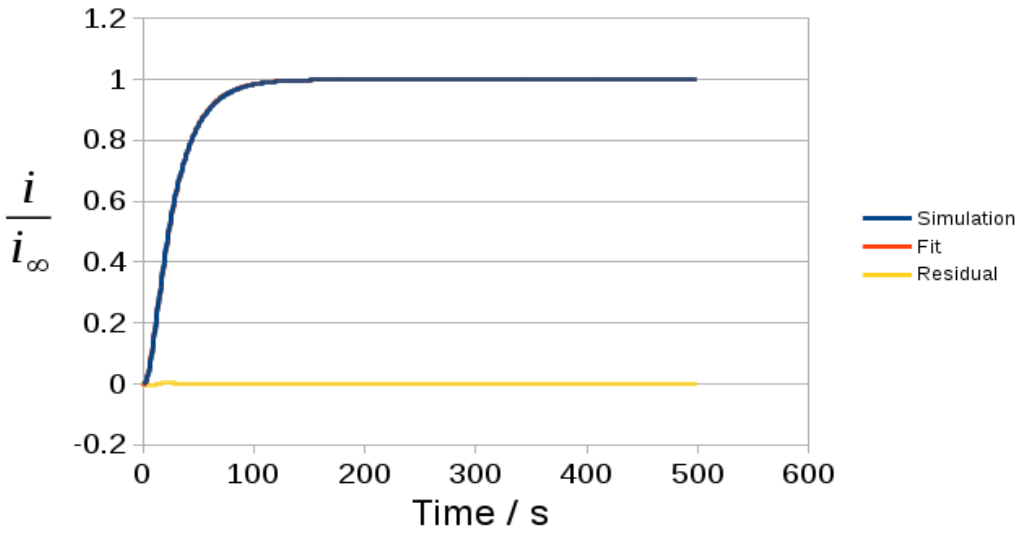

Figure 3.6: Example fit of the regression model of equations 3.4 - 3.5 to a finite difference simulation of a device with two barriers of thickness L_1 = 0.3 cm and L_2 = 0.003 cm. The diffusion coefficients in these two barriers are $D_1 = 10^{-3}$ cm^2s^{-1} and $D_2 = 10^{-5}$ cm^2s^{-1}. The blue curve is a precise finite difference simulation of equation 7.3 on a 100 point spatial grid in each layer. The blue line is the simulation, the orange line is the fit of the regression model defined by equations 3.4 – 3.5 and the yellow line is the residual.

In order to demonstrate the wide utility of equations 3.4 – 3.5 as a regression model, the chronoamperometric response of a more realistic two-barrier model (analogous to that for the steady state in figure 2.26) was simulated by a finite difference solution of equation 3.3. The regression model of equations 3.4 – 3.5 was then fitted to the finite difference solution (Fig 3.5). The parameters chosen for the simulation of figure 3.4 are two barriers of thickness L_1 = 0.3 cm and L_2 = 0.003 cm. The diffusion coefficients in these two barriers are $D_1 = 10^{-3}$ cm^2s^{-1} and $D_2 = 10^{-5}$ cm^2s^{-1}. Such a wide variation in values of *D* was chosen deliberately to test the regression model because equations 3.12 & 3.13 were set up to generate the exact result for equal diffusion coefficients. It is clear from figure 2.30 that the fit of the regression model to the simulation is so close (the magnitude of residual < 1%) that it is acceptable for the analysis of any experimental data in this thesis. The model is not exact and equations 3.12 – 3.13 do not predict exact chronoamperometric responses, nevertheless it is clear that the regression model based on equations 3.4 – 3.5 is sufficient to describe the experimental data in terms of a single effective thickness (*L*) and effective diffusion coefficient (*D*). These values may then be interpreted in terms of the known device structure and physicochemical properties, e.g., typical gas phase or liquid phase diffusion rates.

By using a mathematical model based upon least squares regression (of a model based on diffusion of the gas into the sensor) and the ideal gas law, when the integer number of electrons involved in the initial electrochemical reaction occurring at surface of the Pt working electrode is known (n = 2), plus the value calculated from the literature [124] for the carbon monoxide Henry's law solubility constant at standard room temperature and pressure (H^{cc} = 0.024), we can find the thickness of the layer across which diffusion happens across the semi-permeable membrane gas phase (L) and the diffusion coefficient across the 5 M sulfuric acid solution in the liquid phase (D) for the CO-AF sensor devices.

This is based upon the principle that the time taken for the current to rise from zero (or a suitable baseline) to a steady value depends on the rate of diffusion through the sensor and the thickness of the layers involved. However, the Henry's law constant must be retrieved from the literature for the appropriate temperature [124]. Part of the calculations from the literature is shown below (Eqn 3.14) and an example fit from the dataset (Fig 3.7).

Substance Formula (Other name(s)) [CAS registry number]	H^{cp} (at $T^{\ominus}$) $\left[\frac{\text{mol}}{\text{m}^3\,\text{Pa}}\right]$
carbon monoxide CO [630-08-0]	9.7×10^{-6} 9.7×10^{-6} 9.7×10^{-6} 9.7×10^{-6} 9.4×10^{-6} 7.9×10^{-5} 7.9×10^{-6} 9.7×10^{-6} 9.7×10^{-6} 9.8×10^{-6} 8.7×10^{-6} 9.4×10^{-6} 8.6×10^{-6}

Two greatest outliers removed from calculation of mean value

Table 3.1: Collated Henry's law constants of carbon monoxide. Reproduced from [124]

$\bar{x}$ = 9.46 x10^{-6} mol m^{-3} Pa^{-1} = H^{cp}

$$H^{cc} = H^{cp} * RT \quad (3.14)$$

gas constant (R) = 8.314 m^3 Pa K^{-1} mol^{-1} T = temperature in kelvin

∴ H^{cc} = (1.02 x10^{-5}) * 2437 = 0.024 (± 0.001) = K @ 20° C

Δ I =nFAKDc/L therefore Δ I /(nFAc) = KD/L and $T = L^2/D$ so T*(KD/L) = KL

Δ I and T are values derived from the mathematical modelling.

T_0 = time gas valve opened

steady state current = constant current at long times after the application of analyte

Both T_0 and the steady state current are taken from the chronoamperometry results.

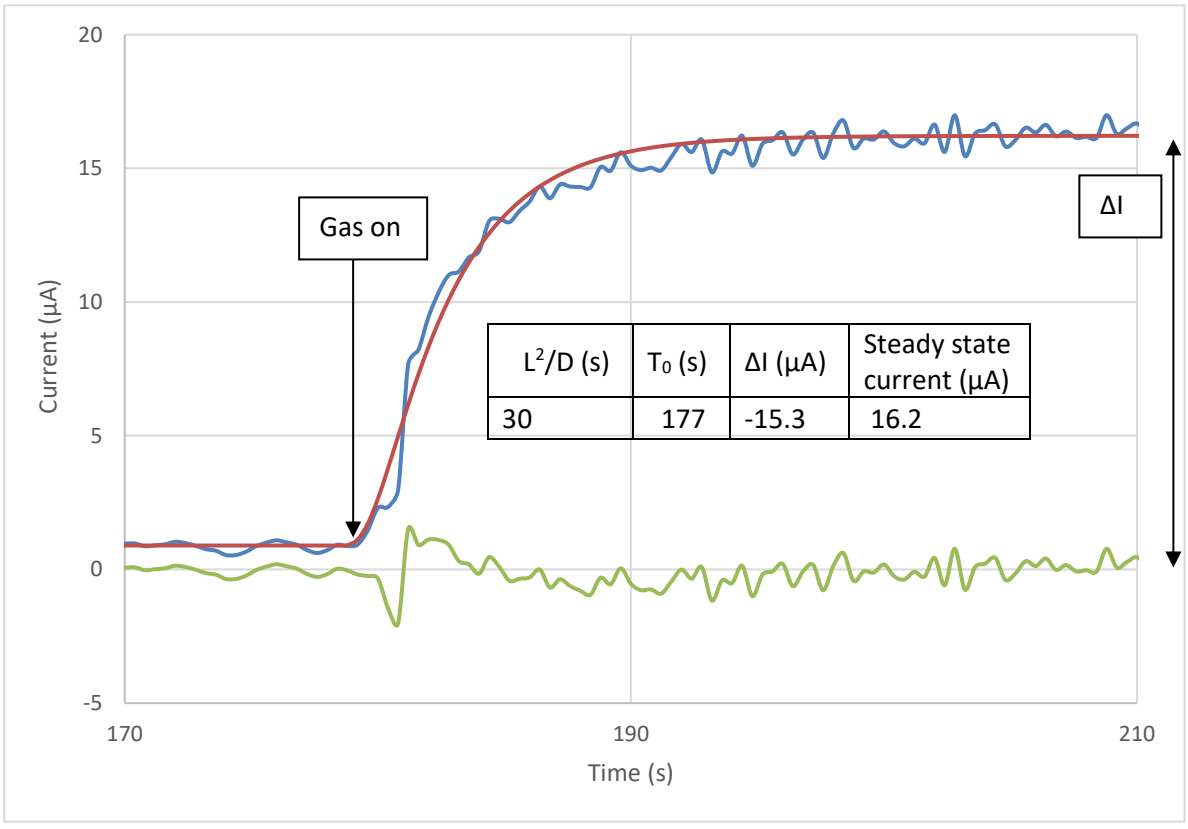

Figure 3.7: Graph showing typical experimental data for current in a CO sensor against time, upon exposure to 300 ppm CO from a background of zero air. Recorded data (blue), line of best fit from mathematical modelling software (red), and the difference between the two values (green).

3.4 Summary

The mathematical model described in this chapter has been developed to determine the main factors influencing the diffusion rate of the analyte through the sensor. The model rests on the assumptions that mass transport is the rate-limiting factor, there is no kinetic barrier at the interfaces between different layers and that the current density is uniform across the device. The latter allows a simple linear diffusion model to be constructed. Evidence for mass transport control is provided by the lack of potential dependence of the analytical signal.

It has been shown that such a model can be easily extended to the practical case in which there are multiple layers in the device, each with their own diffusion coefficient. The model provides a good fit to the experimental data via least squares regression, the output of which is an effective diffusion coefficient and an effective diffusion layer thickness that can be interpreted in terms of the limiting diffusion process. Literature values such as the Henry's Law constant for dissolution of the analyte, the number of electrons transferred at the electrode during the reaction, and the saturated vapour pressure, have also been discussed and applied within the modelling.

Chapter 4

4.0 Amperometric Carbon Monoxide Detection

The commercially available CO-AF sensor (kindly provided by Alphasense) is optimised for the chemically selective detection of carbon monoxide and is warranted to have detection levels around the ppm range (*http://www.alphasense.com/index.php/products/carbon-monoxide-safety/*). These devices operate as a standard three electrode cell with 5M sulfuric acid (H_2SO_4) as the liquid electrolyte within the cell. A three electrode system is used because it allows for the voltage to remain constant whilst current changes. A simple two electrode system enables the current to flow between the working electrode and the counter electrode, which thus ensures a complete circuit for electron flow. Having a third (reference) electrode, that is not involved in the flow of current through the circuit, means the reference electrode can be kept at a constant steady state voltage without affecting the flow of current through the circuit. In a two electrode system it is not possible to guarantee that the applied potential lies on the mass transport limited plateau of the voltammogram.

Sulfuric acid is used as the liquid electrolyte because not only is it relatively cheap and easy to obtain (making the sensors far more economically viable as a commercial product), but it also has a low water vapour pressure (0.014 bar at 20 °C)[126], which allows the sensor to remain operationally effective for a long time (approximately two years in practice, *http://www.alphasense.com/WEB1213/wp-content/uploads/2017/09/COAF.pdf*). This is an area for consideration because the operation of the sensor relies upon the fact that the volume and concentration of the electrolyte remains approximately constant throughout its working lifetime. Sulfuric acid is also highly conductive, which minimises ohmic losses. More concentrated solutions of sulfuric acid are not used because the sensors then become a handling hazard during production and must conform to the Restriction of Hazardous Substances (RoHS) guidelines for control and monitoring equipment.

Figure 4.1a shows a schematic of part of the CO-AF device. The working, counter and reference electrodes are layers of Pt nanoparticles arranged in a stack and electrically isolated from each other by glass fibre. The reference and counter electrodes (not shown) lie below the working electrode and are separated from it and from each other by glass fibre. The sulphuric acid electrolyte reservoir lies below the stack of electrodes. The working electrode is at the top of the electrode stack and is wetted by the electrolyte – in figure 4.1 the thickness of the electrolyte layer is exaggerated for diagrammatic clarity. A layer of potassium permanganate ($KMnO_4$) powder, suspended upon silica, that oxidises any unwanted gaseous sulphur-containing species that might act as catalytic poisons, sits at the top of the sensor. Below this is a semi-permeable Porex membrane (of known porosity and thickness) that provides a diffusion barrier. The semi-permeable membrane is hydrophobic and so not only prevents moisture from entering the sensor, but also hinders the evaporation of water from the sulfuric acid electrolyte. The hydrophobic nature of the semi-permeable membrane also prevents highly polar species from entering the sensor. This aids in the selectivity as CO is relatively non-polar, dipole moment = 0.1 Debyes, compared to liquid water = 3 Debyes [127 - 130]. The gaseous analyte enters from the top of the sensor and passes through the various layers to reach the Pt nanoparticle working electrode (Figs 4.1a and 4.1b) at the base of the semi-permeable membrane.

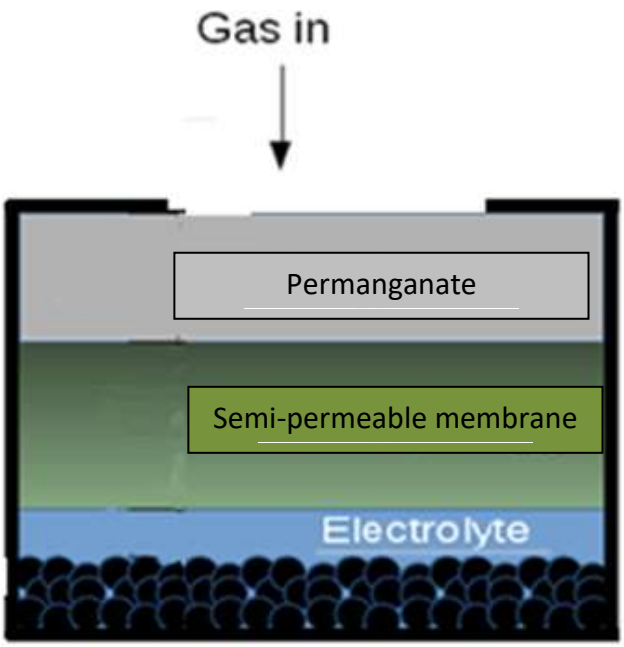

Figure 4.1a: Schematic of layers at the working electrode of a CO-AF sensor. The working electrode comprising platinum nanoparticles is shown at the bottom of the diagram. 5M sulfuric acid electrolyte wets the Pt nanoparticulate electrode which is hot-pressed onto the base of a Porex semi-permeable membrane. Potassium permanganate powder adsorbed on a powdered silica support structure is at the top of the stack.

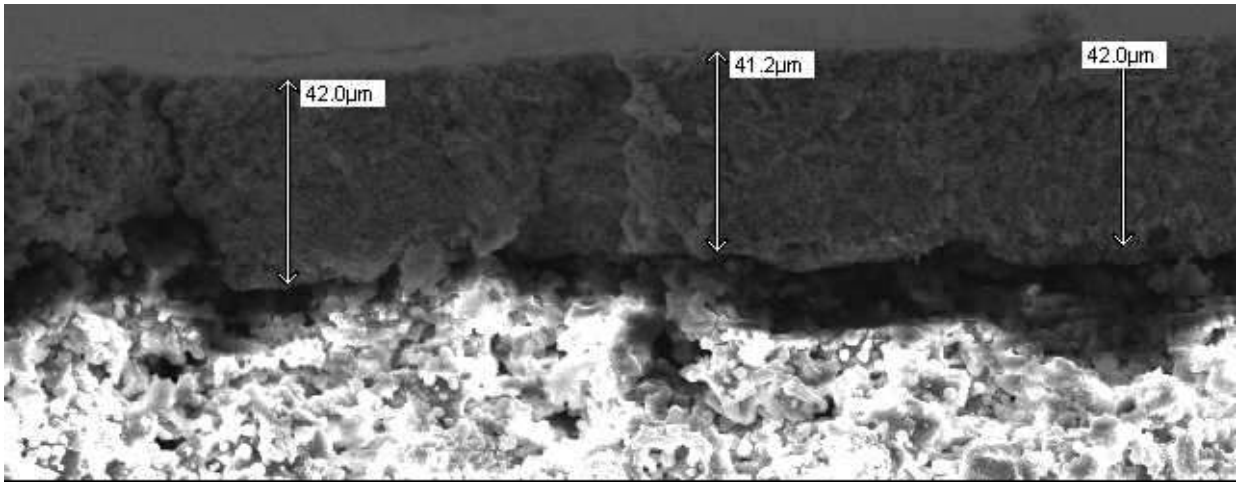

Figure 4.1b: Electron micrograph of the working electrode. The Pt is shown as the black area and the PTFE semi-permeable membrane is shown as the white area.

It can be seen from Figure 4.1b that the Pt layer is uniform across the surface of the membrane. The Pt nanoparticles are closely packed together with no obvious voids or areas of deformation.

The operation of a three electrode sensor system involves the working electrode being the site of the electrooxidation of the analyte gas (CO in this case). The solid metal Pt working electrode is in contact with the liquid 5M sulfuric acid and the analyte gas, thus creating a three phase interface. All three of the electrodes within a CO-AF sensor are monometallic platinum. The platinum catalyses the reactions at the working electrode and can be used multiple times as it does not undergo net chemical change during any of the electrochemical reactions. The sulfuric acid electrolyte allows ionic electrical contact between the working, counter, and reference electrodes. Between each electrode there are hydrophilic separators (glass wool/fibre) to enable capillary transport of the electrolyte. The typical operation of the CO-AF sensor involves maintaining a potentiostatic circuit between the working and reference electrode, whilst measuring the current response between the working and counter electrodes. In terms of the electrochemical reactions occurring within the CO-AF sensor upon exposure to CO gas, the reactions for each electrode are given below (Eqn 4.1):

$$\text{Working electrode: } CO + H_2O \longrightarrow CO_2 + 2H^+ + 2e^- \quad (E^o = -0.11 \text{ V vs SHE})$$

$$\text{Counter electrode: } 0.5\ O_2 + 2H^+ + 2e^- \longrightarrow H_2O \quad (E^o = 1.23 \text{ V vs SHE})$$

$$\text{Overall cell reaction: } 2\ CO + O_2 \longrightarrow 2\ CO_2 \qquad (4.1)$$

It can be seen from the above reactions that at the operating potential of the devices (0 V vs internal reference = 0.34 V vs $Hg/HgSO_4/K_2SO_4$ = 0.98 V vs SHE) electrooxidation of CO is thermodynamically spontaneous at the working electrode. Electroreduction of oxygen is the usual process at the counter electrode. It is worth noting that the counter electrode would normally reduce small amounts of oxygen as long as enough is available within the atmosphere, although if oxygen were not present within the atmosphere surrounding the sensor, the counter electrode could simply reduce the protons that are abundant in the low pH sulfuric acid electrolyte and generate hydrogen gas (Eqn 4.2). it is also possible that Pt oxides are reduced depending on the history of the electrode. However, in all experiments conducted within this thesis there was adequate oxygen in the surrounding atmosphere that was available to the sensor.

Counter electrode: $2H^+ + 2e^- \longrightarrow H_2$ (E^o = 0 V vs SHE) (4.2)

Whilst it is well known that Pt can be used as a electrode material for the electrooxidation of CO, the standard cyclic voltammetry response (Fig 4.2) must be considered. An electrochemical cell was set up using the electrodes previously described (Chapter 2). The working electrode was a 25 µm diameter Pt disk electrode, the reference electrode was a $Hg/HgSO_4$ electrode (E^0 = 0.64 V vs SHE), and the counter electrode was a 3 mm diameter Pt disc electrode. The electrolyte was 5M H_2SO_4 because it is the same electrolyte used within the CO-AF sensor. The cyclic voltammetric response of the CO-AF sensor is shown to have a steady state current (accounting for small fluctuations on the nA scale) that is independent of change in potential between about 0.1 V and 0.35 V, suggesting an area where mass transport-controlled reactions can be subsequently studied.

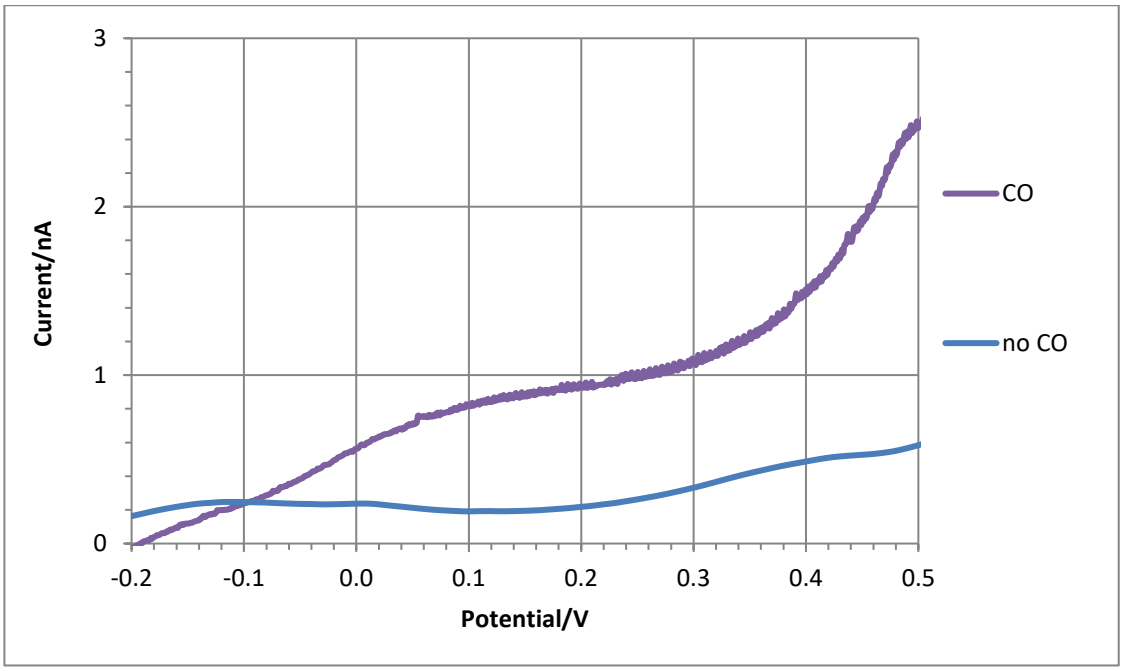

Figure 4.2: Cyclic voltammogram of Pt response to CO (1000 ppm) in 5M H_2SO_4 electrolyte (at 20°C). The working electrode was a 25 micrometre Pt disc, the reference electrode was $Hg/HgSO_4$, saturated K_2SO_4 and the scan rate was 5 mV s^{-1}

4.1 CO-AF Sensor Response to Carbon Monoxide Using Cyclic Voltammetry

In initial experiments, cyclic voltammetry was used to assess the response of the CO-AF sensor to CO. The starting potential applied was 0.0 V because the sensors are conditioned to work at that potential during the manufacturing process. The immediate rise in current is due to charging of the double layer capacitance and the particulate nature of the working electrode. It is not indicative of any faradaic reactions at the electrode surface.

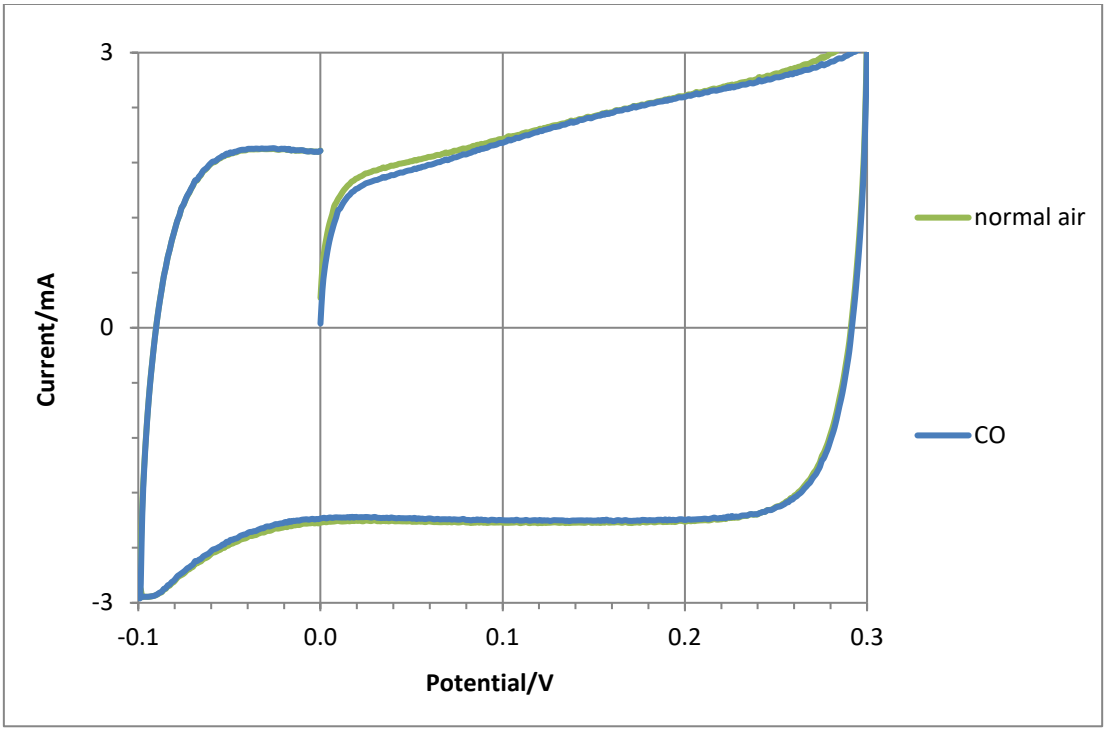

Figure 4.3: Cyclic voltammogram of a CO-AF sensor in different gases at normal scan rate (at 20° C). The potentials are recorded against the sensor internal reference and the scan rate was 10 mV s^{-1}. The CO concentration was 1000 ppm at 20° C and the scan was started at 0.0 V in the positive direction.

As can be seen from the cyclic voltammograms (Figs 4.3 and 4.4), a very slow scan rate is required to differentiate between the sensor response to air and 1000 ppm carbon monoxide in air. This is due to the very large charging current originating from the double layer capacitance of the nanaoparticluate working electrode. Also worth mentioning is the response at negative potentials (about - 0.1 V) during slow scan rate (showing reduction of oxygen in the acid electrolyte).

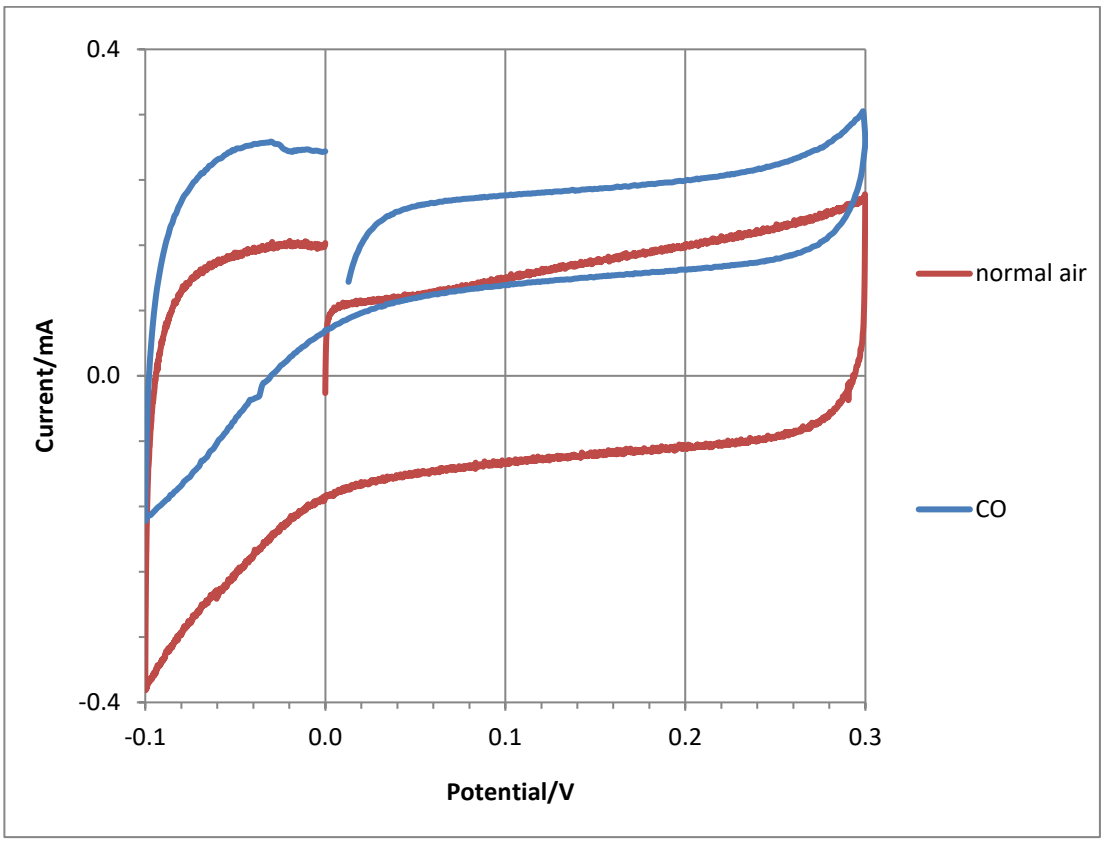

Figure 4.4: Cyclic voltammogram of CO-AF sensor in different gases at a very slow scan rate of 0.5 mV s^{-1} when the CO concentration was 1000 ppm at 20° C and the scan was started at 0.0 V in the positive direction.

The difficulty in distinguishing faradaic and non-faradaic processes at the nanoparticulate electrodes is one motivation for the approach taken in this thesis to use the chronoamperometric response to a concentration change to analyse the mechanism of operation of the sensors.

4.1.1 Impedance Spectroscopy

The results of the impedance spectroscopy experiments on the Alphasense CO-AF sensor at 20° C are shown below (all exposed to the corresponding gas for the duration of the measurements). The EIS (Nyquist plots) conducted on the CO-AF sensors (with and without the permanganate powder) shows the shape of a typical porous electrode as expected. It is a similar shape to other porous electrodes made from materials such as carbon or silicon carbide [155 - 158].

At high frequencies (lower absolute values of impedance) the Nyquist plot has the appearance of a Warburg impedance and is generally considered to indicate currents limited by transport in the pores (inter-particle spaces). At lower frequencies ($f < 0.5$ Hz) the imaginary impedance rises quickly because the pores are almost completely charged during the period of the applied ac signal. In this frequency regime, the porous electrode behaves more like a simple capacitor and the differential capacitance (c) can be extracted from a plot of –Z" against $1/f$ which has a slope of $1/(2\pi c)$. It is also worth noting that the impedance is almost potential independent in this region (Fig 4.5), although it starts to drop noticeably at -0.1 V where the CVs also show evidence of incipient oxygen reduction.

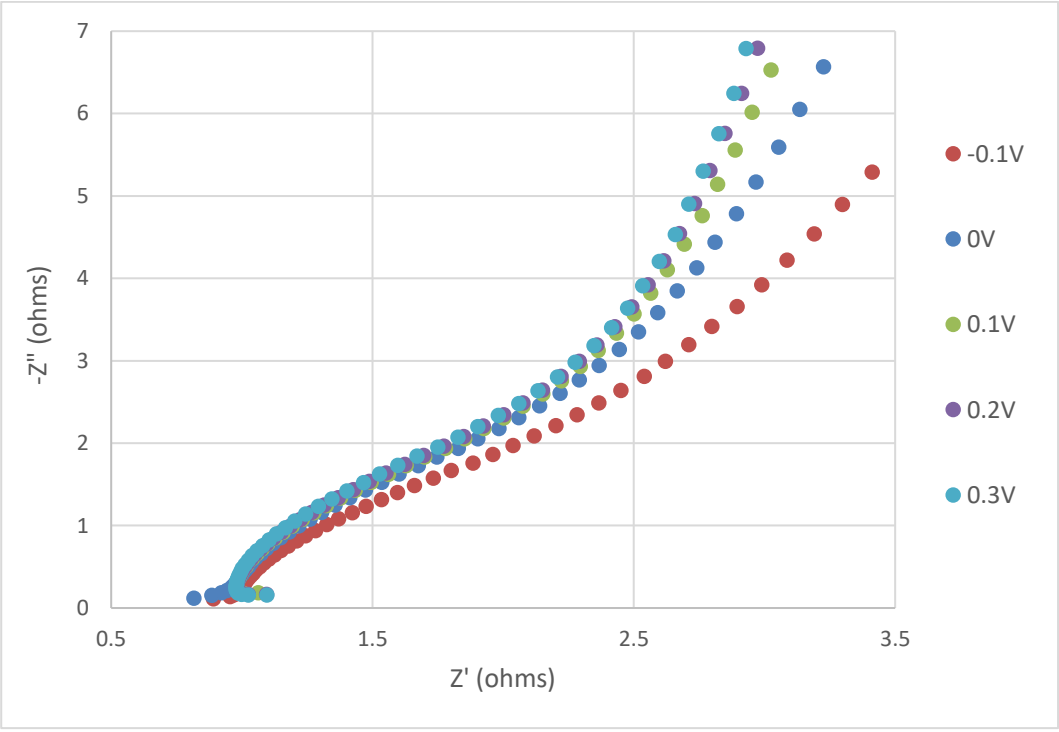

Figure 4.5: Nyquist plot of Alphasense CO-AF sensor in normal air at different dc voltages. The frequency range was 10-0.1 Hz and the ac amplitude was 1 mV.

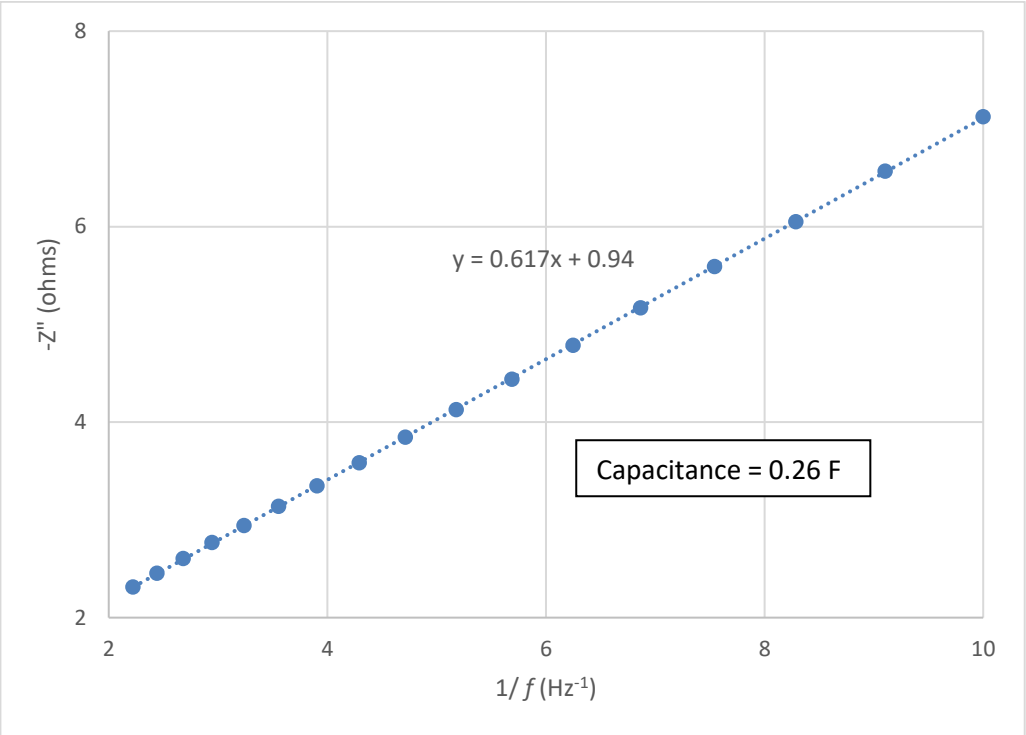

Figure 4.6: Plot of –Z" against inverse frequency (0.5 < *f* < 0.1 Hz) of CO-AF in normal air at 0.0 V applied dc potential (and 20 °C). The differential capacitance determined from this plot was 0.26 F

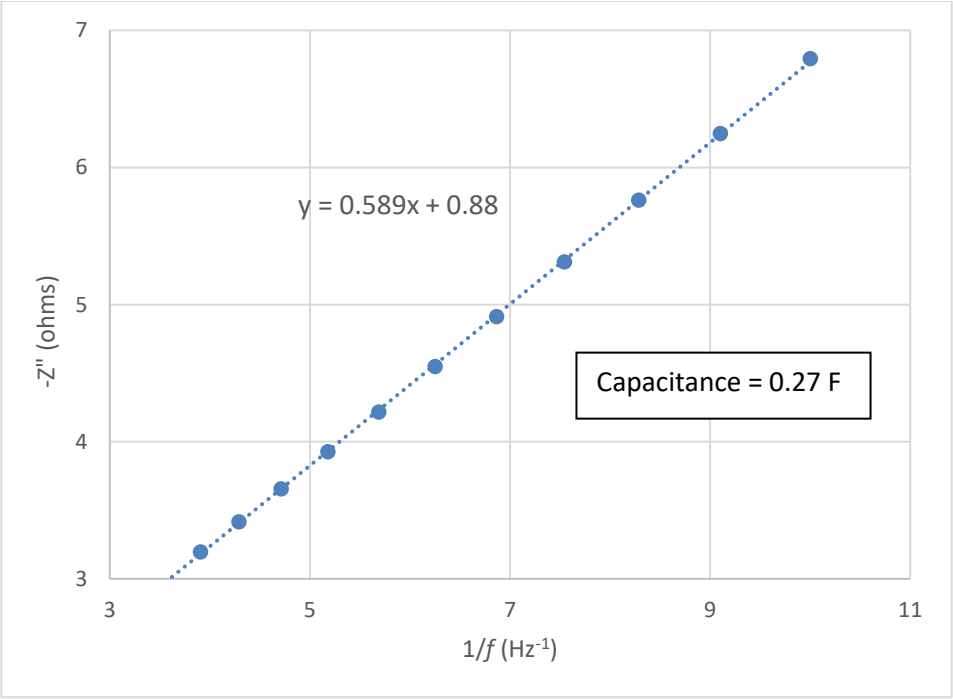

Figure 4.7: Plot of –Z" against inverse frequency (CO-AF at 0.2 V steady state in normal air at 20 °C).

Figures 4.8 and 4.9 shows the imaginary part of the impedance at the lowest frequencies applied. The capacitance extracted from the low frequency data was 0.26 F at 0.0 V and 0.27 F at 0.2 V. The large capacitance is a result of the nanoparticulate nature of the electrocatalyst within the sensor. This gives the sensors a large wetted surface area and helps to ensure that the electrode kinetics are not rate limiting at the operating potential of the sensor. However, it greatly obstructs the use of conventional electrochemical techniques to probe the mechanism of operation because the charging current is very large (Fig 2.14). Indeed, for a capacitance of 0.27 F and a scan rate of 1 mV s^{-1} the charging current is 0.27 mA, which is larger than the steady-state response to CO at 1000 ppm in air.

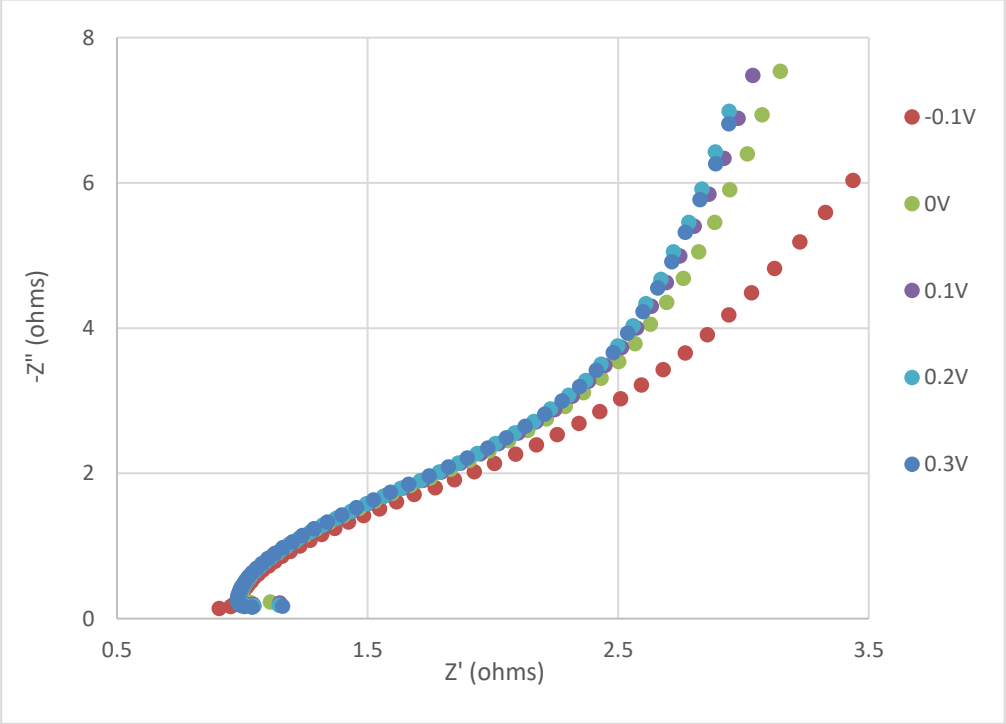

Figure 4.8: Nyquist plot of Alphasense CO-AF sensor in CO at constant gas flow rate (200 ppm) at 20°C at different steady state voltages.

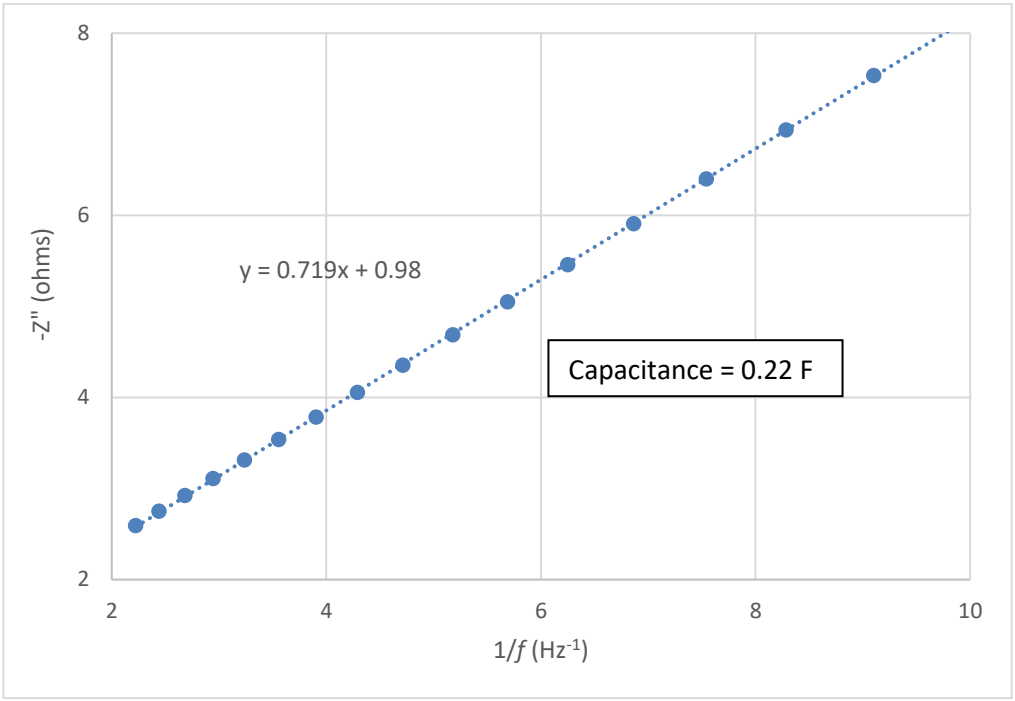

Figure 4.9: Plot of –Z” against inverse frequency of CO-AF in CO at 0.0 V steady state.

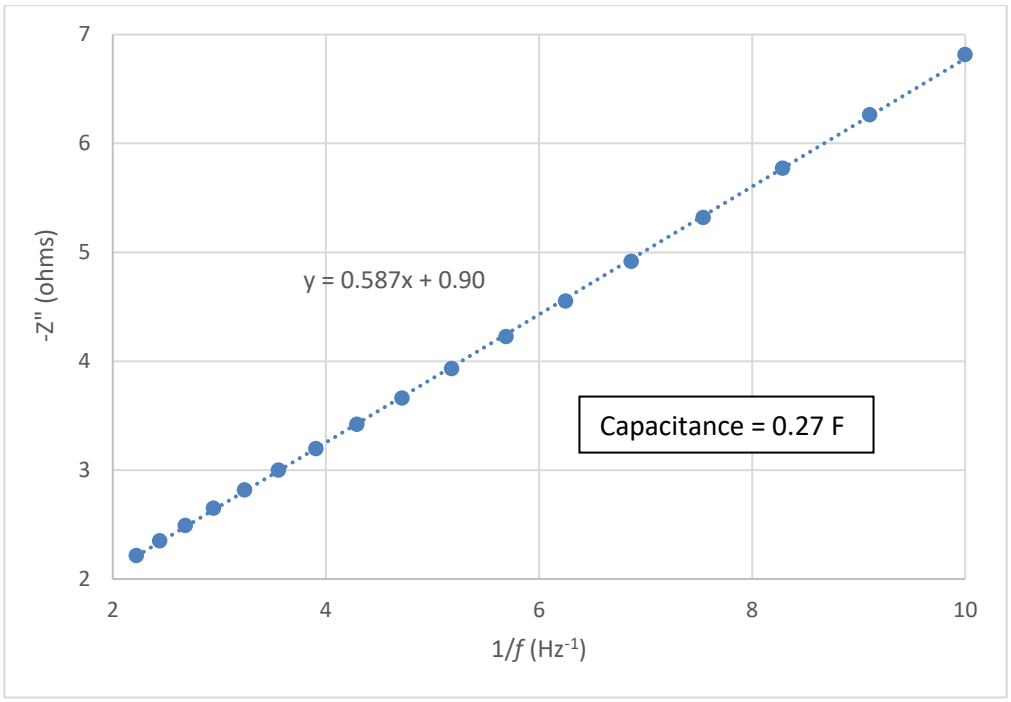

Figure 4.10: Plot of –Z” against inverse frequency of CO-AF in CO at 0.3 V steady state.

Figures 4.7, 4.9 and 4.10 show plots of imaginary impedance against inverse frequency in the presence of 200 ppm CO; all the plots display excellent linearity ($r^2 > 0.9$) and the derived capacitances are of the order of 0.2 – 0.3 F. Such values are extremely large and explain the shape of the cyclic voltammograms, which must be run at scan rates < 1 mV s^{-1} in order for any faradaic current to be discerned. This is enormous (four orders of magnitude greater) when compared to the literature value for smooth Pt(111) electrodes in aqueous media of about 20 µF cm^{-2} [159]. Based upon this estimate of the double layer capacitance, the wetted metal area of the sensing electrodes can be estimated to be on the order of 0.2 / 2 x10^{-5} = 10^4 cm^2 = 1 m^2.

The geometric (apparent) area of each device is approximately 1 cm^2 and the sensor itself fits inside the palm of a hand. Therefore, it is clear that the electrolyte penetrates the electrocatalyst and wets a much larger area than the geometric area of the device. The large (real) apparent area ratio of 10^4 cm^2 also helps explain the mass-transport limited nature of the current, because electrode kinetic-limited currents are proportional to the real surface area and, at long times, diffusion-limited currents are proportional to the geometric area because the diffusion layer extends away from the electrode surface and is governed by the macroscopic shape of the electrode. This indicates that kinetic limitations are likely to be negligible. The huge differential capacitance of the working electrode also partly explains the long conditioning times required after manufacture. The sensors are typically biased at 0.0 V for a period of the order of several hours before they are shipped from the factory. During this period, the working electrode capacitance is charged and the background current stabilised. Figure 4.8 shows the chronoamperometric response of a CO-AF sensor after application of various dc potentials. At the largest potential (0.3 V) the background current remains too large to use the sensor even after 10 minutes of polarisation. At -0.1 V there is a negative current observed at short times; this may be partly oxygen reduction as noted in Fig 4.11 as well as charging of the double layer. The smallest transient and the lowest background currents after 10 minutes of polarisation are observed for a potential of 0.0 V. This is the manufacturers recommended bias for operation of the sensors and also the conditioning potential applied by the manufacturer, which is why the initial current transient is smallest in this case.

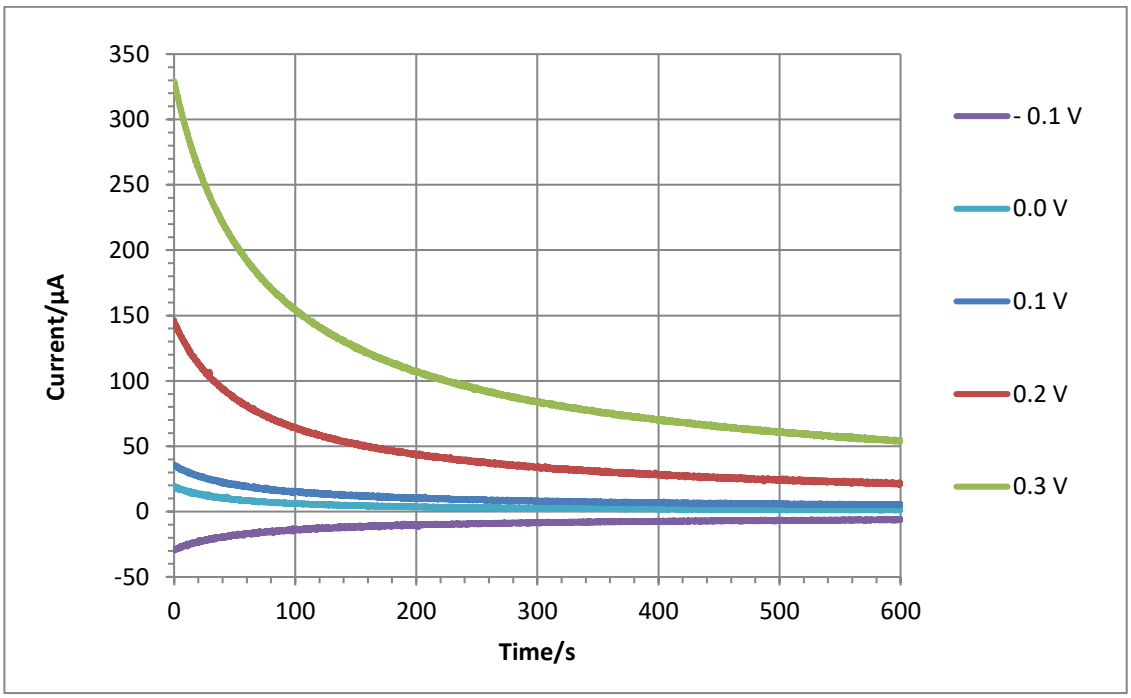

Figure 4.11: Graph showing the initial chronoamperometric response of a CO-AF sensor upon application of different potentials in air.

4.1.2 Chronoamperometry

Owing to the issues discussed in the previous section, cyclic voltammograms of CO-AF devices are swamped by the charging current and therefore a potentiostatic technique: chronoamperometry in response to a concentration step was used as the main electroanalytical tool. In this method, the voltage was held at a fixed value whilst current was measured as a function of time in response to changes in analyte (Fig 4.12).

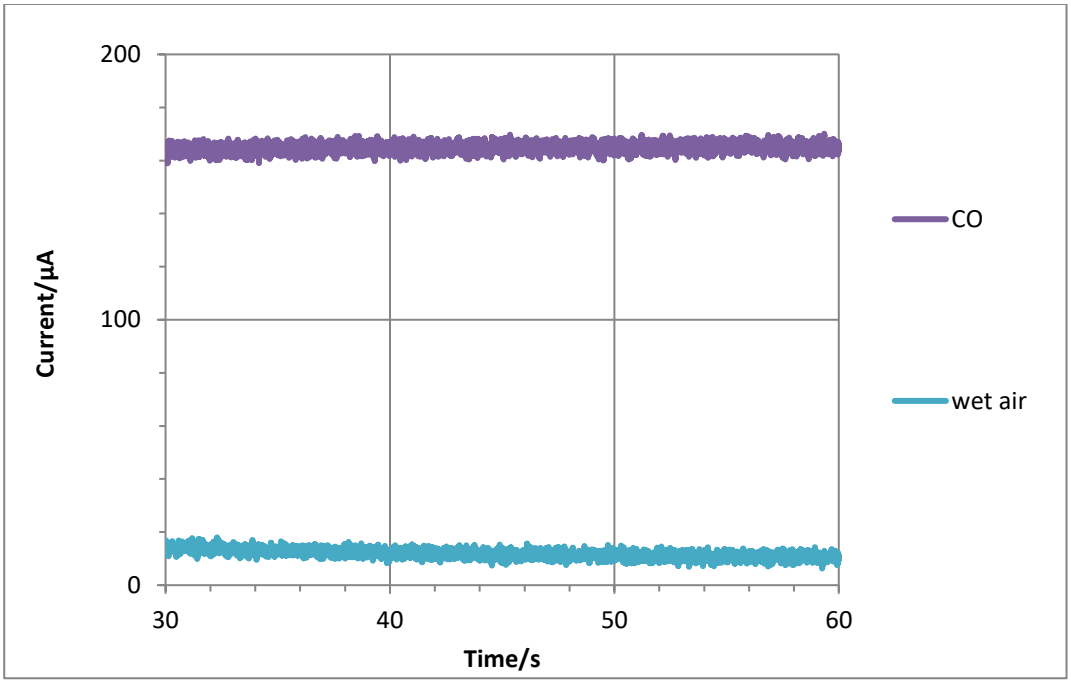

Figure 4.12: Graph showing CO-AF sensor selectivity for CO over H_2O at steady flow rate under standard conditions at 0.0 V (300 ppm, 88 mL/ min flow rate).

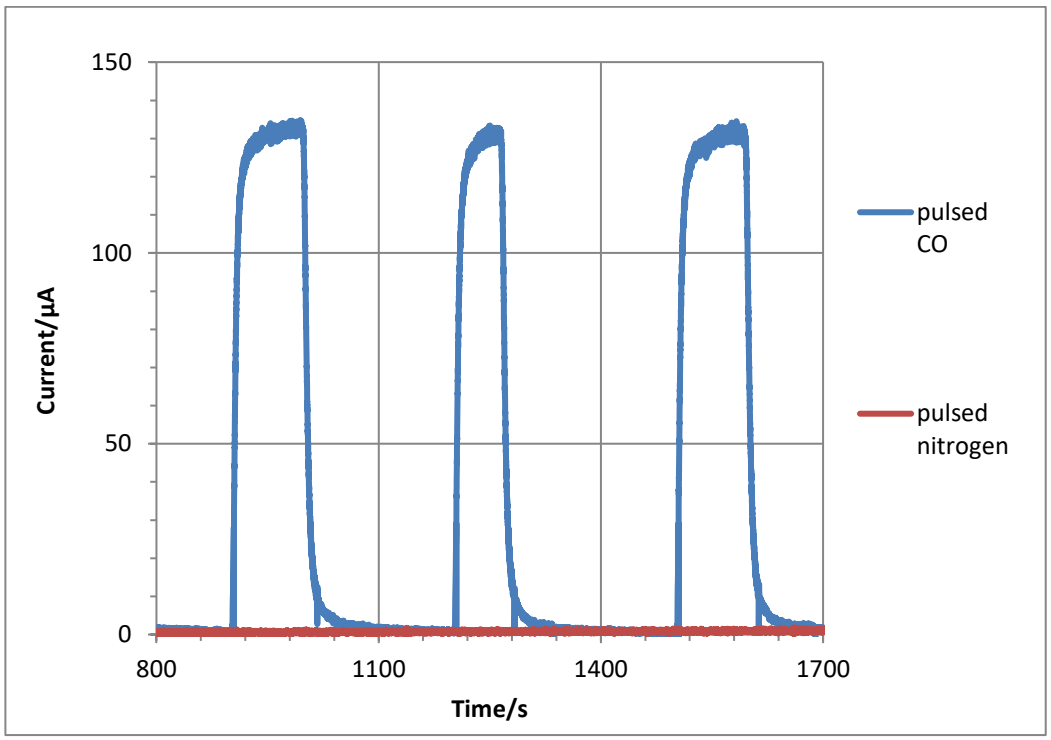

Figure 4.13: Graph showing CO-AF sensor selectivity response to different gases at pulsed intervals (fixed concentration) in standard conditions at 0.0 V steady state (200 ppm, 55 mL/min flow rate).

Figure 4.13 shows the time-dependent response of a CO-AF device to 200 ppm CO or N_2. The current response is clearly reversible in the sense that it returns to the baseline after removing the CO from the gas stream. It is repeatable and is also unaffected by inert gases such as N_2. The response to CO shows a steady-state current is achieved within a few tens of seconds of exposure to CO. The value of this steady-state current is the sensing signal and can be shown to be directly proportional to the CO concentration (Fig 4.14).

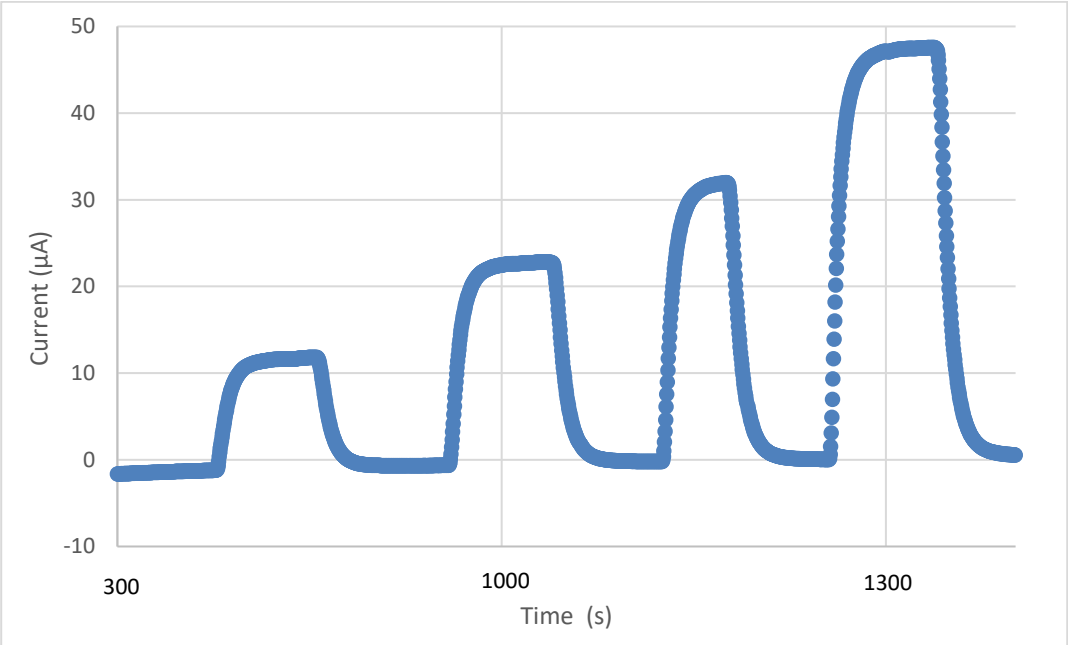

Figure 4.14: Graph showing proportional response to pulses of increasing CO concentrations over time at 0.0 V steady state in standard conditions (100, 200, 300, 400 ppm respectively).

The steady state current at each concentration was then plotted against CO concentration expressed in ppm to produce a calibration curve (Fig 4.15). The CO-AF sensor and subsequent variants (CO-A1, CM-A1) gave linear current responses to increasing concentrations of analyte.

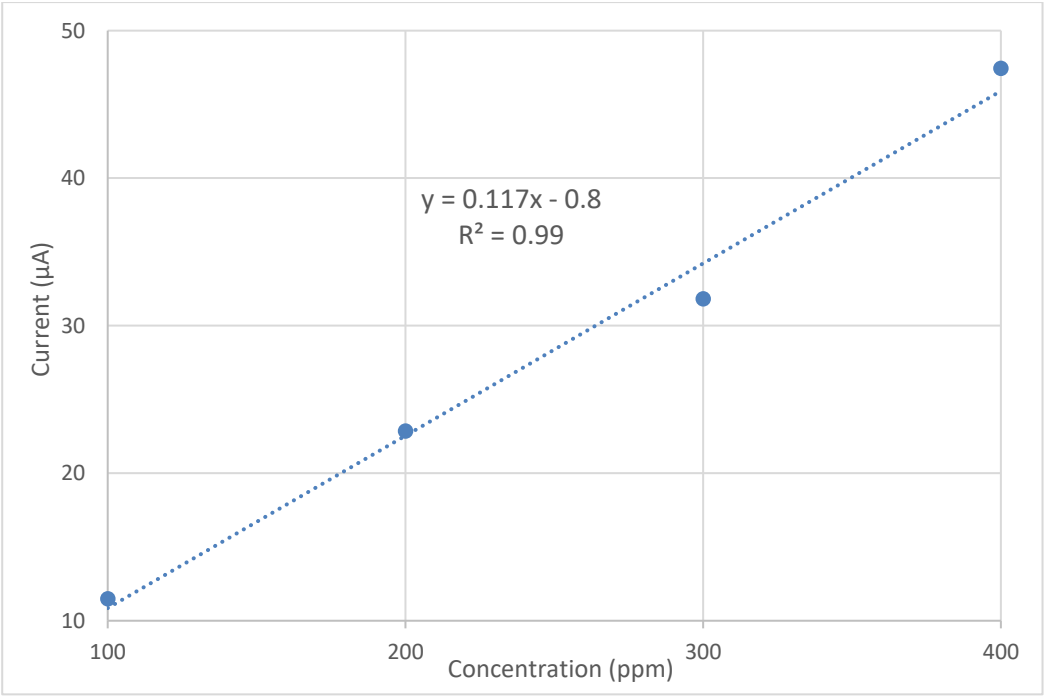

Figure 4.15: Graph showing relationship between amperometric response (steady-state current) and CO gas concentration.

4.1.3 Modelling the Chronoamperometric Response

The basic electroanalytical method used to investigate the mechanism of sensor operation involves analysis of the rising and falling portions of the chronoamperometric responses shown in figures 4.13 and 4.14. A regression model is fitted to this data and used to estimate several parameters related to mass transport inside the device. The regression model is described by the equations within the modelling chapter (chapter 3). The modelled was fitted to the data by least squares regression with L^2/D, T_0, ΔI and the steady state current i_{00} as floating parameters. These parameters are defined below (Fig. 4.16). L is an effective diffusion layer thickness, D is an effective diffusion coefficient, T0 is simply the time at which the analyte flow commenced / stopped and ΔI is the difference between the baseline current in the absence of analyte and the steady-state response in the presence of the analyte. Some typical results for the modelling of the CO-AF sensor chronoamperometric response to CO gas at various concentrations and steady state voltages are shown below with line of best fit (red), actual recorded data (blue), and the difference between the two values, the residual (green):

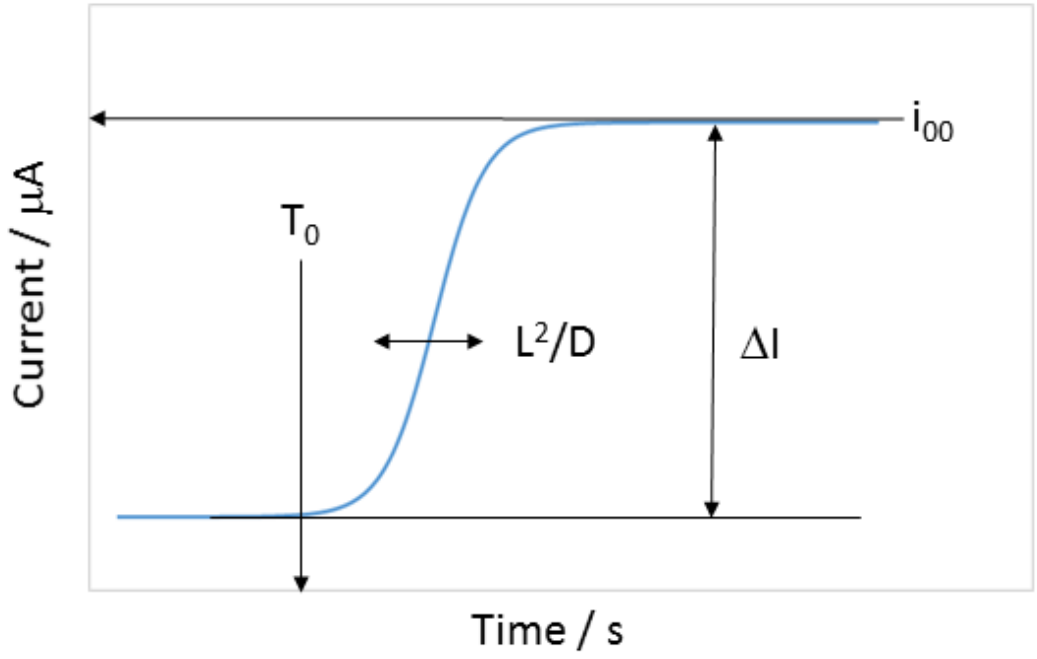

Figure 4.16: Graph showing least squares regression parameters used within mathematical model.

L^2/D (s)	T_0 (s)	ΔI (μA)	Steady state current (μA)
97	589	-14.64	27.02

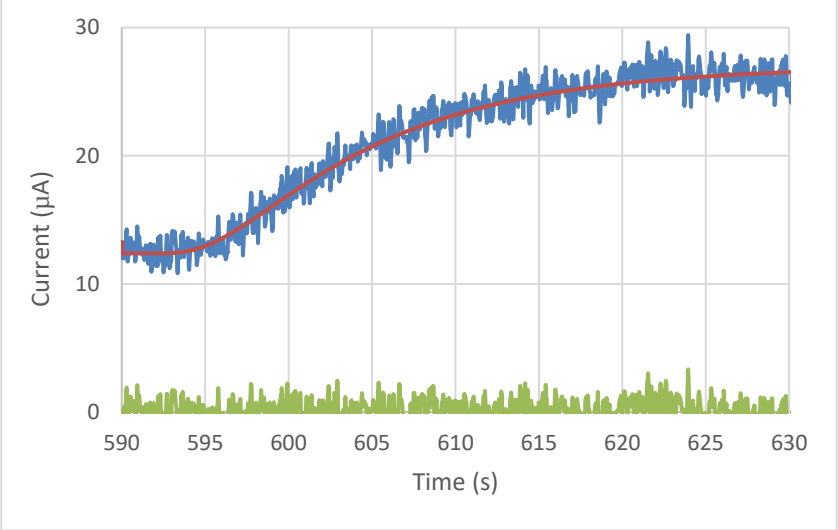

Figure 4.17: Sensor response at 0.0 V steady state in 20 °C pulsed CO (400 ppm) experimental data (blue), line of best fit (red), difference between the two values (green). The table above contains the fitted parameters.

L^2/D (s)	T_0 (s)	ΔI (μA)	Steady state current (μA)
206	240	-14.95	16.92

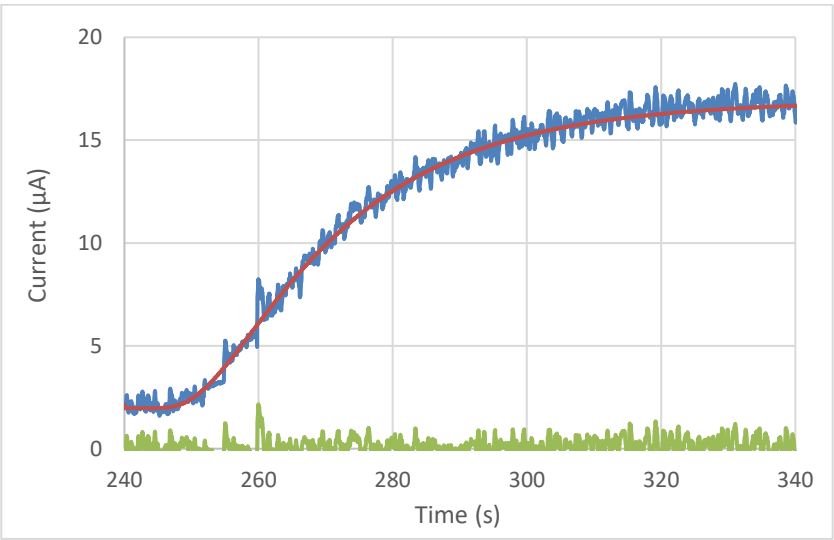

Figure 4.18: Sensor response at 0.0 V steady state in 20 °C pulsed CO (200 ppm) experimental data (blue), line of best fit (red), difference between the two values (green).

It is worth noting that the additional current noise apparent on the traces in figures 4.17 and 4.18 compared to, e.g., figure 4.14 is due to the higher sampling rate of these experiments: 1 measurement every 30 ms as opposed to 1 sample s^{-1} for figure 4.16. This means that less averaging is possible on each measurement.

The model software was also applied to the recovery chronoamperometry curve of the standard CO-AF sensor when the CO gas was shut off. Whilst these results were not used in the calculations of the *D* and *L* values, they help to validate the model because it is an important aspect of the modelling that the L^2/D and ΔI values should be the same within uncertainty for both the response and recovery transients. As can be seen from Figures 4.18 and 4.19 these values are similar, thus validating the model.

L^2/D (s)	T_0 (s)	ΔI (μA)	Steady state current (μA)
258	431	13.26	0.51

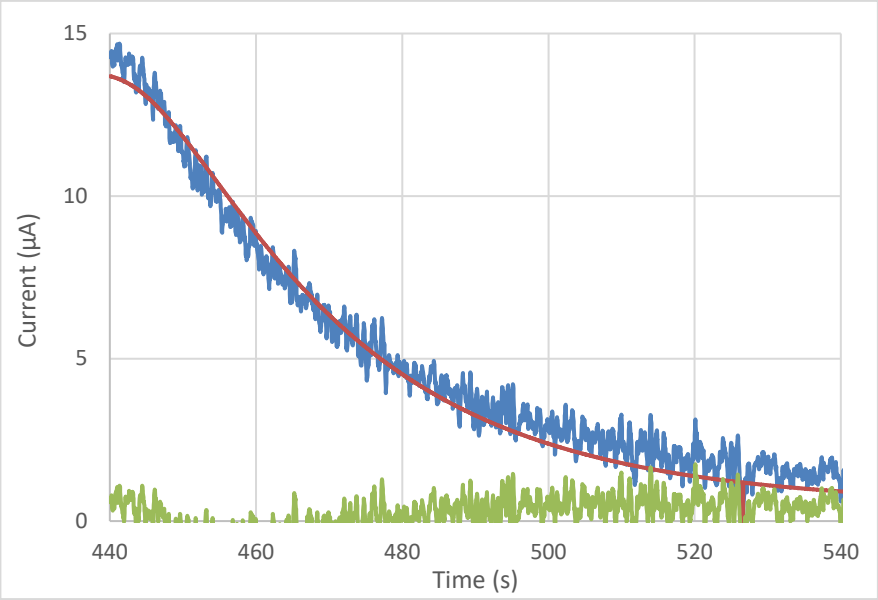

Figure 4.19: Sensor response after 200 ppm CO at 0.0 V steady state in 20° C experimental data (blue), line of best fit (red), difference between the two values (green).

4.1.4 Temperature Dependence

Additional data on standard CO-AF sensors at different temperatures and using a different thickness of semi-permeable membrane was kindly provided by Alphasense. The effective *L* and *D* values from the analysis of this data is shown in the table below. Sensors described as "standard" employed a Porex membrane, pore size 9-12 micrometre, porosity 40-45%, thickness 0.18 mm. Sensors described as "thick membrane" used a different (thicker) Porex membrane, porosity 20%, thickness 0.25 mm.

-20° C	thick membrane	standard
L (cm)	0.40	0.29
D (cm^2s^{-1})	9.34×10^{-4}	1.04×10^{-3}

-10° C	thick membrane	standard
L (cm)	0.37	0.26
D (cm^2s^{-1})	9.98×10^{-4}	1.01×10^{-3}

0° C	thick membrane	standard
L (cm)	0.32	0.30
D (cm^2s^{-1})	1.03×10^{-3}	1.25×10^{-3}

10° C	thick membrane	standard
L (cm)	0.31	0.29
D (cm^2s^{-1})	1.15×10^{-3}	1.35×10^{-3}

20° C	thick membrane	standard
L (cm)	0.31	0.28
D (cm^2s^{-1})	1.26×10^{-3}	1.45×10^{-3}

30° C	thick membrane	standard
L (cm)	0.30	0.23
D (cm^2s^{-1})	1.24×10^{-3}	1.23×10^{-3}

40° C	thick membrane	standard
L (cm)	0.30	0.34
D (cm^2s^{-1})	1.35×10^{-3}	1.88×10^{-3}

Table 4.1: Calculated values for CO-AF sensor in CO (tested by Alphasense, data supplied by Dr. R. P. Baron).

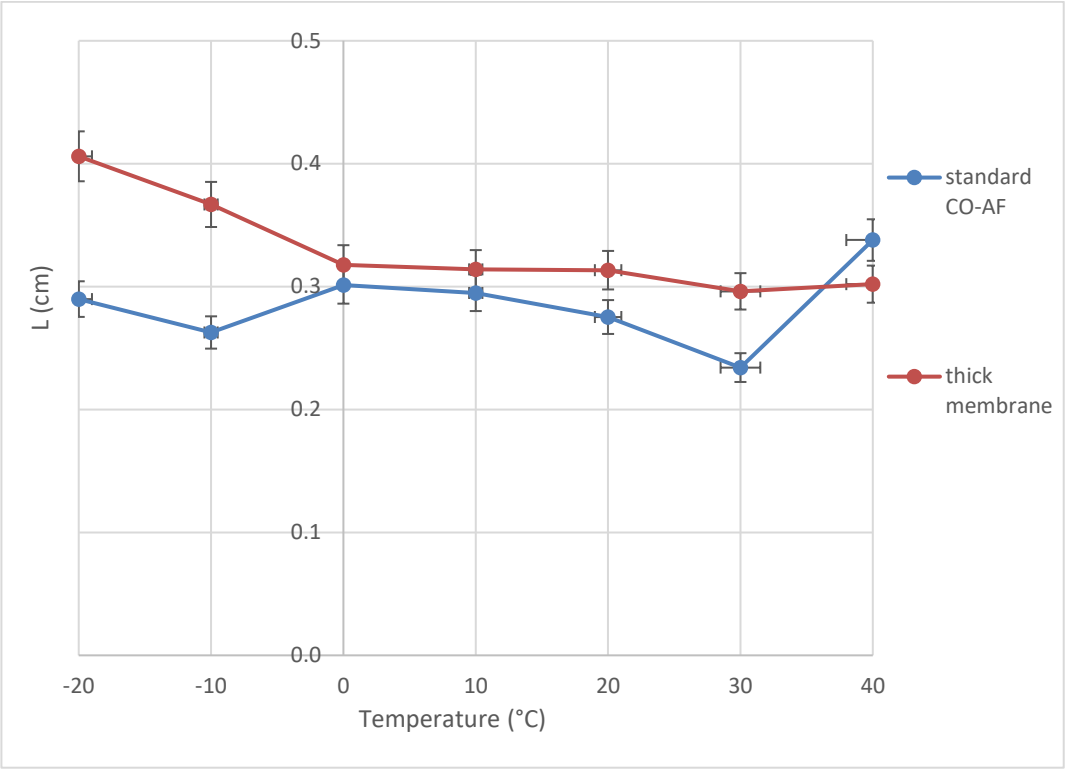

Figure 4.20: Calculated effective layer thickness (*L*) values for CO-AF sensor (data provided by Alphasense).

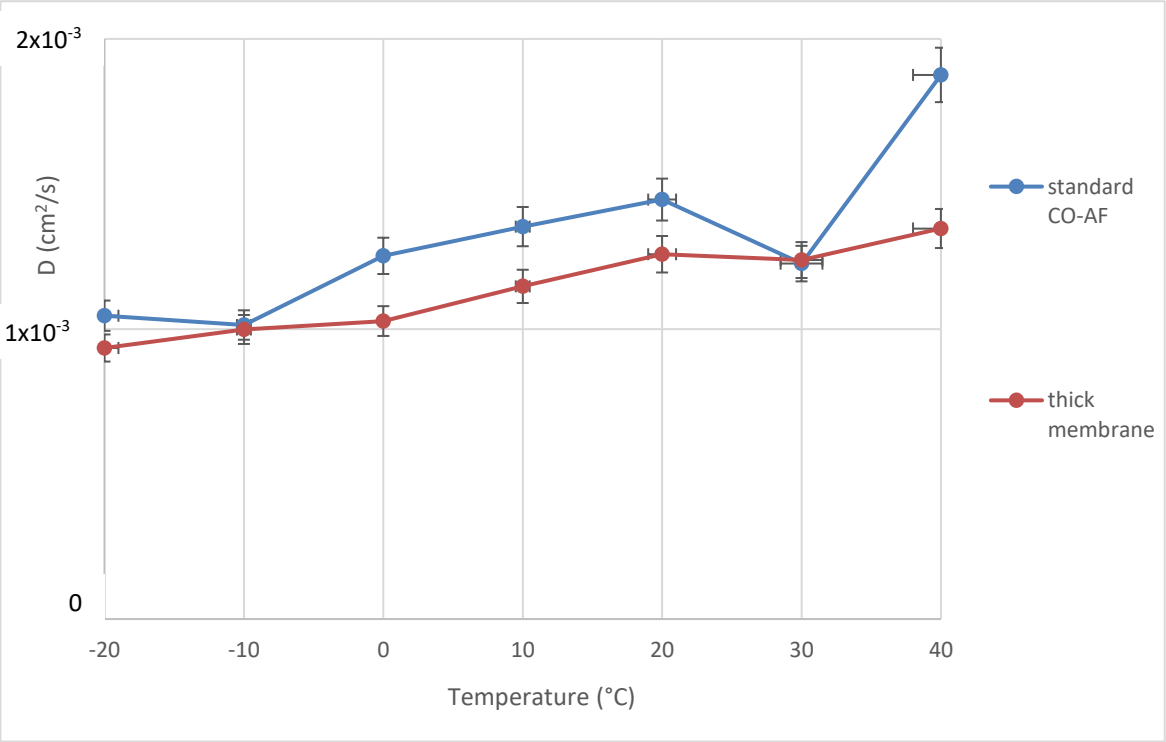

Figure 4.21: Calculated effective diffusion coefficient (*D*) values for CO-AF sensor (data provided by Alphasense).

From Fig 4.20 and 4.21 it can be seen that in the standard CO-AF sensor the apparent layer thickness (*L*) is functionally constant (allowing for slight fluctuations). This is considered to be because the semi-permeable membrane does not experience significant swelling over the temperature range and the layer of liquid covering the working electrode remains relatively constant. The variance is thought to be due to the hygroscopic effect of the sulfuric acid which means more water may enter the electrolyte and vary the liquid electrolyte concentration and volume.

The thick membrane CO-AF sensor shows a similar trend with *L* varying weakly with temperature. The generally greater value of *L* (compared to the standard CO-AF sensor) is as expected due to the thicker membrane and helps validate the modelling parameters used. The thicker membrane also reduces the hygroscopic effects of the sulfuric acid, which enables a more consistent concentration and volume of electrolyte as temperature changes (particularly due to the high water content of the electrolyte). It is worth noting that the effective layer thickness *L* is larger than the Porex membrane thickness and suggests a significant role for the silica/$KMnO_4$ filter layer in the mass transport, this filter layer has a similar actual thickness to the derived values of *L*.

The diffusion coefficients (*D*) of both the standard CO-AF sensor and the thick membrane CO-AF sensor show a general trend of increasing as temperature increases. The minor dips at -10 °C and 30 °C in the standard CO-AF sensor data are thought to be outliers simply due to systematic errors within the experiment procedure. The calculated results for the standard CO-AF sensor in carbon monoxide show that *L* is on the order of 0.3 cm and *D* is on the order of 10^{-3} cm^2s^{-1} across the temperature range. Thus, the calculated values of *L* are considered commensurate with the physical thickness of the membrane and $KMnO_4$ powder (on the silica scaffold) together within the headspace of the sensor. The effective values of *D* are much too great to be explained by diffusion in the electrolyte where $D \sim 10^{-5}$ cm^2 s^{-1}. They are somewhat smaller than values of *D* in the gas phase which are of the order of 0.1 cm^2 s^{-1} [136]. It should be noted however, that diffusion within the filter layer and the semi-permeable membrane will be suppressed by a porosity factor and possible additional factors due to constrictions and the tortuosity of the pores [137].

4.1.5 Voltage Dependence of the CO-AF Sensors

The response of the standard CO-AF sensor during chronoamperometry was measured at different steady state voltages, in order to ascertain the link between applied voltages and measured current. The results show only a small voltage dependence which confirms that whilst there are some kinetic considerations to be made, the main rate limiting step is mass transport of the analyte across the sensor. the good fit of the regression model to the data in the previous section further supports a mass transport limited response.

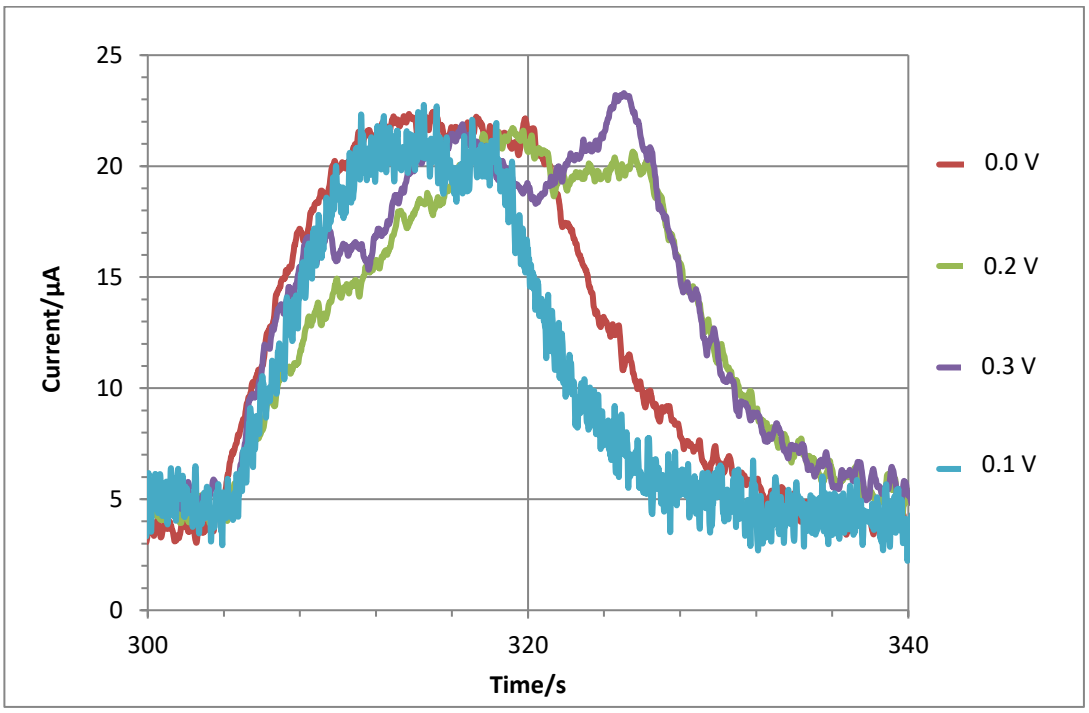

Figure 4.22: Graph showing standard CO-AF sensor response to 1000 ppm CO saturated air at 20° C at different steady state voltages (gas on at 303 secs and off at approximately 316 secs).

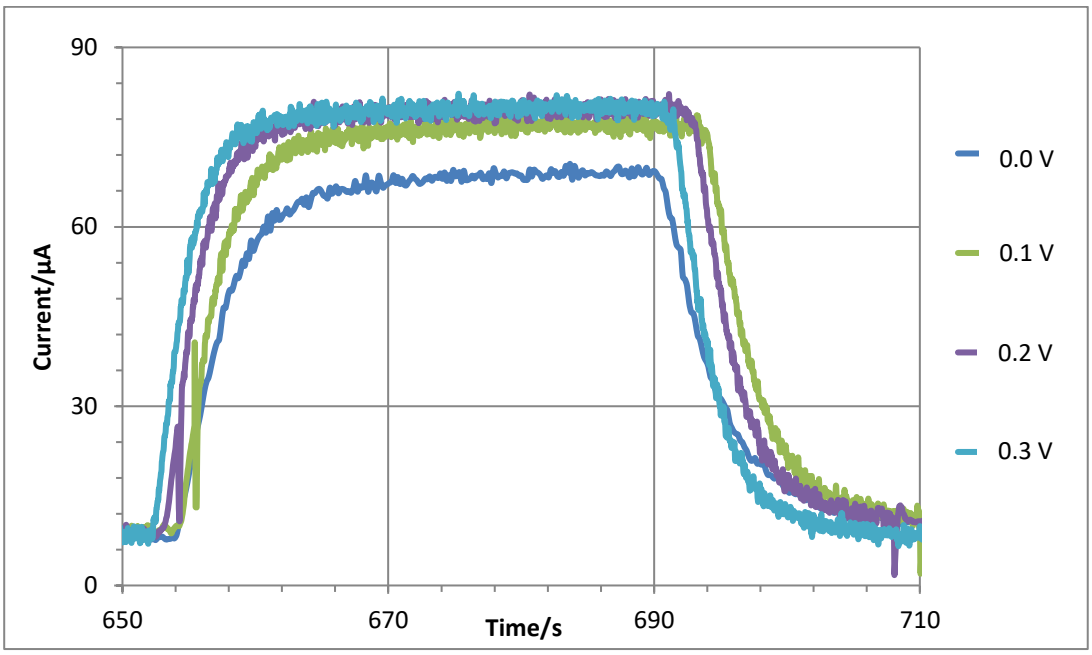

Figure 4.23: Graph showing standard CO-AF sensor response to 1000 ppm CO saturated air at 40° C (gas on at 652 secs and off at 690 secs).

The manufacturer's choice of 0.0 V as the operating potential is a compromise between the desire to have a potential-independent steady-state current signal that is insensitive to drifts in the internal reference potential and the excessive conditioning times and baseline currents in the absence of analyte that are observed at higher voltages.

4.2 Summary

Overall, the CO-AF devices can be satisfactorily modelled by considering the mass-transport of the analyte within the sensor. The regression parameters and the theory outlined in Chapter 3 show that the major diffusion barrier corresponds to the analyte within the gaseous phase of the porous membrane and the interstices of the silica/$KMnO_4$ filter layer. Under the normal operating conditions, mass transport in the liquid layer covering the working electrode nanoparticles appears to be a negligible contribution to the overall diffusion barrier and indicates that the thickness of the liquid layer is very small. This is presumably because the hydrophobic membrane does not easily allow penetration of the aqueous electrolyte.

The fact that the impedance spectroscopy results show a capacitance of 0.2 F confirms that the working electrode has a large microscopic surface area. This is because the literature value for Pt(111) is 20 µF cm^{-2} and so the microscopic surface area of the working electrode within the sensors must be approximately 1 m^2 even though the actual device itself is only 1 cm^2 in size. Such apparent discrepancies are due to the working electrode being a pressed disk of Pt black nanoparticles, as opposed to a smooth disk electrode used in typical electrochemical investigations.

The weak temperature dependence of *D* provides strong support for the assignment of the rate-limiting transport to the membrane and filter layers, because diffusion of CO within aqueous phases is known to show Arrhenius-like temperature dependence with an activation energy of the order of 25 kJ mol^{-1} in water [138] and probably substantially higher in the more viscous sulphuric acid electrolyte employed here. An activation energy of this magnitude would result in an order of magnitude increase in *D* over the temperature range -20 – 40 ^oC under the experimental conditions, which is not observed.

[126] C. H. Greenwalt
Ind. Eng. Chem., 1925, **17**, 522-523

[127] M. Choluj, W. Bartkowiak
Chem. Phys. Letts., 2016, **663**, 84-89

[128] J. S. Muenter
J. Mol. Spectrosc., 1975, **55**, 490-491

[129] P. L. Silvestrelli, M. Parrinello
Phys. Rev. Letts., 1999, **82**, 3308-3311

[130] H. Liu, Y. Wang, J. M. Bowman
J. Phys. Chem. B, 2016, **120**, 1735-1742

[131] S. Park, J. Yoo
Anal. Chem., 2003, **75**, 455-461

[132] Y. Sugawara, A. P. Yadav, A. Nishikata, T. Tsuru
J. Electroanal. Chem., 2011, **662**, 379-383

[133] J. Friedl, U. Stimming
Electrochimica Acta, 2017, **227**, 235-245

[134] M. Kim, I. Oh, J. Kim
Electrochimica Acta, 2016, **196**, 357-368

[135] T. Pajkossy, D. M. Kolb
Electrochimica Acta, 2001, **46**, 3063-3071

[136] E. L. Cussler
Diffusion: Mass Transfer in Fluid Systems, 1997, **2nd Edn.**, New York, Cambridge University press

[137] P. Grathwohl
Diffusion in natural porous media: Contaminant transport, sorption / desorption and dissolution kinetics, 1998, Kluwer Academic

[138] D. L. Wise, G. Houghton
Chem. Eng. Sci., 1968, **23**, 1211–1216

Chapter 5

5.0 CM-A1 Sensor Response to Carbon Monoxide

In order to evaluate the effect of different electrode materials on the performance of the sensor, a batch of sensors was created with working electrode nanoparticles consisting of one third platinum (Pt) and two thirds ruthenium (Ru) by weight (the nanoparticle species were considered to be equally interspersed as it is an alloy). Changing the composition of the working electrode will undoubtedly affect the chemical selectivity of the sensor but should not change the mass transport characteristics. To test the effect on the mass transport characteristics, the permanganate-silica filter was also removed from the sensor (Fig 5.1a). This batch of sensors was designated CM-A1. It is hypothesised that the sensors will have an amperometric response to CO which is similar to the standard CO-AF sensors, due to both Ru and Pt sites being catalytically active towards CO [139 - 142]. Ruthenium is used in many electrochemical sensors and known to be active towards carbon oxide derivatives, oxygen [143, 144] and VOCs such as ethanol [145 - 148]. It is considered worthwhile investigating if the sensors can detect CO at levels relevant to safety monitoring and give proportional amperometric responses to CO concentration. This is because platinum can be nearly four times as expensive as ruthenium, so the sensor may be more economically viable at an industrial level of production.

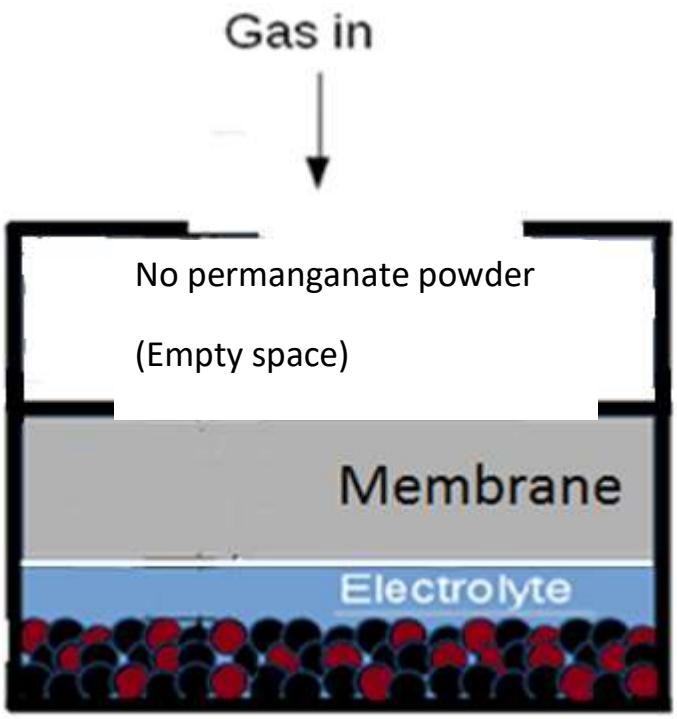

Figure 5.1a: Schematic of CM-A1 sensor. Working electrode shown as Pt (black) and Ru (red) metal alloy. As in chapter 4, the thickness of the electrolyte layer above the working electrode is exaggerated for diagrammatic clarity.

Bright field microscopy images were taken of the working electrode that is mechanically pressed onto the PTFE semi-permeable membrane. It can be seen from the image of the Pt working electrode edge (Fig. 5.1b) that the Pt is much denser than the PTFE semi-permeable membrane. This is to be expected given the semi-permeable nature of the PTFE membrane. The image of the centre point of the working electrode (Fig 5.1c) shows that the Pt nanoparticles are evenly distributed to form a homogenous electrode layer, due to the uniform shading pattern. The image of the working electrode taken from a CM-A1 sensor (Fig 5.1d) shows that the addition of Ru causes a much greater variance in working electrode depth on the microscopic scale. The Pt:Ru electrode is less optically dense which suggests that it is more porous. The liquid electrolyte seeps into the pores of the electrode and the phase boundaries are no longer in well-defined layers. Thus, the effective layer of the liquid electrolyte is seemingly increased as the Pt:Ru electrode is wetted to a greater extent than the much denser Pt electrode. This helps to explain why the results suggest the rate limiting step for diffusion in the CM-A1 sensor is in the liquid phase, whereas it is gas phase limited in the CO-AF sensors.

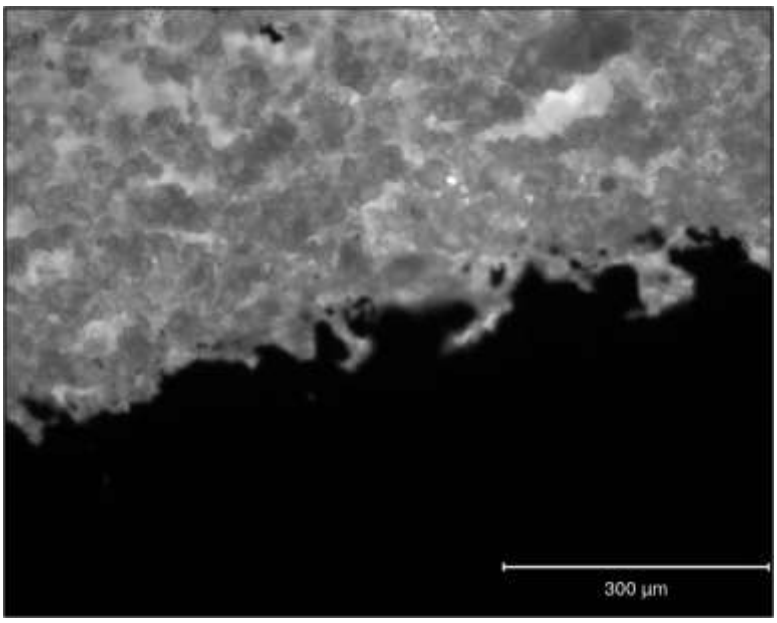

Figure 5.1b: Bright field microscopy image showing edge of Pt working electrode (black) on the PTFE semi-permeable membrane (white).

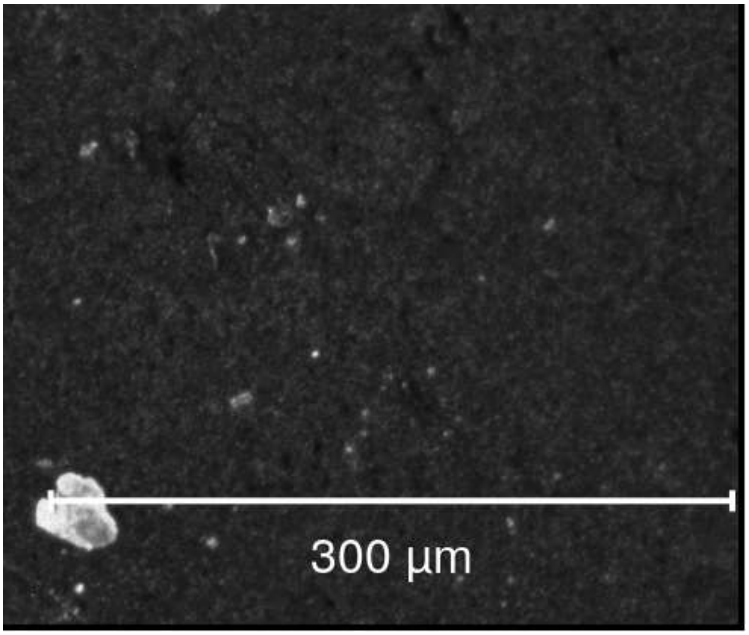

Figure 5.1c: Bright field microscopy image showing Pt (black) on centre point of PTFE semi-permeable membrane.

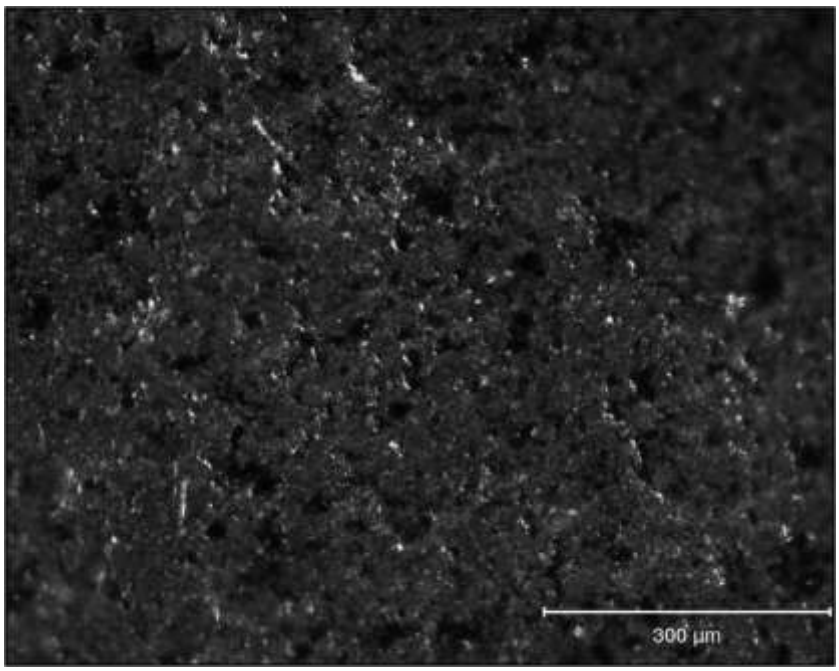

Figure 5.1d: Bright field image of Pt:Ru mixed metal working electrode on PTFE semi-permeable membrane.

5.1 Cyclic Voltammetry at CM-A1 Sensors

The CM-A1 sensor cyclic voltammogram comparative response to CO is shown below (Fig. 5.2). It can be seen that, even at very slow scan rates there is no discernible change in the cyclic voltammetry profiles of the CM-A1 sensor in zero grade air or CO, so different electrochemical methods must be used. As noted in the section on cyclic voltammetry of CO-AF sensors (chapter 4), the currents measured during cyclic voltammetry of CM-A1 sensors (Figs 5.2 and 5.3) are dominated by charging current.

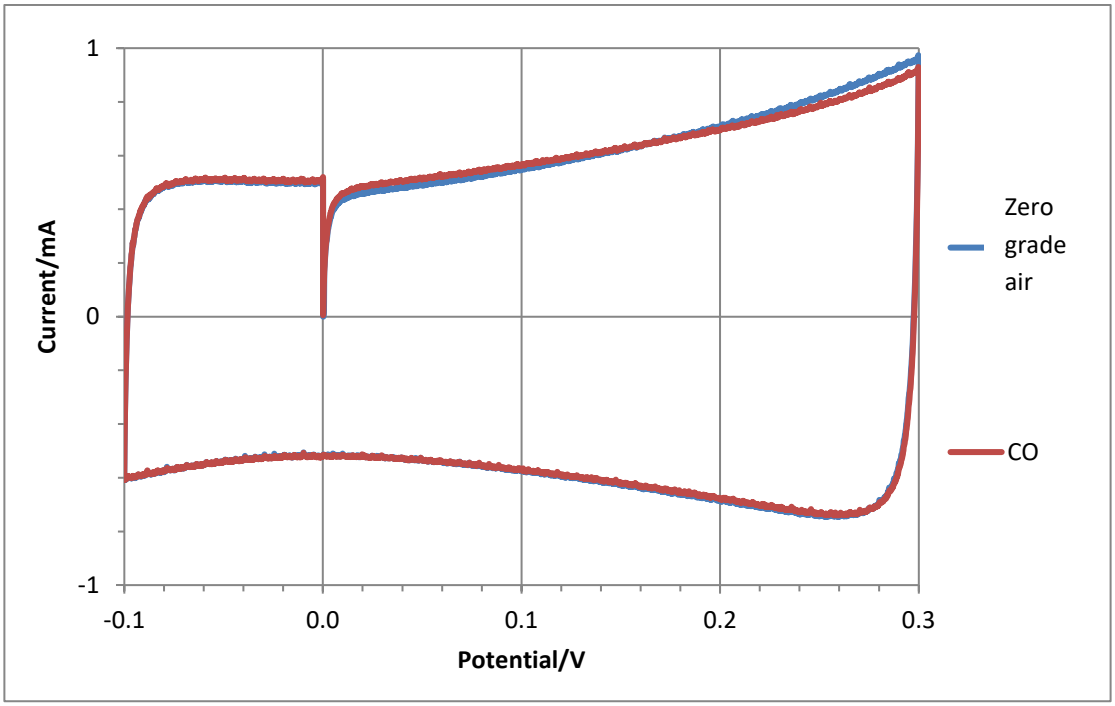

Figure 5.2: Cyclic voltammogram of CM-A1 sensor in normal air compared against 350 ppm CO in normal conditions. The scan rate was 1 mV s^{-1} and the potential scan was started from the usual operating potential of 0.0 V in the positive direction.

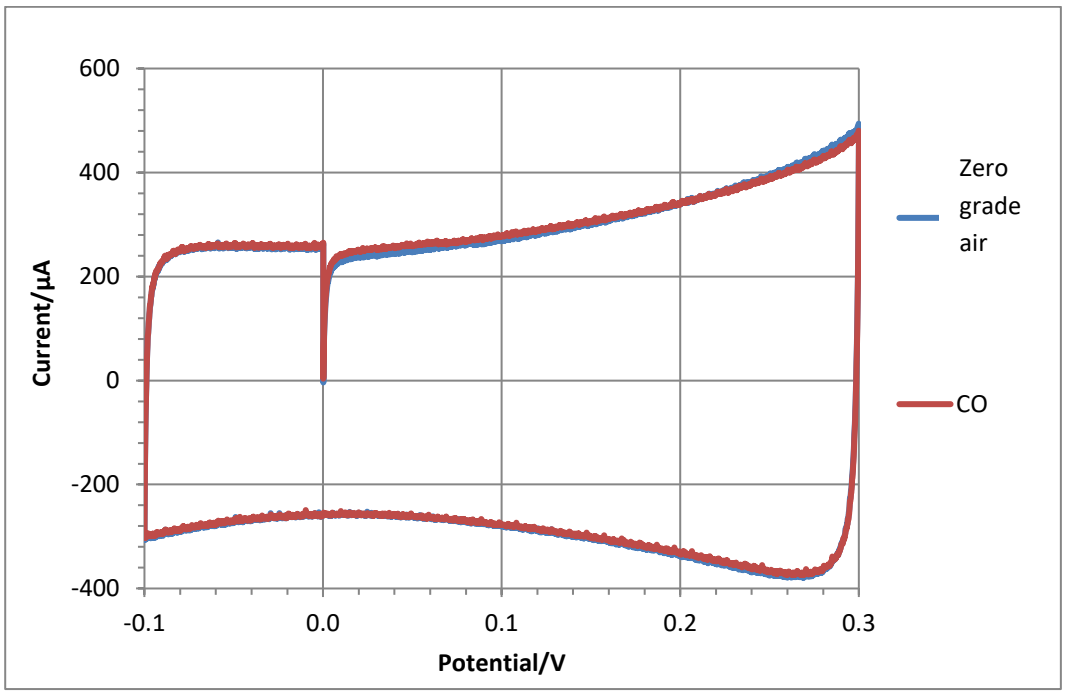

Figure 5.3: Cyclic voltammogram of CM-A1 sensor in normal air compared against 350 ppm CO in normal conditions at a very slow scan rate of 0.5 mV s^{-1} where the potential scan was started from the usual operating position of 0.0 V in the positive direction.

Even at 0.5 mV s^{-1} (Fig 5.3), the faradaic current due to oxidation of 350 ppm CO is barely detectable. As expected, cyclic voltammetry is not a useful technique for electroanalytical studies of the CO response of CM-A1 devices. However, it is worth noting that there is very little evidence of oxygen reduction at - 0.1 V in contrast to the CO-AF devices of chapter 4. Pt is well known to be a superior catalyst for oxygen reduction than Ru [143], however binary alloys have sometimes shown higher activity than pure Pt [144]. The data suggests that the preparations of Pt/Ru used in these devices are a worse electrocatalyst for the oxygen reduction reaction than pure Pt, this may in fact be an advantage in operating environments where oxygen levels fluctuate.

5.2 Impedance Spectroscopy of CM-A1 Sensors

The same parameters for impedance spectroscopy were used as in chapter 4 (with CO-AF devices), there is little difference between the impedance spectra of the CM-A1 sensors exposed to zero grade synthetic air (Fig 5.4) and to 350 ppm CO in air (Fig 5.6). The capacitances in both instances (Fig 5.5 and 5.7) are nearly double that of the CO-AF sensor under similar conditions. This is likely to indicate a larger specific surface area of the Pt/Ru particles.

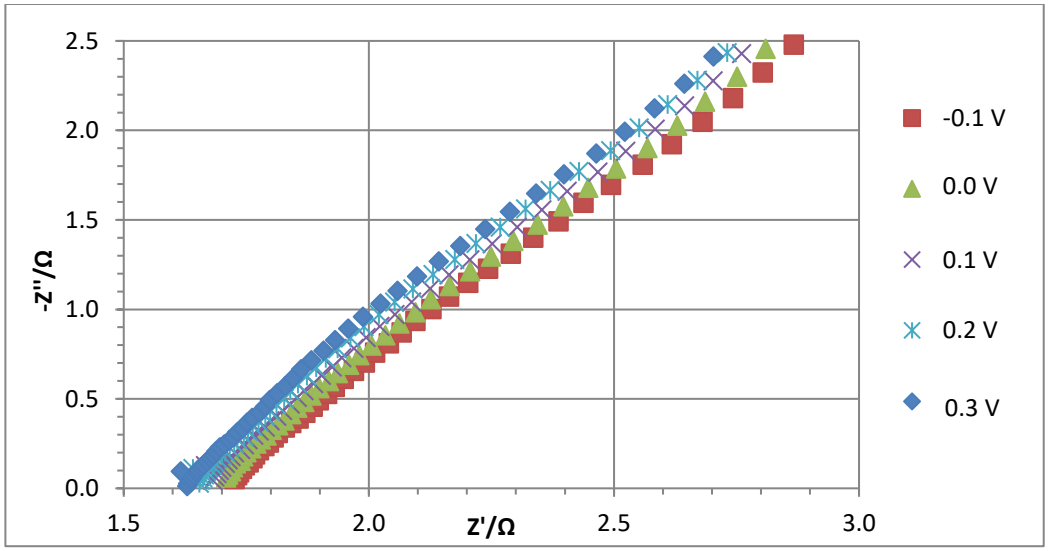

Figure 5.4: Nyquist plot of CM-A1 sensor in normal air at different steady state voltages.

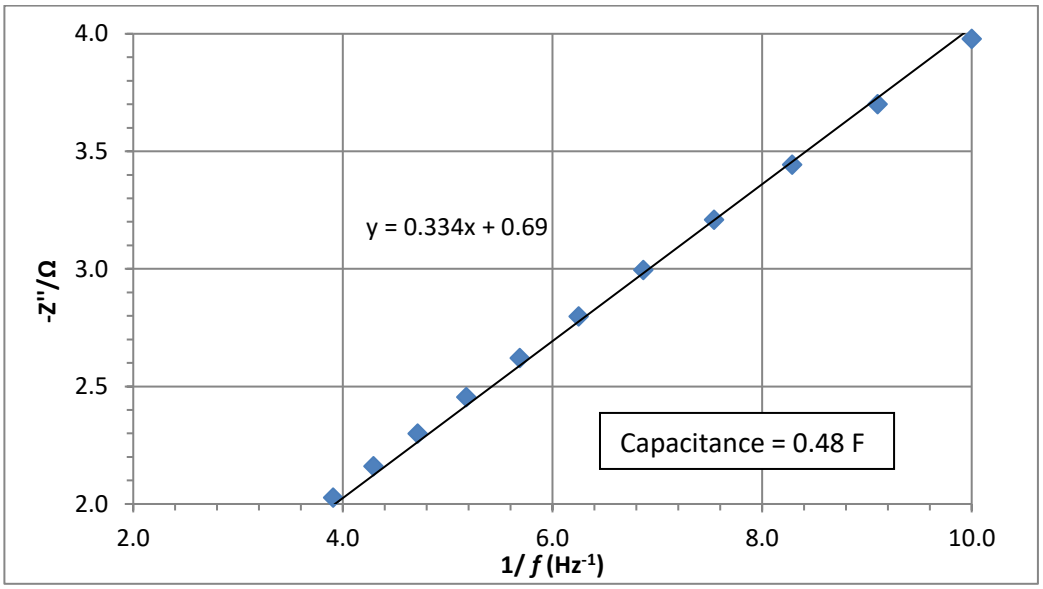

Figure 5.5: Plot of –Z" against inverse frequency of CM-A1 sensor in normal air at 0.0 V dc potential. (data taken from Fig 3.26 above)

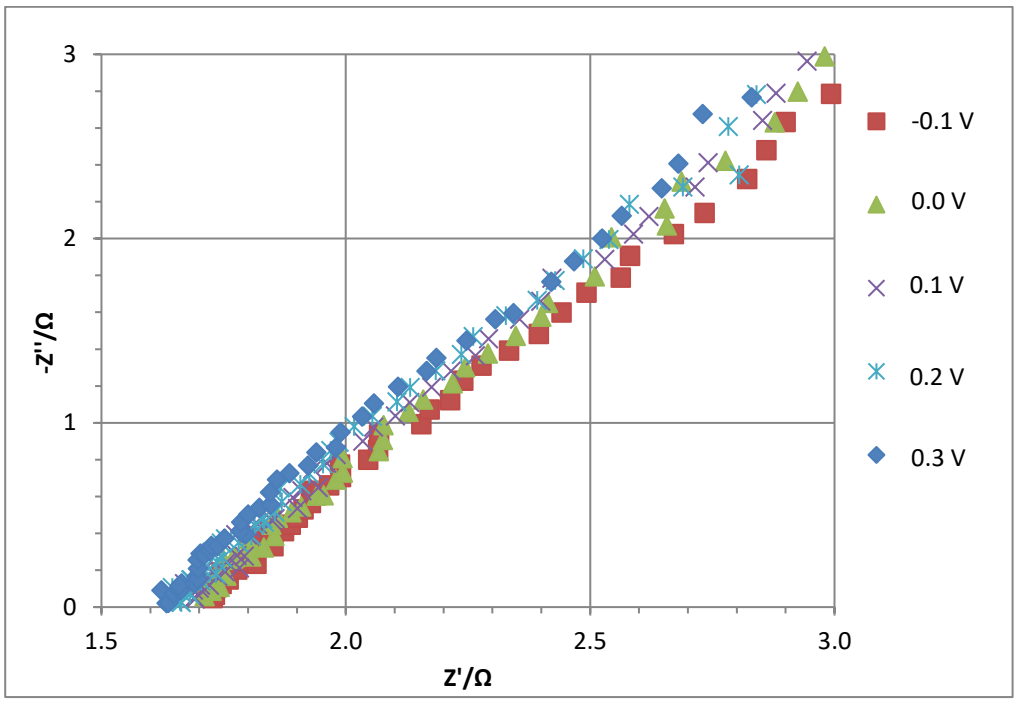

Figure 5.6: Nyquist plot of CM-A1 sensor in CO at constant gas flow rate (350 ppm) at different steady state voltages.

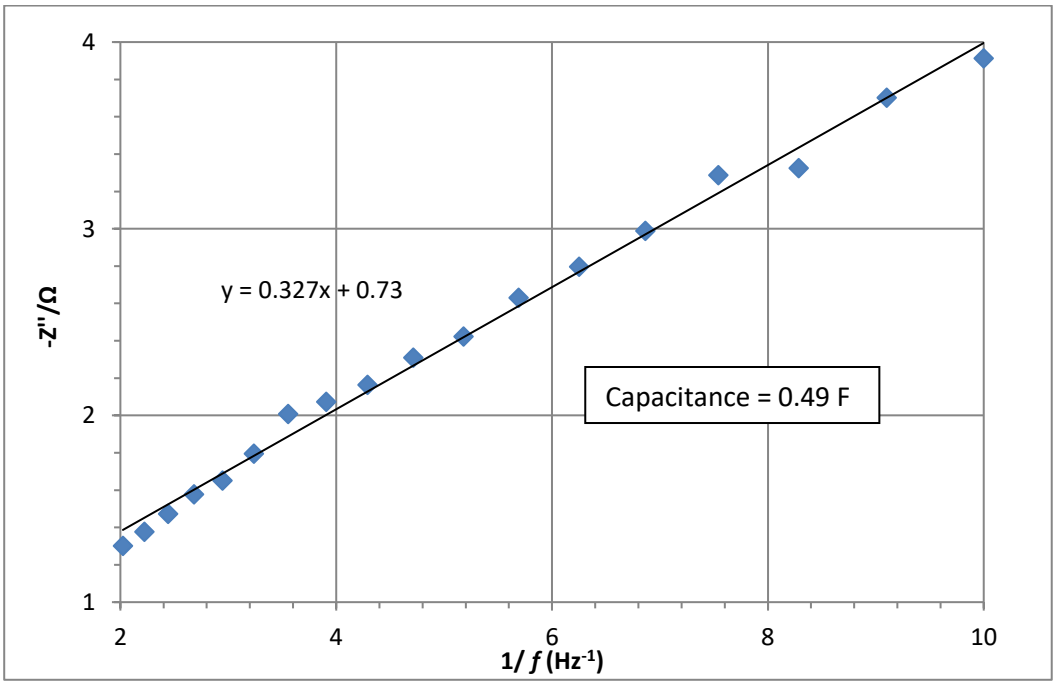

Figure 5.7: Plot of –Z" against inverse frequency of CM-A1 sensor in CO at 0.0 V dc potential. (data taken from Fig 3.28 above)

It is worth noting that the impedance spectra of figures 5.4 and 5.6 are almost identical at different dc potentials; there is no evidence of the decrease in impedance at -0.1 V observed for CO-AF devices due to the onset of oxygen reduction.

5.3 Chronoamperometry at CM-A1 Sensors

Chronoamperometric measurements on the CM-A1 sensor show a current response proportional to the concentration of CO analyte (Fig 5.8 and 5.9). This is the same characteristic as the CO-AF sensor, although it shows a worse signal to noise ratio. Essentially this is because the analytical sensitivity (slope of the signal versus analyte concentration calibration curve) is lower. The reasons for this are addressed in this chapter in the modelling of the device response in section 5.4 later. Figure 5.9 shows the calibration of a CM-A1 device. The calibration is linear over the range 100-500 ppm, but the sensitivity is 9.8 nA ppm^{-1}, which is much smaller than the corresponding sensitivity of the CO-AF device in Chapter 4 (0.1 µA ppm^{-1}).

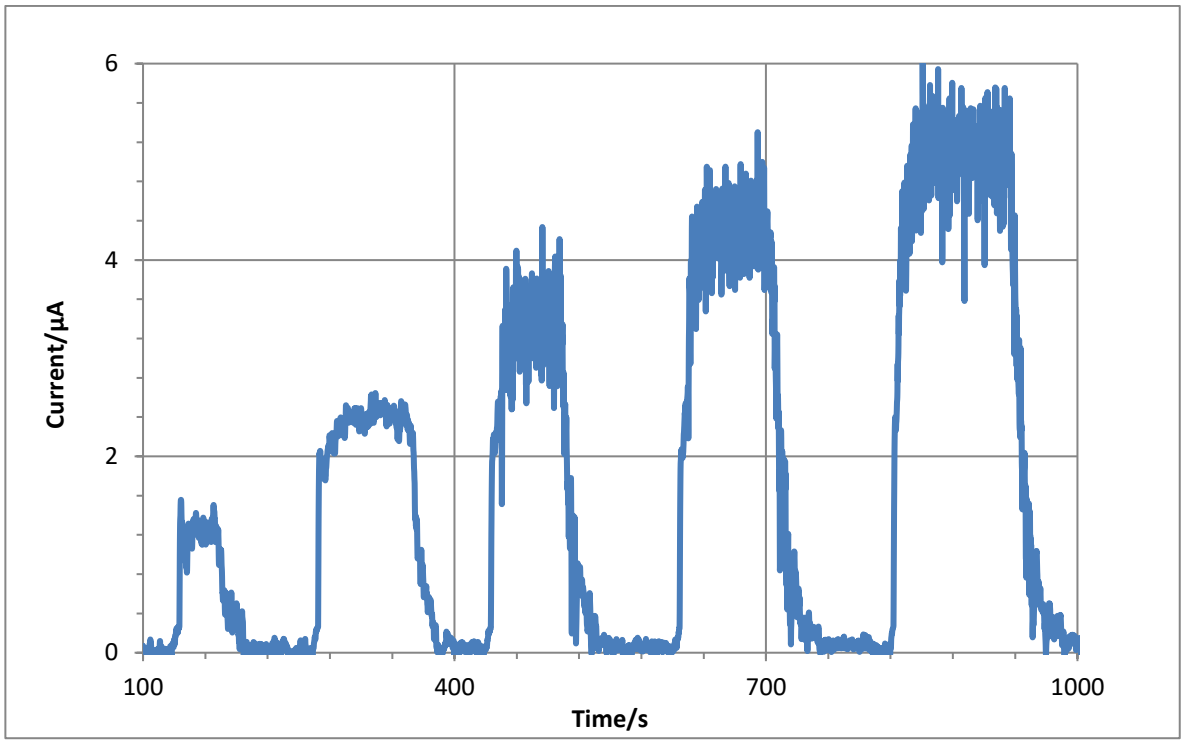

Figure 5.8: Graph showing CM-A1 sensor proportional response to pulses of increasing CO concentrations (100, 200, 300, 400, 500 ppm respectively) over time at 0.0 V steady state in 20° C

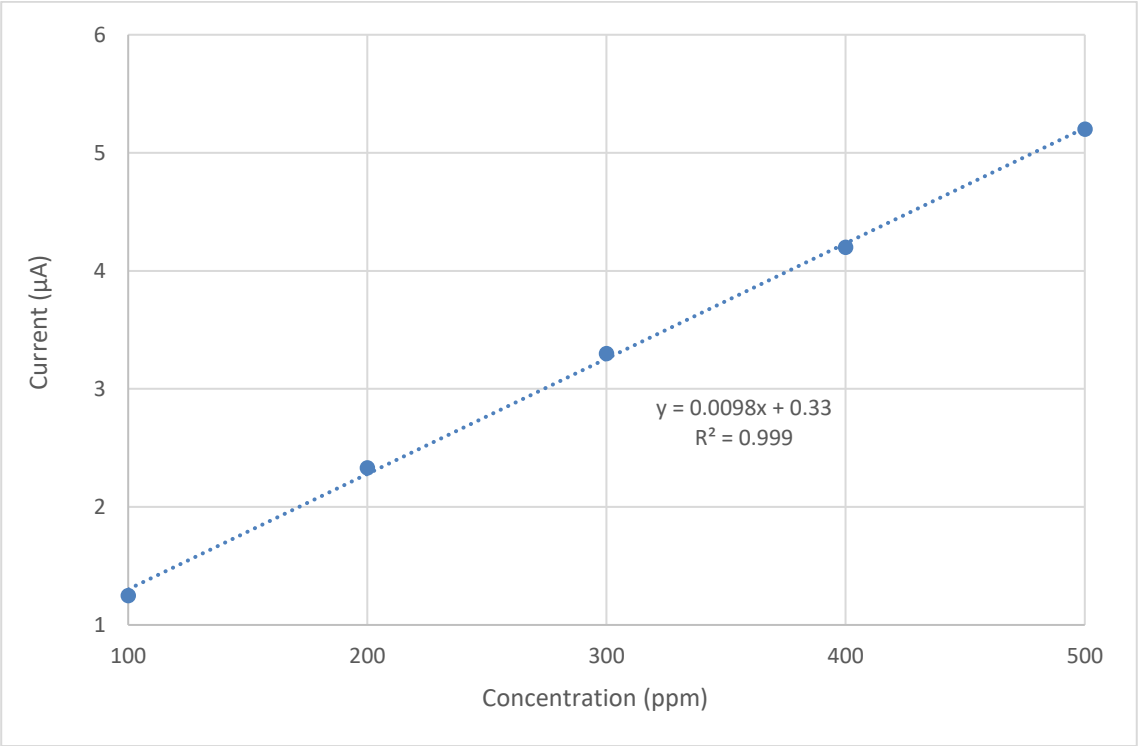

Figure 5.9: Graph showing relationship between amperometric response and CO gas concentration. (data taken from Fig 3.8 above).

5.4 Modelling the Chronoamperometric Response

The CM-A1 sensor was tested at 20° C and the analysis of the curves during chronoamperometric responses to pulses of CO are shown below. The results of the CM-A1 sensor curvature fit modelling show *L* and *D* values which indicate that the rate limiting transport process is diffusion of the CO within the liquid phase that is wetting the Pt/Ru electrode. This appear to be the origin of the different behaviour of CO-AF (gas phase diffusion dominant) and CM-A1 (liquid phase diffusion dominant) devices.

L^2/D (s)	T_0 (s)	ΔI (μA)	Steady state current (μA)
63	429	-3.34	3.37

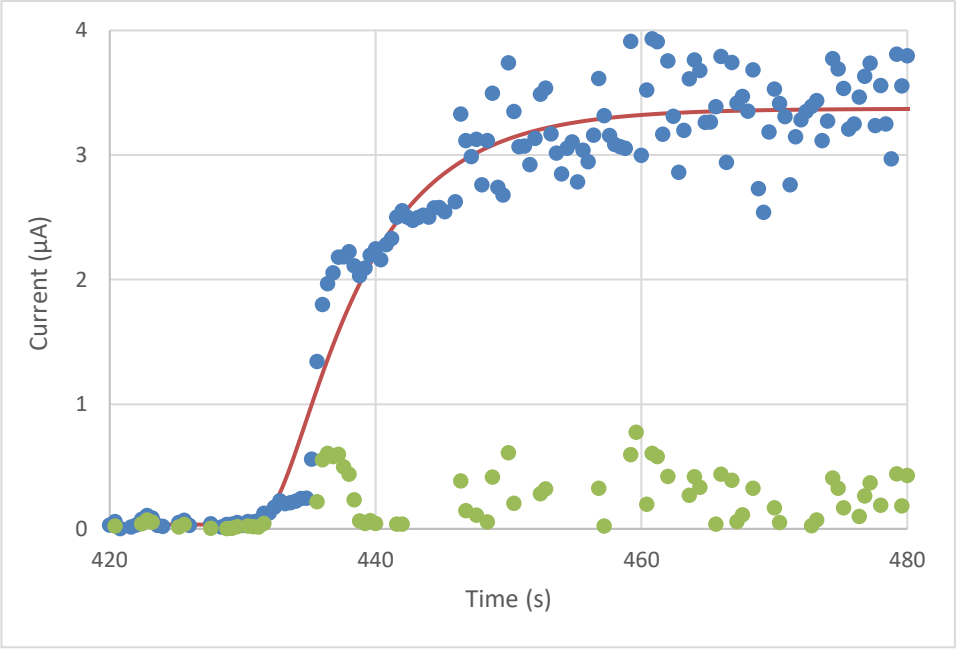

Figure 5.10: Sensor response at 0.0 V steady state in 300 ppm CO saturated air at 20° C experimental data (blue), line of best fit (red), difference between the two values (green).

L^2/D (s)	T_0 (s)	ΔI (μA)	Steady state current (μA)
58	818	-5.07	5.09

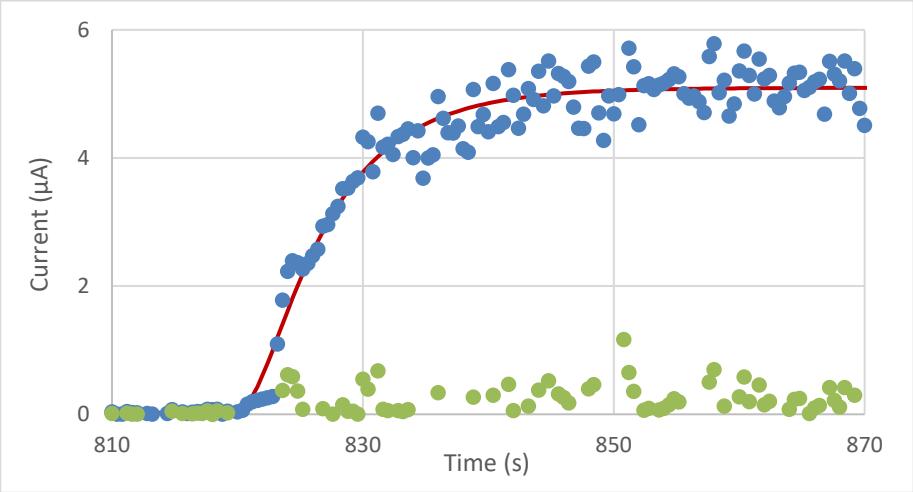

Figure 5.11: Sensor response at 0.0 V steady state in 500 ppm CO saturated air at 20° C experimental data (blue), line of best fit (red), difference between the two values (green).

L^2/D (s)	T_0 (s)	ΔI (μA)	Steady state current (μA)
88	498	3.28	0.08

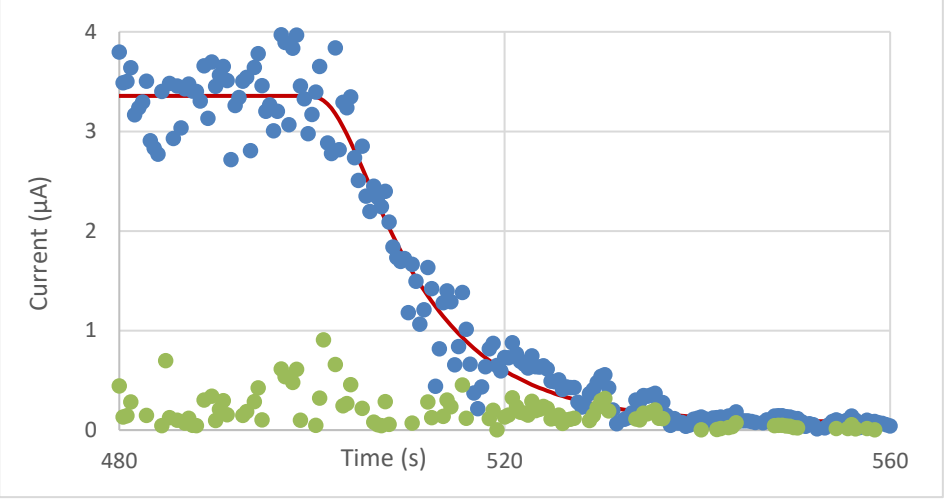

Figure 5.12: Sensor response at 0.0 V steady state after 300 ppm CO saturated air at 20° C experimental data (blue), line of best fit (red), difference between the two values (green).

Conc. (ppm)	**ΔI (μA)**	**L^2/D (s)**	**L (mm)**	**D (cm^2 s^{-1})**
100	1.19	2	0.02	1.39×10^{-6}
200	2.34	36	0.30	2.45×10^{-5}
300	3.34	63	0.49	3.85×10^{-5}
400	4.28	70	0.53	4.00×10^{-5}
500	5.07	58	0.42	2.98×10^{-5}
		Means =	0.35	2.68×10^{-5}

Table 5.1: Compiled values for CM-A1 sensor response to CO at 20°C and the effective diffusion layer thickness (*L*) and effective diffusion coefficient (*D*).

Figures 5.10 and 5.11 show typical chronoamperometric responses for a CM-A1 sensor to 300 ppm and 500 ppm CO in air. The data is somewhat noisy because the sensitivity of the CM-A1 devices is much lower than the CO-AF or CO-A1 devices and the currents are correspondingly smaller. The noise is also increased by the more rapid sampling of the current in the electrically noisy environment of the test rig where long cables between the electronics and the potentiostat are unavoidable. Nevertheless, the data can be reasonably well-described by the regression model based on a single value of effective *L* and *D* with a residual that is essentially random scatter about zero. Figure 5.12 shows the corresponding recovery data after the analyte is replaced with zero air. Again, the fit of the regression model is reasonable despite the noise. The extracted values *L* and *D* for various CM-A1 devices are collected in Table 5.1. Although the overall response time for the sensors is similar to that of the CO-AF sensors, it is clear that the effective diffusion coefficients are much smaller.

Figures 5.13 and 5.14 below indicate that a thicker than normal membrane increases the effective *L* value whilst correspondingly decreasing the *D* value in CO-AF devices. This is as expected and helped to validate the mathematical model in chapter 4. However, it can also be seen that the CM-A1 sensor has very small *L* and *D* values despite a similar construction to the CO-AF device. Thus, the rate limiting step in the CM-A1 sensor is most likely diffusion within the liquid phase of the aqueous electrolyte that covers the working electrode. This is due to the increase in aqueous layer thickness above the working electrode, which causes it to become the rate limiting step. The addition of ruthenium causes this apparent extra wetting of the working electrode. Nevertheless, the analysis of the chronoamperometric data has uncovered a basic difference in the operation of CO-AF and CM-A1 devices that cannot be deduced from measurements of the steady-state current alone. Further, the crucial importance of the wetting behaviour of the working electrode/membrane interface is apparent.

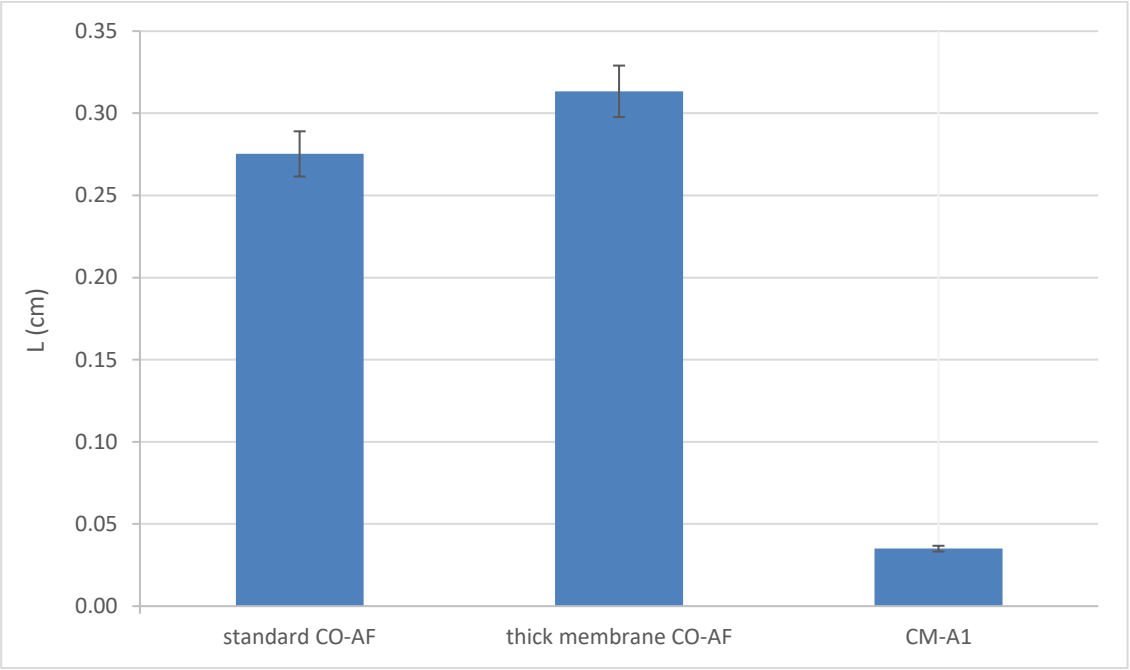

Figure 5.13: Graph of effective layer thickness (*L)* values for response to CO by various sensor types at 20° C

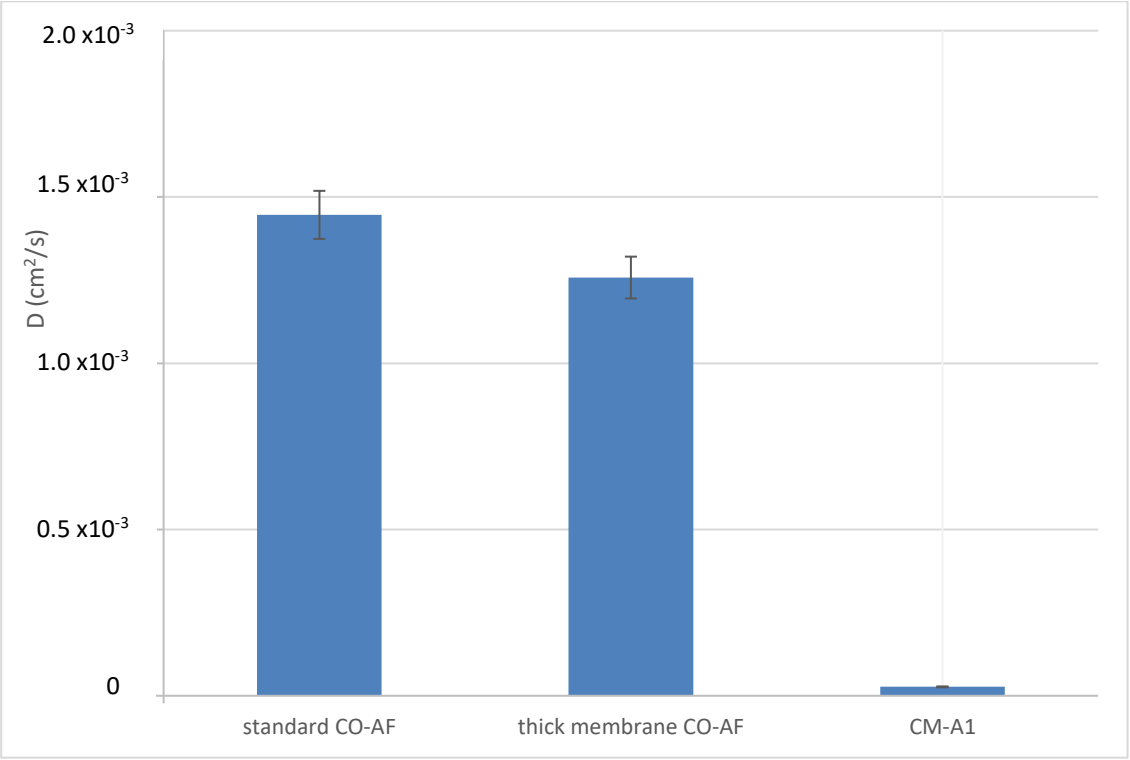

Figure 5.14: Graph of effective diffusion coefficient (*D)* values for response to CO by various sensor types at 20° C

5.5 Voltage Dependence of CM-A1 Sensors

The mathematical model (Chapter 3) applied to analyse the chronoamperometric response to a concentration change assumes that the sensor response is controlled by mass transport effects. There is a weak potential dependence of the measured currents for CM-A1 devices (Fig 5.15). However, such a small effect cannot account for the two order of magnitude difference in the effective diffusion coefficients for CO-AF (10^{-3} cm^2 s^{-1}, Chapter 4) and CM-A1 (10^{-5} cm^2 s^{-1}, Table 5.1). Instead, it is more likely that the electrolyte layer on the Pt/Ru electrode is thicker than on the pure Pt electrode. This is consistent with the decrease in overall sensitivity and the values of effective diffusion coefficient (*D*) obtained from the chronoamperometric data (Figs 5.10 – 5.12).

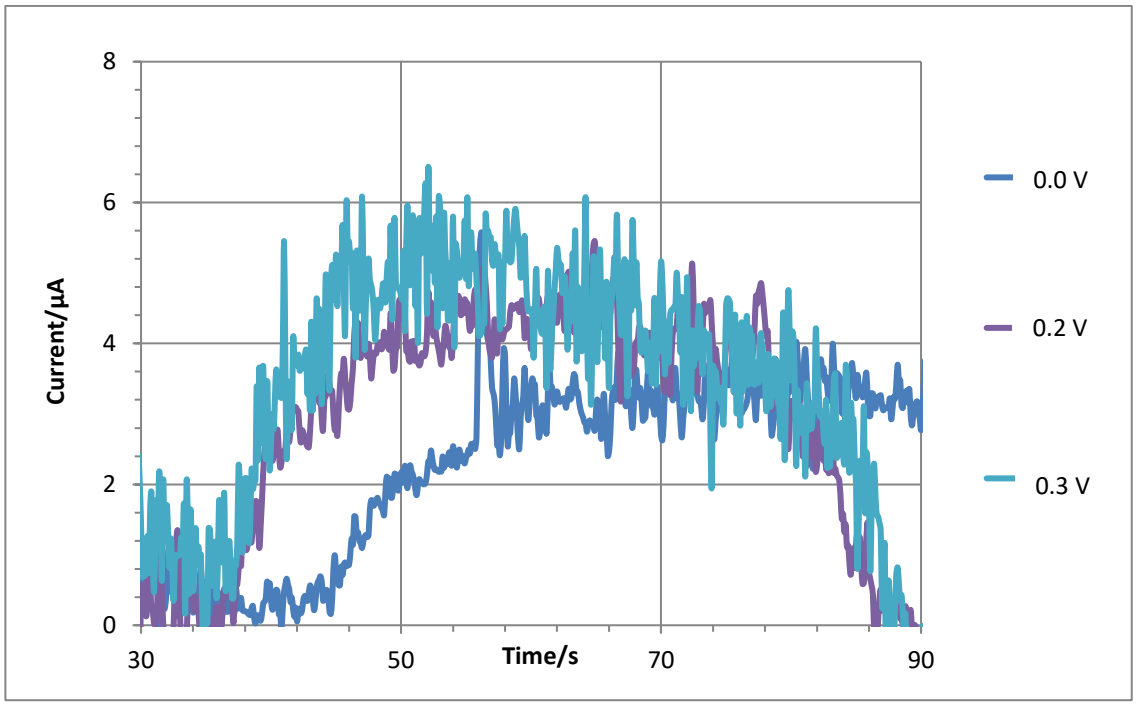

Figure 5.15: Graph showing CM-A1 sensor response to 350 ppm CO saturated air at 20° C (gas on at 40 secs and off at 60 secs).

5.6 Summary

This chapter considers the effect that changing the composition of the metal electrode has on the mass transport characteristics within the sensor. It has been shown that the use of a Pt:Ru alloy metal working electrode causes a change in the mass transport characteristics within the sensor. The current recorded during amperometric response of the CM-A1 sensor to CO gas is much smaller than that of the CO-AF sensor (which has a mono-metal Pt working electrode). The calculated capacitance for the CM-A1 sensor is approximately double that of the CO-AF sensor. This is thought to be due to the differences in sizes between the Pt and Ru nanoparticles, which causes the CM-A1 working electrode to have a larger microscopic surface area than the working electrode of the CO-AF sensor.

The calculated *L* and *D* values indicate that the rate limiting step is mass transport diffusion in the sulfuric acid electrolyte. This is in contradiction to the results from the CO-AF sensor that indicates the rate limiting step is diffusion through the silica and PTFE membrane. The difference in these results can be explained by the fact that Ru is known to be more oxophilic than Pt. This causes the electrolyte layer on the working electrode to effectively increase in thickness along the sensor stack, this phenomenon is called “flooding” and explains the difference in results as the CO analyte has farther to travel through the electrolyte in the CM-A1 sensor than the CO-AF sensor.

It is worth noting that changes to the electrocatalyst may have unintended effects (here, flooding) that are not directly connected with the expected catalytic activity of the material and may degrade the sensor performance. In summary, CM-A1 devices show an order of magnitude decrease in analytical sensitivity to CO compared to CO-AF devices. They are, like CO-AF devices, predominantly mass-transport limited, but the nature of the diffusion barrier (liquid phase) is different to that in the CO-AF (gas phase). Finally, penetration of the porous membrane by the electrolyte is clearly very undesirable for sensor performance.

5.7 References

[139] Q. Ge, S. Desai, M. Neurock, K. Kourtakis
J. Phys. Chem. B, 2001, **105**, 9533-9536

[140] P-Y. Olu, T. Ohnishi, D. Mochizuki, W. Sugimoto
J. Electroanal. Chem., 2018, **810**, 109-118

[141] W. F. Lin, M. S. Zei, M. Eiswirth, G. Ertl, T. Iwasita, W. Vielstich
J. Phys. Chem. B, 1999, **103**, 6968-6977

[142] M. S. Chen, Y. Cai, Z. Yan, K. K. Gath, S. Axnanda, D. W. Goodman
Surface Science, 2007, **601**, 5326-5331

[143] J. K. Norskov, L. Rossmeis, A. Logadotir, L. Lindqvist, J. R. Kitchin, T. Bligaard
J. Phys. Chem. B, 2004, **108**, 17886-17892

[144] U. A. Paulus, A. Wokaun, G. Scherer, T. Schmidt, V. Stamenkovic, N. M. Markovic, P. N. Ross
Electrochimica Acta, 2002, **47**, 3787-3798

[145] A. Oliveira Neto, M. J. Giz, J. Perez, E. A. Ticianelli, E. R. Gonzalez
J. Electrochem. Soc., 2002, **149**, 272-279

[146] F. H. B. Lima, E. R. Gonzalez
Electrochimica Acta, 2008, **53**, 2963-2971

[147] J. Corchado-Garcia, C. Morais, N. Alonso-Vante, C. R. Cabrera
J. Electroanal. Chem., 2017, **799**, 228-234

[148] A. B. Delpeuch, F. Maillard, M. Chatenet, P. Soudant, C. Cremers
Applied Catalysis B: Environmental, 2016, **181**, 672-680

Chapter 6

6.0 CO-A1 Sensor Response to Carbon Monoxide

The standard CO-AF sensor is constructed with the intention of filtering out unwanted gaseous species that may poison the Pt working electrode or give a false positive reading during chronoamperometry. This is achieved by the addition of a potassium permanganate powder impregnated onto a silica support structure, which oxidises unwanted species (principally thiols and other sulphur-containing gases that may be present in some industrial applications) that would otherwise undermine the performance of the sensor. Nevertheless, it may constitute a substantial portion of the diffusion barrier to the analyte in the device. In order to investigate the effect of the permanganate powder on the diffusion rate and mass transport characteristics of the CO through the sensor, the permanganate powder was removed from the sensor during production. This batch of sensors was referred to as CO-A1 sensors.

6.1 Cyclic Voltammetry of CO-A1 Sensors

The response of the CO-A1 sensor to CO gas is shown below (Fig 6.1). It can be seen that the response is very similar to the cyclic voltammogram under zero grade air, even at slow scan rates. This is quite expected on the basis of the data for CO-AF sensors in chapter 4. Again, it rules out cyclic voltammetry as a suitable technique for analysis of the device response.

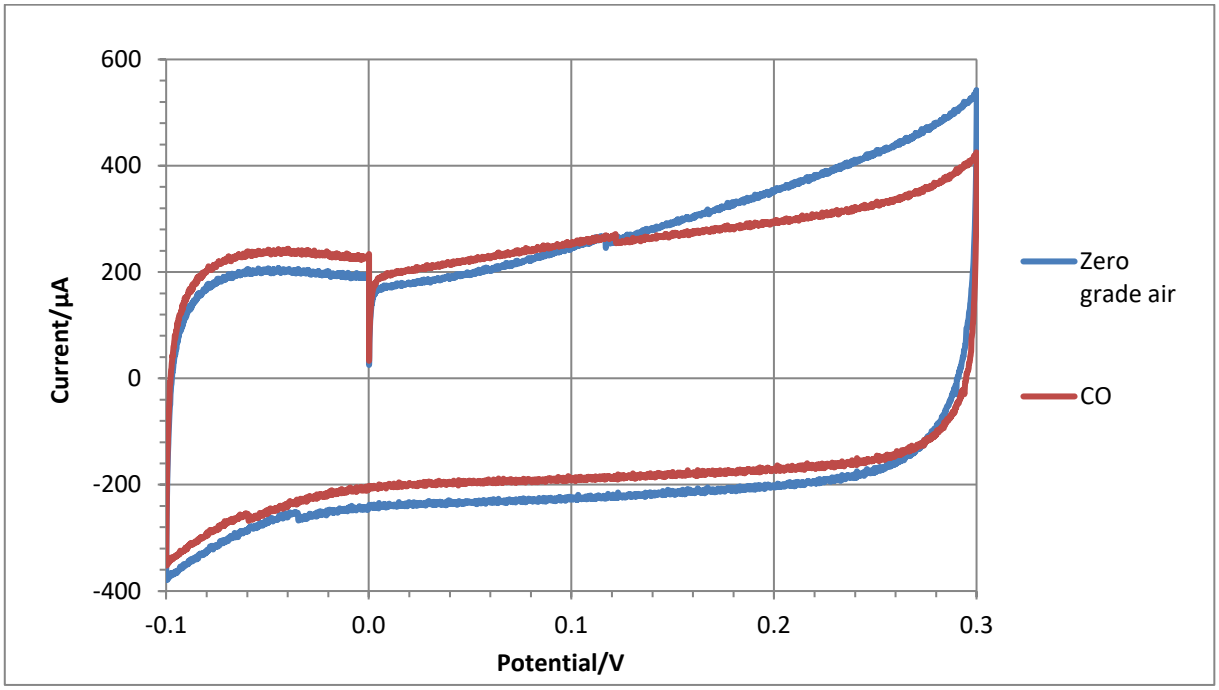

Figure 6.1: Cyclic voltammogram of CO-A1 sensor response to CO (1000 ppm) and zero grade air. Scan rate 1 mV s^{-1} and the starting potential was 0.0 V, the usual operating potential of the device.

6.2 Impedance Spectroscopy of CO-A1 Sensors

The same parameters as before were used for the impedance spectroscopy measurements in order to enable comparison of the results between the three different types of sensors. The Nyquist plots of the CO-A1 sensor impedance spectra under zero grade air (Fig 6.2) and CO (Fig 6.4) show similar features to the CO-AF sensor. As expected, the capacitance in zero grade air (Fig 6.3) and CO (Fig 6.5) is similar to that of the equivalent CO-AF sensor. The impedance spectra are almost potential-independent, except for the spectrum at -0.1 V which shows evidence of the influence of oxygen reduction at Pt.

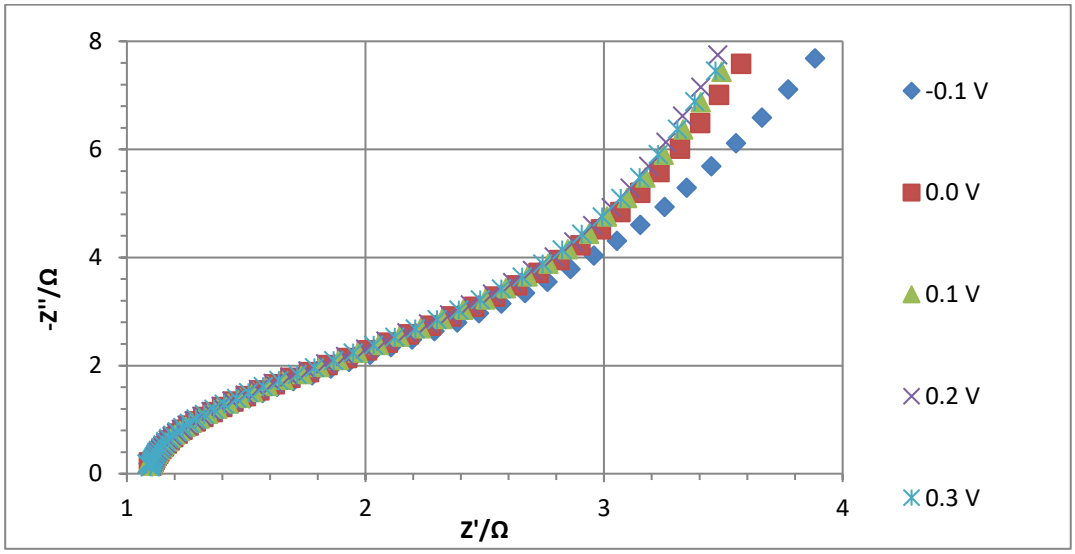

Figure 6.2: Nyquist plot of CO-A1 sensor response to zero grade air at different steady state voltages.

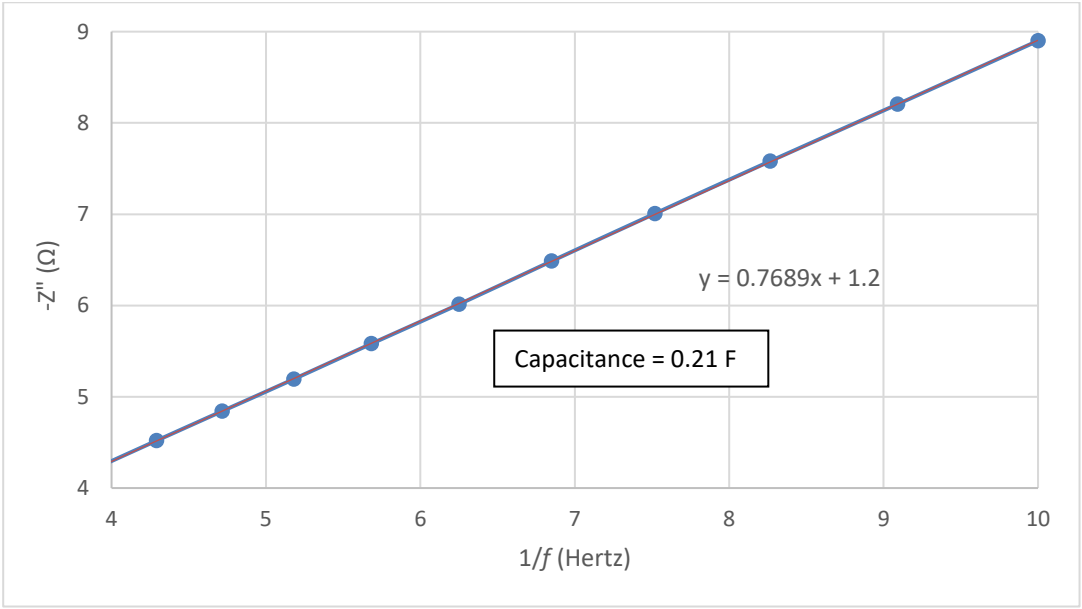

Figure 6.3: Plot of -Z" against inverse frequency of CO-A1 sensor in zero grade air at 0.0 V steady state.

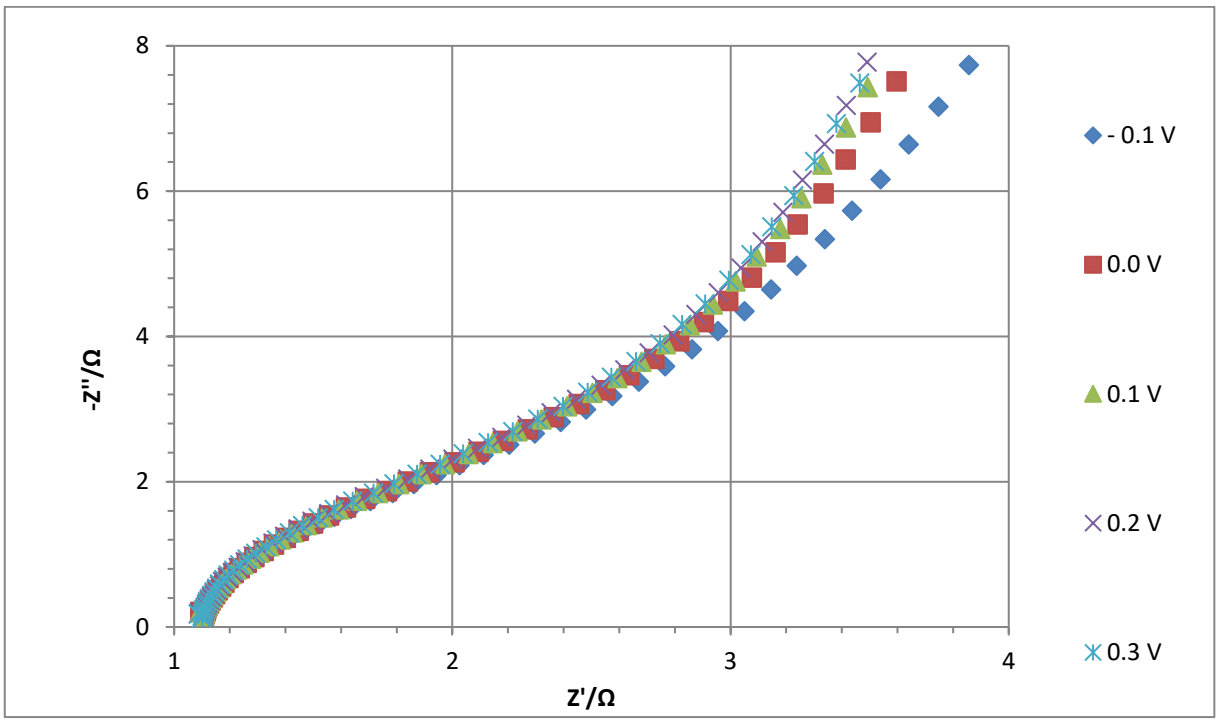

Figure 6.4: Nyquist plot of CO-A1 sensor response to CO at different steady state voltages.

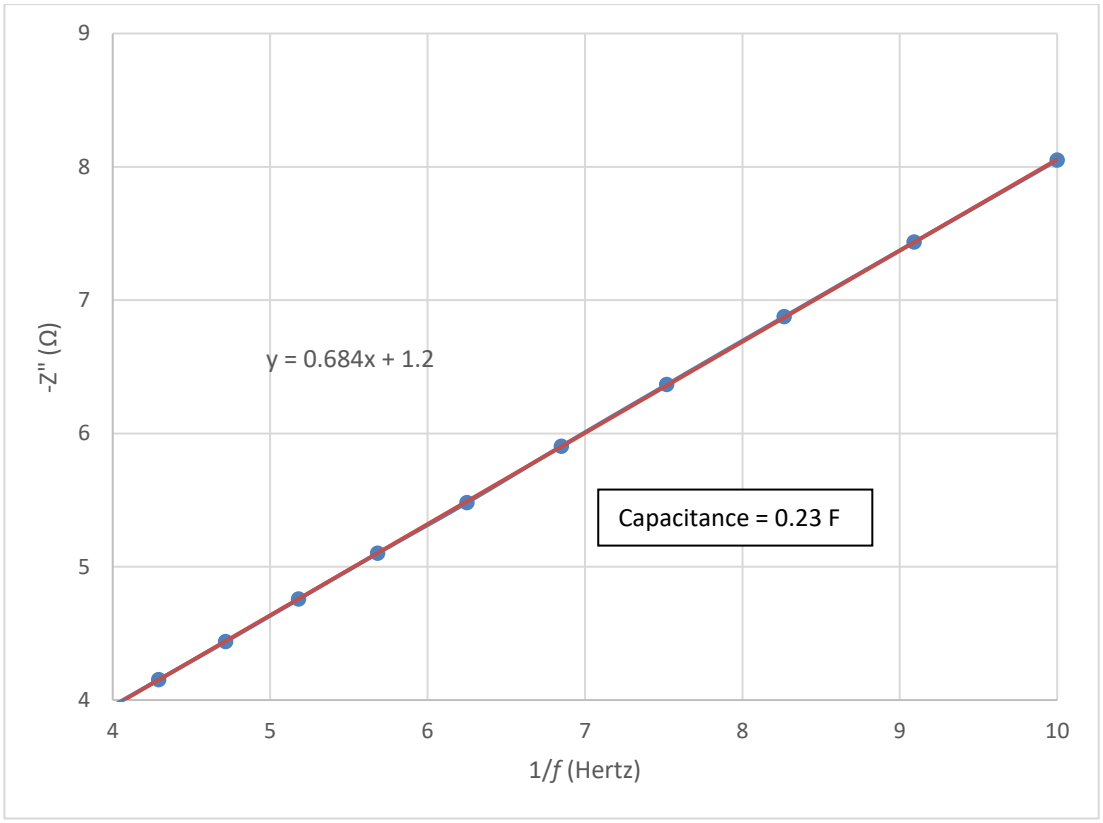

Figure 6.5: Plot of -Z" against inverse frequency of CO-A1 sensor in zero grade air at 0.0 V steady state.

6.3 Chronoamperometry at CO-A1 Sensors

The response of the CO-A1 sensor to CO during chronoamperometry (Fig 6.6) has the same characteristic shape as the CO-AF and CM-A1 sensor devices. It is also shown to give a current response proportional to increasing CO concentrations (Fig 6.7). The analytical sensitivity of this particular device is 8.2 x 10^{-2} µA ppm^{-1} is slightly smaller than that of the CO-AF device data displayed in chapter 4 (1.17 x 10^{-1} µA ppm^{-1}), however, this is typical of the batch-to-batch variation of the devices (*Alphasense data sheet: CO-AF, www.alphasense.com/ /index.php/ safety/downloads*). It is much larger than the sensitivity of the CM-A1 devices of chapter 5 (9.8 x 10^{-3} µA ppm^{-1}).

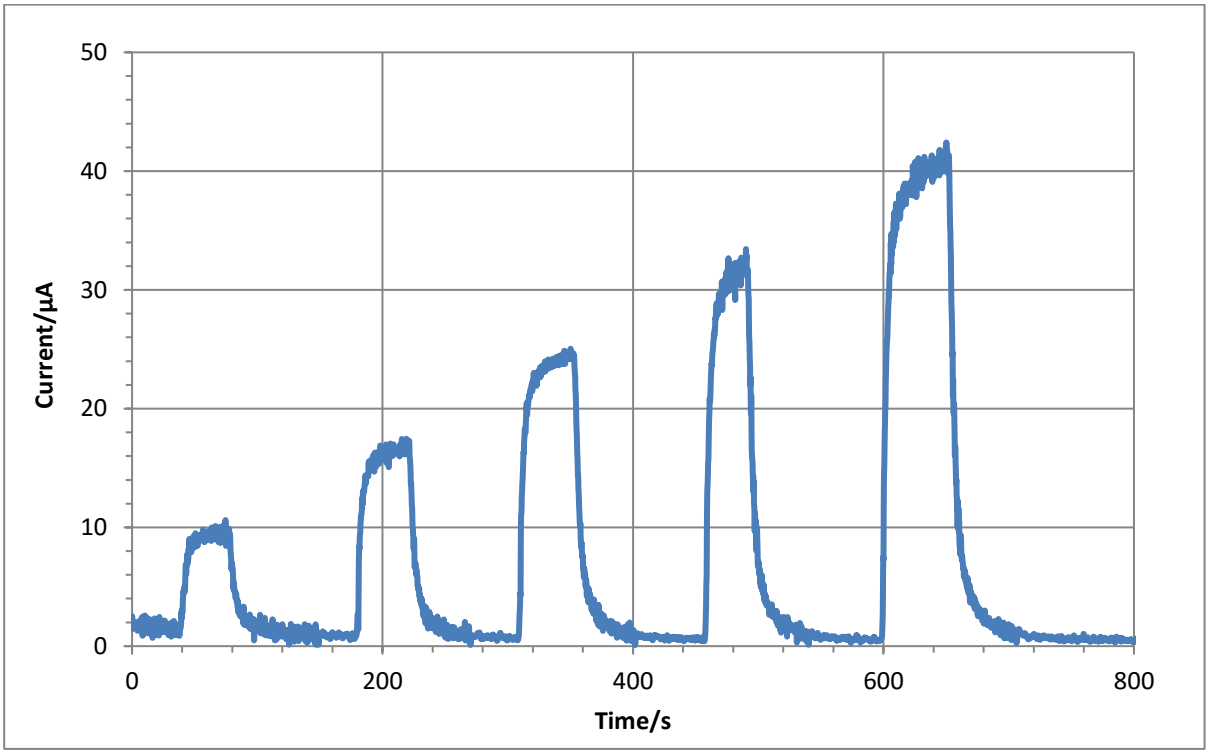

Figure 6.6: Graph showing CO-A1 sensor chronoamperometric response to increasing CO concentrations (100, 200, 300, 400, 500 ppm respectively).

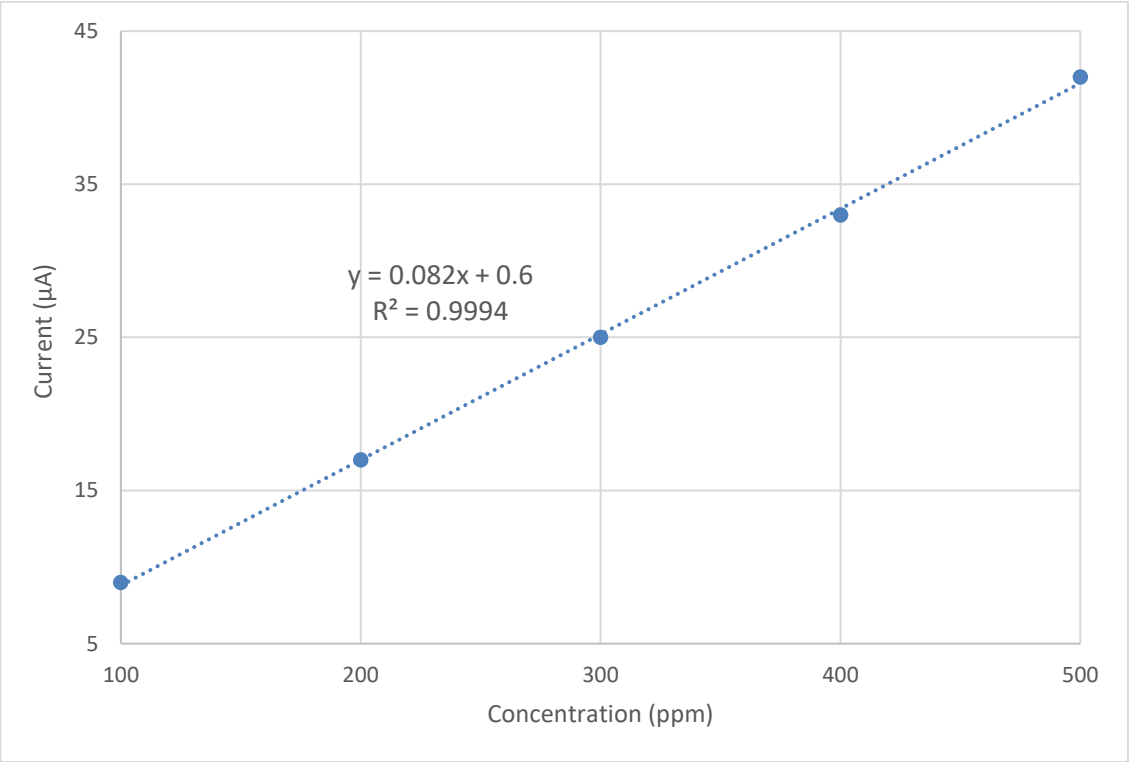

Figure 6.7: Calibration plot showing the relationship between CO-A1 current response and CO concentration over the range 100-500 ppm CO in air.

6.4 Modelling the Chronoamperometric Response of CO-A1 Sensors

The CO-A1 sensor was tested for its response during chronoamperometry to CO at 20 °C at 0.0 V applied dc potential and the mathematical model of chapter 3 was applied to the current pulses. The results suggest that the rate determining step is diffusion in the gas phase, because the *D* values are approximately 0.2 cm^2s^{-1} which is commensurate with CO diffusion in the gas phase. The graphs (Figs 6.11 and 6.12) suggest that the silica support for the permanganate powder is the biggest influence on the CO diffusion rate, due to the *L* values being on the order of 0.9 cm which is nearly the 1.6 cm physical length of the sensor.

Conc. (ppm)	**ΔI (μA)**	**L^2/D (s)**	**L (cm)**	**D (cm^2 s^{-1})**
100	7.82	34	0.91	0.25
200	15.3	30	0.79	0.21
300	23.0	31	0.82	0.21
400	30.3	32	0.83	0.22
500	39.1	37	0.99	0.27
		Means =	0.87	0.23

Table 6.1: Compiled values for CO-A1 sensor response to CO gas.

L^2/D (s)	T_0 (s)	ΔI (μA)	Steady state current (μA)
34	37	7.82	9.36

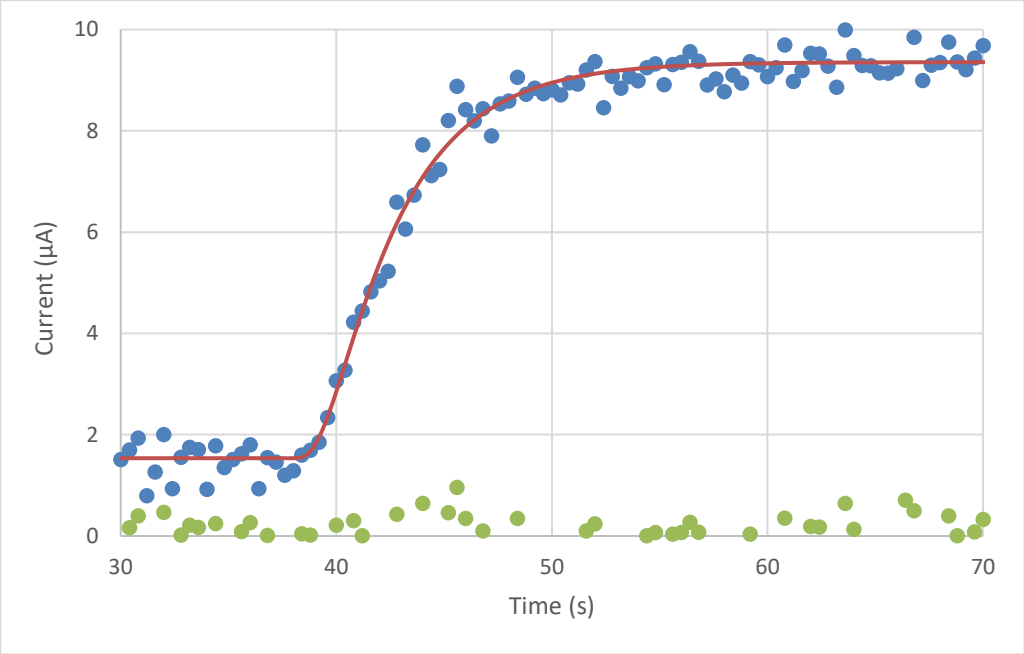

Figure 6.8: Sensor response of CO-A1 sensor to 100 ppm CO saturated air.

L^2/D (s)	T_0 (s)	ΔI (μA)	Steady state current (μA)
31	307	23.0	23.7

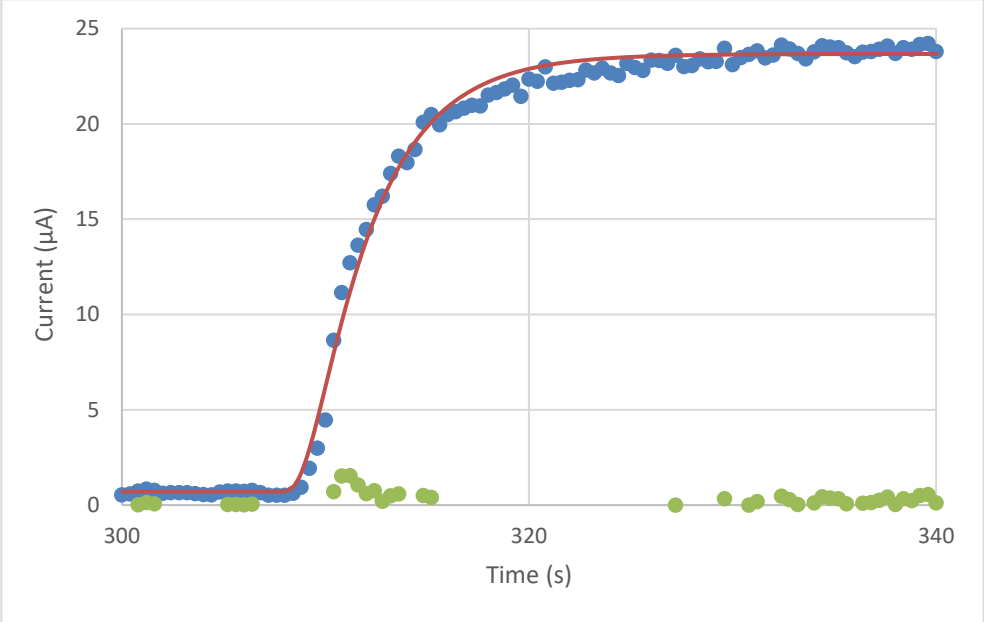

Figure 6.9: CO-A1 sensor response to 300 ppm CO saturated air.

L^2/D (s)	T_0 (s)	ΔI (μA)	Steady state current (μA)
54	349	23.4	0.99

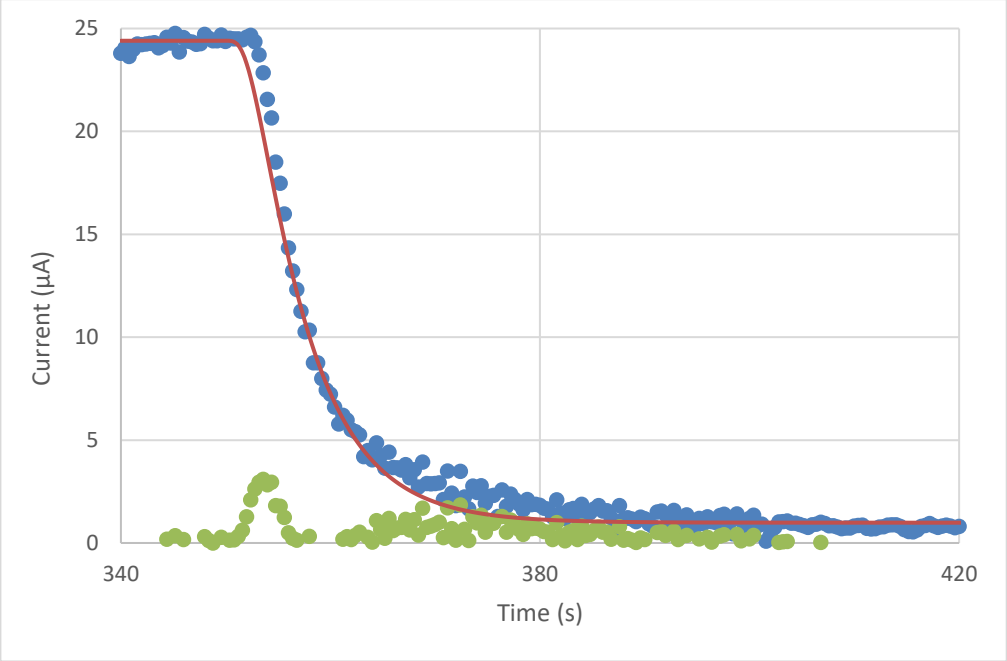

Figure 6.10: CO-A1 sensor response after 300 ppm CO saturated air.

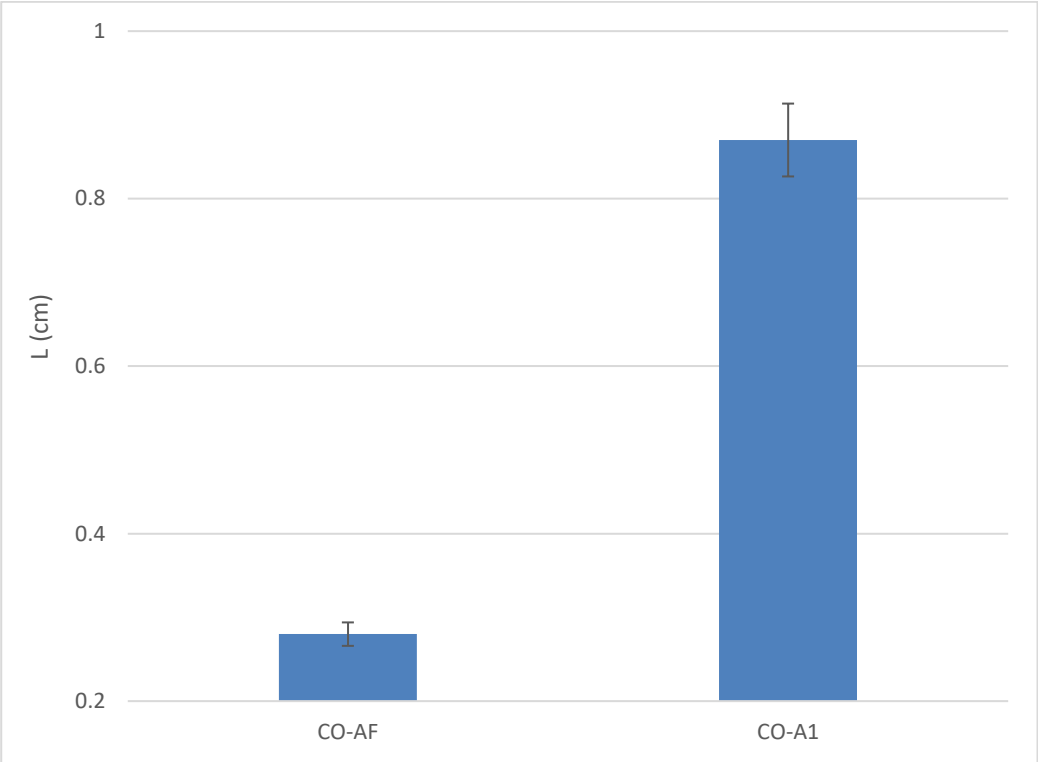

Figure 6.11: Graph of *L* values for sensor response to CO with and without silica supported permanganate powder.

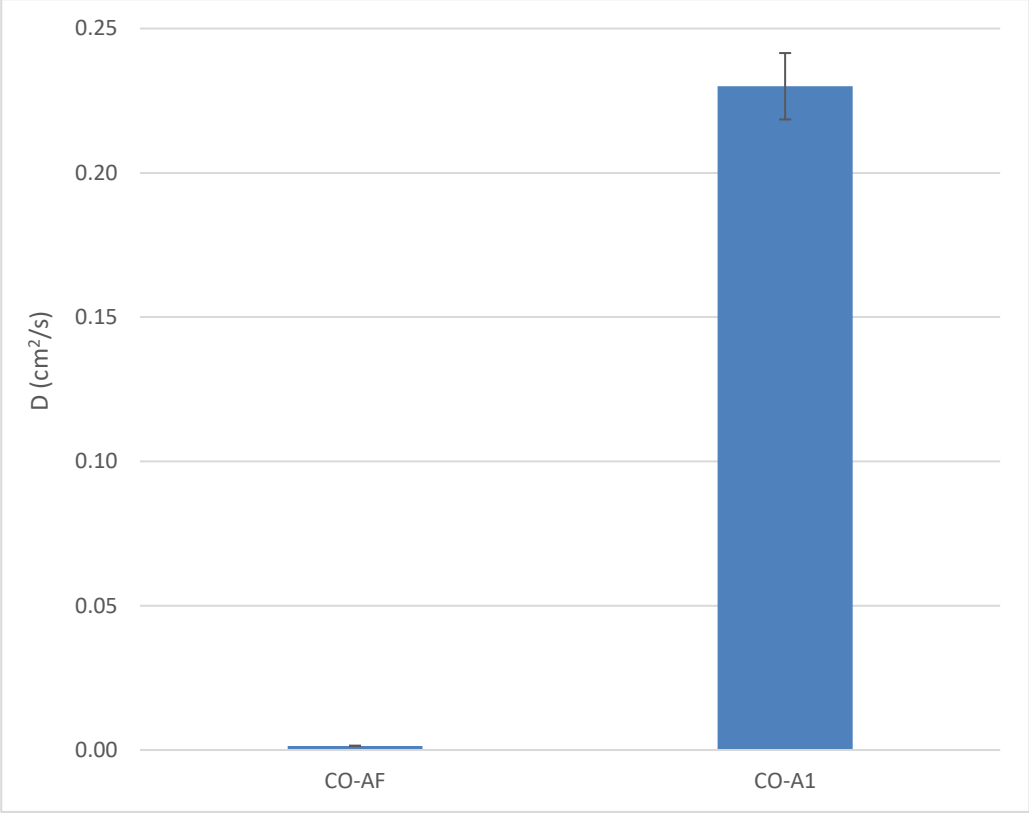

Figure 6.12: Graph of *D* values for sensor response to CO with and without silica supported permanganate powder.

The mean effective diffusion coefficient for CO obtained from the analysis (0.23 cm^2 s^{-1}) is now of precisely the order of magnitude expected for a small molecule in the gas phase. In fact, the reported diffusion coefficient of CO in air is 0.208 cm^2 s^{-1} and the data from the sensor is in good agreement with this [149]. This result suggests also that the filter layer of the CO-AF devices is a very substantial contribution to the overall mass transport barrier.

6.5 Voltage Dependence of CO-A1 Sensor

The CO-A1 sensor was investigated for evidence of current response to CO being independent of steady state voltage applied during chronoamperometry. The graph (Fig 6.13) shows that the magnitude of current recorded as amperometric response to a pulse of CO gas, does not change depending upon the voltage applied during chronoamperometry. This also suggests that at these voltages the current is limited by the mass transfer rate of the analyte through the sensor to the working Pt metal electrode. Thus, the reaction kinetics at the electrode surface are much faster than the mass transfer rate. This is in accordance with the results obtained for the CO-AF sensor response to CO at different dc potentials.

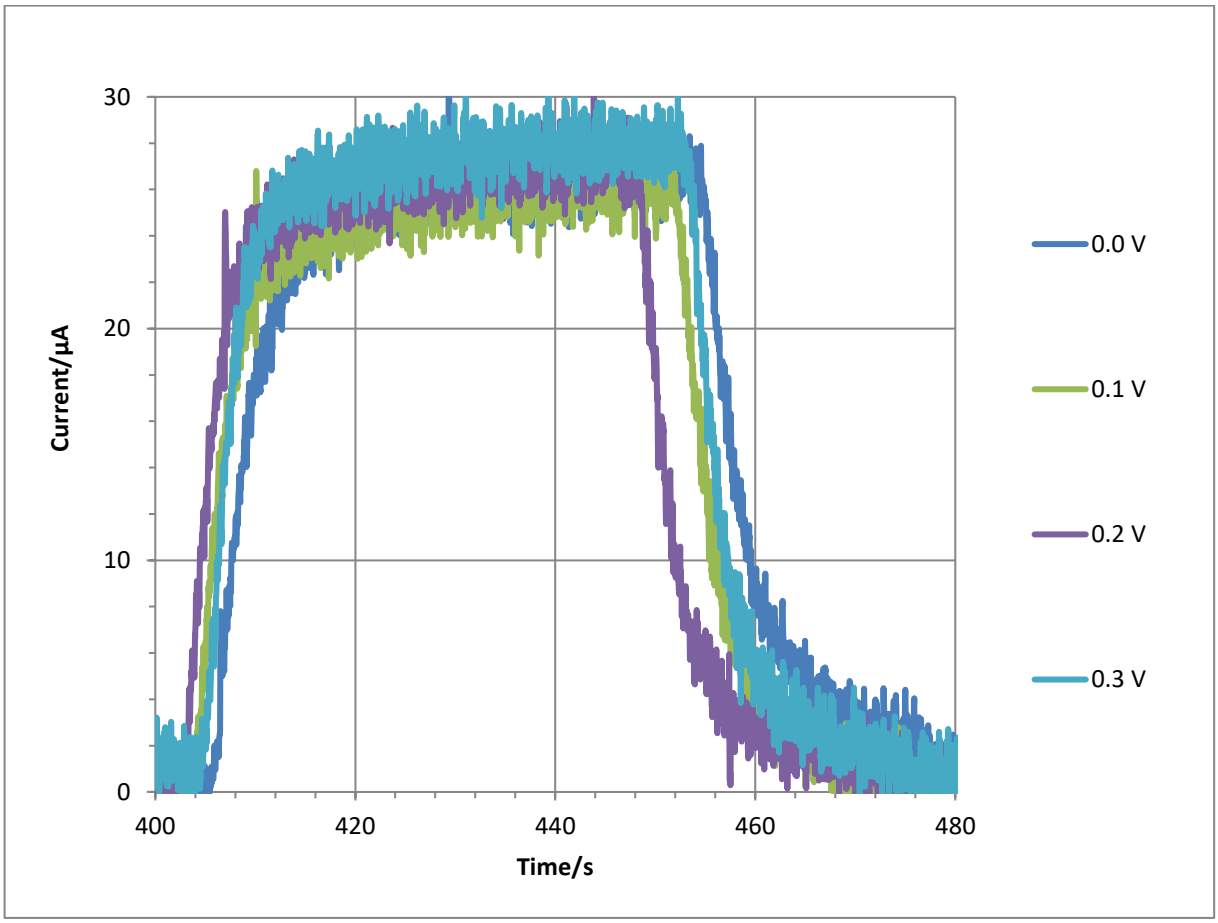

Figure 6.13: Graph showing CO-A1 sensor response to 320 ppm CO at different steady state voltages.

6.6 Summary

All three sensors (CO-AF, CO-A1, CM-A1) gave chronoamperometric responses to CO gas, with a proportional increase in current as the CO concentration increased. The increase of membrane thickness for CO-AF sensors resulted in an increase in the effective *L* values as expected and helped to validate the regression model based on an effective *L* and *D* for the whole sensor. The values of *L* for the standard and thick membrane CO-AF sensors are in the order of 0.3 cm but increases to 0.9 cm for the CO-A1 devices which do not contain the permanganate/silica filter layer. The large increase in capacitance that comes from the addition of Ru (0.48 F in CM-A1 compared to 0.26 F for pure Pt in CO-AF and CO-A1) in the CM-A1 devices is probably a result of a greater specific surface area for the Pt/Ru nanoparticles. Analysis of the chronoamperometric response of the sensors indicates that diffusion within the liquid phase (5 M H_2SO_4) becomes rate-limiting for Pt/Ru electrodes (*D* values of order 10^{-5} cm^2 s^{-1}) instead of diffusion within the gaseous phase, which is rate limiting for pure Pt electrodes (*D* values of order 10^{-3} cm^2 s^{-1} for CO-AF and 10^{-1} cm^2 s^{-1} for CO-A1).

The fact that adding ruthenium into the platinum electrode caused a marked decrease in sensitivity to CO and subsequent large decrease in *L* and *D* shows that overall the amperometric sensor is affected by the electrode material. At first glance it is surprising that the nature of the catalyst (electrode) can affect current which is controlled by a diffusion process, but it is worthwhile to note that the thickness of the liquid electrolyte on the working electrode will be controlled by the wetting behaviour of the electrode. The nanoparticles of the working electrode are hot-pressed into the PTFE gas membrane during manufacture and the optical images show that they comprise a thin layer (thickness about 42 µm) at the base of the membrane. The membrane is hydrophobic, and the electrolyte does not ordinarily penetrate deep into the membrane, but this is possible in the metallised layer where the hydrophobicity may be different. Such 'flooding' of the membrane by electrolyte is undesirable because the diffusion coefficients in liquid are of order 10^{-5} cm^2 s^{-1}, much less than in the gaseous phase. Both the effective diffusion coefficient *D* and the effective thickness *L* decrease strongly, but the former effect outweighs the latter.

In the CM-A1 devices, *L* decreases (compared to the standard CO-AF sensor) to reflect the layer thickness (0.35 mm) of the liquid above the metal working electrode. The net effect is to decrease the analytical sensitivity of the device. The observation that the *D* value for the CO-A1 sensor was commensurate with CO diffusion in the gas phase (0.23 cm^2s^{-1}) whilst the CO-AF sensor gave a *D* value of 10^{-3} cm^2s^{-1} indicates that the silica supported permanganate powder has a substantial effect on the diffusion rate within the sensor, since the removal of the powder changes the *D* values so much and the *D* value for CO-A1 is so close to CO in air under ambient conditions (Fig. 6.12). In this case, the PTFE semi-permeable membrane and liquid electrolyte have barely any effect on the overall current produced by the CO-A1 devices.

Finally, the temperature dependence of the effective diffusion coefficients for CO-AF devices is consistent with gas-phase diffusion in which a weak power-law temperature dependence is expected rather than the Arrhenius-type of temperature dependence for liquid-phase diffusion [149]. This is also an important factor for device performance because the sensors must operate over a wide temperature range (-30 to +50 ^oC is the manufacturer specification, *www.alphasense.com//index.php/safety/downloads*).

[149] E. N. Fuller, P. D. Schettler, J. C. Giddings
Ind. Eng. Chem., 1966, **58**, 18-27

Chapter 7

7.0 VOC Detection

In the previous chapters it was shown that a diffusion-based model was capable of describing the amperometric response of the CO-AF sensor to CO gas. The effect of replacing part of the Pt in the working electrode with Ru (CM-A1 sensor) or of omitting the silica/$KMnO_4$ filter layer of the CO-AF sensors was also investigated. All this work concerned the device response to CO; this chapter is focused on using the same model to describe the amperometric response of CO-A1 sensors to the electrooxidation of volatile organic compounds (VOCs). In principle the Pt working electrode ought to be able to oxidise a range of VOCs and the aim was therefore to develop an amperometric gas sensor for organic vapours.

The standard sensor construction (CO-AF) employs an oxidising filter layer at the top of the stack which is designed to remove certain reducing gases (e.g. H_2S) that can poison the electrocatalysts and interfere with the response of the device to the analyte [150, 151]. Normally, this filter destroys H_2S (an important catalytic poison for CO sensors) via oxidation by the $KMnO_4$/silica powder. This filter layer is however not suitable for a VOC sensor because the oxidant, MnO_4^- , will react with many analytes of interest. In order to detect VOCs the $KMnO_4$/silica filter of a CO-AF sensor was removed from the production line during assembly of a batch of CO-AF sensors (Fig 7.1). These sensors were designated CO-A1 sensors (as previously described in chapter 6).

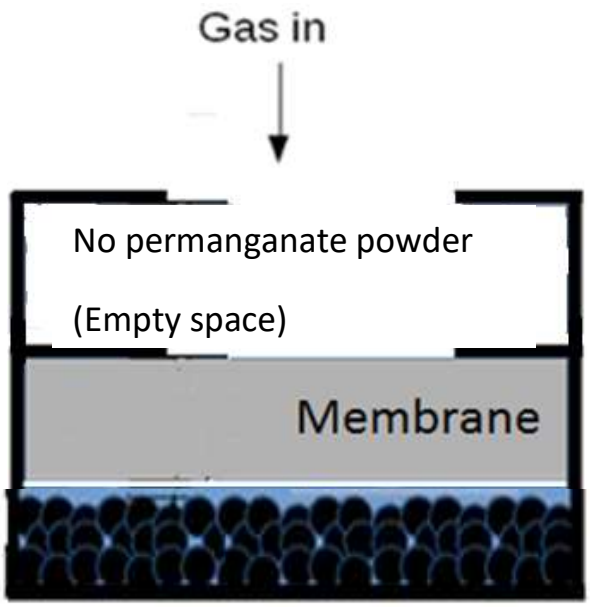

Figure 7.1: Schematic of CO-A1 sensor working electrode. The working electrode platinum particles are shown at the bottom of the diagram and the thickness of the electrolyte layer (blue) is exaggerated for diagrammatic clarity.

7.1 Electrooxidation of VOCs

It is known that alcohols (and some other VOCs) undergo electrooxidation in sulfuric acid solution [152 - 155]; the CO-A1 sensors were therefore used to attempt to detect a range of VOCs with various functional groups containing a carbon oxygen bond. An example of the complete electrooxidation reaction of a primary alcohol at a Pt electrode is shown below (Eqn 7.1).

$$CH_3CH_2OH + 3H_2O \longrightarrow 2CO_2 + 12H^+ + 12e^- \quad (7.1)$$

The actual mechanism is of course complex; however the first steps involve oxidation of the alcohol group and later steps require the breaking of C-C bonds. Owing to the relatively mild conditions of the experiments (< 50 °C) it was expected that the reaction does not go to completion and stops after the formation of ethanoic acid (Eqn 7.2). This is because the thermal energy available is insufficient to initiate the C-C bond cleavage within the alcohol [156, 157].

$$CH_3CH_2OH + H_2O \longrightarrow CH_3COOH + 4H^+ + 4e^- \quad (7.2)$$

The mechanism of alcohol oxidation involves strong interactions of the intermediates with the metal surface. An outline of the relevant parts of the mechanism [158] are given below (Eqns 7.3-7.7):

$$Pt + CH_3CH_2OH \longrightarrow Pt\text{-}CH(OH)CH_3 + H^+ + e^- \quad (7.3)$$

$$Pt\text{-}CH(OH)CH_3 \longrightarrow Pt\text{-}CHOCH_3 + H^+ + e^- \quad (7.4)$$

$$Pt\text{-}CHOCH_3 \longrightarrow Pt\text{-}COCH_3 + H^+ + e^- \quad (7.5)$$

$$Pt + H_2O \longrightarrow Pt\text{-}OH + H^+ + e^- \quad (7.6)$$

$$Pt\text{-}OH + CHOCH_3 \longrightarrow Pt + CH_3COOH + e^- + H^+ \quad (7.7)$$

The first steps are generally considered to be a sequence of electron-proton transfers with adsorption of the intermediates at the Pt surface. Equation (7.3) is written showing the radical chemisorbed via the carbon atom, but it is also possible that the bonding occurs via the oxygen atom. Another coupled electron-proton transfer and desorption leads to the formation of acetaldehyde (ethanol) in equation (7.4). Acetalaldehyde may be electrooxidised to form another adsorbed intermediate $Pt\text{-}COCH_3$

(equation (7.5), which may break apart on the Pt surface to adsorbed CO and adsorbed CH_3. Such a C-C bond breaking process is necessary for the complete oxidation of alcohols to CO_2, which is of primary interest in the fuel cell literature. Such complete oxidation does not appear to occur in our experiments – carboxylic acids do not appear to be oxidised. Instead the oxidised Pt surface species (Pt-OH, equation (7.6)) may react with acetaldehyde to produce acetic acid (ethanoic acid, equation (7.7)). It should be noted that studies of the mechanism motivated by the relevance to fuel cells often use acidic electrolytes with weakly co-ordinating anions such as $HClO_4$ [157]. This is not a practical electrolyte for amperometric gas sensors and the choice of sulphuric acid, which may partially poison the Pt electrocatalyst, is a necessary compromise. It is suggested that the observation of $2e^-$ oxidation or $4e^-$ oxidations only in this work is partly an effect of the electrolyte.

The *n*-values (number of electrons) correspond to the electrooxidation of alcohols to aldehydes (*n* = 2) or to carboxylic acids (*n* = 4) at the metal electrode surface (Fig 7.2). It is hypothesised that an increase in temperature results in an increase in *n*-values due to the greater thermal energy available to over come the activation energy of slow reaction steps. It is considered that for primary alcohols, *n* = 4 is favoured between 20 – 60 °C which leads to formation of carboxylic acids, and complete electrooxidation to CO_2 where *n* = 12 only occurs at temperatures in excess of the operating limits of the Alphasense sensors (maximum recommended 50 °C) [158, 159]. This means that when estimating the effective layer thickness (*L*) and diffusion coefficient (*D*) during steady state limiting current conditions (Eqn 7.8), the calculations used for the primary alcohols assume an *n* = 4 e^- value, and for the rest of the VOCs an *n* = 2 e^- value was assumed throughout the thesis.

$$I = nFAC\frac{D}{L} \tag{7.8}$$

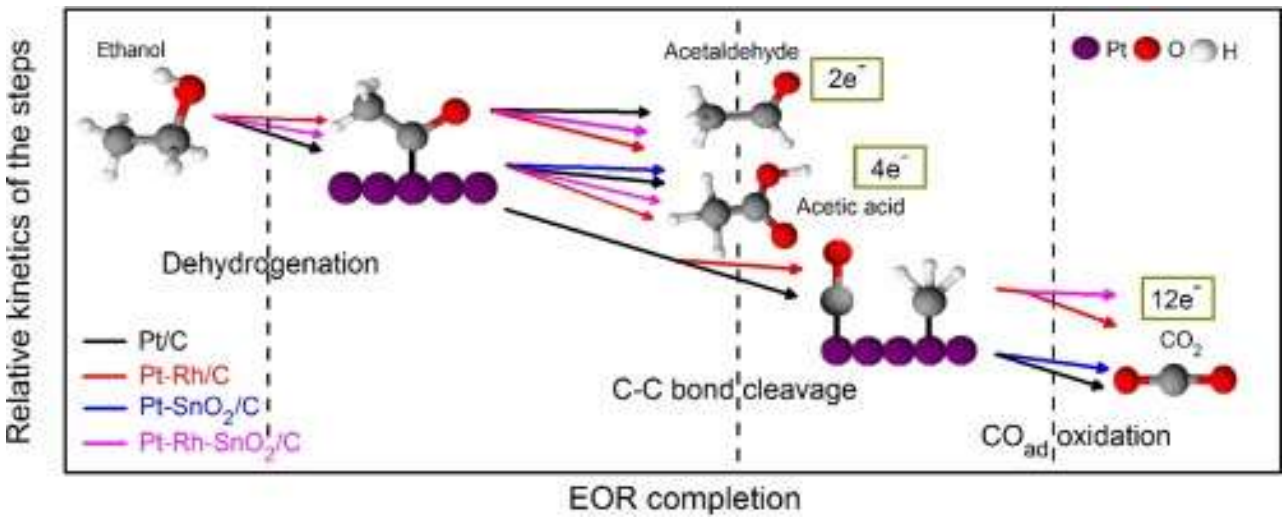

Figure 7.2: Reaction steps of alcohol electrooxidation at the Pt electrode. Reproduced from [160]

7.2 Cyclic Voltammetry

As can be seen from the cyclic voltammograms (Figs 7.3 and 7.4), the CO-A1 sensors respond to both methanol and ethanol vapour. Despite the large capacitances of these electrodes, it is possible to observe the Faradaic current for the electrooxidation of both these primary alcohols because of the high saturated vapour pressure of these liquids. The current does not become potential-independent in either case within the voltage window studied. Even when using bulk Pt electrodes, loss of electrochemically active surface area and changes in the electrode surface can occur at higher cycling voltages due to Pt dissolution into the electrolyte [161 – 164] This fact and the large background currents and long settling times involved in operating sensors at higher potentials meant that potentials greater than + 0.3 V were avoided.

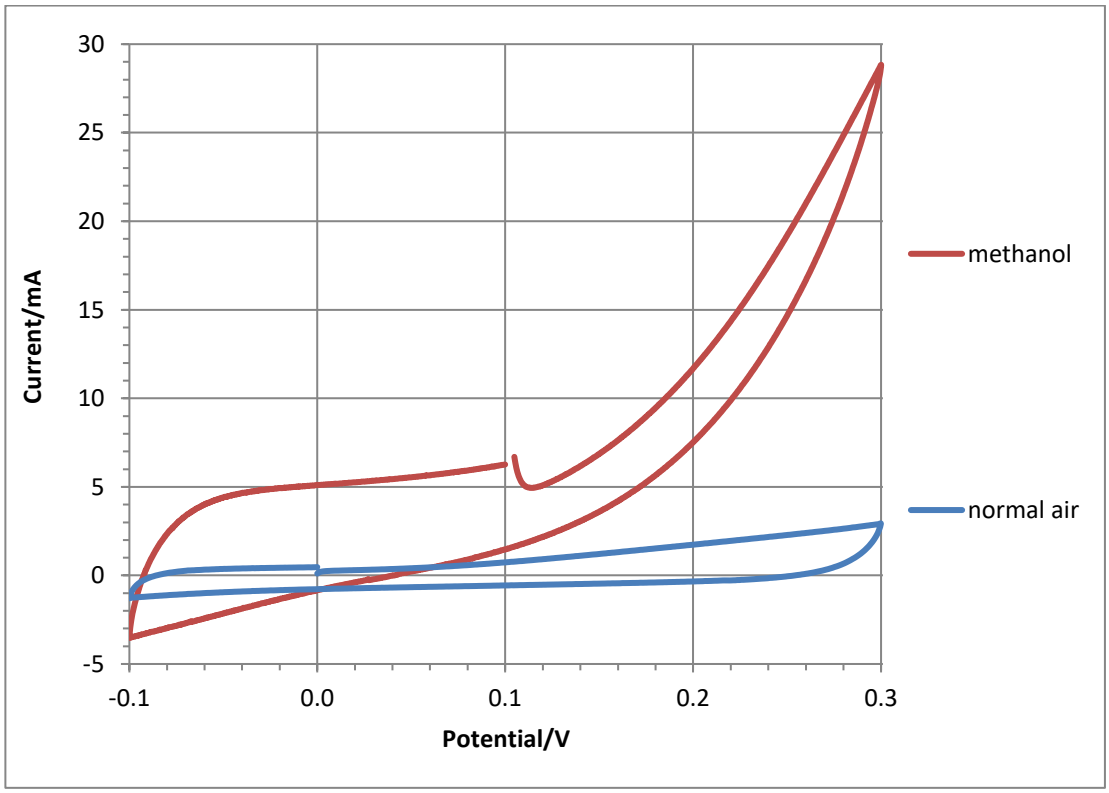

E_1 = 0.1 V E_2 = 0.3 V E_3 = - 0.1 V

Figure 7.3: Cyclic voltammograms of a CO-A1 sensor in air (control) and methanol saturated air. (500 mL min^{-1}, 84800 ppm methanol). The scan rate was 4 mV s^{-1} and the temperature was 20 ^{o}C

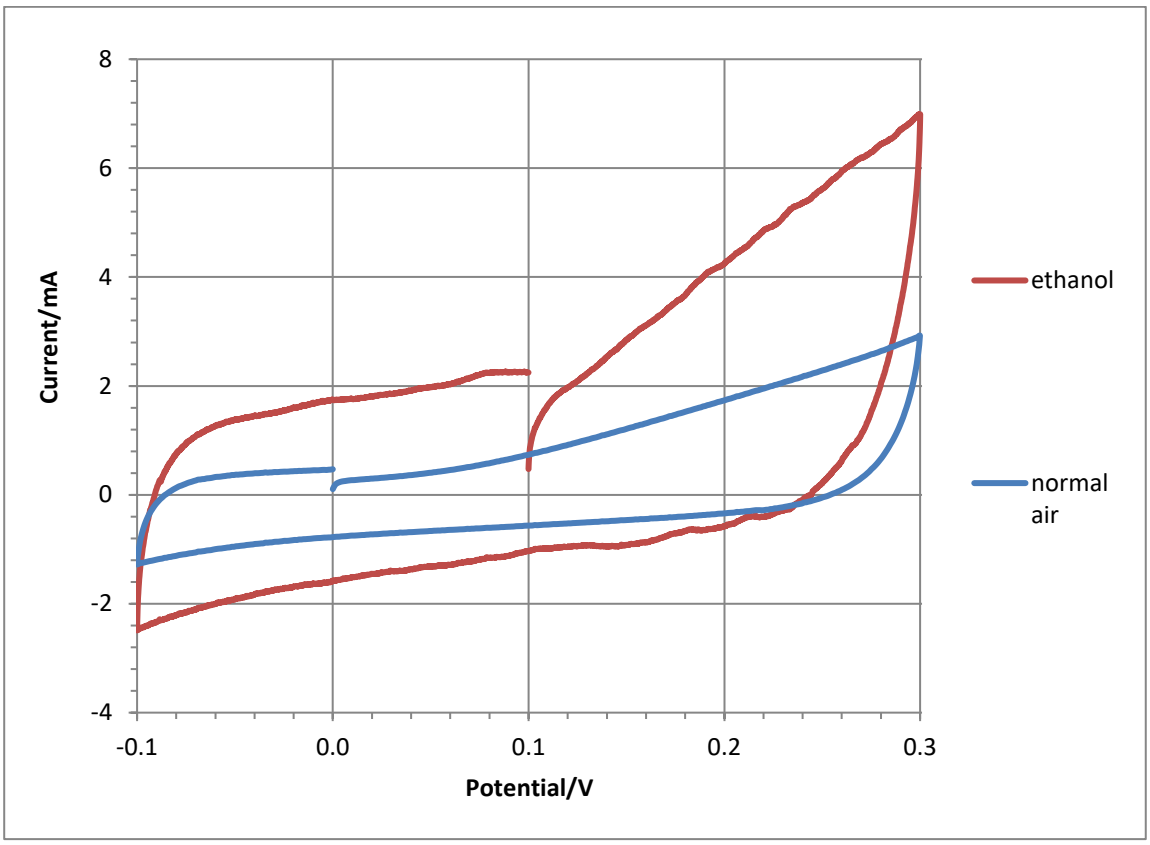

E_1 = 0.1 V E_2 = 0.3 V E_3 = - 0.1 V

Figure 7.4: Cyclic voltammogram of CO-A1 sensor in air (control) and ethanol saturated air. (500 mL min^{-1}, 29400 ppm). The scan rate was 4 mV s^{-1} and the temperature was 20 °C

It is worth noting that the cyclic voltammogram of the CO-A1 sensor response to CO (Fig. 6.1) shows a much lower current across the potential range than its response to methanol (Fig. 7.3) or ethanol (Fig. 7.4). This does not represent more facile kinetics for the alcohols, simply that the alcohol vapour concentrations (ppm) in Figs 7.3 and 7.4 are 90-fold and 30-fold greater than that of CO in Fig 6.1. Unlike CO oxidation, the oxidation of the alcohols is not clearly diffusion controlled. Methanol shows a stronger potential dependence than ethanol and this may be relevant for the interpretation of the chronoamperometric data below.

7.3 Impedance Spectroscopy

Figures 7.5 and 7.7 show that the CO-A1 sensor devices give the familiar impedance spectra as observed for the CO-AF sensors. The capacitance of the CO-A1 sensors (Figs 7.6 and 7.8) is closer to the capacitance values of the CO-AF sensors (0.23 F) than to the CM-A1 (Pt/Ru) sensors (0.49 F).

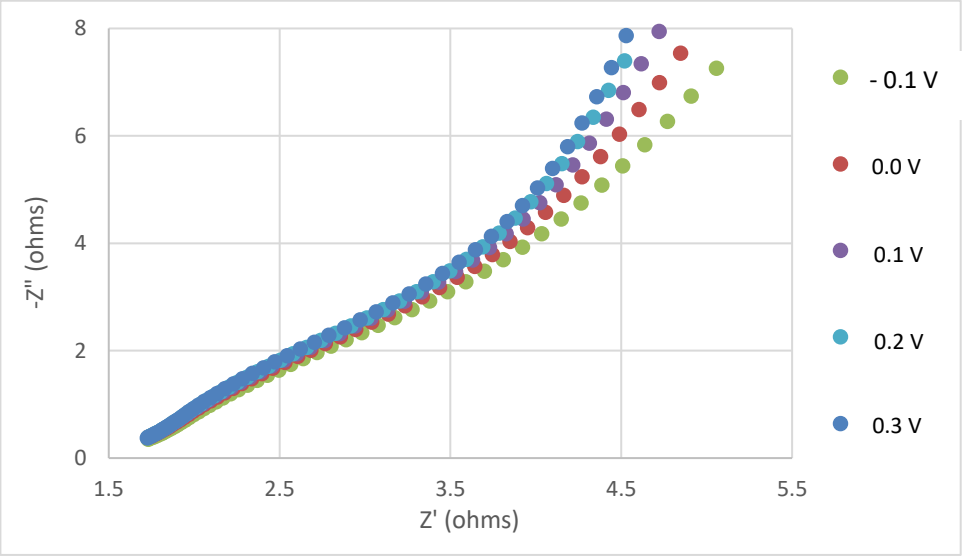

Figure 7.5: Nyquist plot of an Alphasense CO-A1 sensor in heptan-1-ol saturated air at different dc voltages at 20° C. (500 mL min^{-1}, 73 ppm). The frequency range was 0.1 < *f* < 10 Hz

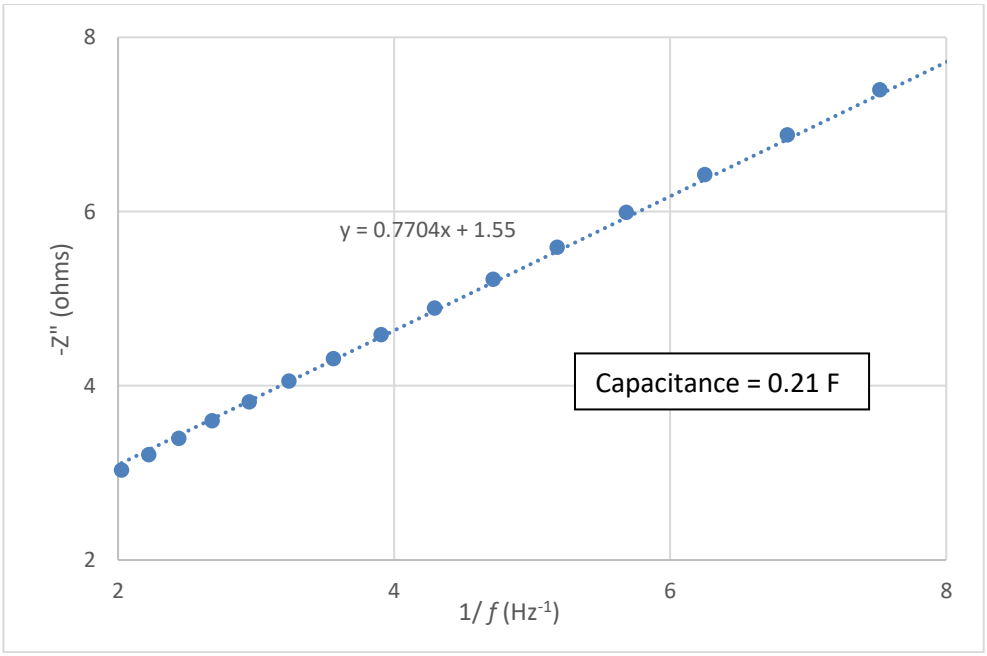

Figure 7.6: Plot of – Z" against inverse frequency of CO-A1 sensor in heptan-1-ol saturated air at 0.0 V dc at 20 °C. (500 mL min^{-1}, 73 ppm)

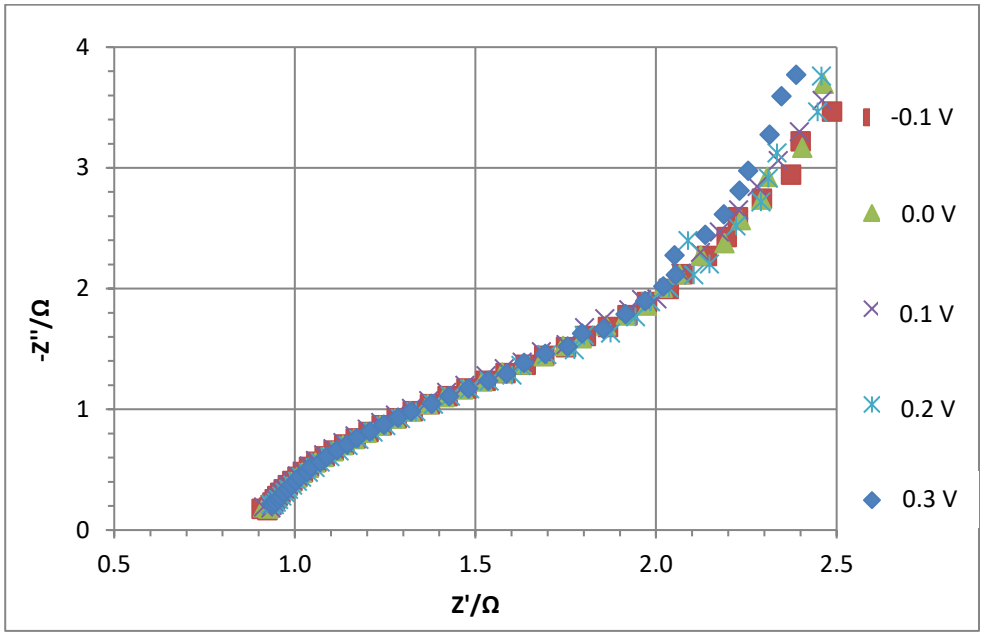

Figure 7.7: Nyquist plot of Alphasense CO-A1 sensor in ethanol saturated air at different dc voltages at 50° C. (500 mL min^{-1}, 29400 ppm) The frequency range was $0.1 < f < 10$ Hz

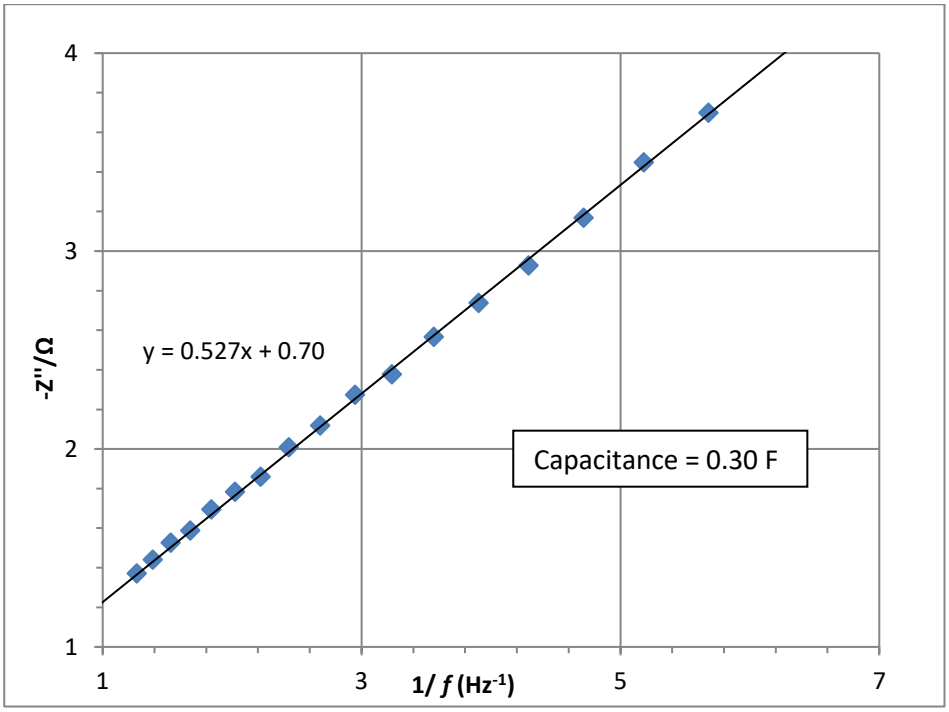

Figure 7.8: Plot of –Z" against inverse frequency of CO-A1 sensor in ethanol saturated air at 0.0 V dc at 50° C. (500 mL min^{-1}, 29400 ppm)

The impedance spectra are relatively insensitive to the presence of alcohol vapours, even ethanol at 29,400 ppm. However, the capacitance increases with temperature, from 0.21 F at 20°C to 0.30 F at 50°C. This is unexpected for a simple aqueous double layer at a metal electrode, because in the framework of the Gouy-Chapman-Stern model, the Helmholtz capacitance is temperature independent (in so far as the solvent permittivity is constant) and the diffuse layer thickness increases with temperature because it is determined by the competition between electrostatic forces and thermal motion. An increase in the diffuse layer thickness corresponds to a decrease in differential capacitance. There are exceptions known, e.g., in ionic liquids where the temperature effect may be due to a decrease of specific adsorption [165]. However, in the present system, the most likely explanation is a change in wetting behaviour and an increase in the penetration of the electrolyte into the membrane resulting in a larger wetted metal area.

7.4 Chronoamperometry

Figures 7.9 and 7.10 show the current response of the CO-A1 sensor to different VOCs bearing a range of oxygen-containing functional groups. Figure 7.1 illustrates the oxidation steps expected for alcohols and which is observed in studies of fuel cells. The low operating temperature of the sensors (compared to the typical operating temperature of an alcohol fuel cell of 80 °C) means only those molecules with protons that are easily stripped give an amperometric response (i.e. only functional groups with no steric or electrostatic hindrance). Bisulphate (or other sulphur containing species within the electrolyte solution) can sometimes hinder the desired electrochemical process at platinum electrodes and cause a reduction in electrocatalytic activity at the working electrode surface [166 – 169]. However, the choice of electrolyte in the sensor is primarily dictated by considerations of safety and volatility as it directly affects the operating lifetime of the sensor.

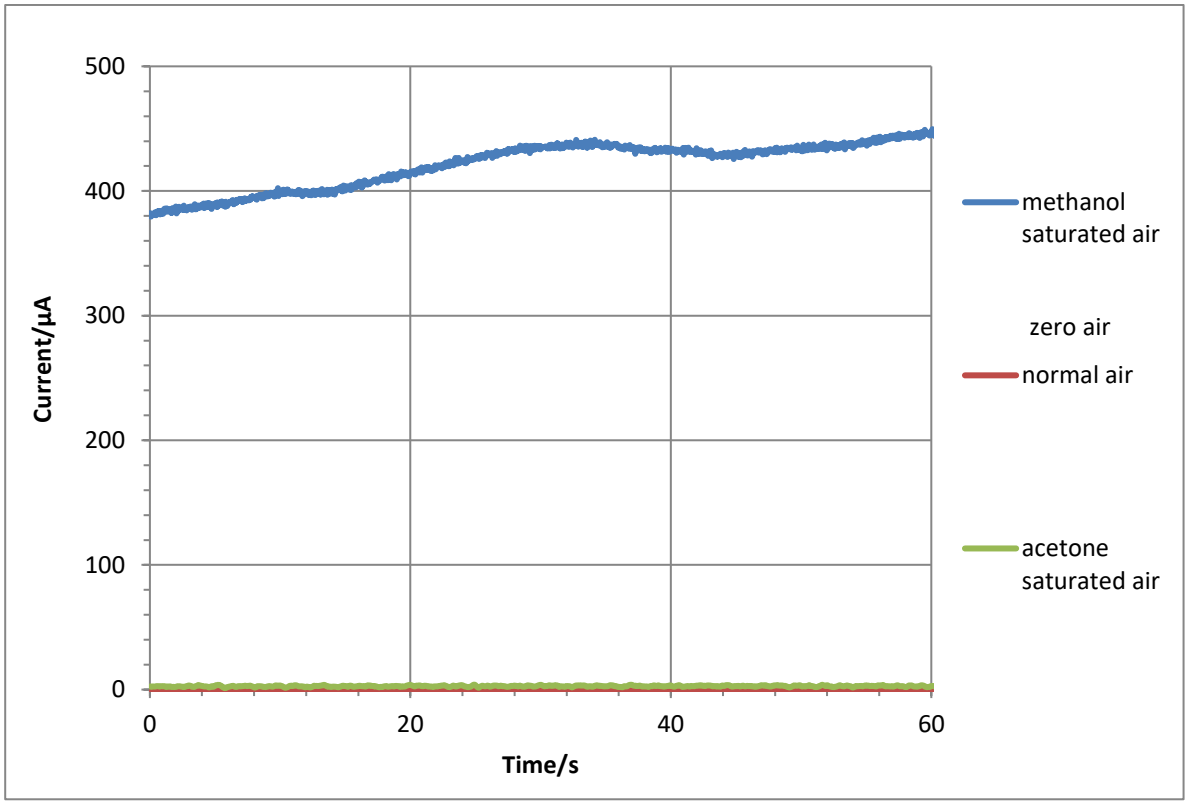

Figure 7.9: Graph showing CO-A1 sensor selectivity response to methanol (17000 ppm) versus acetone (9780 ppm) at steady flow rate in 20° C at 0.0 V dc. (55 mL min^{-1})

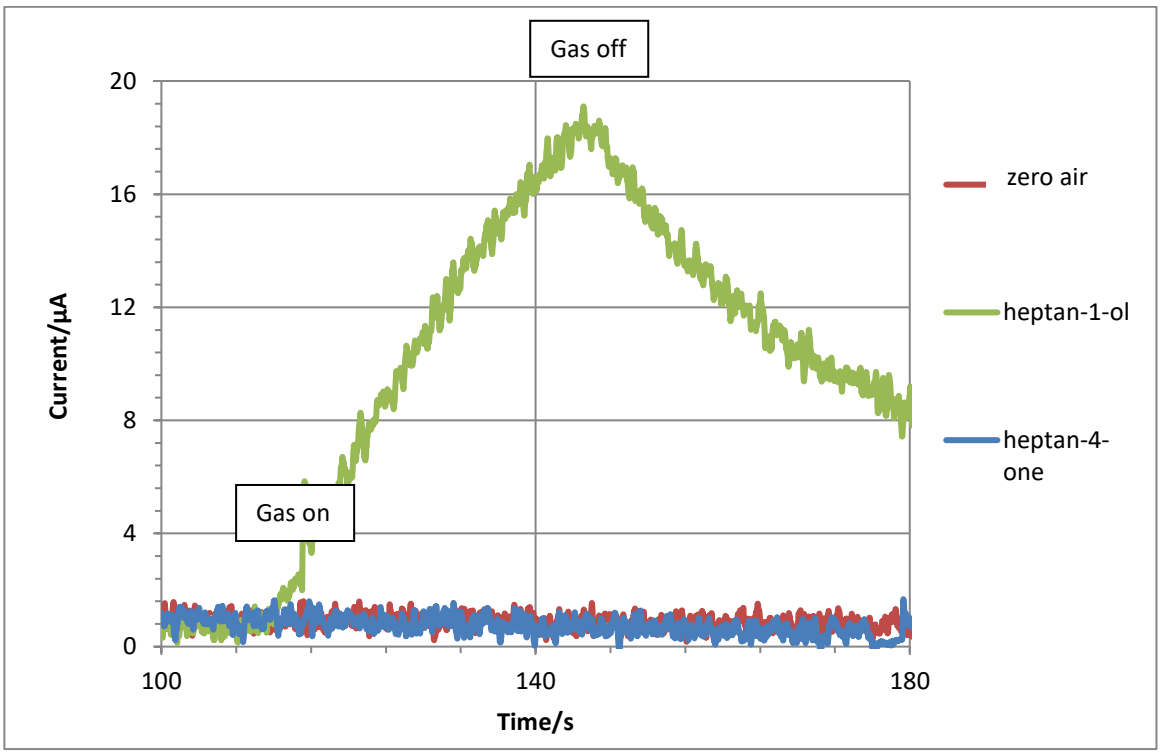

Figure 7.10: Graph showing CO-A1 sensor response to pulsed heptan-1-ol (73 ppm) versus heptan-4-one (28200 ppm) saturated air at 20° C at 0.0 V dc. (500 mL min^{-1})

The fact that alcohols gave an amperometric response, but ketones did not (Figs 7.9 and 7.10), suggests that (at the sensor operating temperature) secondary alcohols will oxidise only as far as the ketone; whereas primary alcohols may form the carboxylic acid. It could be argued that the effect is a result of differences in vapour pressure, however ethanol (with a vapour pressure of 5.95 kPa) gives a much greater current response than ethanoic acid whose vapour pressure is a similar order of magnitude 1.56 kPa. Further, heptan-4-one with a much higher vapour pressure than heptan-1-ol gives a negligible current response (Fig 7.10). Generally, the pattern of reactivity is consistent with a two-electron oxidation of secondary alcohols (n = 2) and a four-electron oxidation of primary alcohols (n = 4).

7.4.1 Selectivity

As can be seen from Figures 7.10 – 7.12, the response times of the CO-A1 sensors to reach maximum current is much slower than that of the CO-AF sensors. This suggests that the transport of the VOCs through the devices is much slower than for CO. It can also be seen (Figs 7.9 and 7.10) that primary alcohols are electrooxidized whilst ketones are not. Thus, secondary alcohols most likely only undergo n = 2 electron- reactions to ketones. Figures 7.11 and 7.12 show functional groups such as carboxylic acids and esters are not electrooxidized, this suggests that the reaction stops after n = 4 electrons, most likely due to a lack of thermal energy to overcome the activation energy required.

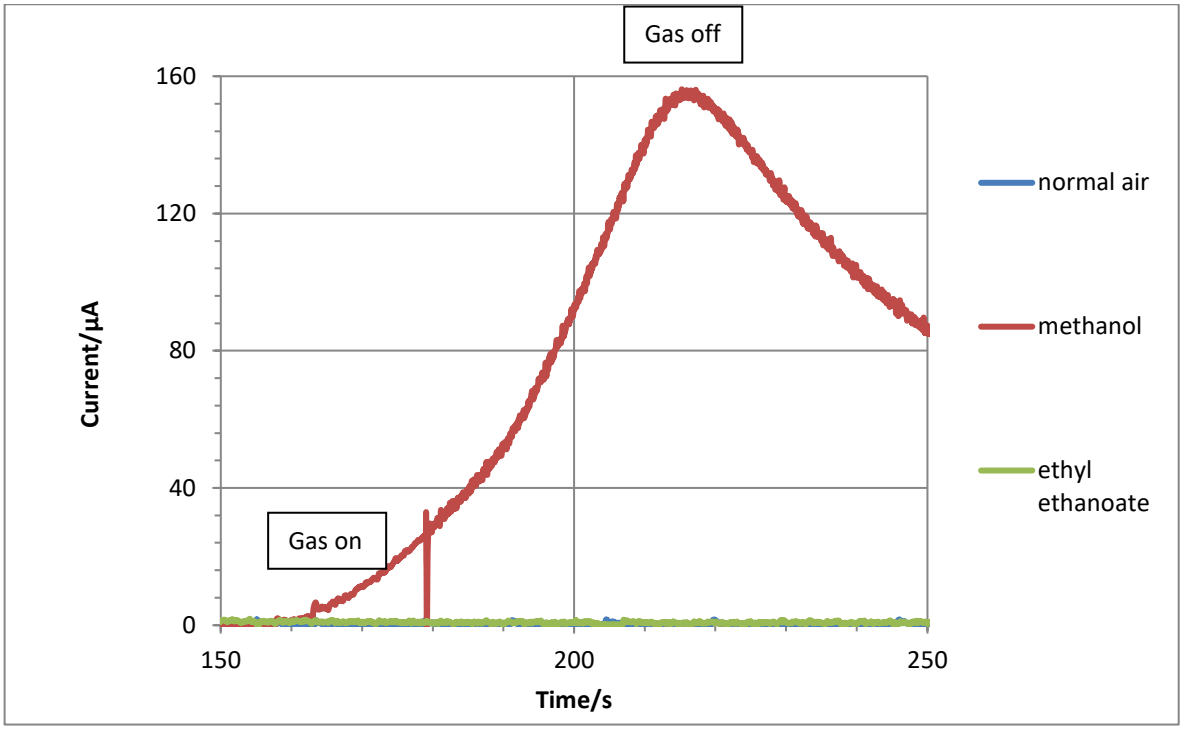

Figure 7.11: Graph showing CO-A1 sensor selectivity response to pulsed methanol (17000 ppm) versus pulsed ethyl ethanoate (9700 ppm) at 20° C at 0.0 V dc. (500 mL min^{-1})

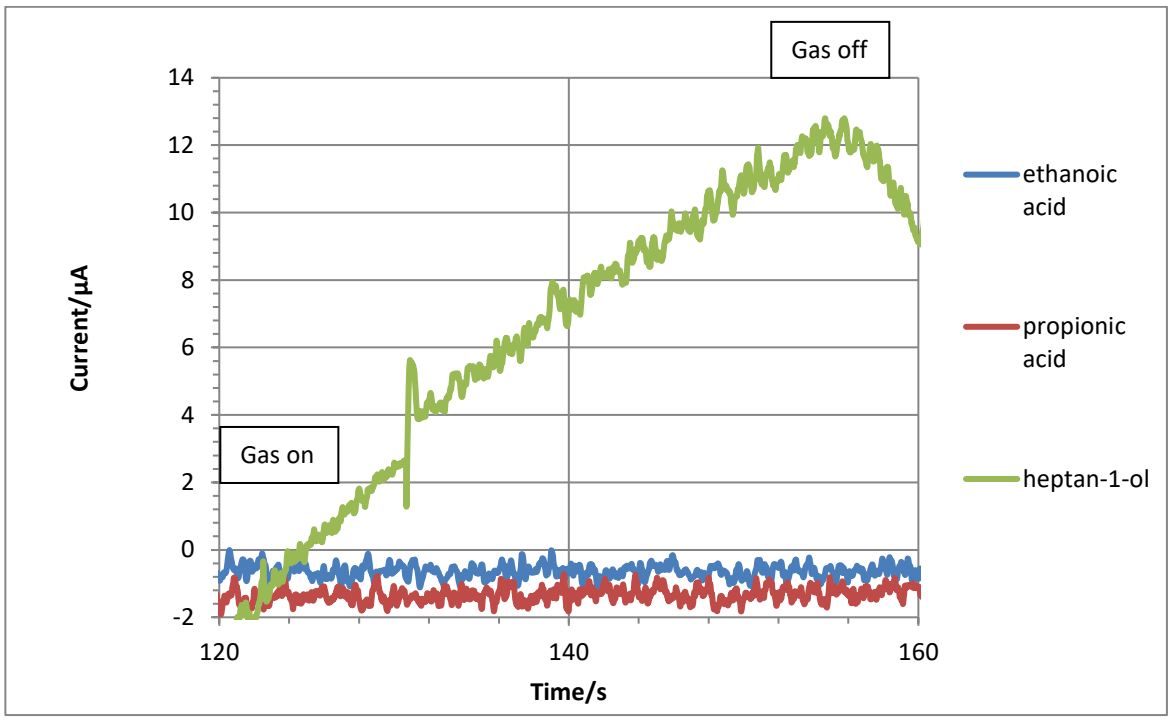

Figure 7.12: Graph showing CO-A1 sensor response to pulsed acetic acid versus propionic acid (313 ppm) versus heptan-1-ol (73 ppm) saturated air at 20° C at 0.0 V dc. (500 mL min^{-1})

7.4.2 Linearity

It can be seen from the relationships between the amperometric response of the CO-A1 sensor to different VOCs (Figs. 7.14 - 7.15b) that each has a different linear calibration. The fact that the CO-A1 sensor can detect ethanol (combined with the small size of the sensor) means that it could possibly be deployed as part of a portable breathalyser kit for use by police on suspected drink drivers, as ethanol is a component of alcoholic beverages that lingers on a person's breath.

The linear calibration of the CO-A1 device for the VOCs is an advantage for the real time determination of VOCs because it facilitates the conversion of the signal to analyte concentration. This further enhances the commercial aspects of the CO-A1 sensor, given that speed and simplicity of analysis is often an important factor in applications outside of centralised laboratory settings and where the operator may not be an analytical chemist. Note that the gradients in table 7.1 are based upon currents in μA and analyte concentration expressed in ppm. It can be seen from table 7.1, that each VOC gives a different linear calibration equation. The sensitivities are within a factor of about 2 apart from the data for tert-butanol and propanal, to which the device is less sensitive. Use of the linear equations also allows the lower limits of detection to be estimated for each VOC. The definition of limit of detection is taken as the concentration that gives a signal three times greater than the standard deviation of a blank. Examination of raw data (Figs 7.10 – 7.12) gives a standard deviation of the current noise of about 1 μA.

VOC	Linear calibration equation at 20 °C	Detection limit (ppm)
methanol	y = 0.011x - 225	270
ethanol	y = 0.017x + 55	180
heptanol	y = 0.025x - 5	120
propan-2-ol	y = 0.023x - 50	130
tert-butanol	y = 0.0006x + 0.39	100
propanal	y = 0.009x - 8	330
hexanal	y = 0.012x - 5	250

Table 7.1: Compiled linear equations of the calibrations for the different VOCs. The slopes are in units of μA ppm^{-1} and the detection limits (3x standard deviation of blank) were estimated using a noise figure of 1 μA on the sensor signal and the analytical sensitivity from the linear calibration.

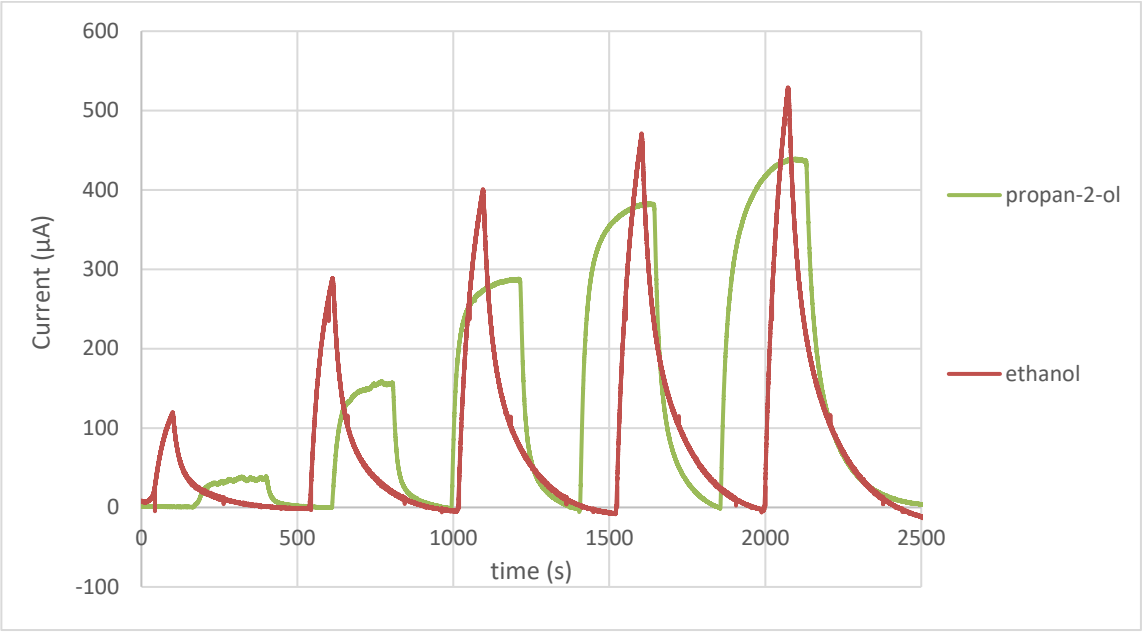

Figure 7.13: Graph showing CO-A1 sensor response to pulses of increasingly concentrated propan-2-ol (4.67 kPa pulsed at 4500, 9000, 15000, 19000, 23000 ppm respectively) and ethanol (5.95 kPa pulsed at 5000, 11000, 19000, 24000, 29000 ppm respectively) saturated air in 20° C at 0.0 V dc.

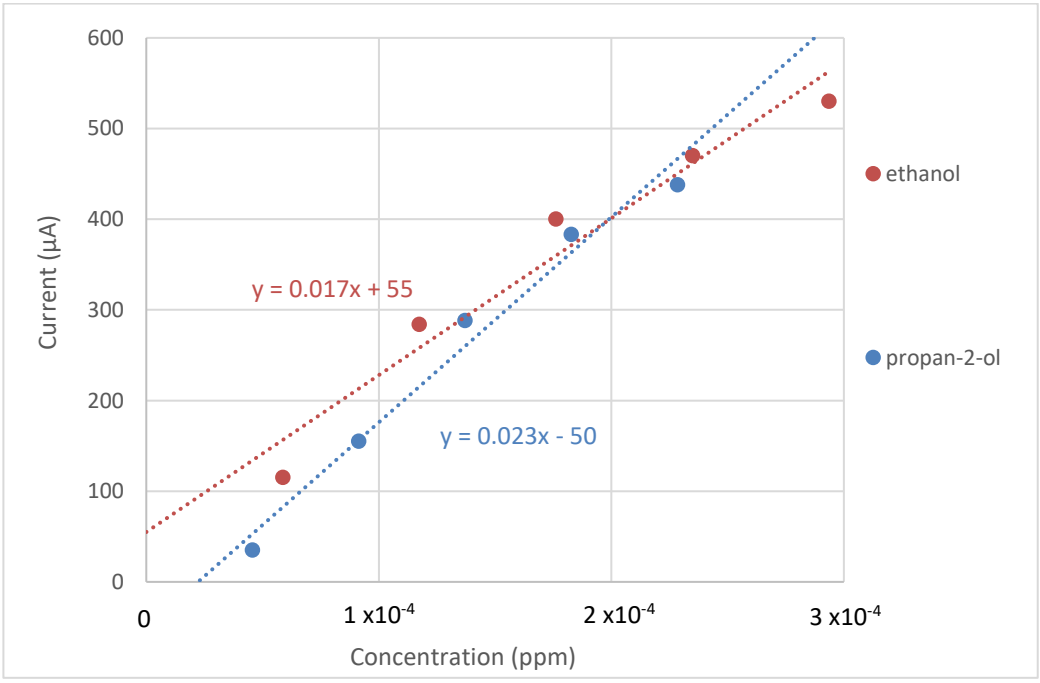

Figure 7.14: Example calibration plots for a CO-A1 sensor to (i) propan-2-ol and (ii) ethanol vapour in separate experiments. Data taken from Fig 7.13.

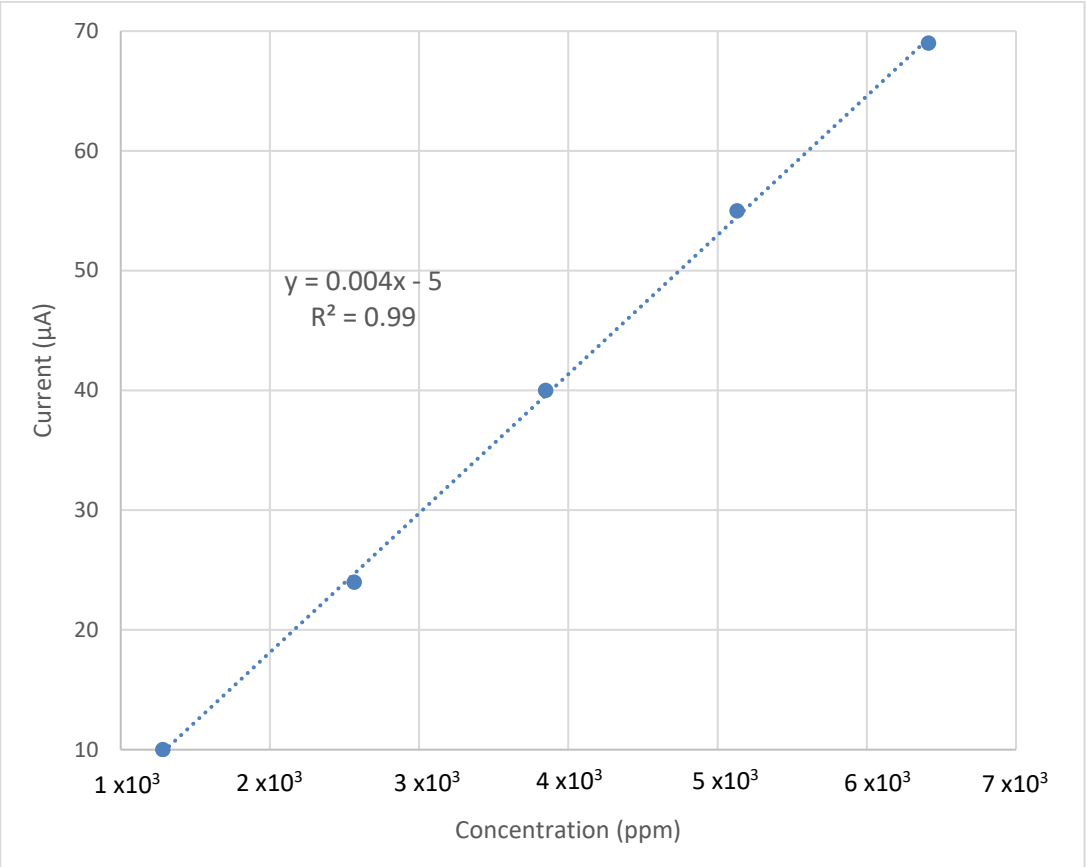

Figure 7.15a: Current response against concentration of hexanal at 20 °C.

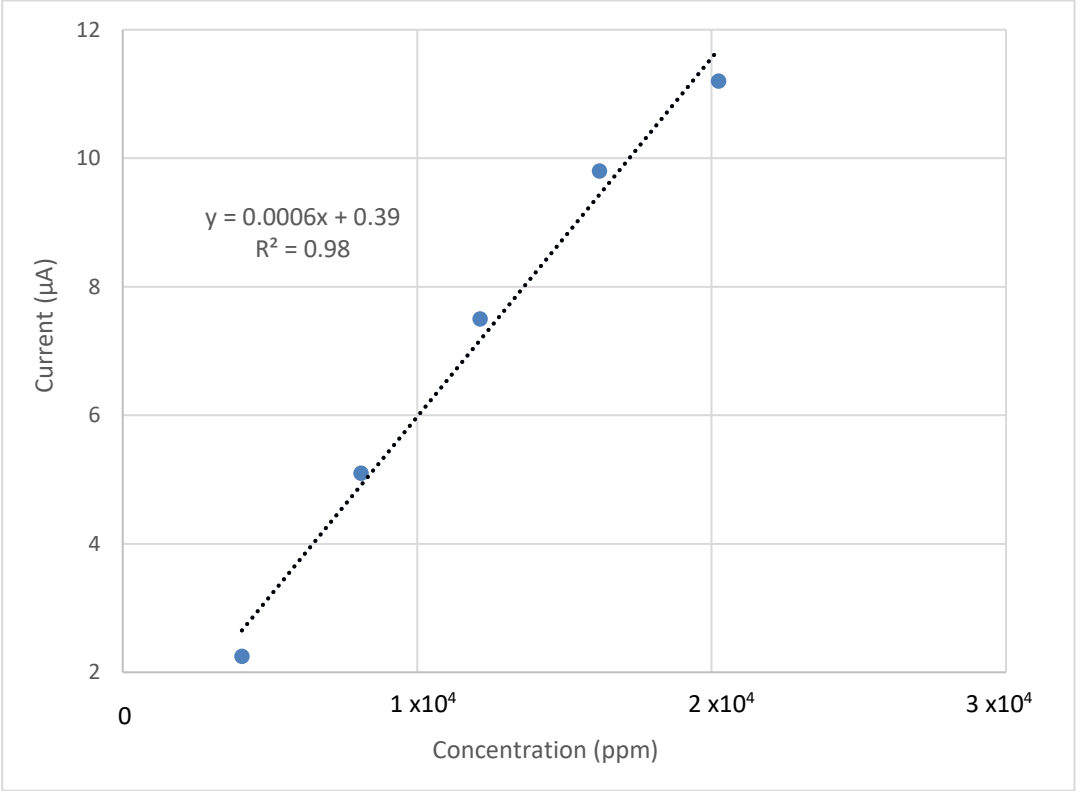

Figure 7.15b: Current response against concentration of tert-butanol at 20 °C.

7.4.3 Sensitivity

In order to evaluate the performance of the CO-A1 sensor against different VOCs, the gradient of the calibration plot of current response against concentration is taken as a measure of sensor sensitivity (Figs 7.15a and 7.15b). From the table below, some general features can be observed. The sensitivity increases amongst the primary alcohols as chain length increases. This may be due to a decrease in polarity (Fig 7.16) and a change in the way the alcohol interacts with the hydrophobic porous membrane. However, in the case of methanol, which shows somewhat anomalous values of *D* in table 7.1, electrode kinetics may also be involved (see section 7.5).

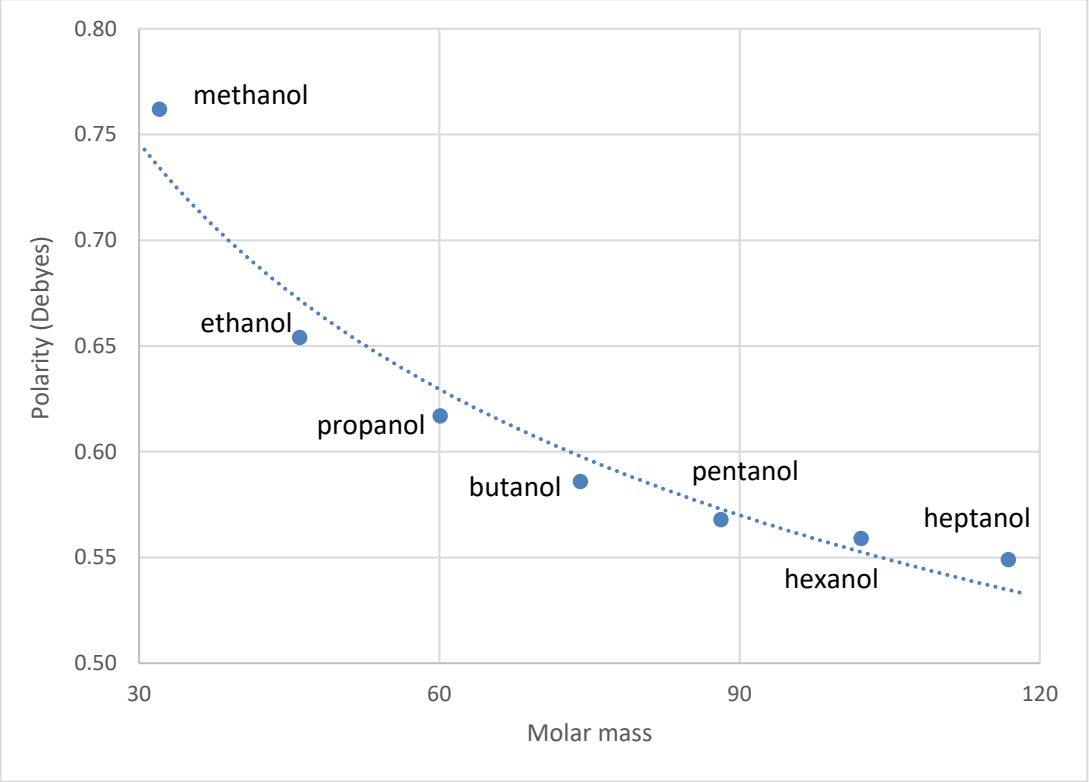

Figure 7.16: Polarity against molar mass of primary alcohols from methanol to heptanol.

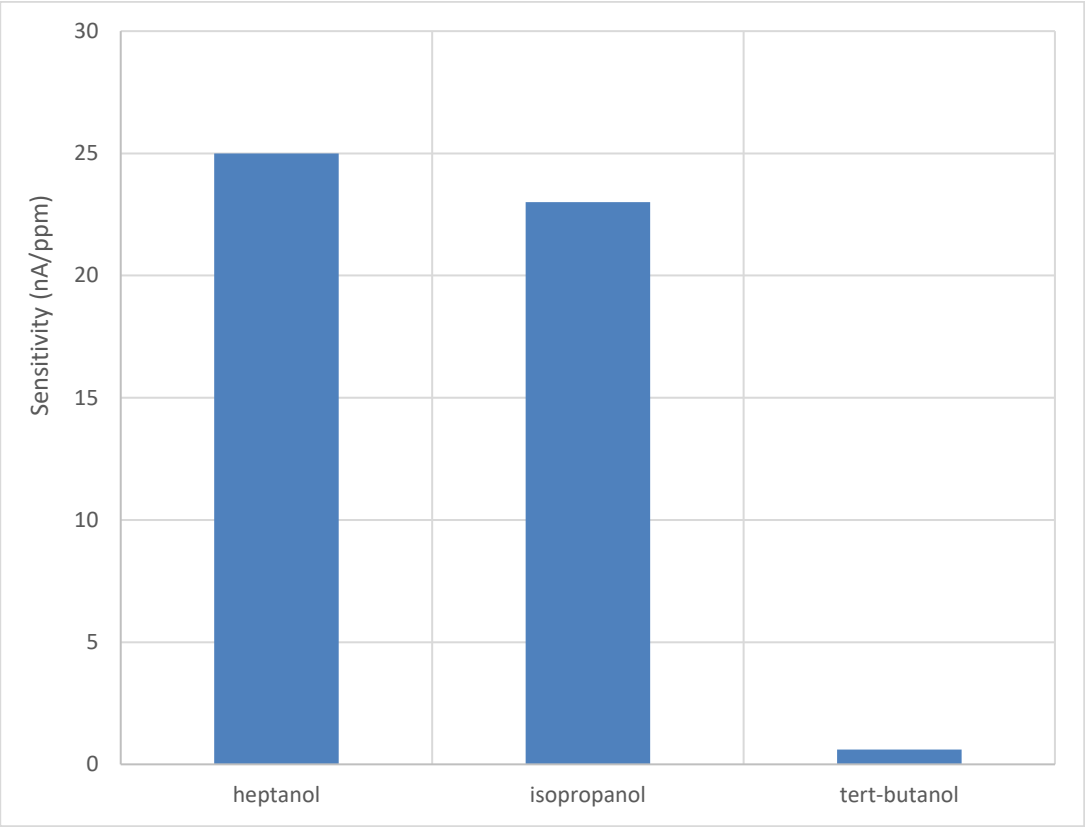

Figure 7.17: Sensitivity of the CO-A1 sensor to a primary, secondary and a tertiary alcohol.

Somewhat surprisingly, the sensitivity increases with molar mass (fig 7.17). This is opposite to the trend of boiling points and of vapour pressures for primary alcohols and indicates factors other than the liquid-gas phase change variables are important. Finally, it is worth noting that the tertiary alcohol shows a much lower response than the primary and secondary alcohols, but the reason is unclear.

7.4.4 Reusability

In addition to linearity and detection limit, the reusability of a sensor is important. The data generally showed (see fig. 7.18 for an example) that the signal returns to baseline for these analytes after the stream of VOC is replaced by pure air. However, it is also of interest to test for cross effects in which the effect of one analyte on a subsequent analyte is considered. In Fig. 7.18 the sensor is first exposed to propanal, then allowed to recover in pure air and final exposed to methanol. It can be seen from fig 7.18 that the sensor responses to the alcohol after being exposed to the aldehyde. This indicates a lack of poisoning of the catalyst and the return of the signal to baseline in air also shows that the VOC is displaced from the various layers of the device in a stream of pure air.

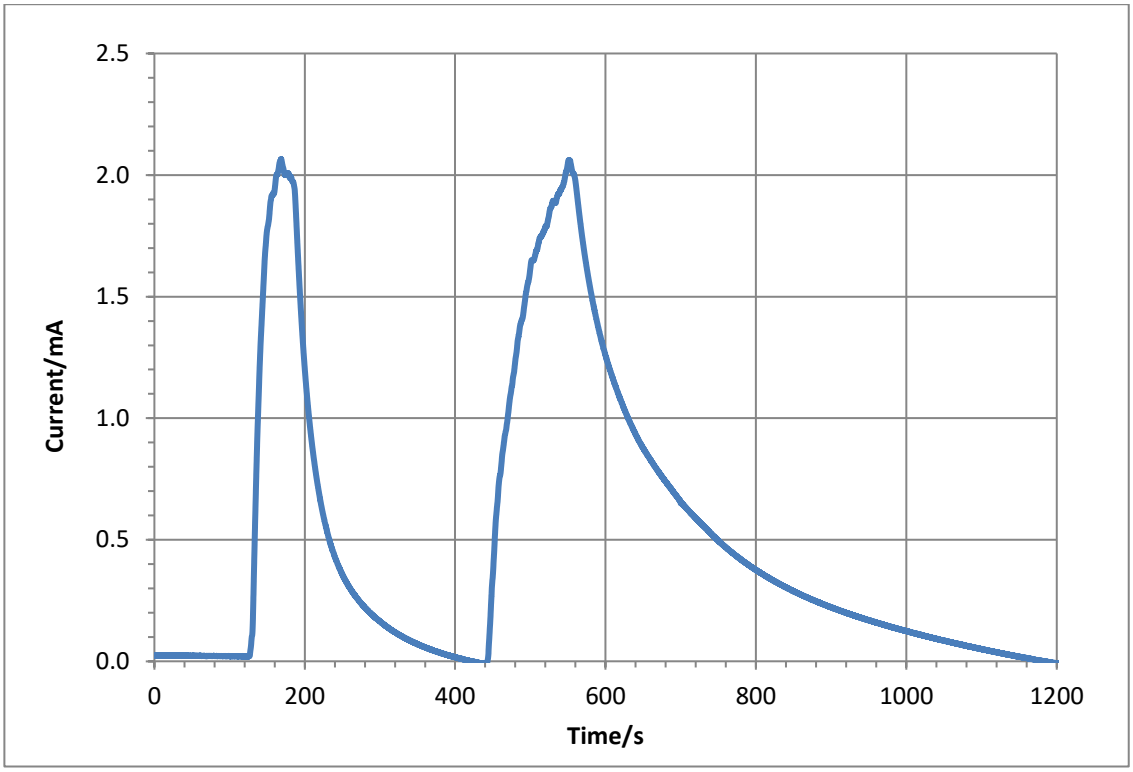

Figure 7.18: Graph of CO-A1 sensor chronoamperometric response to propanal (first peak at 49300 ppm) followed by methanol (second peak at 33900 ppm) at 20°C at 0.0 V dc.

7.5 Voltage Bias

Chronoamperometry was also used to test the response of the CO-A1 sensor to VOCs at different dc voltages (voltage bias) when exposed to the same concentration of each pulsed VOC. Figures 7.19 and 7.20 show that maximum limiting current may be potential dependent for the CO-A1 sensor. There is a strong potential dependence for some VOCs (methanol), but a weaker response to others (propanal). This indicates the reaction is not mass transport controlled and there are kinetic sonierations to take into account, especially for methanol. The values of *L* and *D* extracted from the analysis of the chronoamperometric response to pulses of VOC therefore have to be carefully interpreted as *effective* values because the steady state currents may not be simply proportional to *D*/*L* and are partially controlled by kinetics.

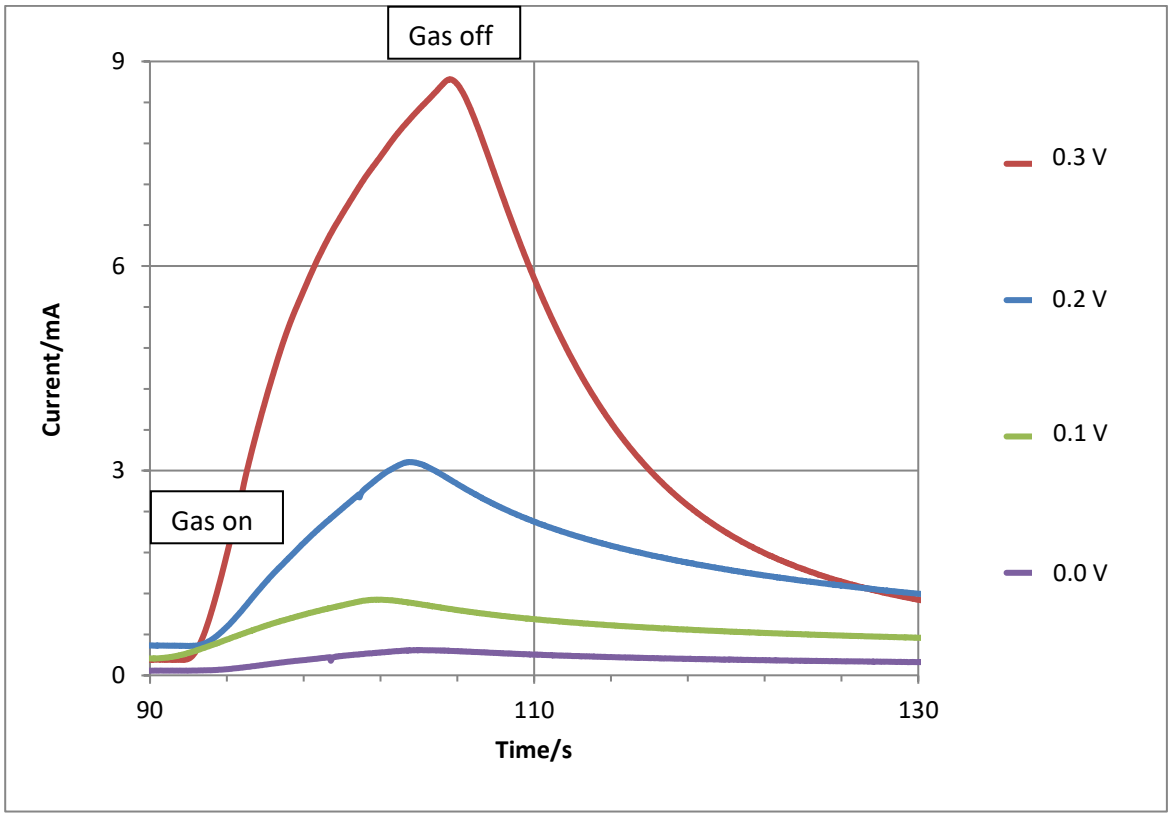

Figure 7.19: Graph showing CO-A1 sensor response to 500 ml min^{-1} methanol saturated air at 20° C

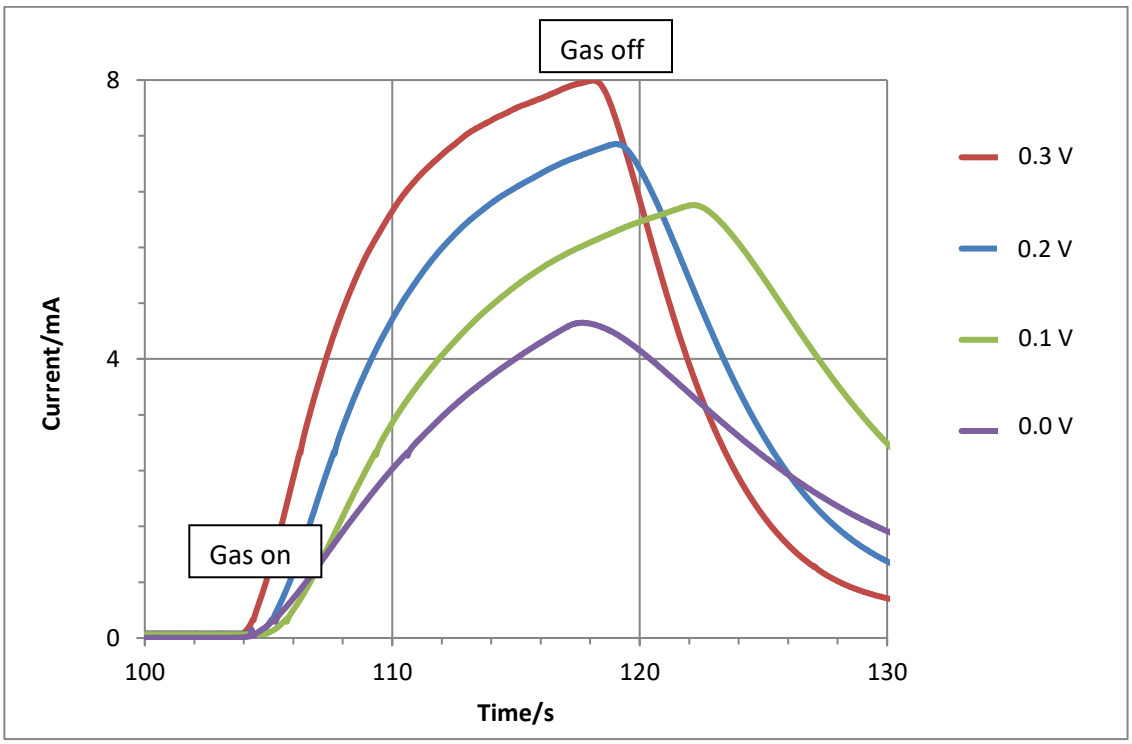

Figure 7.20: Graph showing CO-A1 sensor response to 500 ml min^{-1} propanal saturated air at 20° C

7.6 Modelling the Chronoamperometric Response to VOCs

The mass-transport based regression model of chapter 3 was also applied to the CO-A1 sensor response to VOCs. Whilst it is known that alcohol species detection (via oxidation) by platinum electrodes is diffusion dependent i.e. mass transport controlled [170, 171] under certain conditions, it is not clear if this will hold for the sensors during operation at near ambient temperature. Figs 7.21 - 7.23 show an illustrative selection of experimental data and the fit of the regression model to the data.

L^2/D (s)	T_0 (s)	ΔI (μA)	Steady state current (μA)
180	983	-275	277

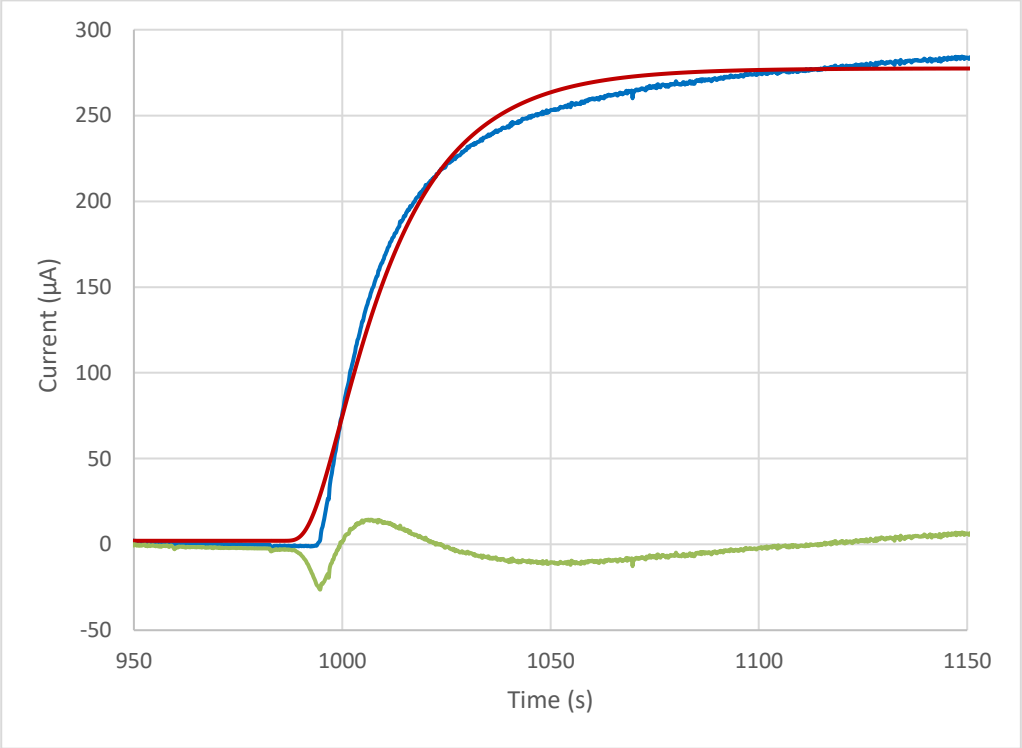

Figure 7.21: Sensor response at 0.0 V dc in isopropanol at 30% of the saturated vapour pressure at 20° C. Experimental data (blue), regression model (red), and residual (green).

L^2/D (s)	T_0 (s)	ΔI (μA)	Steady state current (μA)
926	2400	-67	67

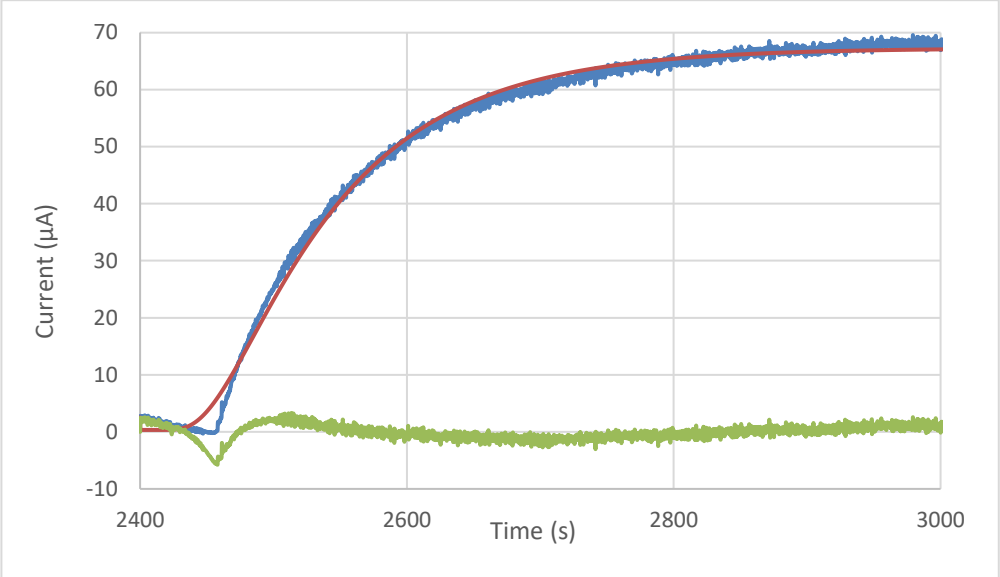

Figure 7.22: Sensor response at 0.0 V dc in hexanal at 50% of the saturated vapour pressure at 20° C. Experimental data (blue), regression model (red), and residual (green).

L^2/D (s)	T_0 (s)	ΔI (μA)	Steady state current (μA)
73	541	-4.84	7.36

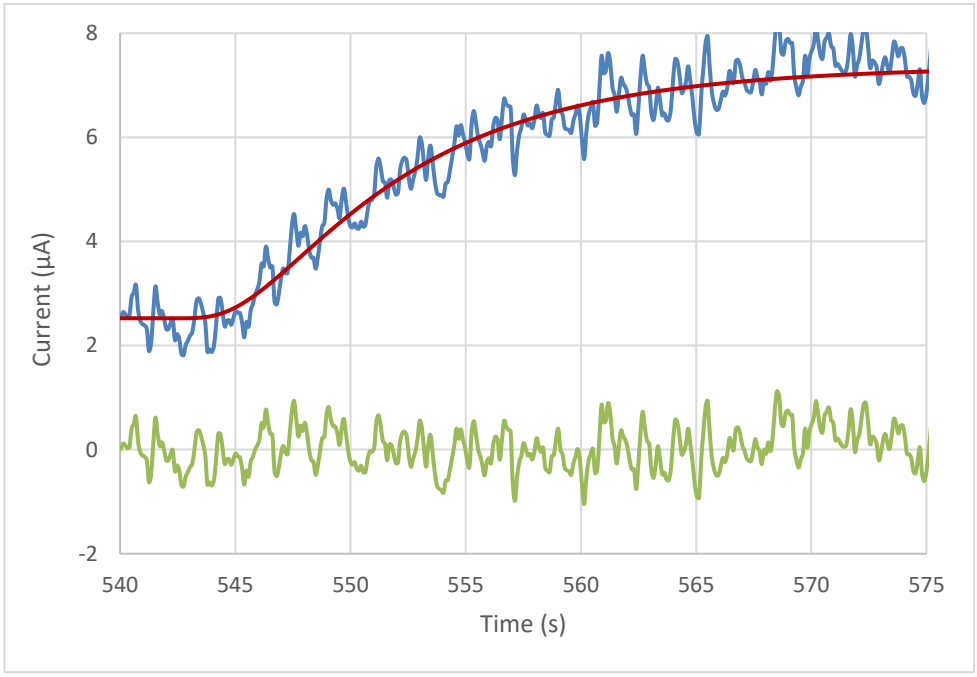

Figure 7.23: Sensor response at 0.0 V dc in tert-butanol at 60% of the saturated vapour pressure at 30° C. Experimental data (blue), regression model (red), and residual (green).

In general, the fit of the regression model to the data is satisfactory, except near the initial gas-on event where the experimental data shows a steeper rise than the model. Such an effect cannot be explained by a variation in mass transport through the layers because, as shown in Chapter 3, this still produces a theoretical curve of the same basic shape. It also cannot easily be explained by kinetic limitations, because these will affect principally the steady-state current and not the transient which is determined by the time taken for the analyte to reach the electrode. The most likely explanation lies in the heterogeneity of the membrane; if portions of the membrane offer a high diffusion barrier and other regions a lower barrier, then the initial rise will be dominated by the latter and the long-time behaviour by the former. Evidence for this interpretation can be found in Fig 7.21 which shows a notably steep rise of the experimental data (low barrier regions), but a long, slow variation as the response nears steady state (high barrier regions). Nevertheless, the overall shape of the response is well-described by the model and the residual is small in Figs 7.22 and 7.23.

An important aspect of a diffusion-based model is that the response of the device to exposure to the VOC and the recovery of the signal after returning to pure air should yield identical time parameters (L^2/D) because diffusion of VOC into the device should be subject to the same law as diffusion of VOC out of the device. The recovery of the sensor (see fig 7.22 for the response) after turning the hexanal saturated vapour off and replacing with a stream of pure air is shown in fig. 7.24. The values of L^2/D obtained from the fit are 926 seconds (response) and 1006 seconds (recovery, in satisfactory agreement).

The current response profile of the sensor after turning the alcohol saturated vapour off is included for completeness:

L^2/D (s)	T_0 (s)	ΔI (μA)	Steady state current (μA)
1006	3019	66.9	1.29

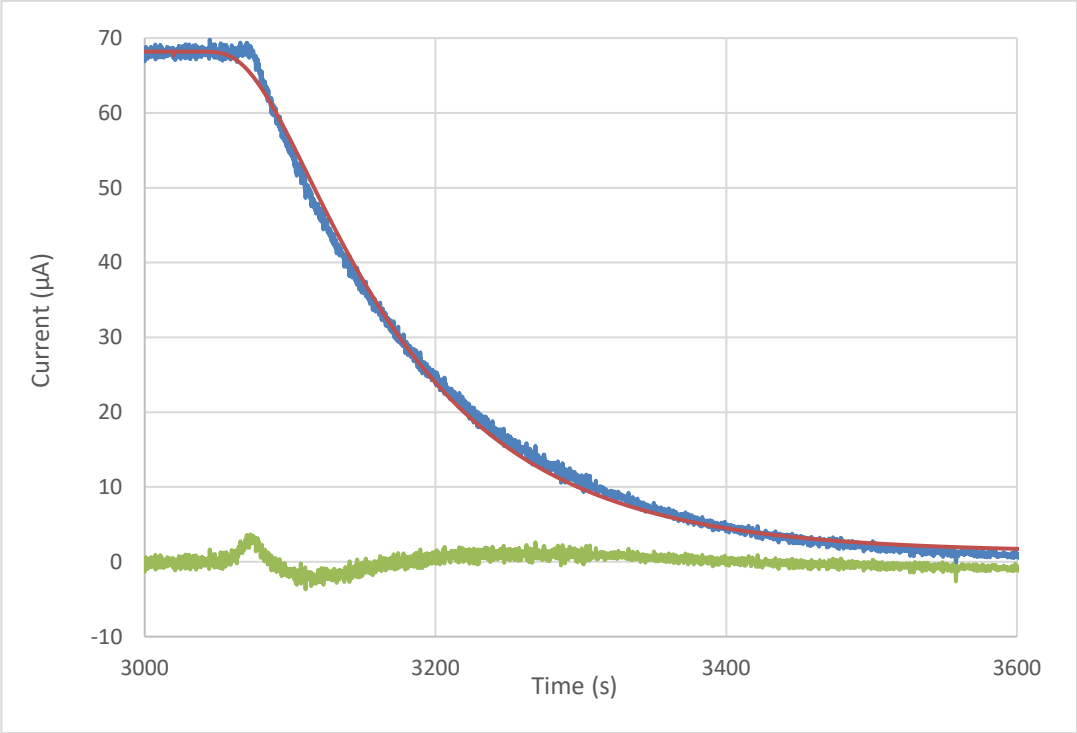

Figure 7.24: Sensor response at 0.0 V dc after switching to pure air from 50% hexanal saturated air at 20° C. Experimental data (blue), regression model (red), and residual (green).

Here the sensor response after the alcohol saturated air has been shut off is given as an example of a VOC for which the response is more rapid:

L^2/D (s)	T_0 (s)	ΔI (μA)	Steady state current (μA)
92	534	957	27.4

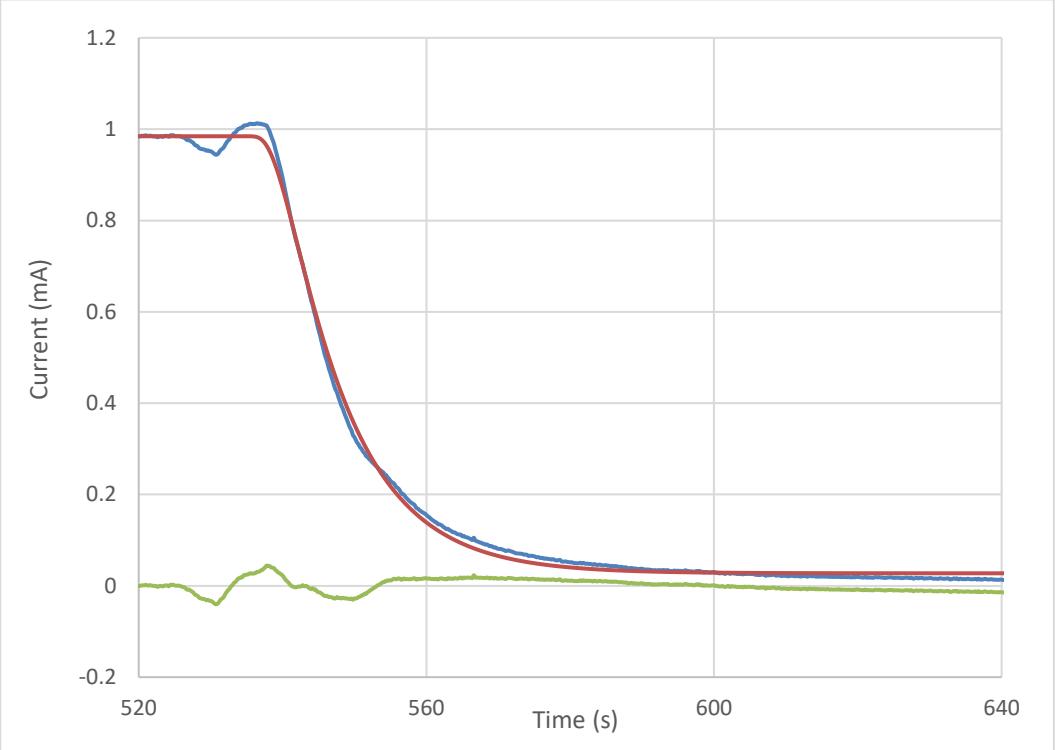

Figure 7.25: Sensor response at 0.0 V dc after 30% propanol saturated air at 30° C. Experimental data (blue), regression model (red), and resdiual (green).

Values of effective thickness *L* and effective diffusion coefficient *D* are collected in Table 7.2 for all the VOCs over a range of concentrations. A literature resource of tabulated Henry's Law values was used to calculate *L* and *D* [124]. The Henry's law constants are necessary to take account of the varying solubility of the VOCs in aqueous electrolyte. First, a comment on the internal consistency of the fitted parameters: in general, despite wide variations between VOCs, *L* and *D* are reasonably consistent for a given VOC over the range of concentrations, although there are exceptions, e.g., the 1330 ppm data for methanol. This suggests that the basic features of the model are sufficient to describe the data.

The calculated values of *L* are consistent with a thin layer of aqueous sulfuric acid coating the platinum particles at the base of the Porex porous membrane, but the interpretation cannot simply be that diffusion occurs in a thin aqueous phase, because the calculated values of *D* are extremely low. Typical values of *D* for diffusion in a thin liquid layer are of the order of 10^{-5} cm^2s^{-1} [172, 173]. The values might be considered to be a result of an electrode kinetic barrier; slow kinetics would reduce the steady-state current (in the model proportional to *D*/*L*) and therefore the value of *D* would be underestimated. This also cannot be the complete explanation because the *D* values are many orders of magnitude lower than expected (10^{-12} cm^2 s^{-1} in several cases) and a purely electrode-kinetic limitation would have the current suppressed by a similar factor. Instead it is suggested that blocking of the membrane pores by condensation of the vapour during transport through the sensor is involved.

			Methanol		
Conc. (ppm)	**ΔI (mA)**	**L^2/D (s)**	**L (µm)**	**D (cm^2 s^{-1})**	**K @293 kelvin**
1330	0.02	396	0.05	6.56 x10^{-14}	5010
2608	0.25	539	0.36	2.39 x10^{-12}	
3912	0.46	367	0.30	2.48 x10^{-12}	
5217	0.73	364	0.36	3.51 x10^{-11}	
6551	1.03	342	0.38	4.16 x10^{-11}	
			0.29	2.52 x10^{-12}	= $\overline{x}$

			Ethanol		
Conc. (ppm)	**ΔI (mA)**	**L^2/D (s)**	**L (µm)**	**D (cm^2 s^{-1})**	**K @293 kelvin**
5872	0.12	253	0.04	5.86 x10^{-14}	4631
11744	0.28	225	0.04	7.54 x10^{-14}	
17617	0.39	396	0.07	1.17 x10^{-13}	
23489	0.51	322	0.05	8.73 x10^{-14}	
29361	0.52	248	0.03	4.57 x10^{-14}	
			0.05	7.68 x10^{-14}	= $\overline{x}$

			Heptan-1-ol		
Conc. (ppm)	**ΔI (mA)**	**L^2/D (s)**	**L (µm)**	**D (cm^2 s^{-1})**	**K @293 kelvin**
7	0.04	104	0.31	9.31 x10^{-12}	1267
15	0.07	66	0.19	5.48 x10^{-12}	
22	0.07	36	0.07	1.50 x10^{-12}	
73	0.11	9	0.01	8.92 x10^{-12}	
			0.15	4.10 x10^{-12}	= $\overline{x}$

			Isopropanol		
Conc. (ppm)	**ΔI (mA)**	**L^2/D (s)**	**L (µm)**	**D (cm^2 s^{-1})**	**K @293 kelvin**
456	0.04	304	0.65	1.40 x10^{-11}	2925
813	0.15	209	0.94	4.24 x10^{-11}	
1370	0.28	180	0.90	4.49 x10^{-11}	
1840	0.36	207	0.99	4.73 x10^{-11}	
2335	0.42	301	1.32	5.81 x10^{-11}	
			0.96	4.13 x10^{-11}	= $\bar{x}$

			Tert-butanol		
Conc. (ppm)	**ΔI (µA)**	**L^2/D (s)**	**L (µm)**	**D (cm^2 s^{-1})**	**K @293 kelvin**
405	2.15	432	0.09	1.93 x10^{-13}	1779
820	4.36	303	0.06	1.38 x10^{-13}	
1230	8.63	638	0.18	5.06 x10^{-13}	
1640	9.18	819	0.18	4.13 x10^{-13}	
2023	8.30	501	0.08	1.32 x10^{-13}	
			0.12	2.76 x10^{-13}	= $\bar{x}$

			Propanal		
Conc. (ppm)	**ΔI (mA)**	**L^2/D (s)**	**L (µm)**	**D (cm^2 s^{-1})**	**K @293 kelvin**
1250	0.15	154	0.17	6.53 x10^{-13}	317
2467	0.17	28	0.12	4.69 x10^{-13}	
4934	0.99	31	0.25	9.65 x10^{-13}	
7500	3.58	156	0.23	6.23 x10^{-13}	
9968	4.12	143	0.09	1.76 x10^{-13}	
			0.17	5.77 x10^{-13}	= $\bar{x}$

			Hexanal		
Conc. (ppm)	**ΔI (µA)**	**L^2/D (s)**	**L (µm)**	**D (cm^2 s^{-1})**	**K @293 kelvin**
128	8.33	624	29.3	1.38 x10^{-8}	97
256	24.2	762	51.9	3.54 x10^{-8}	
384	39.2	781	57.5	4.23 x10^{-8}	
520	53.0	763	57.0	4.25 x10^{-8}	
649	66.9	926	69.8	5.27 x10^{-8}	
			53.1	3.73 x10^{-8}	= $\bar{x}$

Table 7.2: Compiled calculated values of *L* and *D* from CO-A1 sensors at 20° C. *K* is the Henry's law parameter for the dissolution of each VOC in aqueous media [124].

It is considered quite likely that the VOCs have a greater tendency to condense within the membrane pores than CO, given that they are at substantial fractions of their saturated vapour pressures and quite hydrophobic. This is particularly true of the longer chain VOCs. Hexanal shows atypical behaviour compared to the other VOCs with *D* values nearer those expected for simple diffusion in liquids and much greater effective thicknesses (of the order of 50 μm). Hexanal is the most hydrophobic of the VOCs in Table 7.2 and therefore might be expected to interact most strongly with the hydrophobic porous membrane. The more polar VOCs, e.g. the smaller alcohols show very small effective thicknesses.

7.6.1 Temperature Dependence

More information on the sensor mechanism can be obtained from the temperature dependence, which is also directly relevant to the behaviour of the sensor in applications where changes due to variations of the ambient the temperature are important. As can be seen from Figures 7.26 to Figures 7.29 each VOC has a different set of temperature dependence characteristics. Methanol shows a slight increase in *L* values as the operating temperature of the CO-A1 sensor increases. Heptanol and isopropanol show decreases in *L*, as does tert-butanol, except for an anomalous point at 50°C. A decrease in *L* with temperature can be explained in terms of a reduction in the tendency of the VOC to condense in the porous membrane at higher temperature. It should be noted that the temperature here is the temperature of the sensor rather than of the Dreschel bottle, which is constant and serves to fix the partial pressure of the VOC. There is a tendency for the *D* values to increase as the temperature increases, but with some anomalous data, e.g., for heptanol and isopropanol (figs 7.27 and 7.29).

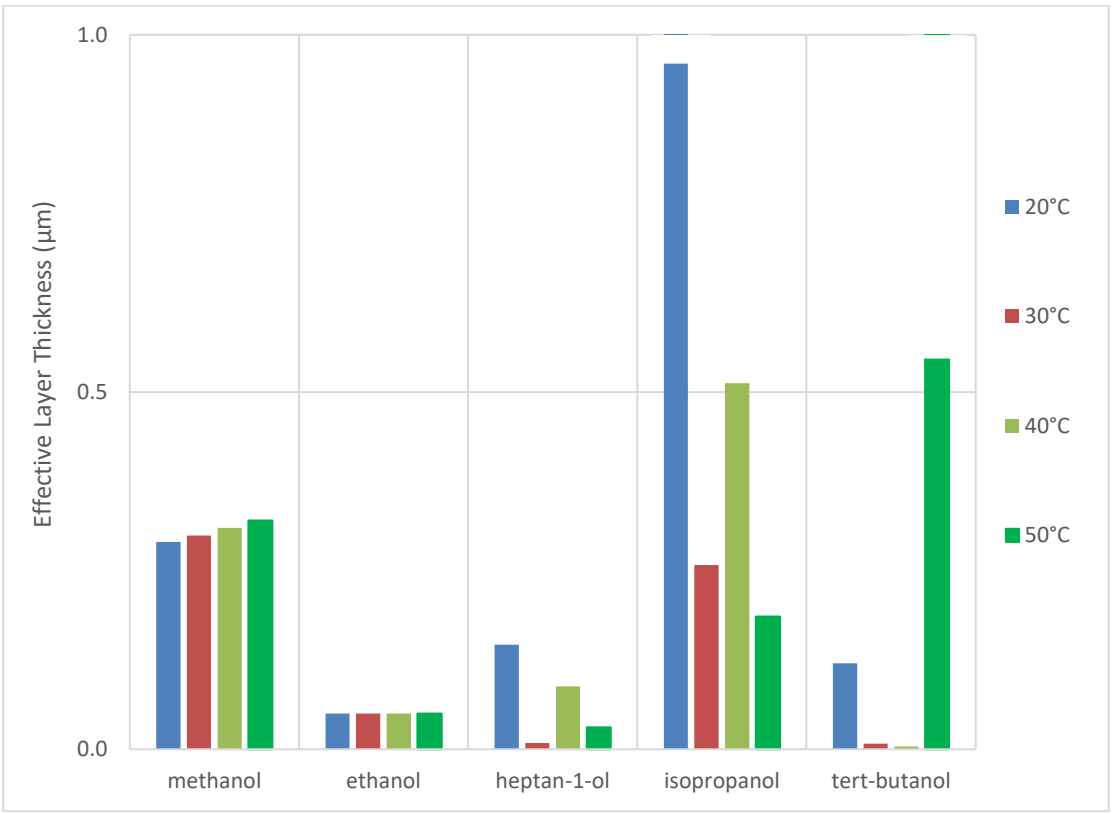

Figure 7.26: Collated effective thickness (*L*) data for the alcohols at all temperatures.

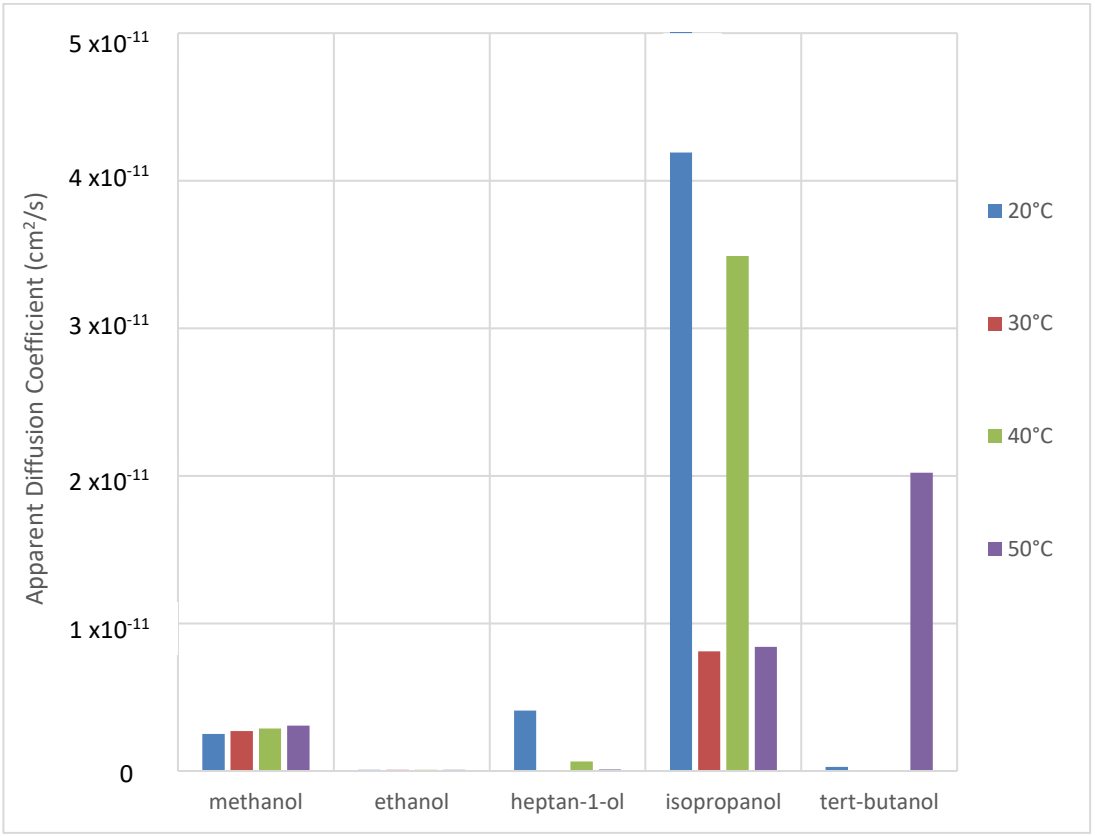

Figure 7.27: Collated apparent diffusion coefficient data (*D*) for the alcohols at all temperatures.

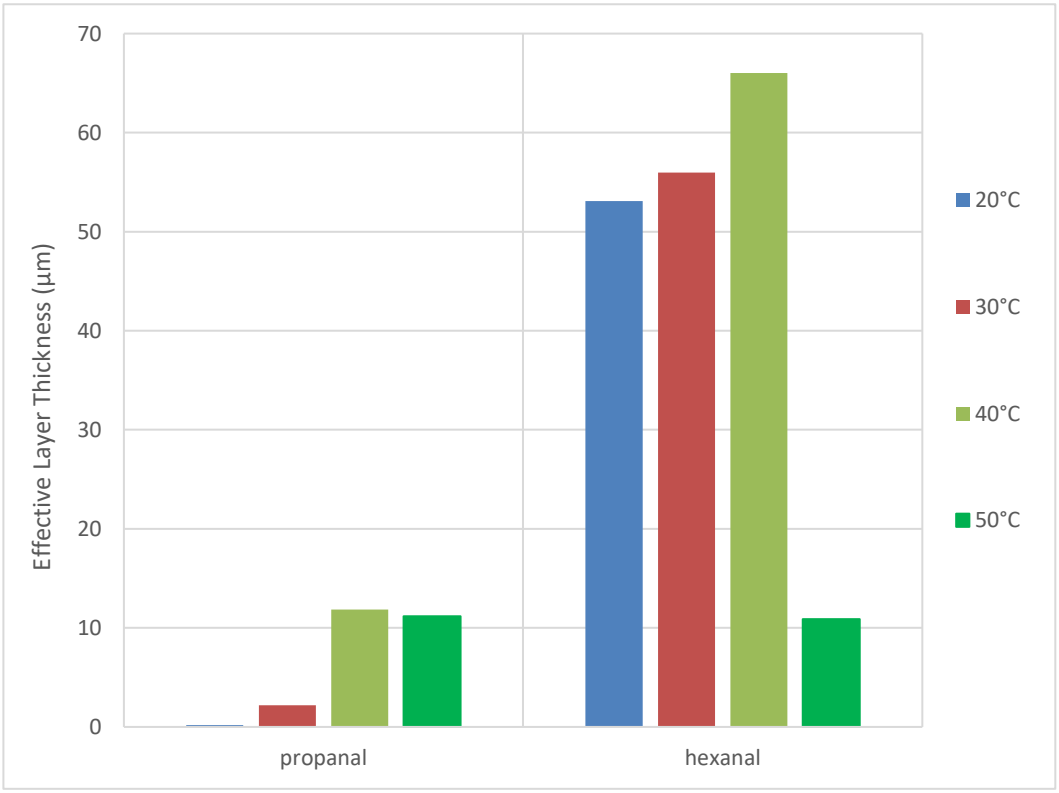

Figure 7.28: Graph of collated *L* data for the aldehydes at all temperatures.

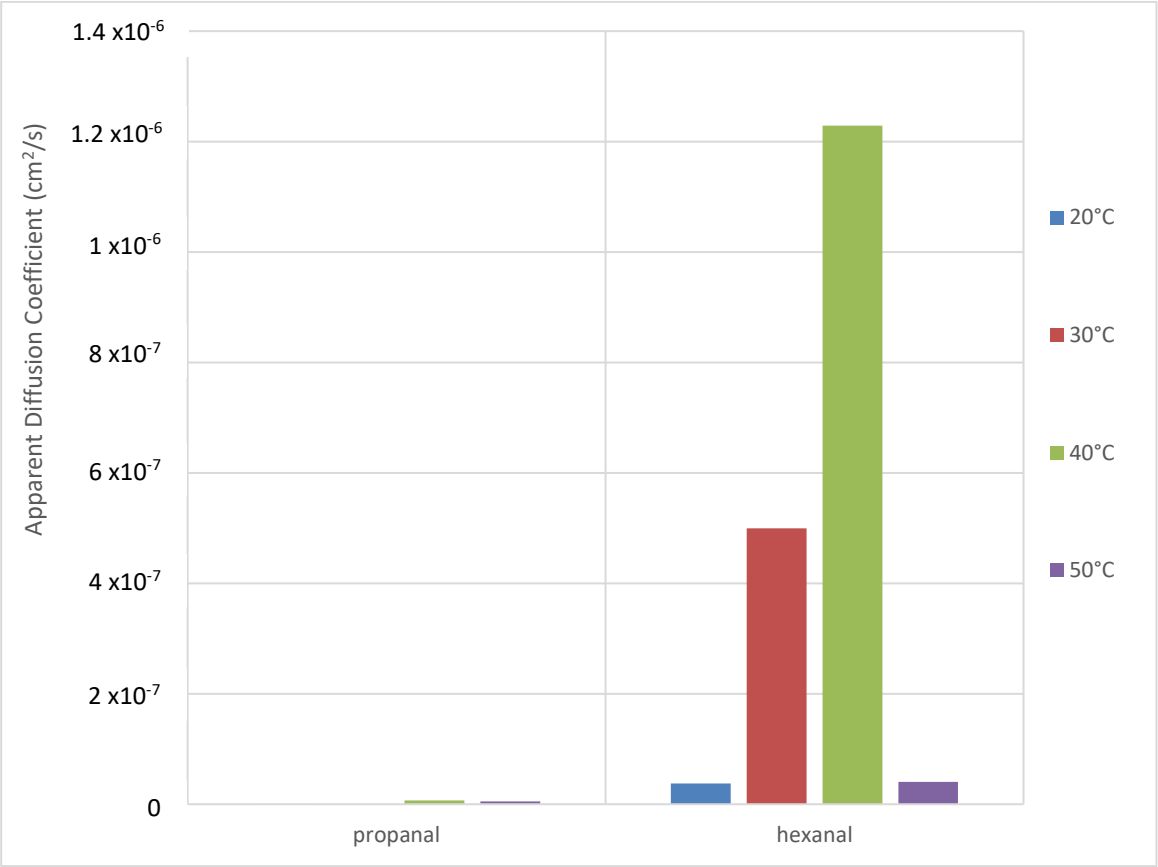

Figure 7.29: Graph of collated *D* data for the aldehydes at all temperatures.

In condensed phases (liquids, solids), diffusion is an activated process and follows an equation similar to the Arrhenius law of chemical kinetics, equation (7.9). A plot of ln *D* against 1/T can then be used to obtain the activation energy for diffusion (Fig 7.30). For those cases in which there is a regular increase in D with temperature, the activation energies obtained from this analysis are collected in table 7.3. It can be seen from the table below that the activation energies for the alcohols agree with the literature [174, 175]. *D* = diffusion coefficient, A = frequency of collisions, E_a = activation energy in kJ/mol, R = gas constant, T = temperature in kelvin

$$D = A\, e^{-\frac{Ea}{RT}} \qquad (7.9)$$

Rearranged to a form suitable for graphical analysis: $\ln D = \frac{-Ea}{R} * \frac{1}{T} + \ln A$ (7.10)

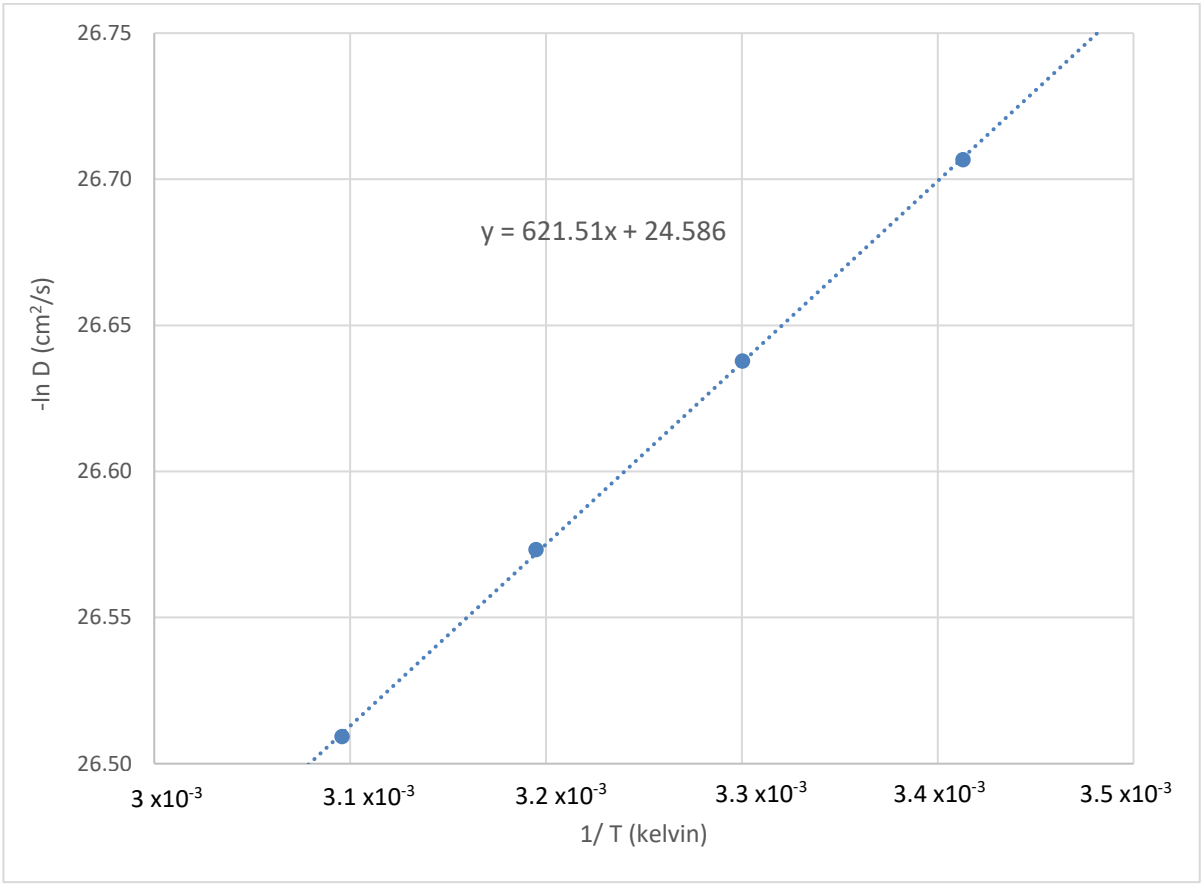

Figure 7.30: Example Arrhenius plot for the apparent diffusion coefficient of methanol in a CO-A1 device.

VOC	Ea (kJ mol^{-1})
methanol	5.17
ethanol	5.13
propanal	23.7
hexanal	11.9

Table 7.3: Activation energies for the apparent diffusion coefficients of alcohols and aldehydes from the Arrhenius analysis of the temperature-dependent *D* data.

Typically activation energies for diffusion are lower than for common chemical reactions (several tens of kJ mol^{-1}) because no bond breaking is involved; the origin of the activation is the requirement for diffusing species to displace neighbouring molecules in order to make a jump to the next site. The data in table 7.3 is consistent with this picture.

7.7 Summary

CO-A1 devices respond linearly to a range of VOCs. Alcohols and aldehydes are oxidised at usable operating potentials of 0.0 – 0.3 V against the internal reference of the sensor. Unlike CO, the response is not clearly mass transport controlled in all cases; in particular, methanol shows a strong potential dependence. The device shows a good linear response to alcohols and aldehydes, but little response to ketones and esters. We interpret this in terms of the general mechanism of oxidation of alcohols via 2 electron pathways to aldehydes/ketones and 4 electron pathways to carboxylic acids. Aldehydes are much more easily oxidised than ketones, suggesting that secondary alcohols follow a 2 electron path in the sensors and primary alcohols may undergo a 4 electron oxidation. The lack of response to esters and ketones also suggests complete oxidation to CO_2 is not observed at the potentials accessible (-0.1 – 0.3 V against internal reference) and at the temperatures of < 50 ^{o}C employed.

The chronoamperometric response of the sensor to pulsed changes in VOC concentrations is satisfactorily fitted by the mass transport-based regression model of Chapter 3. The devices recover the baseline current after being switched to air from the VOC and the time of recovery is approximately the same as the response time. This is also consistent with both being controlled by an effective L^2/D parameter in the diffusion model. The effective values of *L* and *D* deduced from the fitting are very different for the VOCs compared to CO. All the values of effective diffusion coefficient are much lower and indicated that a condensed phase diffusion process must be considered. The effective thicknesses are generally very small (< 1 mm) except for hexanal which shows values of order 50 μm. We interpret the data in terms of condensation of the VOC in the pores of the membrane and a blocking effect on the transport. For some VOCs, especially methanol, we also expect that electrode kinetic limitations reduce the steady-state current and therefore give rise to an underestimation of *D* when a mass transport model is invoked which assumes the steady-state current is proportional to *D*. The temperature dependence of the response is complex, but in some cases (methanol, ethanol, propanal, hexanal) can be interpreted in terms of an activated diffusion process, again, characteristic of transport in a condensed phase rather than the vapour phase.

Finally, the trend in analytical sensitivity is unexpected. The devices show higher sensitivity to alcohols of higher molar mass, when a simple interpretation might have been that larger molecules would have lower mass transport rates and lower vapour pressure. The observations can be rationalised by the differences in polarity and different tendency to adsorb and condense and block the porous membrane.

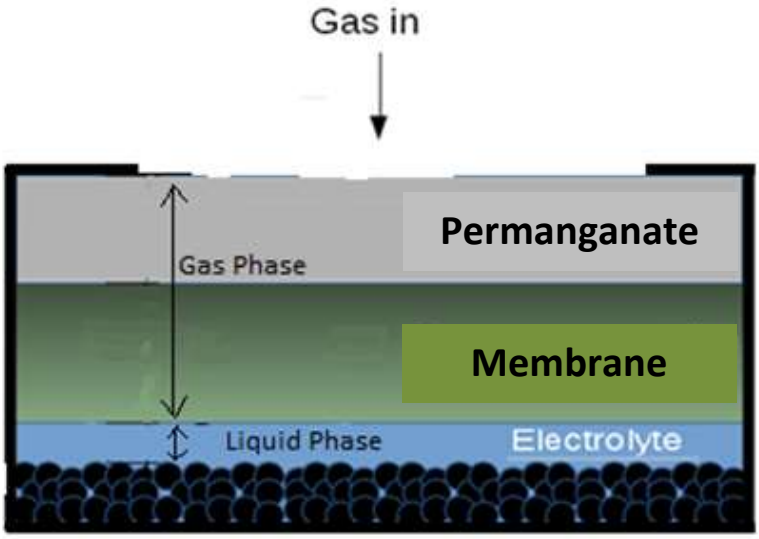

Figure 7.31: Diagram showing the construction of the CO-AF working electrode, porous membrane and permanganate filter layer.

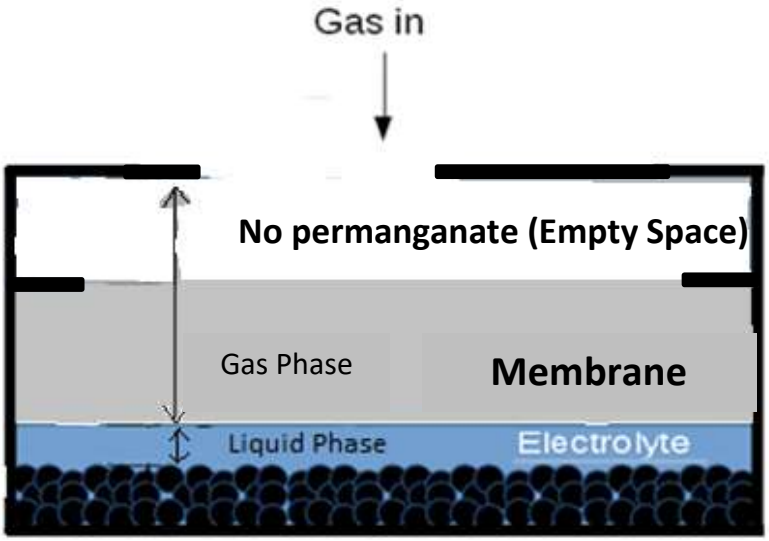

Figure 7.32: Diagram showing the construction of the CO-A1 working electrode and porous membrane as used in this chapter. Unlike the CO-AF devices, there is no permanganate filter layer.

[150] M.-V. Mathieu, M. Primet
Applied Catalysis, 1984, **9**, 361-370

[151] W. Shi, B. Yi, M. Hou, F. Jing, P. Ming
J. Power Sources, 2007, **165**, 814-818

[152] Z. Kowalczyk, K. Stołecki, W. Rarog-Pilecka, E. Miskiewicz, E. Wilczkowska, Z. Karpinski
Applied Catalysis A: General, 2008, **342**, 35-39

[153] R. B. Kutz, B. Braunschweig, P. Mukherjee, R. L. Behrens, D. D. Dlott, A. Wieckowski
J. Catalysis, 2011, **278**, 181-188

[154] L. Han, H. Ju, Y. Xu
Int. J. Hydrogen Energy, 2012, **37**, 15156-15163

[155] S. H. Joo, J. Y. Park, J. R. Renzas, D. R. Butcher, W. Huang, G. A. Somorjai
Nano Lett., 2010, **10**, 2709-2713

[156] S. Rousseau, C. Coutanceau, C. Lamy, J-M. Leger
J. Power Sources, 2006, **158**, 18-24

[157] F. Vigier, C. Coutanceau, F. Hahn, E.M. Belgsir, C.Lamy
J. Electroanal. Chem., 2004, **563**, 81-89

[158] J. Florez-Montano, G. Garcia, O. Guillen-Villafuerte, J. L. Rodriguez, G. A. Planes, E. Pastor
Electrochimica Acta, 2016, **209**, 121-131

[159] S. Sun, M. C. Halseid, M. Heinen, Z. Jusys, R. J. Behm
J. Power Sources, 2009, **190**, 2-13

[160] S-Y. Yan, Y-R. Huang, C-Y. Yang, C-W. Liu, J-H. Wang, K-W. Wang
Electrochimica Acta, 2018, **259**, 733-741

[161] P. Katikawong, T. Ratana, W. Veerasai
J. Chem. Sci., 2009, **121**, 329-337

[162] H. Wang, Z. Jusys, R. J. Behm
J. Phys. Chem. B, 2004, **108**, 19413-19424

[163] K. Kinoshita, J. T. Lundquist, P. Stonehart
J. Electroanal. Chem., 1973, **48**, 157-166

[164] D. A. J. Rand, R. Woods
J. Electroanal. Chem., 1972, **35**, 209-218

[165] V. Lockett, M. Horne, R. Sedev, T. Rodopoulos, J. Ralston
Phys. Chem. Chem. Phys., 2010, **12**, 12499–12512

[166] D. C. Johnson, D. T. Napp, S. Bruckenstein
Electrochimica Acta, 1970, **15**, 1493-1509

[167] M. H. Barley, G. McFiggans
Atmos. Chem. Phys., 2010, **10**, 749–767

[168] A. V. Rudnev, E. B. Molodkina, A. I. Danilov, Y. M. Polukarov, A. Berna, J. M. Feliu
Electrochimica Acta, 2009, **54**, 3692-3699

[169] K. Kunimatsu, M. G. Samant, H. Seki, M. R. Philpott
J. Electroanal. Chem., 1988, **243**, 203-208

[170] E. A. Batisita, G. R. P. Malpass, A. J. Motheo, T. Iwasita
J. Electroanal. Chem., 2004, **571**, 273-282

[171] L. Dong, R. R. S. Gari, Z. Li, M. M. Craig, S. Hou
Carbon, 2010, **48**, 781-787

[172] E. A. Batista, H. Hoster, T. Iwasita
J. Electroanal. Chem., 2003, **554**, 265-271

[173] C. S. Fugivara, P. T. A. Sumodjo, T. Rabockai
Electrochimica Acta, 1989, **34**, 363-370

[174] R. M. Garland, M. J. Elrod, K. Kincaid, M. R. Beaver, J. L. Jimenez, M. A. Tolbert
Atmos. Environ., 2006, **40**, 6863-6878

[175] H. Tatsumi, F. Liu, H.-L. Han, L. M. Carl, A. Sapi
J. Phys. Chem. C, 2017, **121**, 7365-371

Chapter 8

8.0 Hydrogels

Whilst the CO-AF sensors work well as a commercial product and have been proven to generate revenue for the company, there remains a question of lifetime operational endurance. The current configuration of the CO-AF sensor (with a 5M H_2SO_4 liquid electrolyte, monometallic Pt electrodes and a PTFE semi-permeable membrane) has a warranted lifetime of 24 months. The lifetime is determined by the sulfuric acid electrolyte; it must remain at a high, constant concentration in order for the electrochemical sensor to function properly and allow determination of the analyte concentration from the chronoamperometric response. The problem with the sulfuric acid electrolyte is that it is extremely hygroscopic, and, over time, water vapour from the air enters the sensor and leads to a change in the volume and subsequent concentration of the sulfuric acid liquid electrolyte. This is in spite of the hydrophobic semi-permeable PTFE membrane placed above the electrolyte in the sensor stack configuration. This problem is somewhat mitigated by the choice of a high initial sulfuric acid concentration, such that dilution effects are not serious, however, the volume change eventually causes swelling of the sensor and irreparable damage.

Another problem to consider with the use of sulfuric acid is that it is quite corrosive, and it can cause chemical burns to those handling it [176]. This is particularly relevant to the manufacturing process of the sensors, as worker safety is of paramount concern to any modern company. The substance also falls under REACH compliance legislation (EU law) requirements and so incurs an additional cost to the business using it, since they must register their use of it with the appropriate authorities [177]. Sulfuric acid is also listed under the UN transport of dangerous goods article, this means extra cost is incurred by the business when transporting the sensors as they contain sulfuric acid (albeit in small quantities). It therefore stands to reason that finding a replacement electrolyte which is less corrosive and less hygroscopic would reduce these manufacturing issues and enable the sensor to have a much longer operational lifetime.

In this chapter the possibility of using hydrogels as electrolytes in place of sulfuric acid is explored in a preliminary way. Hydrogels, such as polyacrylic acid, are solid-like in their mechanical properties and therefore easier to handle, do not have the same potential to leak and are relatively non-toxic. It is not however, known if they can function as electrolytes with low resistance and with no interfering faradaic processes. Nor is it known if they can remain stable for long time periods or whether their vapour pressure will prove to be too high to avoid long-term degradation of the sensor performance because of evaporation, or in humid air, because of condensation of water vapour.

The use of hydrogels as a replacement electrolyte was investigated using a selection of aqueous redox couples as test analytes because this avoids the need to assemble the hydrogel into a complete sensor for gas-phase analytes. The hydrogels were prepared by adding polyacrylamide co-acrylic acid potassium salt (PAA) to demineralised water. This was mainly driven by the desire to find a less toxic and less hygroscopic alternative to the 5M sulfuric acid used within the sensors. Another reason for investigating the use of hydrogels is that they may have sufficiently low water vapour pressures to enable sensors to have a longer operating lifetime. The physical properties of hydrogels (namely their gelatinous nature) also ensures that the risk of possible flooding of the permanganate powder and semi-permeable membrane by the electrolyte is greatly reduced. Flooding of the membrane by the electrolyte depresses the sensor sensitivity because the diffusion coefficients of analytes in the electrolyte are typically 3 - 4 orders of magnitude lower than in the gaseous phase (Fig 8.1).

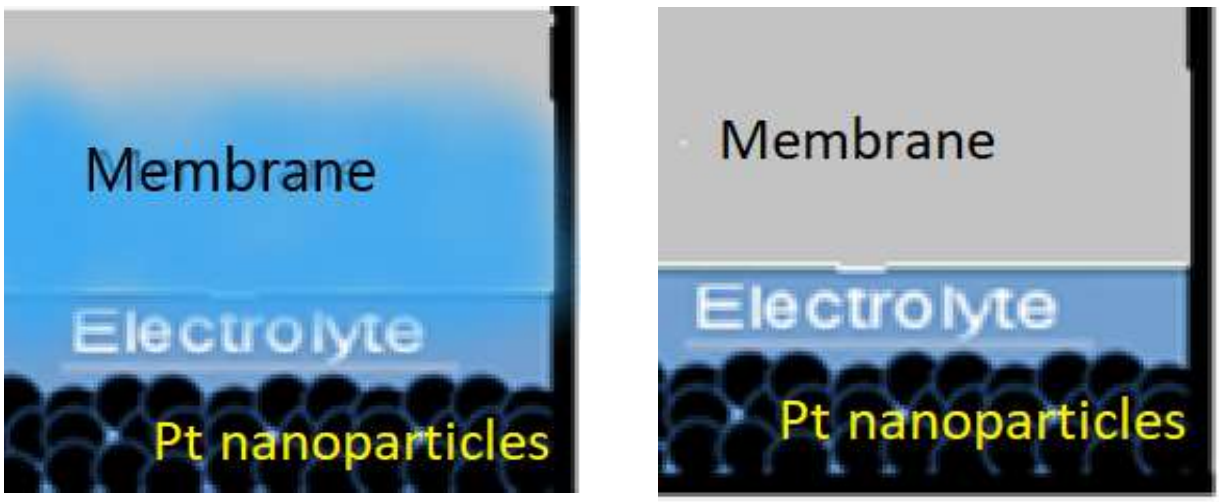

a) **b)**

Figure 8.1: Flooding of the sensor by sulfuric acid electrolyte. a) flooded membrane and b) normal membrane.

All gels were made on the same day within quick succession of each other in order to ensure accurate tracking of any water loss or change in electrochemical performance over time. They were then tested again at intervals of several days. The hydrogels are homogenous cross-linked polymeric matrices at sufficiently high weight percentages. The observed characteristics of the PAA hydrogels were that they are highly viscous from 1 % to 5 % weight PAA but at 20 % weight PAA and above they no longer flow even when the sample is inverted in a vial. This was as expected since PAA is known to be extremely hydrophilic and so readily absorbs water into its cross-linked polymer structure. Rheological data confirming these interpretations of simple observations are presented in section 8.1 of this chapter.

Weight tracking measurements are presented in section 8.2 of this chapter. These measurements simply involve the recording of the mass of a sample of hydrogel as a function of time in an atmosphere of controlled relative humidity. They simulate the effects of sensor storage on the electrolyte. In order to investigate the viability of hydrogels as electrolytes, electrochemically active redox couples were added into the hydrogels. In order to investigate the basic electrochemistry of these media and determine if the background currents and the diffusion rates in the hydrogels were appropriate for their use in sensors, the redox couples were investigated in a simple three electrode cell setup (as described in chapter 2), rather than attempt to construct an entire sensing device with hydrogel

electrolyte. The reason for this choice is that a whole sensor may fail for many reasons unconnected with the electrolyte, but by focusing on the basic electrochemical behaviour of the hydrogels, it can be determined if they are suitable at all.

8.1 Hydrogel Characterisation

A polymer hydrogel comprises a *three-dimensional* network which is able to retain the aqueous phase. Polyacrylic acid (PAA) molecules are capable of forming gels because of the possibility for cross-link between individual chains. The PAA chains cross link by forming weak bonds such as hydrogen bonds with other polymer chains (Fig 8.2). The polymer network can then retain the solvent (water) by hydrogen bonds between water molecules and the O and N atom H-bond acceptors in the polymer chain. PAA is provided as the potassium salt; in this case the deprotonated carboxylic groups may also form salt bridges with K^+ ions between two carboxylates [178, 179]. Gel formation is usually confirmed by rheology, there is much literature on the rheology, glass transition temperature, and different effects on the mechanical characteristics of hydrogels [180 - 183]. The PAA hydrogels have been characterised, to confirm whether they are gels at the concentrations employed.

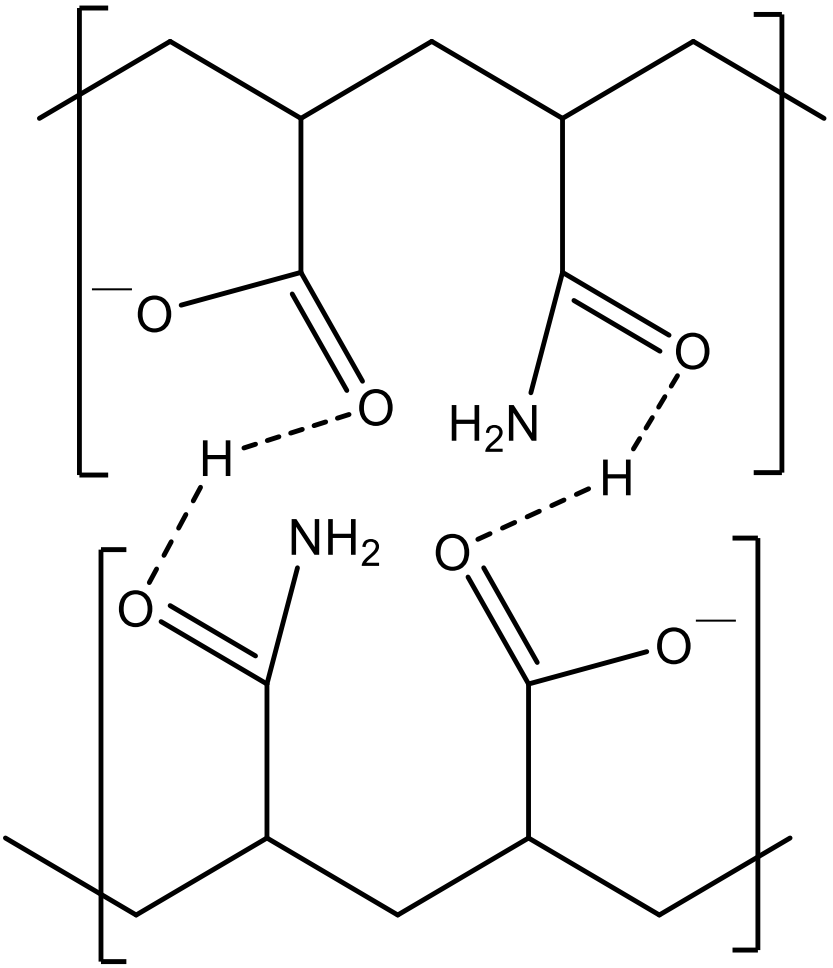

Figure 8.2: Poly acrylic acid illustrating the interchain hydrogen bonds responsible for gelation.

In order to assess the rheological aspects of the PAA hydrogel it was decided that shear rheology using a linear shear rheometer would be appropriate. The results are shown below (Figs 8.3 and 8.4) and indicate that the hydrogels exhibit behaviour consistent with a non-Newtonian fluid model (viscosity not independent of stress, as shown in chapter 2). The viscosity is essentially the slope of the shear stress against shear rate plot which in Fig. 8.3 is clearly non-linear. The hydrogels become less viscous at high shear rate, a behaviour known as shear thinning.

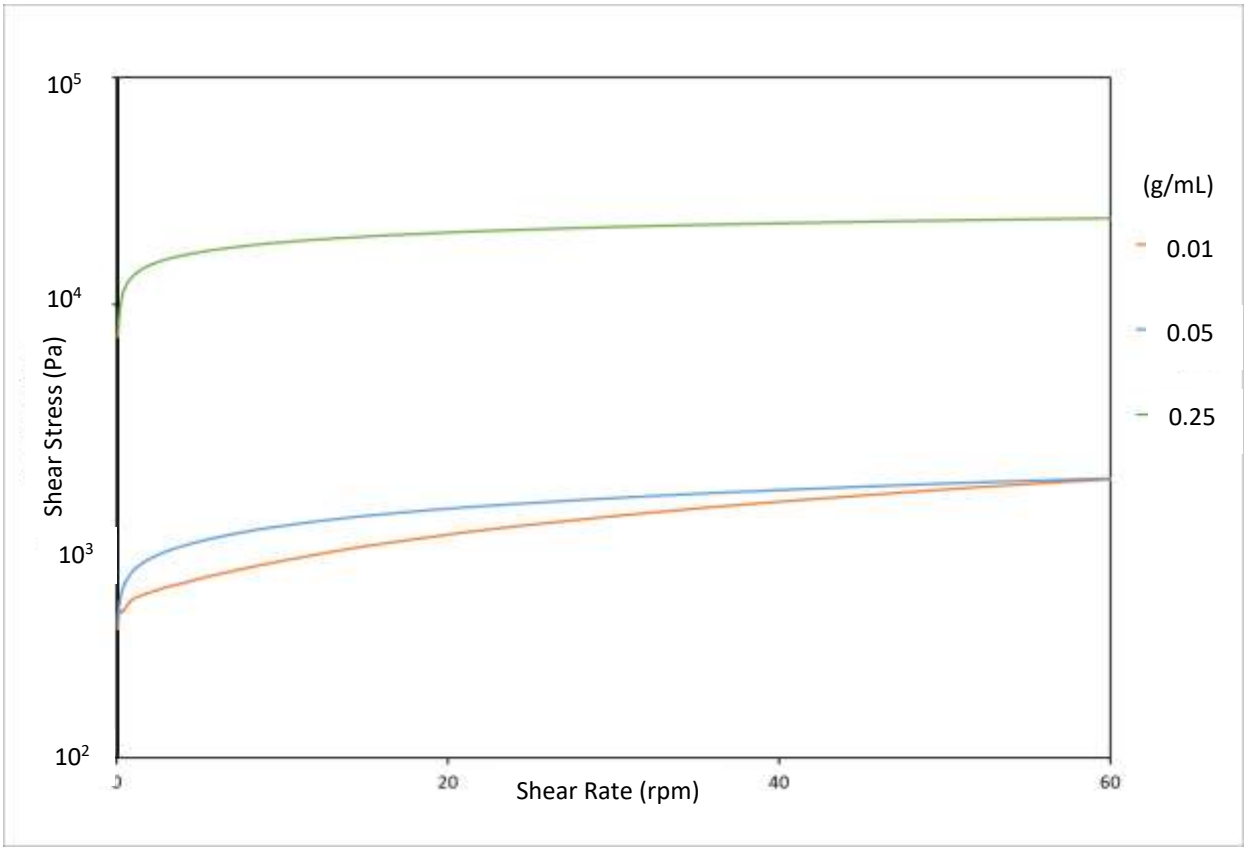

Figure 8.3: Shear stress as a function of shear rate. Behaviour typical of non-Newtonian fluids.

The graph above shows the relationship between shear rate and shear stress for the hydrogels. At 1 % w/v and 5 % w/v PAA the hydrogels have similar values of shear stress at the same shear rates. At 25 % PAA concentration the hydrogel shows an order of magnitude more shear stress at the same shear rates than the lower PAA concentrations. This indicates that there is an increase in the number of crosslinked polymer chains as the PAA concentration increases.

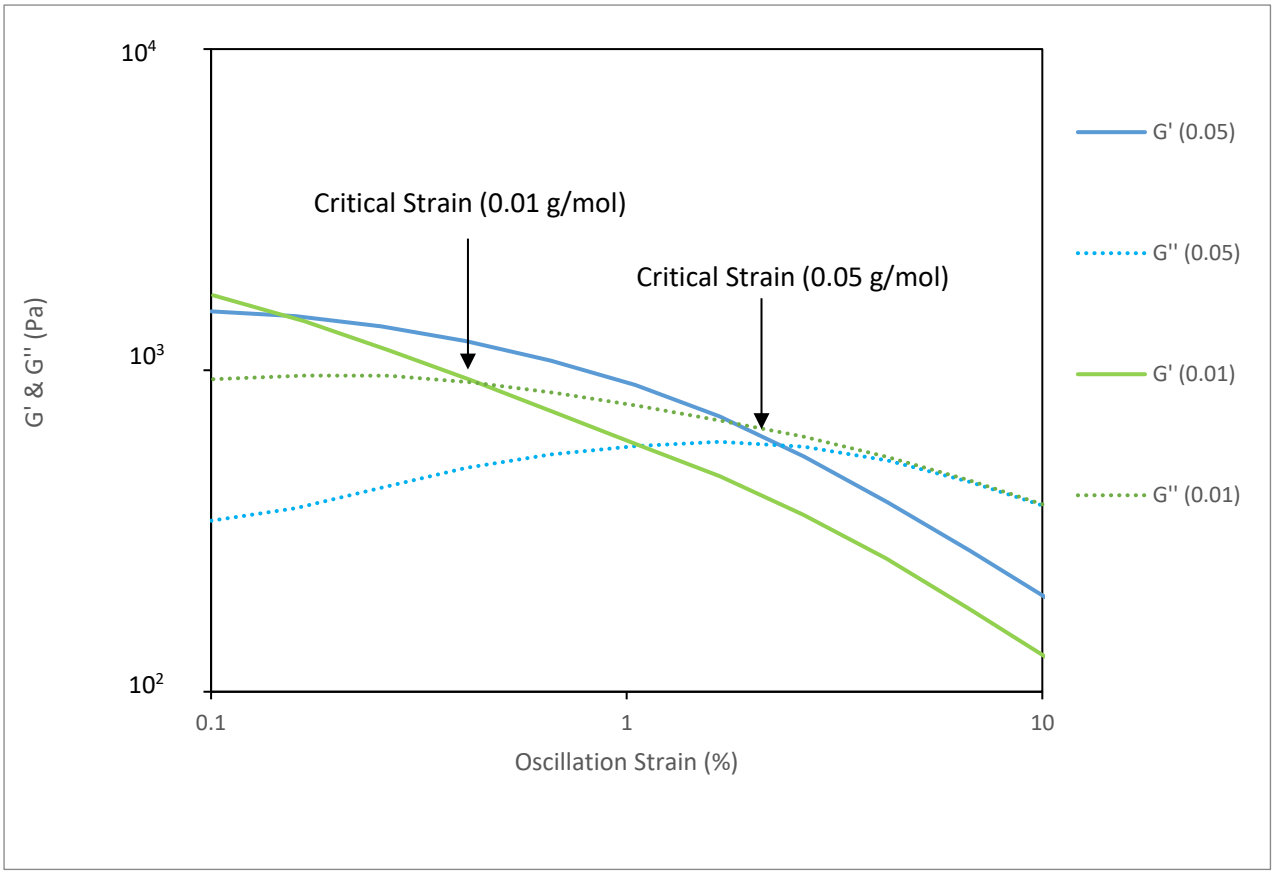

Figure 8.4: Critical strain points of hydrogels at different PAA concentrations (green = 1 % PAA concentration, blue = 5 % PAA concentration)

In addition to shear rate, it is also relevant to study the effect of strain because gels have properties that are intermediate between solids and liquids. This was done under conditions of oscillating strain and the response of the gel contains both in-phase (G') and out-of-phase components (G''). G' is a measure of the elasticity of the hydrogel and represents the solid-state behaviour of the hydrogel. G" is a measure of the viscosity of the hydrogel and represents the liquid-state behaviour of the hydrogel. When G' > G" the hydrogel is more characteristic of a solid and the crosslinking polymer chains can absorb the oscillation strain energy without causing permanent deformation of the lattice matrix. When G' < G" the hydrogel is more characteristic of a liquid and flows more easily due to the crosslinking polymer chains having been broken by the mechanical energy of the oscillation strain from the instrument. The critical strain point is where G' = G" and represents the transition of the material from gel to liquid, due to the intermolecular hydrogen bonds between the cross-linked polymer chains being broken under the strain of the measurement.

A critical strain point at a higher oscillation strain indicates a greater amount of polymer crosslinking in the hydrogel. As expected, the rheological measurements involving an oscillating strain show that increasing the PAA concentration of the hydrogel increases the critical strain point (Fig 8.4). Nevertheless, even for 1 % w/v PAA, a critical strain point is observed, and the sample has gel-like behaviour at very low strain.

8.2 Hydrogel Weight Tracking

By tracking the weight of the hydrogels over the course of several weeks, trends in evaporation rates between the different PAA weight/volume percentages can be studied. It was expected that there would be an initial decrease in weight due to water evaporation into the atmosphere, but then the gel would reach a stable weight (accounting for minor fluctuations) within a week or so. It can be seen from the results (Fig 8.5) that, unfortunately, this was not the case. The hydrogels continued to lose mass through water evaporation at a steady rate, until only dry gel remained (xerogel). Given the fact that the PAA forms cross-linked chains within the hydrogel, it was assumed that the intermolecular forces would be strong enough to prevent significant evaporation of the water molecules, or at least set up an equilibrium with the water vapour in the air to give the appearance of no change in hydrogel weight.

The results of the hydrogel weight tracking experiments are shown below (in order of unsealed samples, Fig 8.5 and samples sealed in controlled humidity, Fig 8.6). As can be seen from the graphs below, there is a rapid decline in weight with time (Fig 8.5) for the unsealed sample. It was noted that after 43 days the samples were completely dry and did not take up water from the surrounding air. In contrast, the samples sealed in humid air retain of the order of 90% of their mass for 60 days.

PAA (g)	demin. water (mL)	start weight (g)	2 days	5 days	7 days	14 days	43 days	Δ% weight
0.05	9.95	10.1	9.32	8.35	7.58	5.84	0.46	95
0.10	9.90	10.1	9.36	8.30	7.55	5.64	0.39	96
0.15	9.85	10.1	9.39	8.43	7.79	6.03	0.59	94
0.20	9.80	9.97	9.10	8.02	7.31	5.46	0.58	94
0.25	9.75	10.1	9.11	8.03	7.23	5.21	0.69	93
0.30	9.70	10.1	9.06	7.76	6.86	4.57	0.71	93
0.35	9.65	9.97	8.79	7.49	6.56	4.30	0.74	93
0.40	9.60	10.1	8.92	7.51	6.54	4.02	0.96	91
0.45	9.55	10.2	9.14	7.80	6.89	4.61	1.06	90
0.50	9.50	10.3	9.20	7.81	6.83	4.53	1.08	90

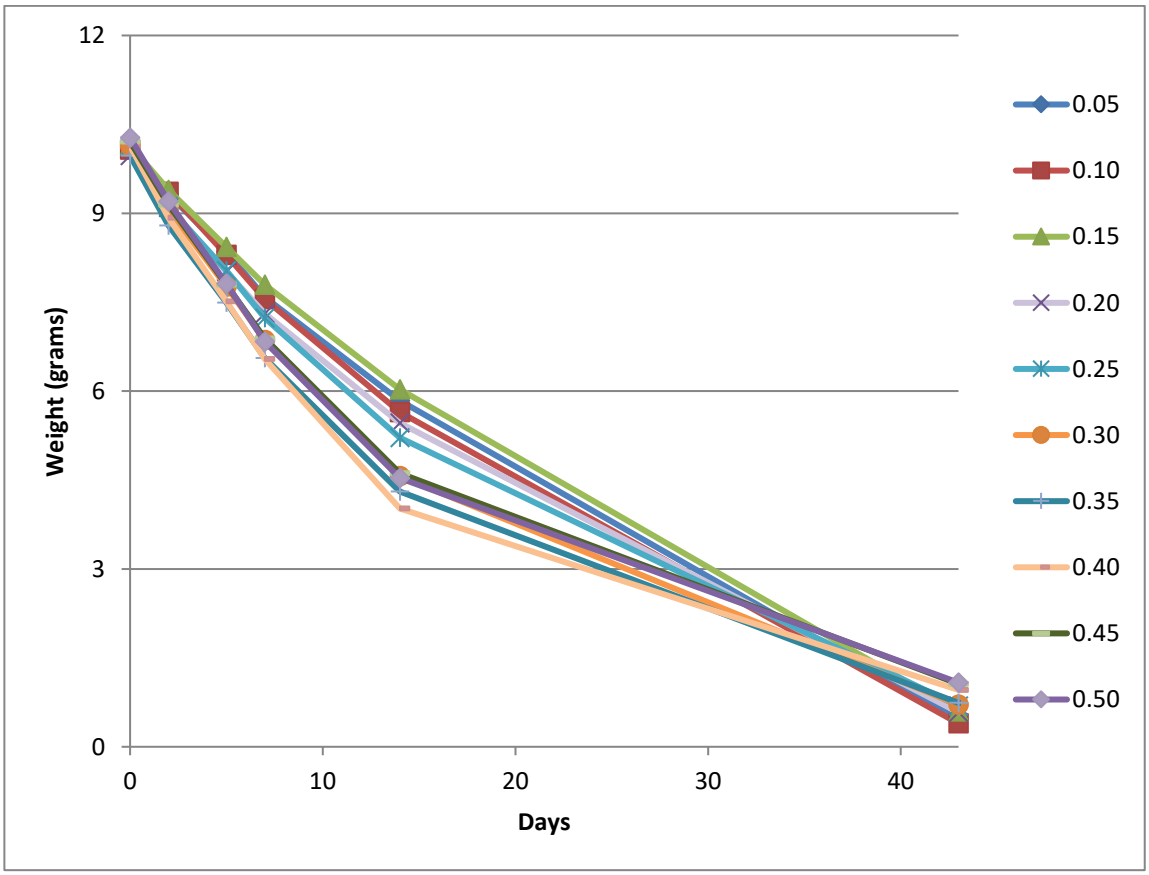

Figure 8.5: Graph of different PAA weights with their recorded weights against days spent exposed to air in normal laboratory conditions.

PAA (g)	demin. water (mL)	start weight (g)	2 days	7 days	14 days	30 days	60 days	Δ% weight
0.05	9.95	10.6	10.6	10.52	10.5	10.3	10.2	4
0.10	9.90	10.0	9.97	9.59	9.41	9.34	9.02	10
0.15	9.85	9.77	9.67	9.65	9.53	9.34	9.10	7
0.20	9.80	9.74	9.71	9.65	9.54	9.14	8.85	9
0.25	9.75	10.1	10.1	9.99	9.91	9.68	9.44	6
0.30	9.70	9.76	9.72	9.66	9.58	9.45	9.27	5
0.35	9.65	9.82	9.74	9.64	9.58	9.34	9.07	8
0.40	9.60	10.1	10.1	10.0	9.86	9.52	9.26	8
0.45	9.55	9.70	9.66	9.59	9.44	9.30	9.10	6
0.50	9.50	10.0	9.95	9.85	9.75	9.64	9.45	6

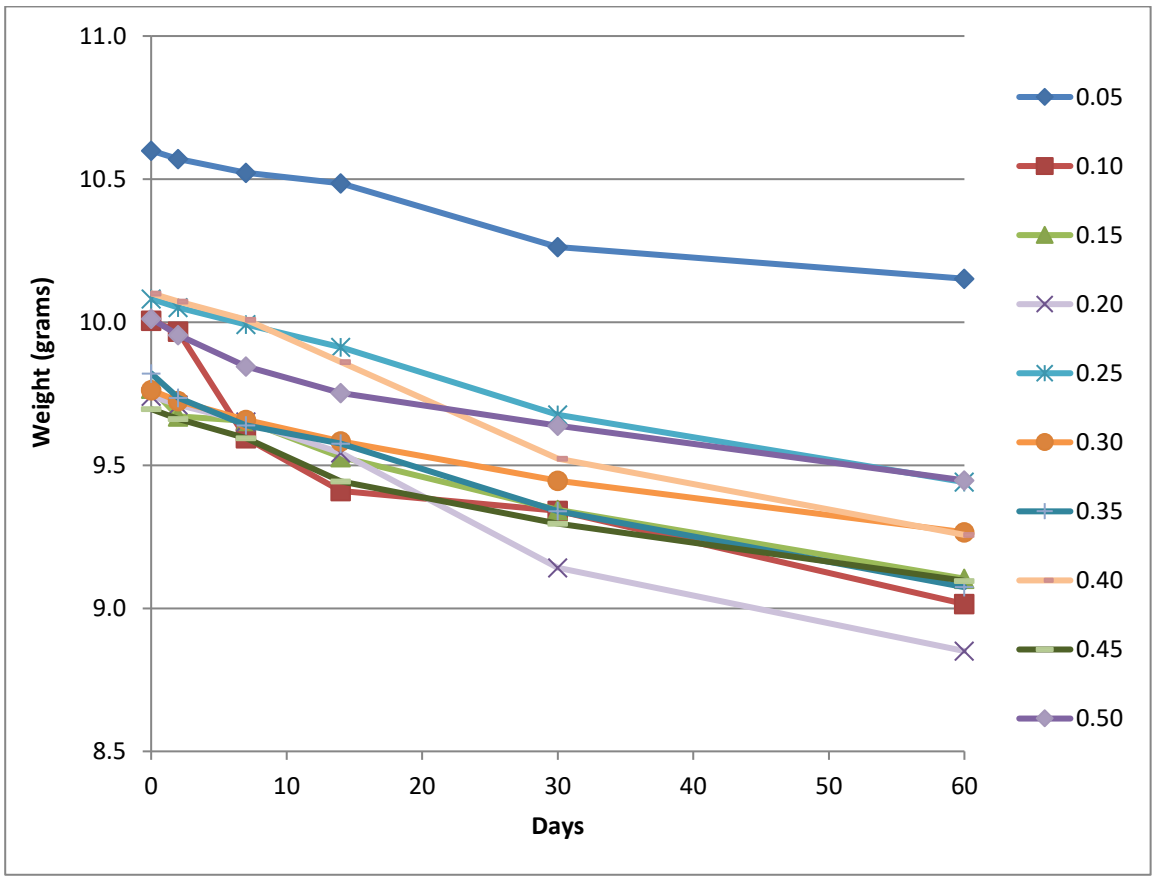

Figure 8.6: Graph of different PAA weights with their recorded weights against days spent exposed to humid air in a sealed vessel.

The weight tracking results show that humidity levels drastically affect the evaporation rates of PAA hydrogel, with low humidity causing extreme water loss over time. The results can be explained by the fact that in high humidity the water cannot readily evaporate as the air is already saturated with water vapour. The applications of the devices are such that they will have to operate in a range of humidity and temperatures. The fact that there appears to be no discernible difference between the behaviour of the different weights of PAA hydrogels indicates that the PAA has no demonstrable effect on the evaporation rate of the water. This suggests that the van der Waals forces between the PAA cross-linked polymer chains and the water molecules are not sufficiently strong. The loss of approximately 90% mass by weight over a relatively short period of time (compared to the warrantied 24-month lifetime of the CO-AF sensor) shows that any sensors fitted with hydrogels would require regular maintenance and attention, such as ensuring water levels and subsequent electrolyte concentrations remained constant. Whilst this would be of little concern for a sensor used within an academic laboratory for electrochemical studies, it renders such a sensor unfit for commercialisation, given that the CO-AF sensors are typically deployed into remote (and sometimes environmentally hostile) locations. Despite the disappointing stability of the gels over time, their electrochemical behaviour was investigated.

8.3 Cyclic Voltammetry of Hydrogels Containing Redox Couple Compounds

The hydrogels with electrochemically active redox species were investigated using cyclic voltammetry at 25 µm diameter Pt microelectrodes in a three-electrode cell as described previously within the methods chapter. The normal expectation is that the microelectrode voltammograms will have a sigmoidal shape with a time-independent steady-state transport limited current. Ferrocyanide, $FeCN_6^{4-}$ is a well-known model redox compound; it undergoes a one-electron oxidation to ferricyanide that has been well-studied [184, 185].

PAA (g)	Demin. Water (mL)	$K_4Fe(CN)_6$ concentration (mM)
0.1	9.9	0.9
0.2	9.8	
0.4	9.6	

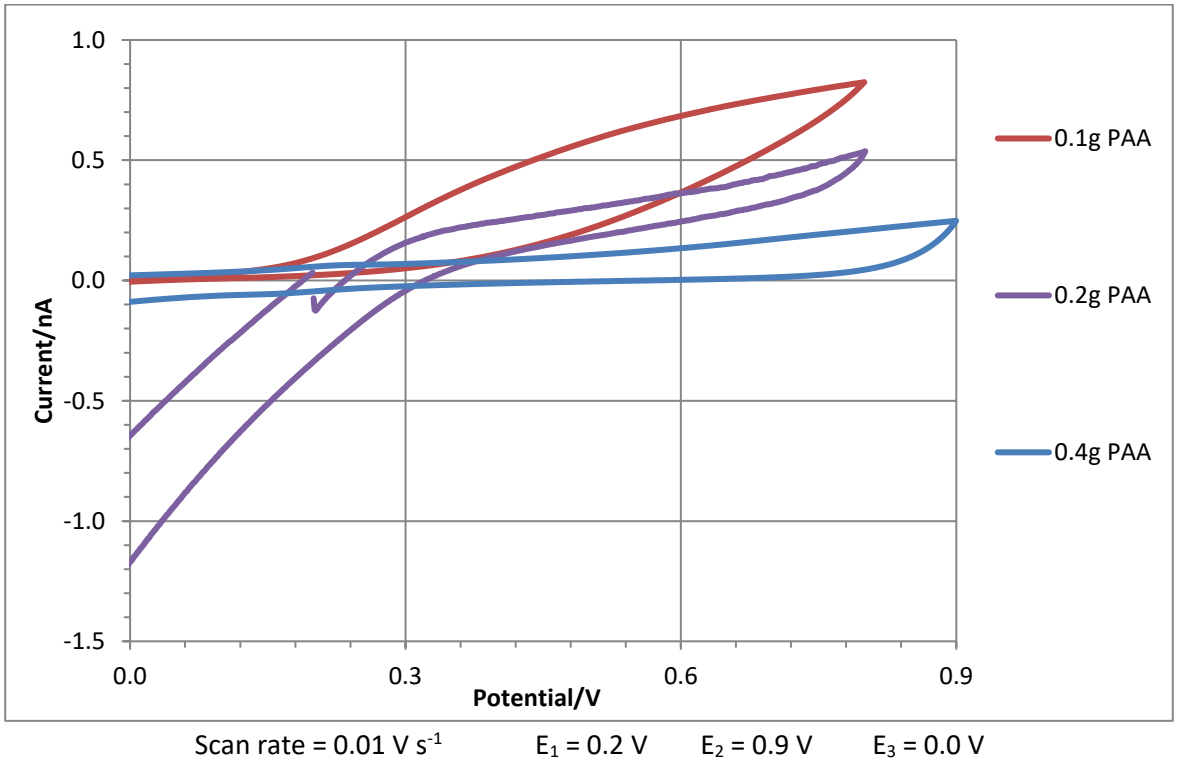

Figure 8.7: Cyclic voltammogram of potassium ferrocyanide gels with different amounts of PAA. (WE = 25 µm Pt disc, CE = 3 mm Pt disc, Ref = Ag/AgCl aq. 1 M KCl(aq))

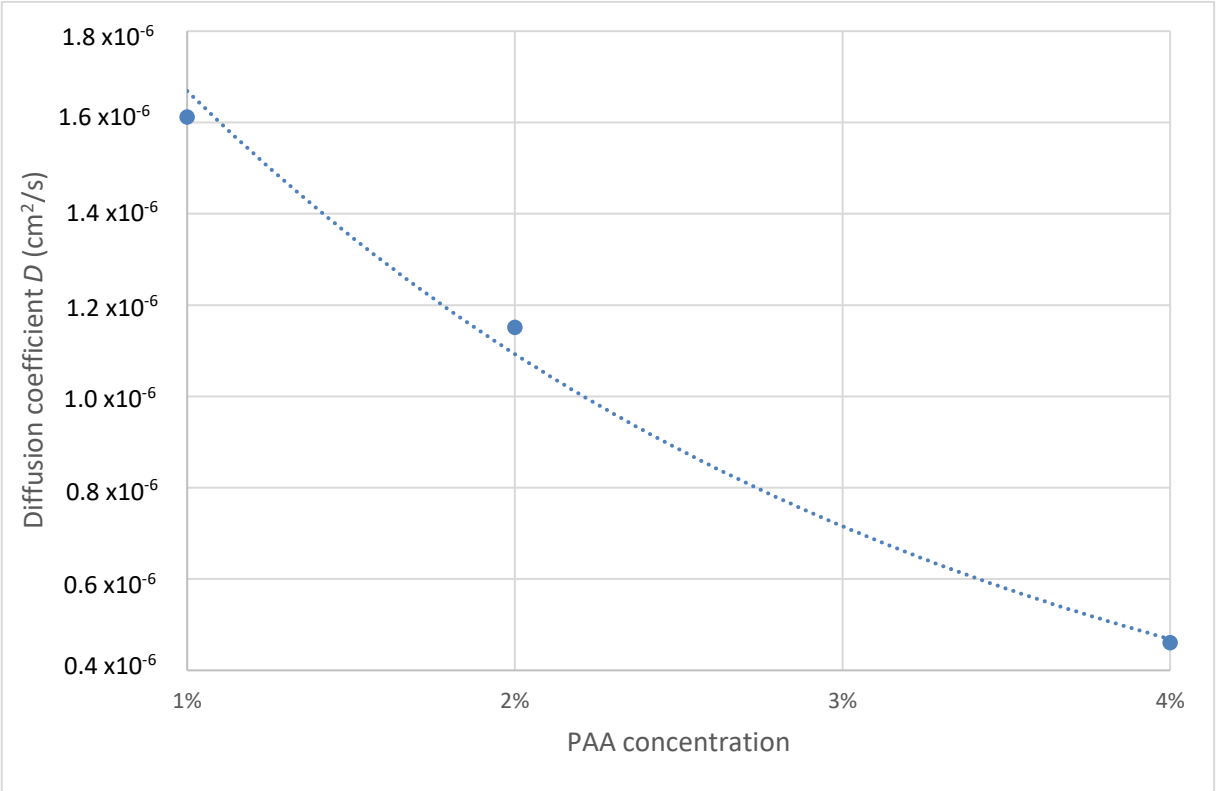

Figure 8.8: Potassium ferrocyanide diffusion coefficient estimated by steady-state microelectrode voltammetry against PAA concentration.

In Fig. 8.7 an anodic wave is observed at potentials > 0.25V due to oxidation of $FeCN_6^{4-}$. However, it can be seen from Figs 8.7 and 8.8 that the current due to oxidation of $FeCN_6^{4-}$ drops as the weight % of PAA increases. Assuming that the current at +0.6V is mass-transport limited and given by the usual equation for a microdisc of i_L=4nF*Dcr*, the effective diffusion coefficient for $FeCN_6^{4-}$ can be estimated. There is a relationship between diffusion coefficient and PAA concentration. The diffusion coefficients are of the expected order of magnitude expected for a small molecule moving through an aqueous medium (on the order of 10^{-6} cm^2s^{-1}), though slightly low. Despite the increase in macroscopic viscosity of PAA gels. The diffusion coefficients are of the expected order of magnitude expected for a small molecule moving through an aqueous medium (on the order of 10^{-6} cm^2s^{-1}), though slightly low. Despite the increase in macroscopic viscosity of PAA gels, it is known that there are diffusion pathways such as holes and voids within the network [186, 187].

Increasing the PAA concentration causes the diffusion coefficient to decrease. This indicates that the polymer chains are retarding the movement of the ferrocyanide molecule through the hydrogel. This is most likely to be a result of the anionic nature of the polymer hydrogel and strong repulsive interactions between the polymer network and $FeCN_6^{4-}$, which restricts access to channels between the polymer chains at high concentration. The effect appears analogous to Donnan exclusion [188].

PAA (g)	Demin. Water (ml)	$Ru(NH_3)_6Cl_3$ concentration (mM)
0.1	9.9	0.9
0.2	9.8	
0.4	9.6	

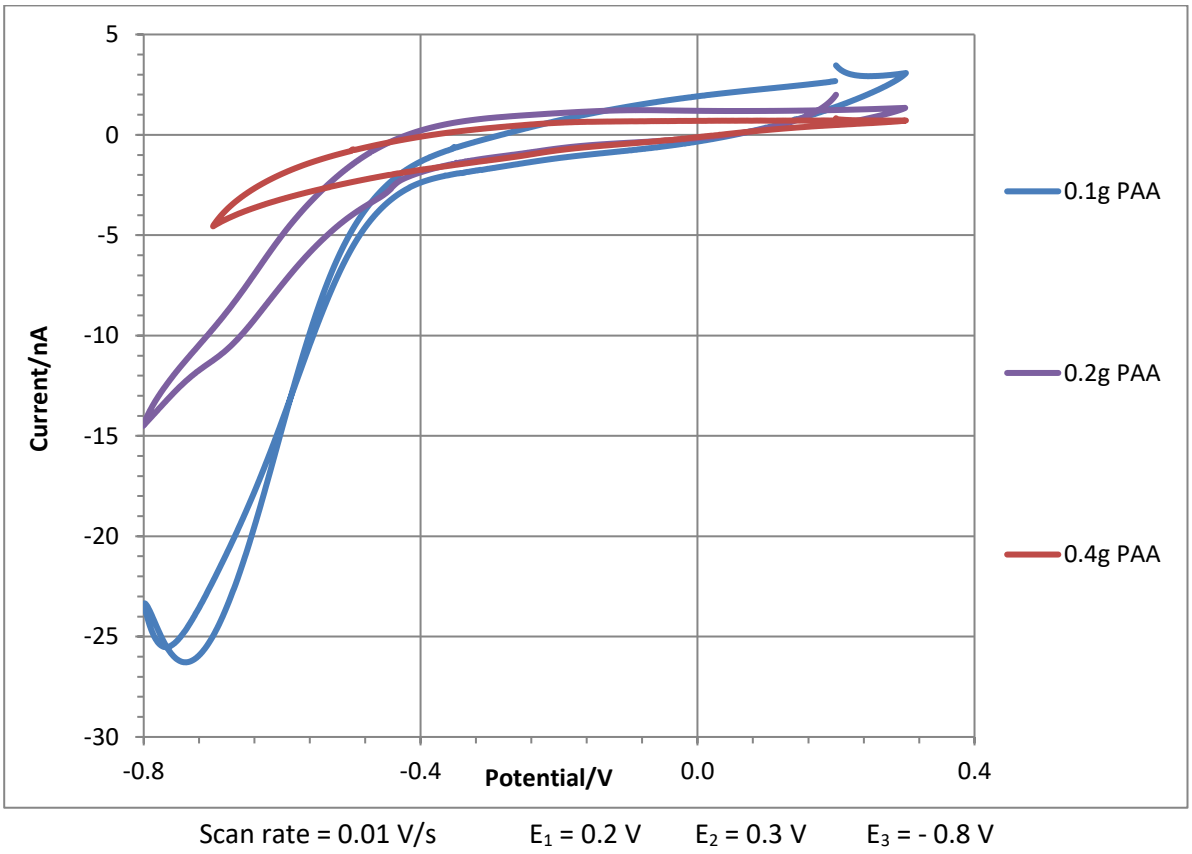

Figure 8.9: Cyclic voltammogram of hexaammineruthenium chloride gels with different amounts of PAA. (WE = 25 µm Pt disc, CE = 3 mm Pt disc, Ref = Ag/AgCl aq. 1 M KCl(aq))

Ruthenium hexaammine is another model redox couple, but in contrast to ferrocyanide is cationic. It undergoes a one-electron reduction [189]. Fig. 8.9 shows the corresponding data for $Ru(NH_3)_6^{3+}$. Even at the lowest concentration of PAA, the voltammetric shape is strongly distorted from the expected

sigmoidal steady-state wave. There is a clear cathodic process at potentials < -0.4V which may be used to make only very rough estimates of the diffusion coefficient because a well-defined limiting current is not clear in any of the voltammograms. The diffusion coefficient data is shown in Fig. 8.10 and, as expected, the diffusion coefficients are particularly small (order of magnitude 10^{-7} cm^2 s^{-1}). This is expected because the trication will be strongly bound to the anionic polymer.

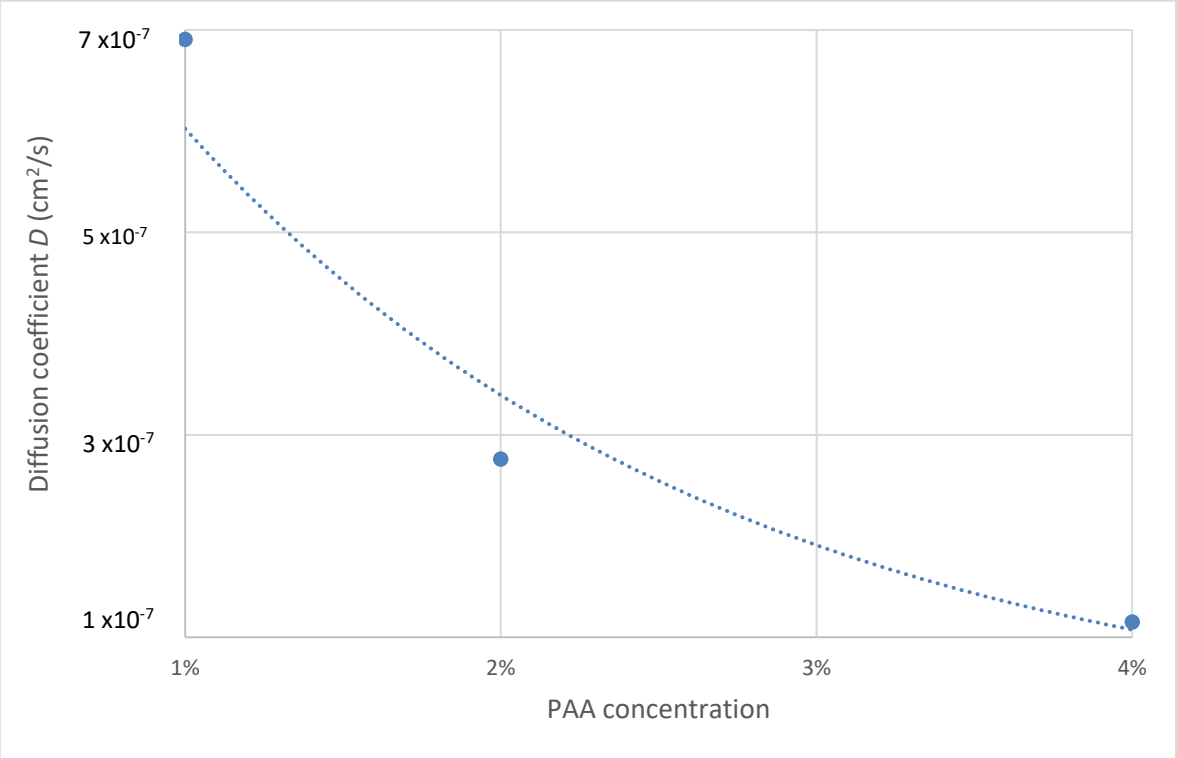

Figure 8.10: Hexaaminеruthenium chloride diffusion coefficient determined by steady-state microelectrode voltammetry against PAA concentration

PAA (g)	Demin. Water (ml)	1,4-BQ concentration (mM)
0.1	9.9	0.9
0.2	9.8	
0.4	9.6	
0.5	9.5	

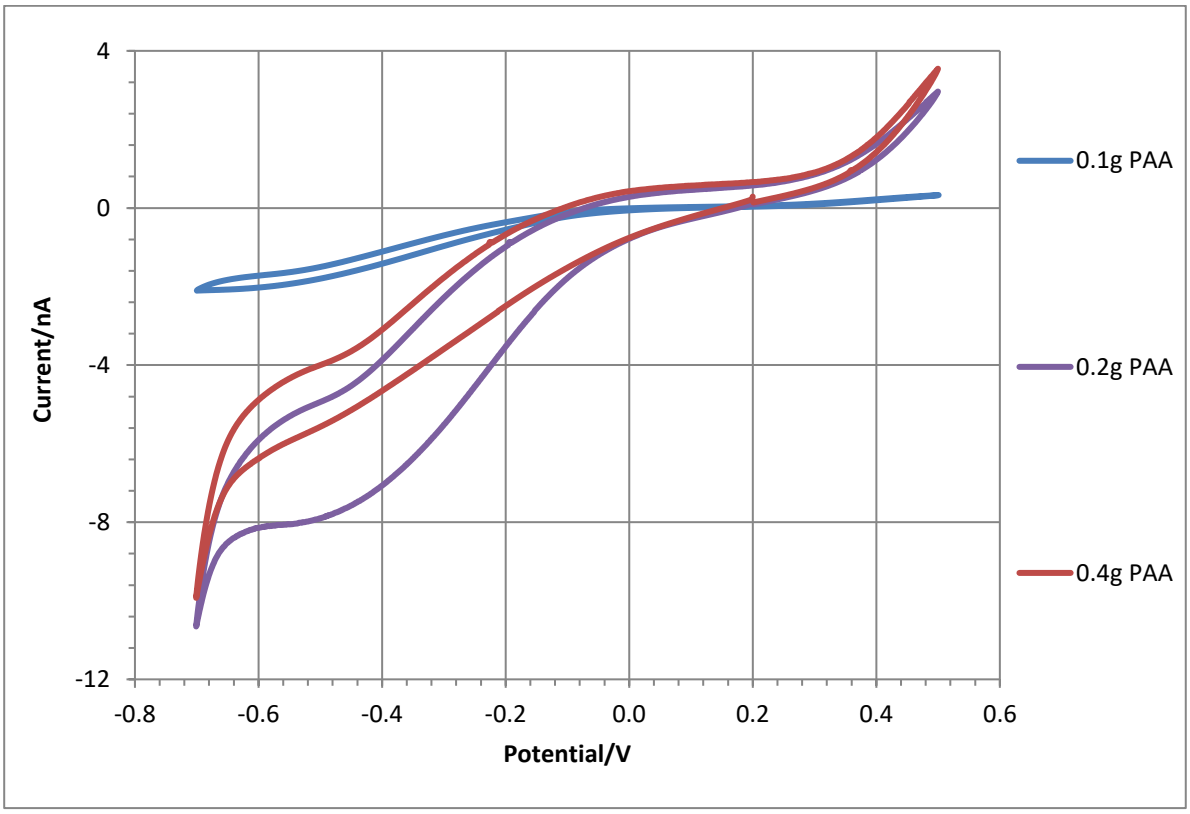

Scan rate = 0.01 V/s E_1 = 0.2 V E_2 = 0.5 V E_3 = - 0.7 V

Figure 8.11: Steady-state microelectrode voltammograms of para-benzoquinone-containing gels with different amounts of PAA. (WE = 25 µm Pt disc, CE = 3 mm Pt disc, Ref = Ag/AgCl aq. 1 M KCl(aq))

Fig. 8.11 shows the voltammetry of the final redox couple: benzoquinone / hydroquinone. This couple was chosen because both forms are neutral (each electron transfer is coupled to a rapid proton transfer) [190 - 193]. In this case there is a reasonably well-defined steady-state voltammogram at all concentrations of PAA. The cathodic process at E < -0.2 V is the reduction of benzoquinone and a steady-state current is clearly visible in the range -0.6 V < *E* < -0.4 V. The diffusion coefficients are of the order of 10^{-6} cm^2 s^{-1} as would be expected for a small molecule in aqueous solution. Unexpectedly, the diffusion coefficients actually increase slightly as more PAA is added.

The origin of this effect is unclear, but it is noticeable that the shape of the voltammograms is more distorted and they do not retrace at higher PAA concentrations. The hysteresis between forward and backward scans is not understandable on the basis of a diffusion mechanism but could be caused by adsorption of redox active material at the electrode surface.

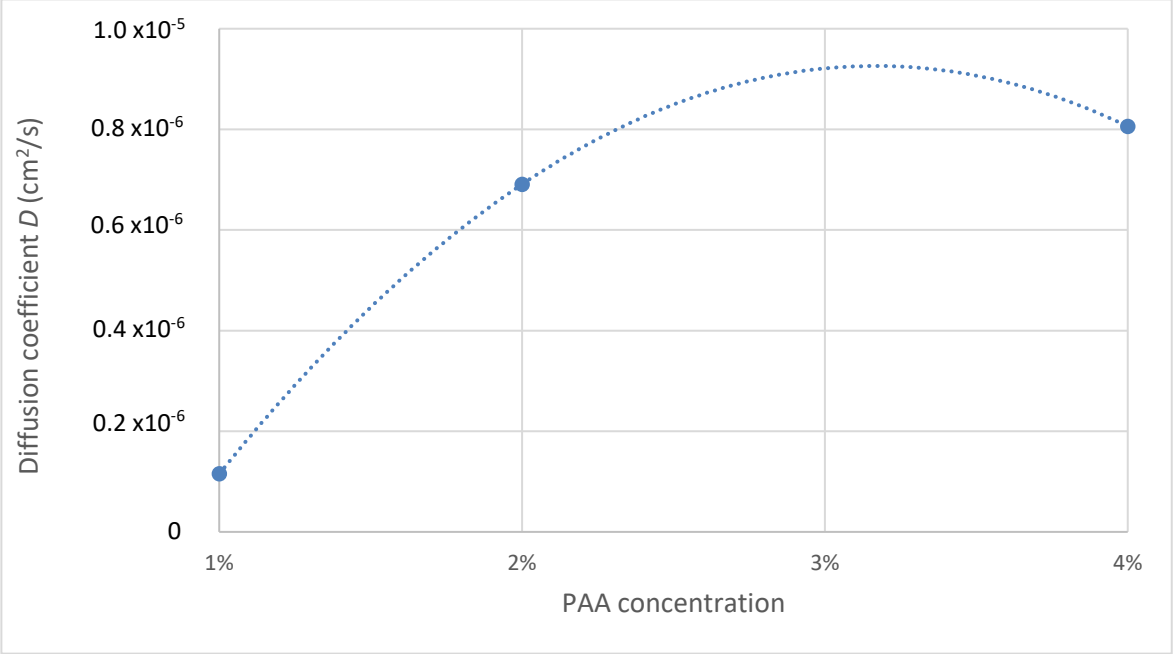

Figure 8.12: Para-benzoquinone diffusion coefficient estimated by steady-state microelectrode voltammetry against PAA concentration.

The voltammetric results from the three different redox couple species show that the hydrogel has a substantial influence on the electrochemical characteristics of each couple. This is as hypothesised, due to the fact that the redox species have different ionic charges. It is clear that the cationic redox couple is too strongly affected by the gel for it to be a useful electrolyte, however the neutral benzoquinone shows reasonable voltammetry. It should also be noted that the hydrogels have a relatively small electrochemical window (compared to gels) for cyclic voltammetry and other such electrochemical investigations, due to the high volume percentage of water in the electrolytes [194, 195]

8.4 Summary

The PAA hydrogels were investigated for their possible utility as electrolytes in gas sensors. The rheology measurements confirm that the PAA hydrogels behave as non-Newtonian fluids. At low shear rate there is a large increase in shear stress but at high shear rate there is only a small change in shear stress. Whilst the hydrogels would be under relatively low shear stress if they were deployed in the Alphasense electrochemical sensors, the fact that they are in a gel form makes them safer in the event of a physical breakage of the wall of the electrochemical cell. This is due to the hydrogels' viscosity makes it slower to leak out and subsequently easier and safer to handle when cleaning up a spillage. This is an important consideration in the transportation of commercial products that contain potentially harmful substances such as acidic electrolyte. Unfortunately, the hydrogels proved to be too susceptible to loss of water over storage times of several days. This might be ameliorated by development of the hydrogel composition in the future and therefore an assessment of their electrochemical behaviour was nevertheless made.

Anionic, cationic and neutral redox couples showed very different electroanalytical behaviour. For potassium ferrocyanide, there is a clear limiting current at potentials > 0.3 V for low PAA concentrations (Fig 8.7). However, this limiting current generally gets smaller as the amount of polyacrylamide co-acrylic acid (PAA) increases. This behaviour is probably connected to the repulsion between the PAA anion and the anionic ferrocyanide and the exclusion of the ferrocyanide from the pores and voids in the network that would otherwise facilitate diffusion.

For the cationic couple, $Ru(NH_3)_6^{3+/2+}$, the shape of the voltammograms is rather distorted and a clearly-defined steady-state wave is not observed. The voltammograms, though retraceable, do not have the expected sigmoidal shape and even show a current maximum at the lowest PAA concentration. This indicates a non-ideal behaviour of the couple in this electrolyte. This observation is expected based on a strong ionic interaction between the trication and the anionic polyelectrolyte.

Only the electrically neutral couple (p-benzoquinone/hydroquinone) shows voltammograms that are of the expected sigmoidal shape. The diffusion coefficients determined are compared to small molecules in aqueous solution. The weight-loss behaviour indicates that, the PAA hydrogels are unsuitable electrolytes for amperometric gas sensors. If the hydrogel could be engineered to retain at least part of the water and keep a stable mass after a conditioning phase, then the PAA gels would be viable as an alternative to sulphuric acid electrolytes. It is worth noting that the current devices do need a stabilisation period of about 24 hrs anyway because of the large capacitive currents and slow decay of the background discussed in previous chapters (Chapters 4 and 5). The issues with charged redox couples suggest that analytes which dissolve to form ionic species (SO_2, CO_2, NOx, HCl) would be difficult to sense with gel-electrolyte based devices. However, many relevant gaseous analytes (CO, H_2) produce only neutral species upon dissolution in water and the further development of gel electrolytes would be of interest.

[176] Agency for Toxic Substances and Disease Registry
Public Health Statement for Sulfur Trioxide and Sulfuric Acid, 1998

[177] ECHA website accessed May 2019
European Chemicals Agency

[178] S. Zhu, R. H. Pelton, A. E. Hamielec
Eur. Polym. J., 1998, **23**, 376-381

[179] J. E. Elliott, M. Macdonald, J. Nie, C. N. Bowman
Polymer, 2004, **45**, 1503-1510

[180] S. Tamburic, D. Q. M. Craig
Pharm. Res., 1996, **13**, 279-283

[181] L. Bromberg, M. Temchenko, V. Alakhov, T. A. Hatton
Int. J. Pharm., 2004, **282**, 45-60

[182] F. C. Carvalho, G. Calixto, I. N. Hatakeyama, G. M. Luz, M. P. D. Gremiao, M. Chorilli
Drug Dev. Ind. Pharm., 2013, **39**, 1750-1757

[183] S. Nesrinne, A. Djamel
Arab. J. Chem., 2017, **10**, 539-547

[184] T. Gennet, M. J. Weaver
Anal. Chem., 1984, **56**, 1444–1448

[185] D. O. Wipf, E. W. Kristensen, M. R. Deakin, R. M. Wightman
Anal. Chem., 1988, **60**, 306–310

[186] A. O'Mahony, D. Silvester, L. Aldous, C. Hardacre, R. Compton
J. Chem. Eng. Data, 2008, **53**, 2884–2891

[187] R. White (ed.)
Modern Aspects of Electrochemistry, 2009, **45th Edn.**, Springer, New York

[188] *https://goldbook.iupac.org/terms/view/DT06889*

[189] T. Iwasita, W. Schmickler, J. W. Schultze
Phys. Chem., 1985, **89**, 138–142

[190] D. Kim, J. Wang, J. Yang, H. Kim, G. Swain
J. Phys. Chem. C, 2011, **115**, 10026-10032

[191] R. Janek, W. Fawcett
Langmuir, 1998, **14**, 3011-3018

[192] S. J. Konopka, B. McDuffie
Anal. Chem., 1970, **42**, 1741-1746

[193] D. Corrigan
J. Electrochem. Soc., 1987, **134**, 377-384

[194] A. Lee, D. Vella, S. Perkin, A. Goriely
J. Phys. Chem. Lett., 2015, **6**, 159−163

[195] M. Allian, A. Germain, F. Figueras
Catalysis Letters, 1994, **28**, 409-415

Chapter 9

9.0 Conclusions

Amperometric gas sensors are difficult to study by common electroanalytical techniques because the nanoparticulate nature of the working electrodes results in a very large differential capacitance. As discussed in chapters 5-6, the amount of information that can be obtained by cyclic voltammetry and impedance spectroscopy is limited. Instead, potentiostatic measurements are required. A diffusion model has therefore been developed for commercial (Alphasense) amperometric gas sensors. Three sensor types were studied: (i) CO-AF which is a standard, successful CO sensor in which the gas membrane is covered with a silica/permanganate filter layer to remove sulphur-based catalytic poisons and maintain the activity of the Pt nanoparticle working electrode; (ii) CM-A1 where the electrocatalyst is a Pt/Ru alloy and (iii) CO-A1 where the silica filter layer of CO-AF is omitted. The model is based on the transient response of the sensor under potentiostatic conditions to a sudden change in analyte concentration.

The results of chronoamperometric experiments show that the steady-state and transient response of amperometric gas sensors in CO can be modelled using the diffusion equation. The analysis provides an effective diffusion coefficient, *D* and an effective thickness of the diffusion barrier, *L* for a layer structure of arbitrary complexity. For both the standard and thick membrane CO-AF sensors, the values of *D* (on the order of 10^{-3} cm^2s^{-1} at 20 °C) are more readily interpreted in terms of diffusion in the gas phase than liquid, when compared to the CO diffusion coefficient literature values of approximately 0.2 cm^2s^{-1} in air and 2 $x10^{-5}$ cm^2s^{-1} in water when measured via computational simulation and experimental procedures [196, 197]. Although the diffusion coefficients are smaller than in air, they can be interpreted in terms of gas phase diffusion in pores and voids but are two orders of magnitude larger than reasonable liquid phase values. The regression model indicates that the rate limiting diffusion step is when the CO is in the gas phase within the silica supported permanganate powder, before reaching the semi-permeable membrane and the electrolyte.

The weak temperature dependence of the diffusion coefficients in CO-AF devices is further evidence for a gas-phase transport mechanism, rather than the activated behaviour typical in condensed phase diffusion. However, the CM-A1 sensor response to CO showed *D* and *L* values that are more typical of diffusion in the liquid phase, having a *D* value on the order of 10^{-5} cm^2s^{-1} and a much smaller *L* value than the CO-AF sensor (approximately 0.04 cm and 0.27 cm respectively). For the VOC measurements with the CO-A1 sensor, the final oxidation product is either a carboxylic acid or ketone (when *n* = 2 or 4). The small effective *D* values along with the fact that the steady state current response is potential dependent for some analytes (especially methanol), suggests kinetic limitations at the electrode surface and condensation of the VOCs in the pores of the membrane. Nevertheless, the CO-A1 device shows promise for the detection of primary, secondary alcohols and aldehyde vapours.

Finally, an investigation into the possibility of replacing the standard sulphuric acid electrolyte with polyacrylic acid hydrogels was made. Rheological data shows that the potassium salt of polyacrylic acid forms hydrogels at a relatively low weight percentage of PAA and satisfactory voltammetry of a neutral test redox couple (p-benzoquinone/hydroquinone) was obtained. However, both anionic and cationic redox probes (ferrocyanide, ruthenium hexaamine) showed poorly defined voltammetric responses and, especially in the case of ruthenium hexamine, the diffusion rates were suppressed in the gel. Nevertheless, the PAA gels appear usable electrolytes for neutral species. The major issue with the gels was their lack of stability on storage under ambient conditions, owing to evaporation of water.

There is a trend in shear stress as PAA concentration increases in the hydrogels (Fig. 9.1). The increase in shear stress as PAA concentration increases indicates that the PAA causes a change in the morphology of the hydrogel. The long chains of PAA for a lattice matrix and cause the hydrogel to act more like a solid as they increase the stiffness of the hydrogel. By measuring the shear stress at different hydrogel concentrations, the integrity of the polymer lattice matrix can be determined.

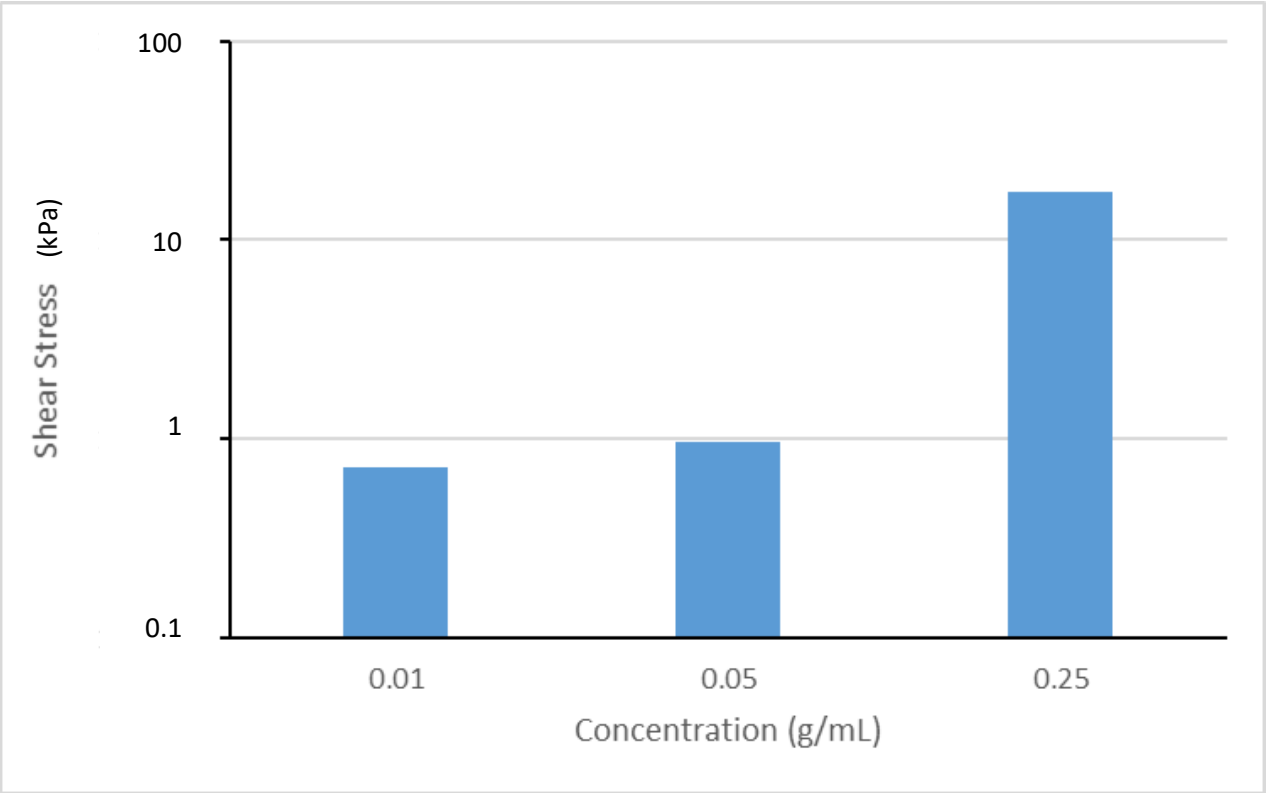

Figure 9.1: Shear stress of different hydrogel concentrations at constant shear rate

9.1 Future Work

Any future work would ideally involve the use of different techniques such as IR spectroscopy and HPLC to identify the actual bonds formed and surface coverage during the electrochemical process. Whilst such techniques combined with electrochemistry are already described in the literature [198 - 201], they are difficult to implement on a high surface area electrode under the normal operating conditions of a commercial sensor. It would also help to clarify the type of adsorption occurring at the electrode surface as different types can occur during electrochemistry. Computational results based upon small molecule reactions on a Pt surface indicate that multiple reaction mechanisms are viable [202, 203]. This would lead to a greater understanding of the reaction pathways and mechanism as it would allow back calculation of the number of electrons involved in the reaction and confirmation of the activation energy requirements for different pathways. The activation energy requirements could also be investigated via computational chemistry. There are already reports in the literature of DFT calculations for electrochemical characterisation of Pt as the working electrode [204 - 207], albeit usually with much simpler molecules such as hydrogen. These show that things such as water adsorption on the Pt surface can affect the electrochemical response of the sensor and that differences in surface geometry such as Pt(111) compared to Pt(332) affect the adsorption energy characteristics.

It would also be useful to test more primary alcohols to give a better understanding of the trends in *L* and *D* values. Ideally, we could eventually expand the list of compounds investigated to include hydroxylamine and such functional groups as amines and amides (and possibly other functional groups), as this would reveal more information as to the nature of the proton stripping and adsorption sites. If a different pattern of selectivity were obtained with a different electrocatalyst, then usage of multiple devices and chemometric analysis may allow the identification of species rather than detection of classes of VOC. The condensation of the VOCs in the porous membrane appears to be a limiting factor and therefore investigation of the effect of membrane hydrophobicity on the selectivity and sensitivity would be relevant; at present the devices only use a single membrane type, which is very hydrophobic.

Testing the VOCs at different temperatures with different types of semi-permeable membranes could yield more information as to the diffusion coefficient and layer thickness contributing factors of the CO-A1 sensors. Investigation into the electrooxidation of CO by the use of different electrode materials such as carbon, gold, silver, iron oxide or tin compounds would also be beneficial to enable comparison of the electrochemical properties of different metals. This would serve as a starting point for evaluating metal alloys that can be used for the next generation of CO or VOC sensors. Whilst similar investigations have already been undertaken in the literature, they use a relatively simple experimental setup compared to the complex multi-phase stack system employed within the CO-AF sensors [208 - 211]. Thus, it is worthwhile conducting the investigations as part of further work in the future stemming from this thesis. Use of different platinum metal alloys (such as Pt-Sn) for the electrooxidation of VOCs (such as short chain primary alcohols) and other organic compounds in acidic and alkaline media has already been extensively reported in the literature [212 - 215], although again only investigated in relatively simple systems.

It may be of interest to increase the range of potentials used during cyclic voltammetry. This would give insight into the limits of the capabilities of the sensor and the corresponding amperometric detection of CO (via electrooxidation) at large positive potentials. Such a voltammogram is shown below (Fig. 9.2), although the potential range used throughout the thesis is – 0.1 V to 0.3 V due to the sensor design for low current and voltage on a PCB board to ensure longer operating lifetimes. It can be seen from the voltammogram that between 0.0 V to 0.3 V the background current is relatively potential independent. It should be noted that the currents in figure 9.2 are not due to oxidation of CO but are related to the high surface area of the working electrode as shown in chapter 4. At higher potentials, the background current increases rapidly (this may be due to oxidation of Pt) and it becomes much more difficult to obtain a stable baseline and to distinguish the background from the analytical signal.

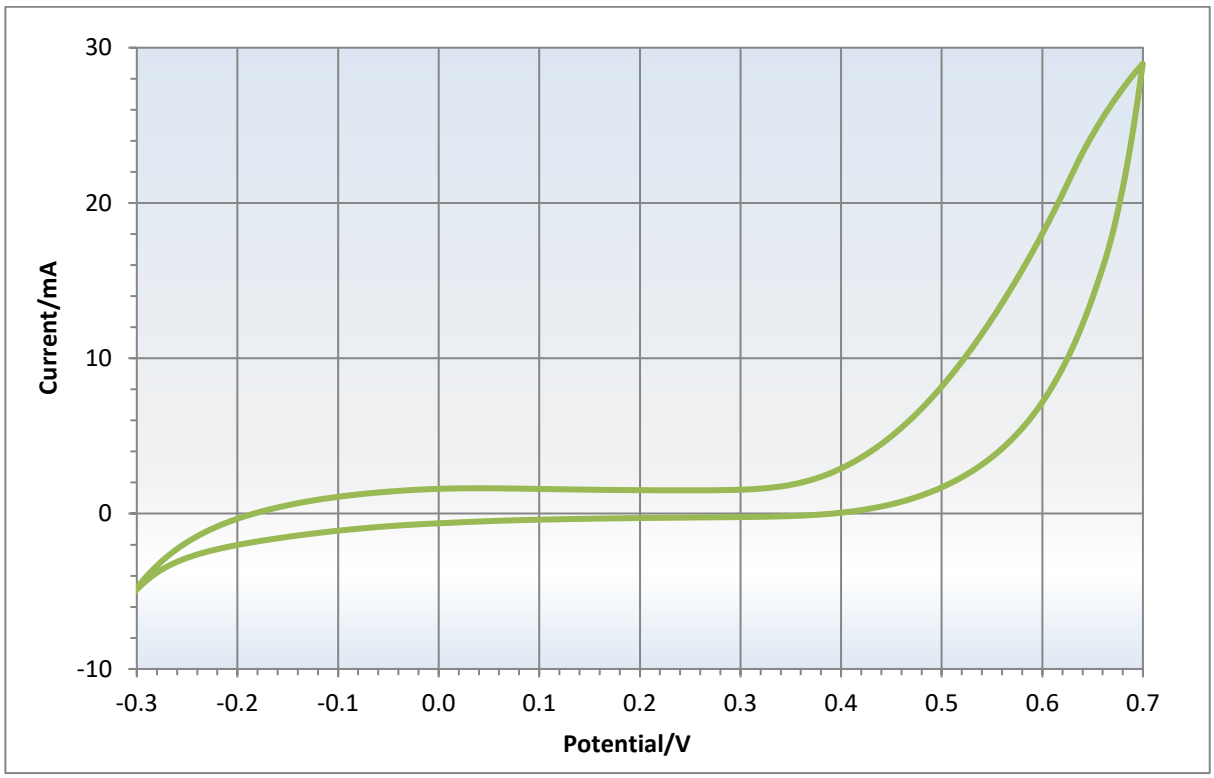

Figure 9.2: Cyclic voltammogram of CO-AF sensor with wide current range

(CO at constant 200 ppm at 20 °C at a scan rate of 1 mV/s)

[196] W. J. Massman
Atmos. Environ., 1998, **32**, 1111-1127

[197] I. Poudyal, N. P. Adhikari
J. Mol. Liq., 2014, **194**, 77-84

[198] P. A. Christensen, D. Linares-Moya
J. Phys. Chem. C, 2010, **114**, 1094-1101

[199] T. Iwasita, W. Vielstich
J. Electroanal. Chem., 1988, **257**, 319-324

[200] A. Santasalo-Aarnio, Y. Kwon, E. Ahlberg, K. Kontturi, T. kallio, M. T. M. Koper
Electrochem. Commun., 2011, **13**, 466-469

[201] R. Parsons
Surface Science, 1980, **101**, 316-326

[202] R. Parsons, G. Ritzoulis
J. Electroanal. Chem. Inter. Chem., 1991, **318**, 1-24

[203] E. Skulason, G. S. Karlberg, J. Rossmeisl, T. Bligaard, J. Greeley, H. Jonsson, J. K. Nørskov
Phys. Chem. Chem. Phys., 2007, **9**, 3241-3250

[204] A. Ferre-Vilaplana, R. Gisbert, E. Herrero
Electrochimica Acta, 2014, **125**, 666-673

[205] R. Jinnouchi, T. Hatanaka, Y. Morimoto, M. Osawa
Electrochimica Acta, 2013, **101**, 254-261

[206] R. Jinnouchi, K. Kodama, Y. Morimoto
J. Electroanal. Chem., 2014, **716**, 31-44

[207] F. Liu, C. Wu, G. Yang, S. Yang
J. Phys. Chem. C, 2015, **119**, 15500-15505

[208] A. Boulahouache, G. Kons, H-G. Lintz, P. Schulz
Applied Catalysis A: General, 1992, **91**, 115-123

[209] Y-N. Sun, Z-H. Qin, M. Lewandowski, E. Carrasco, M. Sterrer, S. Shaikhutdinov, H-J. Freund
J. Catalysis, 2009, **266**, 359-368

[210] M. E. Moragues, A. Toscani, F. Sancenon, R. Martinez-Manez, A. J. P. White, J. Wilton-Ely
J. Am. Chem. Soc., 2014, **136**, 11930-11933

[211] G. Shi, T. Yoon, S. Cha, S. Kim, M. Yousuf, N. Ahmed, D. Kim, H.-W. Kang, K. S. Kim
ACS Sens., 2018, **3**, 1102-1108

[212] A. S. Aricò, V. Antonucci, N. Giordano, A.K. Shukla, M.K. Ravikumar, A. Roy, S.R. Barman, D.D. Sarma
J. Power Sources, 1994, **50**, 295-309

[213] J. Zeng, J. Y. Lee
J. Power Sources, 2005, **140**, 268-273

[214] Y. Wang, S. Zou, W-B. Cai
Catalysts, 2015, **5**, 1507-1534

[215] R. Rizo, D. Sebastian, M. J. Lázaro, E. Pastor
Applied Catalysis B: Environmental, 2017, **200**, 246-254